Experimental and Theoretical Study of the Stress and Strain Fields Around Fatigue Cracks and Plasticity-Induced Crack Closure

Thesis

UNRESTRICTED

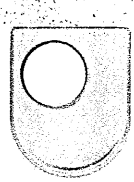

The Open University

Experimental and Theoretical Study of the Stress and Strain Fields around Fatigue Cracks and Plasticity-Induced Crack Closure

Md. Moshiur Rahman
BSc Eng, MSc

Thesis submitted to the Department of Design, Development, Environment and Materials of The Open University, UK for the degree of Doctor of Philosophy

February 2008

DATE OF SUBMISSION: 12 FEBRUARY 2008
DATE OF AWARD: 4 JUNE 2008.

ProQuest LLC.
789 East Eisenhower Parkway
P.O. Box 1346
Ann Arbor, MI 48106 – 1346

Abstract

This work investigates experimentally and theoretically the local crack tip stress and strain fields, and plasticity-induced crack closure acting on the crack flanks behind the crack tip, in fine-grained aluminium alloy 5091 (Al-Mg-Li-C-O) compact tension fatigued specimens. Compressive residual stresses ahead of the crack tip and plasticity-induced crack closure are often attributed to be the two main mechanisms responsible for crack growth retardation. Specimens investigated were prepared: with constant amplitude fatigue; with constant amplitude fatigue followed by a single overload; and finally with constant amplitude fatigue followed by a single overload followed by further constant amplitude fatigue. Experimental crack tip strain (and hence stress) measurements have been carried out along the mid-thickness of the specimens using energy dispersive X-ray diffraction (EDXRD) at the European Synchrotron Radiation Facility (ESRF), Grenoble, France. The very small grain size of aluminium alloy 5091 allows minimization of the sampling volume in order to maximize the spatial resolution achievable with EDXRD. High spatial resolution is essential for measuring highly localized crack tip stresses. For theoretical investigations of the crack tip stress and strain fields, existing analytical solution (Westergaard, 1939) and the finite element code ABAQUS (ABAQUS Inc., 2004) have been used. Crack closure has been investigated by finite element analysis and compliance experimental technique. Finite element analyses for both stress fields and crack closure have been carried out in plane stress and plane strain. A possible link between the stresses ahead of the crack tip and the plasticity-induced crack closure on the crack flanks behind the crack tip has been investigated.

Acknowledgements

I would like to express my profound gratitude to my supervisors Dr Mike Fitzpatrick and Prof Lyndon Edwards for their sincere guidance, encouragement and support during this work.

I would acknowledge the financial support of The Open University, UK for this research. I also acknowledge the access to beam time for experiments at the European Synchrotron Radiation Facility (ESRF), Grenoble, France under the proposal HS-2252. The finite element code ABAQUS was provided under academic license from ABAQUS Inc.

I would like to thank all the staff and students of the Materials Engineering Group for their support throughout this research. Particular thanks are due to Dr David Liljedahl for his help with the finite element analysis. Thanks are also due to Pete Ledgard, Stan Hiller, Ian Norman and Dr Jim Moffatt for their help and technical support. I would like to thank Dr Sumit Pratihar, Dr Supriyo Ganguly, Mehmet Kartal, Dr Mulyadi, Olivier Zanellato, Ashwin Rao and Susan Storer for their friendly help and cooperation during this work.

I am profoundly grateful to my late mother whose dream inspired me to pursue this study. My deepest thanks and regards are due to my father, father-in-law and mother-in-law for their continuous support, encouragement and good wishes over the years during this work. I would like to express my gratitude to my grandma and aunts for their good wishes. Thanks are due to my brothers, brother-in-law, family members and relatives for their support and encouragement during this work.

Finally, I would like to express my deepest thanks to my wife, Nazma Parvin and daughter, Nishat Tarannum for their continuous support and inspiration over the years.

Declaration

This thesis is submitted for the degree of Doctor of Philosophy of The Open University, UK. The work described in this thesis was carried out in the Department of Design, Development, Environment and Materials of The Open University, between October 2004 and February 2008 under the co-supervision of Dr. Mike Fitzpatrick and Prof Lyndon Edwards. The work reported here is the original work of the author except where referenced. None of this work has been submitted for a degree or other qualification at this or any other university. Some of the work has been submitted for publication as follows:

M. Rahman, M.E. Fitzpatrick, L. Edwards, S. Pratihar, M. Peel and T. Buslaps, Investigation of the stress fields around a fatigue crack in aluminium alloy 5091, Materials Science Forum (accepted for publication in 2007).

A. Steuwer, M. Peel, T. Buslaps, L. Edwards, M. Rahman and M.E. Fitzpatrick, The high resolution determination of residual stresses using energy dispersive X-ray diffraction, submitted to MECASENS III conference, 17-19 October 2005, Santa Fe, USA for publication in Journal of Neutron Research.

Nomenclature

σ_{ij}	Stress tensor
$\sigma_{11}, \sigma_{22}, \sigma_{33}$	Normal stresses in the x_1, x_2 and x_3 directions respectively
$\sigma_{xx}, \sigma_{yy}, \sigma_{zz}$	Stress components in the x, y and z directions respectively
σ_m	Hydrostatic stress
σ_n	Normal stress
$\sigma_{12}, \sigma_{23}, \sigma_{31}$	Shear stresses
$\sigma_1, \sigma_2, \sigma_3$	Principal stresses
$\sigma_{max}, \sigma_{min}$	Maximum and minimum applied stresses in a fatigue cycle respectively
σ_y	Yield strength
τ_{max}	Maximum shear stress
τ_{min}	Minimum shear stress
τ_y	Shear yield strength
ε_{ij}	Strain tensor
$\varepsilon_1, \varepsilon_2, \varepsilon_3$	Principal strains
$\varepsilon_{11}, \varepsilon_{22}, \varepsilon_{33}$	Normal strains in the x_1, x_2 and x_3 directions respectively
$\varepsilon_{xx}, \varepsilon_{yy}, \varepsilon_{zz}$	Strain components in the x, y and z directions respectively
$\gamma_{12}, \gamma_{23}, \gamma_{31}$	Shear strains
ν	Poisson's ratio
E	Young's modulus
G	Shear modulus

$\bar{\sigma}$	Equivalent stress
$\bar{e}$	Equivalent strain
$\bar{e}^p$	Equivalent plastic strain
$d\bar{e}^p$	Equivalent plastic strain increment
$d\varepsilon_1^p, d\varepsilon_2^p, d\varepsilon_3^p$	Principal plastic strain increments
$d\varepsilon_{11}^p, d\varepsilon_{22}^p, d\varepsilon_{33}^p$	Non-principal plastic strain increments
$d\gamma_{12}^p, d\gamma_{23}^p, d\gamma_{31}^p$	Shear plastic strain increments
$\varepsilon_{11}^{el}, \varepsilon_{22}^{el}, \varepsilon_{33}^{el}$	Normal elastic strain components
$\gamma_{12}^{el}, \gamma_{23}^{el}, \gamma_{31}^{el}$	Shear elastic strain components
K	Stress intensity factor
K_I, K_{II}, K_{III}	Mode I, mode II and mode III stress intensity factors respectively
K_{IC}	Mode I fracture toughness
K_{max}, K_{min}	Maximum and minimum applied stress intensity factors in a fatigue cycle respectively
K_{op}, K_{cl}	Stress intensity factors at which a crack opens and closes respectively
K_c	Critical stress intensity factor, i.e., the fracture toughness
K_{ol}	Overload stress intensity factor
ΔK	Stress intensity factor range in a fatigue cycle
ΔK_{th}	Threshold stress intensity factor range
ΔK_{eff}	Effective stress intensity factor range
R	Ratio of K_{min} to K_{max}
T	T-stress, a uniaxial stress parallel to the crack flanks
G	Energy release rate

r	Distance from the crack tip
r_y	Plastic zone size at the crack tip
$r_{y(monotonic)}$	Monotonic plastic zone size at the crack tip
$r_{y(reverse)}$	Reverse plastic zone size at the crack tip
$r_{y(ol)}$	Overload plastic zone size at the crack tip
λ	Wavelength of incident beam
E	Energy of incident beam
d	Inter-planar spacing of stressed material
d_0	Inter-planar spacing of unstressed material
a	Lattice parameter of stressed material
a_0	Lattice parameter of unstressed material
θ	Bragg angle
h	Planck's constant
c	Speed of light
m	Mass of neutron
v	Velocity of neutron
t	Time-of-flight of neutron
l	Flight path length
W, B, a	Width, thickness and crack length of specimen respectively
n	Strain hardening exponent
ε	True strain
ε_p	True plastic strain

Contents

Chapter 1 Introduction

Engineering components (mechanical or structural) may contain cracks or defects, which may compromise their structural integrity under fatigue loading. Fatigue crack propagation analysis is intended to ensure the safety of components and structures such as aircraft wings, railway axles, components of nuclear installations and chemical plants for avoiding loss of life and providing financial savings.

Much research has been carried out in the last four decades in order to provide insight into the mechanism of fatigue crack propagation. Although researchers have had some degree of success in establishing methods for analysing constant amplitude fatigue (Paris et al., 1961, Paris and Erdogan, 1963, Weertman, 1966, Forman et al., 1967, Elber, 1970, Klesnil and Lucas, 1972, Donahue et al., 1972, McEvily, 1988), questions have still been unanswered about crack growth mechanisms and overload-underload interactions under variable amplitude fatigue. Compressive residual stress fields ahead of the crack tip (Wheeler, 1972, Matsuoka and Tanaka, 1978, Lang and Marci, 1999) and plasticity-induced crack closure on the crack flanks behind the crack tip (Elber, 1971, Shin and Fleck, 1987, Ward-Close et al., 1989, Damri and Knott, 1991) are often discussed to be the two main mechanisms responsible for retardation of fatigue crack growth. Fatigue crack growth is driven by the stress intensity factor range, ΔK (K_{max}–K_{min}) and the R ratio (the load ratio, K_{min}/K_{max}) of the fatigue cycle. An overload produces compressive residual stresses ahead of the crack tip (Schijve, 1961, Ramos et al., 2003), which alter the local crack tip stresses under baseline loading, i.e., at K_{max} and K_{min} of the fatigue cycle. On the other hand, due to plasticity-induced crack closure the crack

remains closed at K_{min} of the fatigue cycle. Therefore, in this case ΔK is computed from K_{op}, the stress intensity factor at which the crack opens, instead of using K_{min}. As a result, plasticity-induced crack closure reduces ΔK (as $K_{op}>K_{min}$), resulting in crack retardation. Therefore, determination of crack tip stress fields both on the surface and deep inside the material of the component, and investigation of any possible link between crack tip stress fields and plasticity-induced crack closure, for both constant and variable amplitude fatigue, are essential in assessing component fatigue life.

There have been theoretical studies (Westergaard, 1939, Williams, 1957, Hutchinson, 1968a&b, Newman, 1976, Ogura and Ohji, 1977, Sun and Sehitoglu, 1992) and surface X-ray measurements (Allison, 1979, Holloway, 1979, Wang et al., 1999, Ramos et al., 2003) concerning the stress fields around the tips of stationary and growing fatigue cracks. However, until recently direct measurement of the highly-localized stresses around the crack tip in the interior of the specimen has not been possible due to the unavailability of an appropriate technique. With the current generation of synchrotron X-ray sources, sub-millimetre sampling dimensions (Knapp et al., 1996, Lienert et al., 2001, Tamura et al., 2002) are now possible, and coupled with fine-grained alloys it has become possible to evaluate directly the stresses at the tip of a fatigue crack in the interior of the specimen, as a reasonably high penetration depth is achievable with this technique (Lebrun et al., 1995, Daymond and Withers, 1996, Webster et al., 1996, Withers and Webster, 2001).

Efforts have been made to establish a possible link or separation between the generation of the compressive residual stresses ahead of the crack tip and the crack

closure acting on the crack flanks behind the crack tip affecting the crack growth rate (Lang and Marci, 1999, McEvily and Ishihara, 2001). Lang and Marci (1999) have discussed that under variable amplitude loading crack growth is governed mainly by the compressive residual stresses ahead of the crack tip and the crack closure has only a small secondary influence, which could even be neglected. McEvily and Ishihara (2001) have concluded that the overload compressive residual stresses ahead of the crack tip and the level of crack closure behind the crack tip are intimately related for a crack growing through the overload plastic zone.

This thesis investigates experimentally and theoretically the local crack tip stress and strain fields and plasticity-induced crack closure, and thereby any possible correlation between the crack tip stress fields and plasticity-induced crack closure for fatigued, fatigued-overloaded and fatigued-overloaded-fatigued cracks in fine-grained aluminium alloy 5091 (Al-Mg-Li-C-O) compact tension specimens. The experimental stress measurements have been carried out using energy dispersive X-ray diffraction (EDXRD) at the European Synchrotron Radiation Facility (ESRF), Grenoble, France. For the theoretical investigations of the crack tip stress fields existing analytical solution (Westergaard, 1939) and a finite element model using ABAQUS (ABAQUS, Inc., 2004) have been applied. Crack closure has been investigated using the finite element code ABAQUS and the compliance experimental technique.

Most of the previous experimental investigations of the stress fields around fatigue cracks were based on the surface X-ray measurements (in plane stress region). The main aim of this thesis is to investigate what is believed to be the first direct

EDXRD measurements of the 2D crack tip strain and stress fields deep within the loaded aluminium alloy 5091 specimens (in plane strain region) at a high spatial resolution (with 25×25μm lateral gauge dimensions). Results are presented under in-situ loading for constant amplitude fatigue as well as during and after an overload event. The experimental results are compared to and validated by the results obtained using finite element analysis. The additional objective of this work is to provide a clear understanding of the plasticity-induced crack closure phenomenon in aluminium alloy 5091 compact tension specimens under constant amplitude fatigue and after a single overload event.

Following this introductory chapter, Chapter 2 reviews the basic concepts of stress, strain, elastic stress-strain relations, plane stress and plane strain, yield criteria and plasticity, and concludes with the fundamental concepts of fracture mechanics related to fatigue crack growth. Chapter 3 discusses diffraction techniques used for strain measurements in engineering components. Chapter 4 presents experimental and theoretical results of the strain and stress fields around fatigue cracks in aluminium alloy 5091 compact tension specimens. Chapter 5 discusses results of a detailed finite element investigation of the stress fields around fatigue cracks, and a comparison of these results with the experimental results presented in Chapter 4. Numerical and experimental results of plasticity-induced crack closure investigation are presented in Chapter 6. Finally, Chapter 7 concludes the present work with a future direction.

Chapter 2 Review of the relevant concepts

2.1 Introduction

This chapter reviews the basic concepts of the mechanics of materials, and fracture mechanics related to fatigue crack growth, which are relevant to the present work. Part of the discussion includes stress, strain and their relations in elasticity and plasticity, plane stress and plane strain, yield criteria and residual stress. The review on fracture mechanics and fatigue includes stress intensity factor, crack tip stress fields, fatigue crack growth and crack tip plasticity in fatigue, and concludes with a brief overview on plasticity-induced crack closure. This will form the basis of the investigations presented in this thesis.

2.2 Stress

The concept of stress is fundamental to the mechanics of materials, which indicates how a force is transmitted through a solid body. Stress is defined as a force experienced by a point inside a body, when the area surrounding the point approaches zero. To illustrate this, consider a small cubic element surrounding a point in a body subjected to arbitrary forces in a three dimensional Cartesian co-ordinate system x_i (i=1, 2, 3) (Figure 2.1). As the element is small, the forces are assumed to be uniformly distributed over the faces of the element. Force is a vector F_j, and A_i is the area of a face normal to the i direction. The stress on the element can be defined as:

$$\sigma_{ij} = \lim_{A_i \to 0} \frac{F_j}{A_i} \tag{2.1}$$

where i, j=1, 2, 3. Stress, σ_{ij} is a second order tensor (which connects the force vector to the position vector), in which the first suffix, i refers to the direction of the normal to the plane on which the stress acts, and the second suffix, j refers to the direction of the force component. Normal stresses occur when i=j and shear stresses when i≠j. Thus a normal stress σ_{11} evolves from the force component on a plane in the x_1 direction and where the direction of the normal to the plane is also x_1. As illustrated in Figure 2.1, the stress components σ_{11}, σ_{22}, σ_{33} are the normal stress components on the element in the x_1, x_2 and x_3 directions. σ_{12} and σ_{13} are the shear stress components on the x_2x_3 face. Similarly σ_{21} and σ_{23} are the shear stress components on the x_1x_3 face, and σ_{31} and σ_{32} are the shear stress components on the x_1x_2 face. Equilibrium of moments requires that $\sigma_{ij}=\sigma_{ji}$ allowing the stress tensor at a point to be described by six independent components σ_{11}, σ_{22}, σ_{33}, σ_{12}, σ_{23} and σ_{31}.

The maximum and the minimum normal stresses on an element are the principal stresses. The planes on which principal stresses act are called principal planes, which are not subject to shear stresses. Using Mohr's circle in Figures 2.2a & b, the maximum and minimum normal stresses i.e., the principal stresses on the element can be given as:

$$\sigma_{1,2} = \frac{\sigma_{11} + \sigma_{22}}{2} \pm \sqrt{\left(\frac{\sigma_{11} - \sigma_{22}}{2}\right)^2 + \sigma_{12}^2} \tag{2.2}$$

The principal planes and the principal stresses are shown in Figure 2.2c, and are perpendicular to each other.

Consideration of the element shown in Figure 2.2 indicates that the maximum and minimum shear stresses on the element, obtained from Mohr's circle construction are:

$$\tau_{\substack{max \\ min}} = \pm\sqrt{\left(\frac{\sigma_{11}-\sigma_{22}}{2}\right)^2 + \sigma_{12}^2} \qquad (2.3)$$

The minimum shear stress is negative with an absolute value equal to the maximum shear stress. Figure 2.2d shows the maximum and the minimum shear stresses and the planes on which they occur. The two planes are orthogonal. The normal stresses, σ_n on the planes of maximum and minimum shear stresses are identical and can be given as:

$$\sigma_n = \frac{\sigma_{11}+\sigma_{22}}{2} \qquad (2.4)$$

The plane of maximum shear stress makes an angle of 45° with principal planes.

2.3 Strain

Strain is a measure of the distortion of a body under applied stress. A body under an external force may undergo deformation as well as a rigid body motion. Strain is

caused by the relative movements (displacements) of two or three points in a body due to deformation under an external force. Like stress, strain is a second order tensor, which connects the displacement vector to the position vector. The strain components are also denoted as normal and shear strains. A normal strain is defined as the change in length of a line segment between two points divided by the original length of the segment. A shear strain is defined as the angular change between two line segments which were originally perpendicular to each other. Like stress, the normal and shear strain components give the strain values of an infinitesimal element, which was initially parallel to the co-ordinate axes. In multiaxial loading, strain in the element is specified by the components of strain in x_1, x_2 and x_3 directions. Normal strains are denoted by ε_{ij} (i=j) and shear strains by γ_{ij} (i≠j). If the displacement components of a particle in a deformed body in x_1, x_2 and x_3 directions are u, v, and w respectively, the normal and shear strain components can be written as:

$$\varepsilon_{11}=\frac{\partial u}{\partial x_1},\ \varepsilon_{22}=\frac{\partial v}{\partial x_2},\ \varepsilon_{33}=\frac{\partial w}{\partial x_3} \tag{2.5}$$

$$\gamma_{12}=\frac{\partial u}{\partial x_2}+\frac{\partial v}{\partial x_1},\ \gamma_{23}=\frac{\partial v}{\partial x_3}+\frac{\partial w}{\partial x_2},\ \gamma_{31}=\frac{\partial w}{\partial x_1}+\frac{\partial u}{\partial x_3} \tag{2.6}$$

2.4 Elastic stress strain relations

Consider a bar of isotropic linear-elastic material subjected to uniaxial tensile stress σ_{22} as illustrated in Figure 2.3. The corresponding strains are:

$$\varepsilon_{22} = \frac{\sigma_{22}}{E},\ \varepsilon_{11} = \varepsilon_{33} = -\nu\frac{\sigma_{22}}{E} \tag{2.7}$$

where ε_{11}, ε_{22} and ε_{33} are the strain components in the x_1, x_2 and x_3 directions respectively, E is Young's modulus and ν is Poisson's ratio. Similarly for uniaxial tensile stresses σ_{11} and σ_{33} the stress strain relations are:

$$\varepsilon_{11} = \frac{\sigma_{11}}{E},\ \varepsilon_{22} = \varepsilon_{33} = -\nu\frac{\sigma_{11}}{E} \tag{2.8}$$

$$\varepsilon_{33} = \frac{\sigma_{33}}{E},\ \varepsilon_{11} = \varepsilon_{22} = -\nu\frac{\sigma_{33}}{E} \tag{2.9}$$

By superimposing these equations for the strain components, the stress strain relations for multiaxial loading can be given as:

$$\varepsilon_{11} = \frac{1}{E}[\sigma_{11} - \nu(\sigma_{22} + \sigma_{33})]$$

$$\varepsilon_{22} = \frac{1}{E}[\sigma_{22} - \nu(\sigma_{11} + \sigma_{33})]$$

$$\varepsilon_{33} = \frac{1}{E}[\sigma_{33} - \nu(\sigma_{11} + \sigma_{22})] \tag{2.10}$$

The shear strain components are obtained from the shear stresses as:

$$\gamma_{12} = \frac{\sigma_{12}}{G},\ \gamma_{23} = \frac{\sigma_{23}}{G},\ \gamma_{31} = \frac{\sigma_{31}}{G} \tag{2.11}$$

where G is the shear modulus, which can be written in terms of Young's modulus, E and Poisson's ratio, ν:

$$G = \frac{E}{2(1+\nu)} \tag{2.12}$$

Stresses in terms of strains can be written as:

$$\sigma_{11} = \frac{E}{(1+\nu)(1-2\nu)}[(1-\nu)\varepsilon_{11} + \nu(\varepsilon_{22} + \varepsilon_{33})]$$

$$\sigma_{22} = \frac{E}{(1+\nu)(1-2\nu)}[(1-\nu)\varepsilon_{22} + \nu(\varepsilon_{11} + \varepsilon_{33})]$$

$$\sigma_{33} = \frac{E}{(1+\nu)(1-2\nu)}[(1-\nu)\varepsilon_{33} + \nu(\varepsilon_{11} + \varepsilon_{22})] \tag{2.13}$$

$$\sigma_{12} = G\gamma_{12},\ \sigma_{23} = G\gamma_{23},\ \sigma_{31} = G\gamma_{31} \tag{2.14}$$

2.5 Plane stress and plane strain

Plane stress and plane strain are concepts which are intended to simplify full three dimensional problems allowing them to become more amenable to analysis. The plane stress approach is applied when the body is thin compared to its lateral dimensions. On the other hand, the plane strain approach is adopted when the body is very thick compared to its lateral dimensions.

2.5.1 Plane stress

Consider a thin plate, loaded as in Figure 2.4. The forces are uniformly distributed over the boundary of the plate, and act parallel to its plane, such that there is no stress component in the direction perpendicular to the plane of the plate (i.e., in the x_3 direction), and other stress components (x_1 and x_2) do not vary in that direction. This state is defined as plane stress and can be specified by the stress components σ_{11}, σ_{22} and σ_{12}. Plane stress is defined such that

$$\sigma_{33} = \sigma_{13} = \sigma_{23} = \gamma_{13} = \gamma_{23} = 0 \text{ and } \frac{\partial \sigma_{ij}}{\partial x_3} = 0 \qquad (2.15)$$

2.5.2 Plane strain

Consider a long cylindrical body loaded as in Figure 2.5. The forces are uniformly distributed over the surface of the body, and act parallel to the faces of the cylinder. The stress components (x_1, x_2 and x_3) do not vary along the longitudinal axis (the x_3 direction) of the cylinder. Moreover, the cylinder is fixed between two rigid plates, such that it does not displace in the axial direction. Therefore, the strain components of the body in the x_3 direction are zero. This state is defined as plane strain. Like plane stress, plane strain can be specified by the stress components σ_{11}, σ_{22} and σ_{12}. Plane strain is defined such that

$$\varepsilon_{33} = \gamma_{13} = \gamma_{23} = \sigma_{13} = \sigma_{23} = 0 \text{ and } \frac{\partial \sigma_{ij}}{\partial x_3} = 0 \qquad (2.16)$$

Substituting $\varepsilon_{33}=0$ in Equation 2.10, the normal stress in the x_3 direction in plane strain can be given as:

$$\sigma_{33} = \nu(\sigma_{11} + \sigma_{22}) \tag{2.17}$$

The out of plane stress, σ_{33} maintains the plane strain condition.

2.6 Yield criteria

Under uniaxial tension, material yields when the uniaxial tensile stress equals the yield strength of the material. Under multiaxial loading, i.e., when several stress components are present, yielding is expected to occur at some combination of these components. Yield criteria are intended to describe when multiaxially loaded material undergoes plastic deformation. Two well known yield criteria are described below. Both criteria are based on the assumption that yielding occurs due to shear stress rather than tensile stress.

2.6.1 The Tresca yield criterion

The Tresca yield criterion (Tresca, 1864) suggests that yielding occurs in multiaxially loaded material when the maximum shear stress reaches the value it appears to show when yielding occurs in a tensile test. The shear yield strength appears to be one-half the tensile yield strength. The maximum shear stress for yielding can be given as:

$$\tau_{max} = \tau_y = \frac{\sigma_y}{2} = \frac{(\sigma_1 - \sigma_3)}{2} \tag{2.18}$$

where σ_1, σ_2 and σ_3 are the three principal stresses and $\sigma_1 > \sigma_2 > \sigma_3$, τ_{max} is maximum shear stress, σ_y is tensile yield strength and τ_y is shear yield strength.

2.6.2 The von Mises yield criterion

The von Mises yield criterion (Mises, 1913) indicates that yielding occurs in multiaxially loaded material when the root mean square of the differences between the principal stresses reaches the value obtained when yielding occurs in a tensile test. At yielding in a tensile test, the principal stress, $\sigma_1 = \sigma_y$, the yield strength of material, and the other principal stresses, $\sigma_2 = \sigma_3 = 0$ (uniaxial loading). Therefore, the root mean square of the differences between the principal stresses can be written as:

$$\begin{aligned} &\sqrt{\frac{1}{3}\left[(\sigma_1 - \sigma_2)^2 + (\sigma_2 - \sigma_3)^2 + (\sigma_3 - \sigma_1)^2\right]} \\ &= \sqrt{\frac{1}{3}\left[(\sigma_y - 0)^2 + (0 - 0)^2 + (0 - \sigma_y)^2\right]} \\ &= \sqrt{\frac{2}{3}}\sigma_y \end{aligned} \tag{2.19}$$

By simplifying Equation 2.19 it can be shown that yielding occurs in multiaxially loaded material when

$$\sigma_y = \sqrt{\frac{1}{2}\left[(\sigma_1 - \sigma_2)^2 + (\sigma_2 - \sigma_3)^2 + (\sigma_3 - \sigma_1)^2\right]} \qquad (2.20)$$

Equation 2.20 states the von Mises yield criterion in terms of principal stresses. This criterion can be expressed in terms of non-principal stresses as:

$$\sigma_y = \sqrt{\frac{1}{2}\left[(\sigma_{11} - \sigma_{22})^2 + (\sigma_{22} - \sigma_{33})^2 + (\sigma_{33} - \sigma_{11})^2\right] + 3\sigma_{12}^2 + 3\sigma_{23}^2 + 3\sigma_{31}^2} \qquad (2.21)$$

2.7 Equivalent stress and equivalent strain

If yielding is assumed to occur under the von Mises yield criterion, the tendency for further plastic flow can be quantified by the equivalent stress, $\bar{\sigma}$, which can be expressed in terms of principal stresses, $\sigma_1, \sigma_2, \sigma_3$ as:

$$\bar{\sigma} = \sqrt{\frac{1}{2}\left[(\sigma_1 - \sigma_2)^2 + (\sigma_2 - \sigma_3)^2 + (\sigma_3 - \sigma_1)^2\right]} \qquad (2.22)$$

The equivalent stress can also be written in terms of non-principal stresses as:

$$\bar{\sigma} = \sqrt{\frac{1}{2}\left[(\sigma_{11} - \sigma_{22})^2 + (\sigma_{22} - \sigma_{33})^2 + (\sigma_{33} - \sigma_{11})^2\right] + 3\sigma_{12}^2 + 3\sigma_{23}^2 + 3\sigma_{31}^2} \qquad (2.23)$$

In uniaxial tension the equivalent stress, $\bar{\sigma}$ is equal to the yield or flow strength of the material. For an elastic-perfectly plastic material during plastic deformation the equivalent stress remains constant. However, if the material strain hardens, the

equivalent stress increases with plastic deformation, due to changes in the dislocation structure of the material.

Since the equivalent stress depends on strain, it is necessary to quantify strain with a parameter which corresponds to the equivalent stress, $\bar{\sigma}$. The appropriate parameter is the equivalent strain, $\bar{e}$, which can be defined as:

$$\bar{e} = \sqrt{\frac{2}{9}\left[(\varepsilon_1 - \varepsilon_2)^2 + (\varepsilon_2 - \varepsilon_3)^2 + (\varepsilon_3 - \varepsilon_1)^2\right]} \tag{2.24}$$

where ε_1, ε_2 and ε_3 are the three principal strains. The equivalent strain is defined in a way such that it equals the tensile strain in a uniaxial tensile test (assuming incompressible deformation). The equivalent strain in terms of non-principal strains can be given as:

$$\bar{e} = \sqrt{\frac{2}{9}\left[(\varepsilon_{11} - \varepsilon_{22})^2 + (\varepsilon_{22} - \varepsilon_{33})^2 + (\varepsilon_{33} - \varepsilon_{11})^2\right] + \frac{1}{3}\gamma_{12}^2 + \frac{1}{3}\gamma_{23}^2 + \frac{1}{3}\gamma_{31}^2} \tag{2.25}$$

For incremental plasticity the equivalent plastic strain increment can be given as:

$$d\bar{e}^p = \sqrt{\frac{2}{9}\left[(d\varepsilon_1^p - d\varepsilon_2^p)^2 + (d\varepsilon_2^p - d\varepsilon_3^p)^2 + (d\varepsilon_3^p - d\varepsilon_1^p)^2\right]} \tag{2.26}$$

where $d\varepsilon_1^p$, $d\varepsilon_2^p$ and $d\varepsilon_3^p$ are the principal plastic strain increments. Using non-principal strains the equivalent plastic strain increment can be given as:

$$d\bar{e}^p = \sqrt{\frac{2}{9}\left[(d\varepsilon_{11}^p - d\varepsilon_{22}^p)^2 + (d\varepsilon_{22}^p - d\varepsilon_{33}^p)^2 + (d\varepsilon_{33}^p - d\varepsilon_{11}^p)^2\right] + \frac{1}{3}(d\gamma_{12}^p)^2 + \frac{1}{3}(d\gamma_{23}^p)^2 + \frac{1}{3}(d\gamma_{31}^p)^2} \qquad (2.27)$$

The equivalent plastic strain is then given by summing the equivalent plastic strain increments over the strain history as:

$$\bar{e}^p = \int d\bar{e}^p \qquad (2.28)$$

The equivalent plastic strain, $\bar{e}^p$ quantifies the total dislocation activity associated with a shape change. In uniaxial tension the equivalent plastic strain increment, $d\bar{e}^p$ is equal to the tensile plastic strain increment, $d\varepsilon_1^p$ as plastic deformation occurs with no volume change. Under uniaxial tension $(\sigma_2 = \sigma_3 = 0)$ an axial tensile plastic strain increment $d\varepsilon_1^p = +0.02$, gives rise to the transverse plastic strain increments $d\varepsilon_2^p = d\varepsilon_3^p = -0.01$. Although the change of volume $(d\varepsilon_1^p + d\varepsilon_2^p + d\varepsilon_3^p)$ is zero, the equivalent plastic strain increment is $d\bar{e}^p = d\varepsilon_1^p = +0.02$. Now if the material is compressed with a compressive strain increment $d\varepsilon_1^p = -0.02$ $(d\varepsilon_2^p = d\varepsilon_3^p = +0.01)$, the corresponding equivalent plastic strain increment will be $d\bar{e}^p = +0.02$. Thus a tensile plastic strain increment of +0.02 followed by a compressive plastic strain increment of –0.02 recovers the original shape of the body leaving a total equivalent plastic strain $\bar{e}^p = +0.04$.

2.8 Stress strain relations in plasticity

The plastic stress-strain equations can be written in similar form to the elastic Equations 2.10 and 2.11. As mentioned earlier, plastic deformation occurs with no volume change, but solely with shape change (distortion). Therefore, volumetric strain can be given as:

$$\frac{\Delta V}{V} = \varepsilon_{11} + \varepsilon_{22} + \varepsilon_{33} = 0 \tag{2.29}$$

Substituting from Equations 2.10, Equation 2.29 gives:

$$\frac{\Delta V}{V} = \frac{1-2\nu}{E}(\sigma_{11} + \sigma_{22} + \sigma_{33}) = 0 \tag{2.30}$$

Equation 2.30 shows that for an incompressible (constant volume) deformation Poisson's ratio is ½, giving the shear modulus, $G = E/3$ from Equation 2.12. To describe non-linear deformation, the modulus of elasticity, E, can be replaced with the ratio of equivalent stress to equivalent strain, $\bar{\sigma}/\bar{e}$. Substituting E and G in Equations 2.10 & 2.11 gives a set of equations:

$$\varepsilon_{11} = \frac{\bar{e}}{\bar{\sigma}}[\sigma_{11} - \frac{1}{2}(\sigma_{22} + \sigma_{33})],\ \gamma_{12} = 3\frac{\bar{e}}{\bar{\sigma}}\sigma_{12}$$

$$\varepsilon_{22} = \frac{\bar{e}}{\bar{\sigma}}[\sigma_{22} - \frac{1}{2}(\sigma_{11} + \sigma_{33})],\ \gamma_{23} = 3\frac{\bar{e}}{\bar{\sigma}}\sigma_{23}$$

$$\varepsilon_{33} = \frac{\bar{e}}{\bar{\sigma}}[\sigma_{33} - \frac{1}{2}(\sigma_{11} + \sigma_{22})],\ \gamma_{31} = 3\frac{\bar{e}}{\bar{\sigma}}\sigma_{31} \tag{2.31}$$

These equations describe deformation plasticity i.e., non-linear elasticity. A non-linear elastic material cannot be distinguished from a plastic material unless unloading is allowed, and given this type of loading history Equations 2.31 are applicable to both linear and non-linear elasticity.

Non-linear elastic and plastically deforming materials can be distinguished if the deformation history involves unloading as the elastic strains are recovered on unloading and plastic strains are permanent. The total plastic strain is the sum of the increments of the strain in the deformation history. Replacing strains by plastic strain increments, Equations 2.31 gives the flow rule as:

$$d\varepsilon_{11}^{p} = \frac{d\bar{e}^{p}}{\bar{\sigma}}[\sigma_{11} - \frac{1}{2}(\sigma_{22} + \sigma_{33})],\ d\gamma_{12}^{p} = 3\frac{d\bar{e}^{p}}{\bar{\sigma}}\sigma_{12}$$

$$d\varepsilon_{22}^{p} = \frac{d\bar{e}^{p}}{\bar{\sigma}}[\sigma_{22} - \frac{1}{2}(\sigma_{11} + \sigma_{33})],\ d\gamma_{23}^{p} = 3\frac{d\bar{e}^{p}}{\bar{\sigma}}\sigma_{23}$$

$$d\varepsilon_{33}^{p} = \frac{d\bar{e}^{p}}{\bar{\sigma}}[\sigma_{33} - \frac{1}{2}(\sigma_{11} + \sigma_{22})],\ d\gamma_{31}^{p} = 3\frac{d\bar{e}^{p}}{\bar{\sigma}}\sigma_{31} \qquad (2.32)$$

Equations 2.32 describe incremental plasticity, where the total strain is obtained from the elastic strain calculated from instantaneous stress and the total plastic strain obtained by summing the plastic strain increments:

$$\varepsilon_{11} = \varepsilon_{11}^{el} + \int d\varepsilon_{11}^{p},\ \gamma_{12} = \gamma_{12}^{el} + \int d\gamma_{12}^{p}$$

$$\varepsilon_{22} = \varepsilon_{22}^{el} + \int d\varepsilon_{22}^{p},\ \gamma_{23} = \gamma_{23}^{el} + \int d\gamma_{23}^{p}$$

$$\varepsilon_{33} = \varepsilon_{33}^{el} + \int d\varepsilon_{33}^{p},\ \gamma_{31} = \gamma_{31}^{el} + \int d\gamma_{31}^{p} \qquad (2.33)$$

2.9 Residual stress

Residual stresses can be defined as the stresses (tension or compression) that remain within a body while the body is not under any external load. Thus, residual stresses do not play any role in maintaining equilibrium between the body and its environment as they self-equilibrate within the body (Withers and Bhadeshia, 2001). Residual stresses originate from misfits within the body in its usual shape (Withers and Bhadeshia, 2001). Such misfits within a body may occur in three different ways (Withers and Bhadeshia, 2001): (i) misfits between different regions, which may be caused by non-uniform plastic deformation, (ii) misfits between different parts as for example in the case of rivet joints, and finally (iii) misfits between different phases, which usually occur in composites.

Residual stresses can be introduced to a component either during manufacturing process or by plastic deformation during service. They have significant effects on the load bearing capacity and useful service life of structures or components. Residual stresses can be either beneficial or harmful to a component or a structure depending on the type of the stresses (tension or compression) and on the size and the orientation of the applied external load. Tensile residual stresses may contribute to the initiation and propagation of fatigue cracks from surface defects. On the other hand compressive residual stresses increase the fatigue life by delaying the initiation and propagation of cracks.

Residual stresses can be categorised on the basis of the length scales (Withers, 2001), over which they self-equilibrate: (i) macro-stresses or type I stresses, which

equilibrate over long distances that may be to the extents of the component or structure dimensions, (ii) micro-stresses or type II stresses, where stresses equilibrate over a number of grains, and finally (iii) micro-stresses or type III stresses, which exist and equilibrate over several atomic distances within a single grain.

2.10 Stress intensity factor and crack tip stress fields

The Stress Intensity Factor (henceforth SIF) characterises the amplitude of the stress singularity at the tip of a crack in a linear elastic material. If the SIF is known, all the components of stress, strain and displacement at a point near the crack tip can be determined as a function of distance from the crack tip r and angle θ. Using a cylindrical co-ordinate system centred at the crack tip the first two terms of the Williams (1957) expansion of the asymptotic elastic field can be given as:

$$\sigma_{ij} = \frac{K}{\sqrt{2\pi r}} f_{ij}(\theta) + \begin{bmatrix} T & 0 \\ 0 & 0 \end{bmatrix} \quad (i, j=1, 2) \qquad (2.34)$$

where σ_{ij} is the stress tensor, $f_{ij}(\theta)$ is a dimensionless function of θ, K is the stress intensity factor and T is a uniaxial stress (tensile or compressive) parallel to the crack flanks. The first term in Equation 2.34 is singular at the crack tip and K describes the amplitude of singularity. T-stress is independent of radial distance but depends on geometry and load.

The stress intensity factor is denoted by K_I, K_{II} and K_{III} depending upon the mode of

loading (i.e., opening, in-plane shear and out-of-plane shear respectively). Figure 2.6 illustrates the three different modes of loading. In mode I, the load is applied normal to the crack plane, and the crack opens symmetrically about the crack plane. Mode II corresponds to in-plane shear loading and tends to slide one crack face with respect to the other. Mode III corresponds to out of plane shear. Focussing on the first term of the Williams (1957) expansion, the asymptotic stress field for mode I loading can be given as:

$$\sigma_{ij} = \frac{K_I}{\sqrt{2\pi r}} f_{ij}(\theta) \tag{2.35}$$

where K_I is the mode I stress intensity factor. Consider an element located at (r,θ) near the crack tip in Figure 2.7. Westergaard (1939) has given the mode I stresses on the element in Cartesian co-ordinates:

$$\sigma_{11} = \frac{K_I}{\sqrt{2\pi r}} \cos\left(\frac{\theta}{2}\right)\left[1 - \sin\left(\frac{\theta}{2}\right)\sin\left(\frac{3\theta}{2}\right)\right]$$

$$\sigma_{22} = \frac{K_I}{\sqrt{2\pi r}} \cos\left(\frac{\theta}{2}\right)\left[1 + \sin\left(\frac{\theta}{2}\right)\sin\left(\frac{3\theta}{2}\right)\right]$$

$$\sigma_{12} = \frac{K_I}{\sqrt{2\pi r}} \cos\left(\frac{\theta}{2}\right)\sin\left(\frac{\theta}{2}\right)\cos\left(\frac{3\theta}{2}\right) \tag{2.36}$$

On the crack plane, $\theta = 0$, Equations 2.36 can be written as:

$$\sigma_{11} = \sigma_{22} = \frac{K_I}{\sqrt{2\pi r}}$$

$$\sigma_{12} = 0 \tag{2.37}$$

On the crack plane the shear stress is zero. Therefore, for mode I loading the crack plane is a principal plane. The normal and shear stresses in the x_3 direction are:

$$\sigma_{33} = \nu(\sigma_{11} + \sigma_{22}), \text{ in plane strain}$$

$$\sigma_{33} = 0, \text{ in plane stress and}$$

$$\sigma_{13} = \sigma_{23} = 0, \text{ both in plane stress and plane strain} \tag{2.38}$$

Cartesian stresses (Westergaard, 1939) on the element in Figure 2.7 due to mode II loading can be given as:

$$\sigma_{11} = -\frac{K_{II}}{\sqrt{2\pi r}} \sin\left(\frac{\theta}{2}\right)\left[2 + \cos\left(\frac{\theta}{2}\right)\cos\left(\frac{3\theta}{2}\right)\right]$$

$$\sigma_{22} = \frac{K_{II}}{\sqrt{2\pi r}} \sin\left(\frac{\theta}{2}\right)\cos\left(\frac{\theta}{2}\right)\cos\left(\frac{3\theta}{2}\right)$$

$$\sigma_{12} = \frac{K_{II}}{\sqrt{2\pi r}} \cos\left(\frac{\theta}{2}\right)\left[1 - \sin\left(\frac{\theta}{2}\right)\sin\left(\frac{3\theta}{2}\right)\right] \tag{2.39}$$

Linear elastic fields can be superimposed to produce a general mixed mode I/II loading. The stresses for mixed mode I/II are given by summing Equations 2.36 and 2.39. The stress intensity factors for mixed mode loading are not additive directly, however, they can be added in terms of energy release rate, G as:

$$G = \frac{K_I^2}{E'} + \frac{K_{II}^2}{E'} \qquad (2.40)$$

where $E' = E$ for plane stress, and $E' = E/(1-\nu^2)$ for plane strain.

2.11 Fatigue

When a component is subjected to cyclic loading, it may undergo progressive and localised structural damage. This type of structural damage of the material of the component is defined as fatigue. The fatigue process in a material starts with dislocation movement, which eventually initiates cracks. In fatigue, crack initiation and propagation in a component may occur at a stress level much lower than the yield strength. Aircraft wings, railway axles etc. are all practical examples of components that experience fatigue loading.

Fatigue situations in materials can be categorized as high-cycle fatigue and low-cycle fatigue. In the case of low applied stress, deformation is primarily elastic, where a relatively large number of cycles (more than 10^4 cycles) are required for material failure. This situation is called high-cycle fatigue, where stress is the appropriate parameter to be considered in failure analysis. In the case of low-cycle fatigue, the stress is high enough to cause plastic deformation, and strain is the appropriate parameter to be accounted for.

A fatigue process in a component comprises three consecutive stages: crack initiation, crack propagation and finally catastrophic failure. It should be mentioned

that a structure or component may already contain a defect or crack resulting from manufacturing, machining or surface treatment process. In that case the fatigue process starts with propagation of a pre-existing defect or crack. In most cases, initiation of fatigue occurs at the surface of the component from scratches, dents or corrosion damage on the surface.

2.12 Fatigue crack propagation

According to Linear Elastic Fracture Mechanics (LEFM), in a component under mode I (opening) static loading, a crack propagates when the applied stress intensity factor K_I exceeds a critical value K_{IC}, the fracture toughness of the material. Following Paris and Erdogan (1963), stress intensity factor has also been used as a fatigue crack propagation correlating parameter under constant amplitude loading, provided that crack tip plasticity satisfies small scale yielding. Under fatigue loading, a crack propagates when the stress intensity factor range, ΔK exceeds a threshold value, ΔK_{th}. Figure 2.8 schematically illustrates fatigue loading. The stress intensity factor range, ΔK is determined from the maximum and the minimum applied stress intensity factors in a fatigue cycle. For a cracked component under mode I loading as in Figures 2.9 and 2.10, the applied stress intensity factor can be given as:

$$K_I = Y\sigma\sqrt{\pi a} \qquad (2.41)$$

where Y is a dimensionless geometric factor, σ is the remotely applied stress and a

is the half crack length for a central through cracked component (Figure 2.9) or the crack length for an edge cracked component (Figure 2.10). In a fatigue cycle the stress intensity factor range, ΔK can be written as:

$$\Delta K = K_{max} - K_{min} \tag{2.42}$$

where K_{max} and K_{min} are the maximum and the minimum applied stress intensity factors in the fatigue cycle as shown in Figure 2.8, which can be given as:

$$K_{max} = Y\sigma_{max}\sqrt{\pi a} \tag{2.43}$$

$$K_{min} = Y\sigma_{min}\sqrt{\pi a} \tag{2.44}$$

where σ_{max} and σ_{min} are the maximum and the minimum stresses in a fatigue cycle. The fatigue crack growth rate can be given by the Paris-Erdogan equation (Pook, 1983) as:

$$\frac{da}{dN} = C(\Delta K)^m \tag{2.45}$$

where a is the crack length, N is the number of cycles, and C and m are material constants determined empirically. Equation 2.45 shows that for all combinations of crack length, a and applied stress, σ giving the same ΔK, the crack propagation rate is constant. It should be mentioned that the mode I stress intensity factor, K_I in a fatigue cycle cannot be negative as compressive stress simply closes the mode I crack. Therefore, ΔK is calculated only from the positive part of the cycle (Hudson,

1969), which opens the crack and contributes to propagating the crack.

Now by replacing ΔK with an effective stress intensity factor range, ΔK_{eff} as in Figure 2.8, Equations 2.42 and 2.45 can be written as:

$$\Delta K_{eff} = K_{max} - K_{cl} \qquad K_{cl} > K_{min} \tag{2.46}$$

$$\frac{da}{dN} = C(\Delta K_{eff})^m \tag{2.47}$$

where K_{cl} is the stress intensity factor at which the crack closes, which can be defined as the effective minimum stress intensity factor in a fatigue cycle.

It should be mentioned that there is a debate about the cyclic position of the effective minimum stress intensity factor i.e., if it is the crack opening point, K_{op} of the loading part or the crack closing point, K_{cl} of the unloading part (Figure 2.8) in a fatigue cycle. However, in most practical cases these two points appear to be indistinguishable (Fleck, 1982, Banerjee, 1984, Mageed et al., 1992).

Figure 2.11 illustrates a typical fatigue crack propagation curve for metals, which is a log-log plot of da/dN versus ΔK, and is sigmoidal in nature. The curve shows three distinct regions I, II and III. Region I indicates a threshold value, ΔK_{th} at which the crack propagation rate is zero. With increasing ΔK, the crack growth rate increases nonlinearly in this region. In region II the curve is linear. This region is called the Paris regime, which can be described by the Paris-Erdogan law (Paris and Erdogan, 1963) given by Equation 2.45. In this region, the crack growth rate

depends only on ΔK, but is insensitive to the R ratio ($R=K_{min}/K_{max}$). In the nonlinear region III, the crack growth rate accelerates as K_{max} approaches a critical stress intensity factor K_c, the fracture toughness of the material. To describe the entire crack growth curve McEvily (1988) derived the following equation:

$$\frac{da}{dN} = C(\Delta K - \Delta K_{th})^2 \left(1 + \frac{\Delta K}{K_c - K_{max}}\right) \tag{2.48}$$

It should be mentioned that under constant amplitude fatigue, for a given material the crack growth rate depends only on ΔK and R, as in this case the size of the plastic zone at the crack tip depends only on K_{max} and K_{min} in the fatigue cycle. However, under variable amplitude fatigue, the crack growth rate in a given cycle depends not only on K_{max} and K_{min} but also on the loading history i.e., on any prior plastic deformation. For example, if a single overload is imposed during constant amplitude fatigue, this will create a bigger monotonic plastic zone at the crack tip. This bigger plastic zone results in compressive residual stresses at the crack tip region, which retard the crack growth rate. Following retardation the original crack growth rate resumes once the crack has grown through the overload plastic zone.

2.13 Crack tip plasticity in fatigue

According to LEFM as discussed earlier, all stresses are singular at the crack tip and the stress intensity factor, K describes the amplitude of the stress singularity. The region close to the crack tip, where the stress singularity dominates, is referred to as the singularity dominated zone or K-dominated zone and the stress field is known as

a K-field. However, in practice crack tip stresses are finite due to local yielding over a region at the crack tip, which is known as the plastic zone. As mentioned earlier, despite the plasticity at the crack tip, K is still considered to be a valid parameter for characterizing crack tip conditions if the plastic zone is small compared to the in-plane dimensions. Figure 2.12 is a schematic of a typical crack tip stress field under monotonic loading in a non-hardening material showing the plastic zone at the crack tip. According to Irwin (1961) the crack tip plastic zone radius under mode I loading can be given as:

$$r_y = \frac{1}{\beta\pi}\left(\frac{K_I}{\sigma_y}\right)^2 \tag{2.49}$$

where K_I is the mode I stress intensity factor, σ_y is the yield strength of the material, and $\beta=2$ for plane stress and $\beta=6$ for plane strain.

In the case of fatigue loading, a cyclic plastic zone develops at the crack tip, and the growing crack leaves behind it a wake of plastic zone, which is called the plastic wake as shown in Figure 2.13. In fatigue cycling the monotonic plastic zone developed at the crack tip on loading is compressed by the surrounding elastic material upon unloading. This leads to a compressive stress at the crack tip, which will eventually reach the yield stress resulting in a compressive i.e., reverse plastic zone within the monotonic plastic zone. Under constant amplitude fatigue, this region of reverse plasticity repeatedly yields under tension and compression and is often referred to as the cyclic plastic zone. Figure 2.14 is a schematic of the crack tip stress fields under fatigue loading showing the monotonic and cyclic (reverse)

plastic zones at the crack tip. Following Irwin (1961) and Rice (1967), the radii of the monotonic and the reverse plastic zones can be given as:

$$r_{y(monotonic)} = \frac{1}{\beta\pi}\left(\frac{K_{max}}{\sigma_y}\right)^2 \tag{2.50}$$

$$r_{y(reverse)} = \frac{1}{\beta\pi}\left(\frac{\Delta K}{2\sigma_y}\right)^2 \tag{2.51}$$

where K_{max} is the maximum stress intensity factor in the fatigue cycle, $\Delta K = K_{max} - K_{min}$ (K_{min} is the minimum stress intensity factor of the fatigue cycle). For $K_{min} = 0$ the reverse plastic zone size is estimated to be one-quarter of the monotonic plastic zone.

As mentioned earlier, when a constant amplitude fatigue process is perturbed by an overload, it will affect the crack growth rate by retarding the growth. This retardation effect is predominantly due to the change of the stress field ahead of the crack tip resulting from the overload plastic zone. According to Wheeler (1972) the overload plastic zone radius at the crack tip can be given as:

$$r_{y(ol)} = \frac{1}{\beta\pi}\left(\frac{K_{ol}}{\sigma_y}\right)^2 \tag{2.52}$$

where K_{ol} is the overload stress intensity factor. It should be mentioned here that β in Equations 2.50 to 2.52 is the same as in Equation 2.49.

2.14 Plasticity-induced crack closure

Crack closure in fatigue is a phenomenon whereby the fracture surfaces of a fatigue crack come into contact during the unloading portion of a load cycle and load is transferred across the crack (ASTM E 647, 2002). Crack closure can be induced by the plasticity at the crack tip of a growing crack, by the presence of oxides on the crack surfaces produced in a corrosive environment, or by the roughness of the crack surfaces. Plasticity-induced crack closure has been central to fatigue crack propagation studies as it appears to be the most common phenomenon having an influence on fatigue crack growth rate in metallic materials. Elber (1970) was the first to discuss crack closure under cyclic loading. According to his observation, the crack remains fully open for only a portion of the loading cycle (tension-tension) as a result of the permanent tensile plastic deformation at the crack tip, which leaves a plastic wake behind the tip of a propagating crack (Figure 2.13). Consequently, crack closure retards the crack growth rate by reducing the nominal crack driving force ΔK to ΔK_{eff} with an increase of K_{min} to K_{cl} or K_{op} (Figure 2.8).

McEvily and Ishihara (2001) have discussed that the compressive residual stresses ahead of the crack tip (mainly due to overload effects) are responsible for plasticity-induced crack closure. According to them, as a crack advances through the residual compressive stress zone, the residual compressive stresses in the element now just behind the crack tip are relaxed and the material in this element expands thereby contributing to crack closure.

2.15 Conclusion

A brief review of the fundamental concepts has been presented in this chapter as the framework of the present study. Following this chapter, different diffraction techniques for stress measurement will be discussed in Chapter 3.

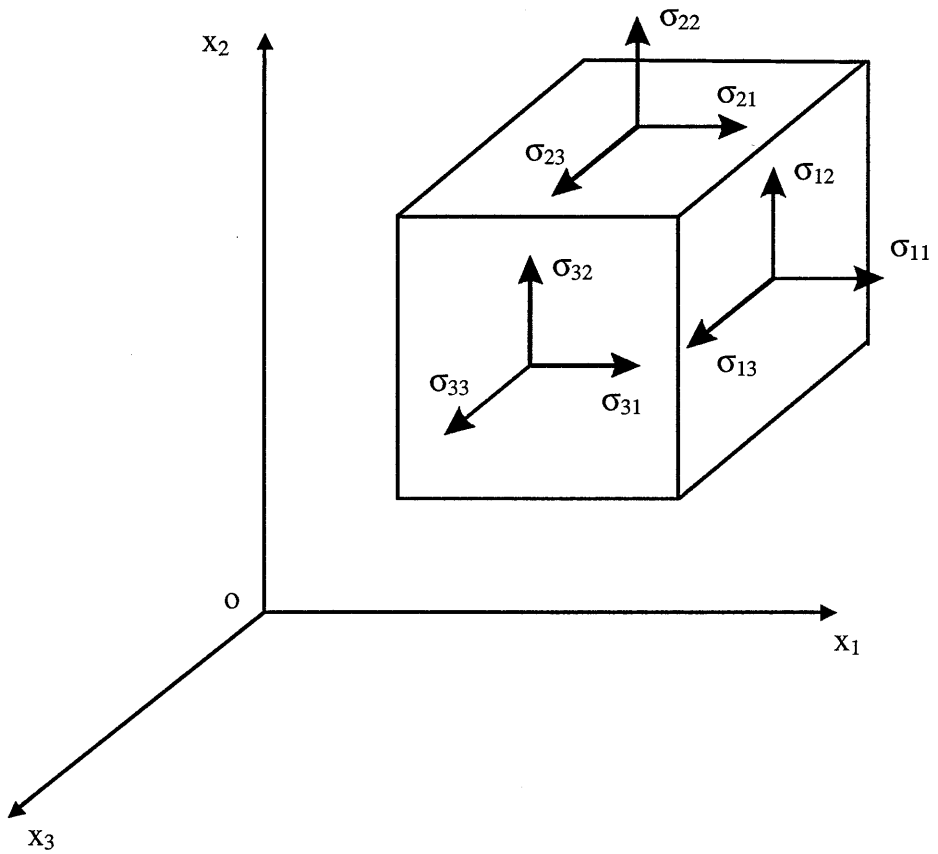

Figure 2.1: Stress components referred to Cartesian co-ordinate axes.

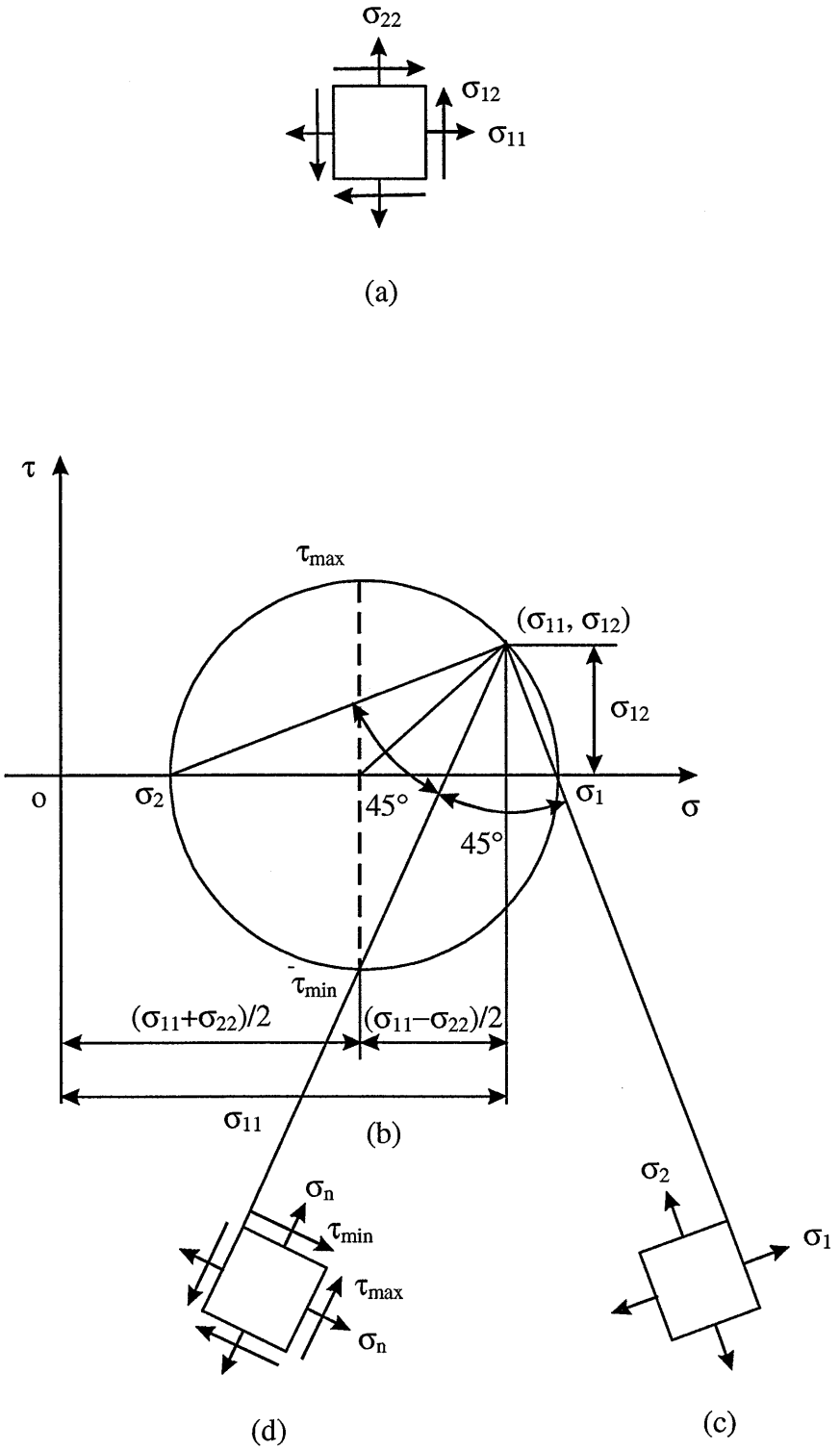

Figure 2.2: Stresses on element (a) and its corresponding Mohr's circle (b) showing the principal stresses (c) and maximum and minimum shear stresses (d).

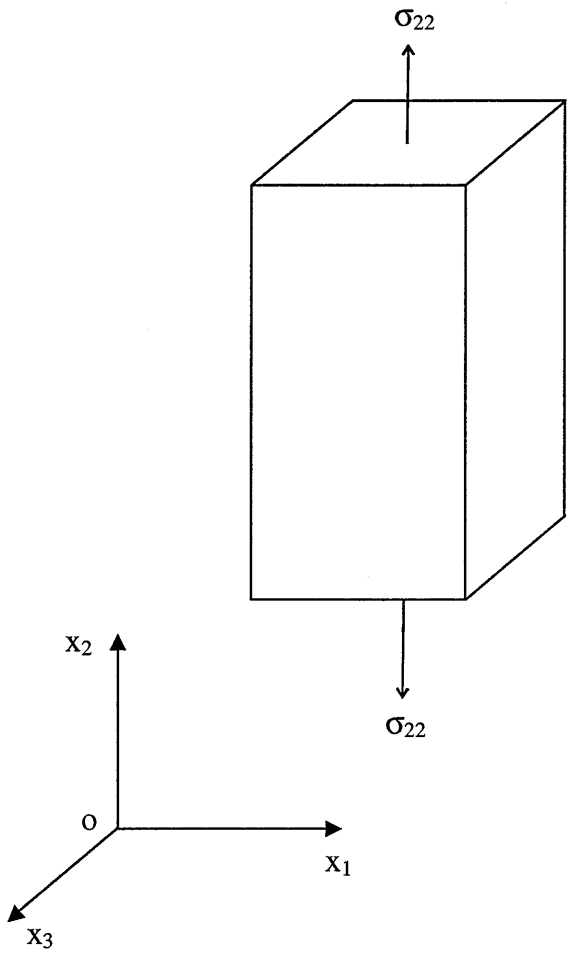

Figure 2.3: Bar subjected to uniaxial tension.

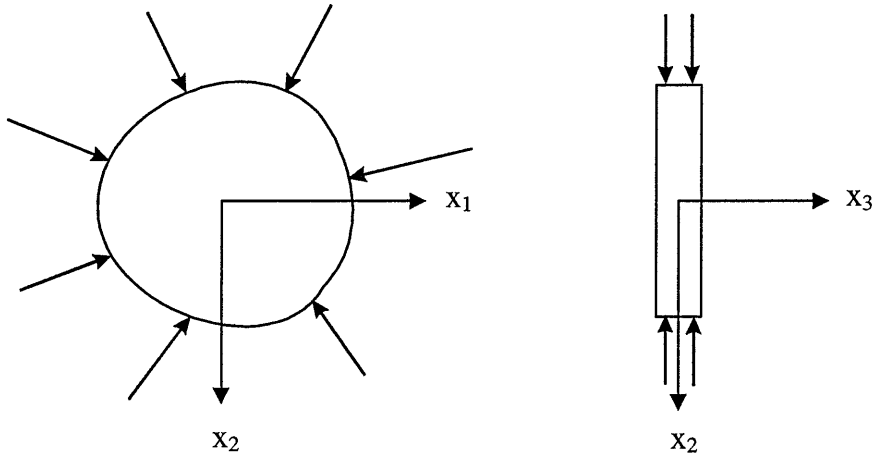

Figure 2.4: Forces at the boundary of a thin plate.

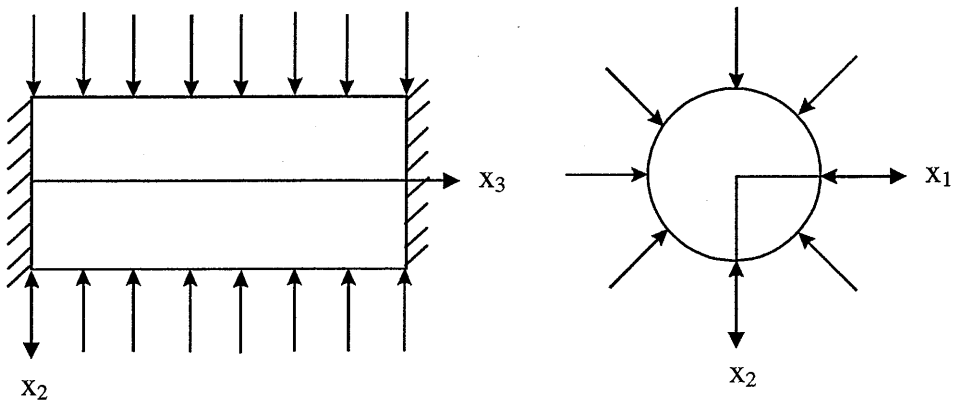

Figure 2.5: Cylindrical body loaded by forces perpendicular to the longitudinal axis.

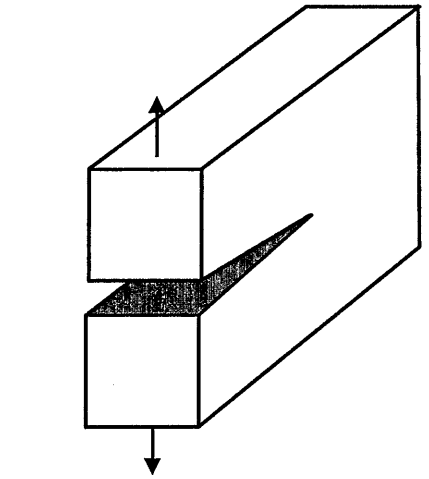

a) Mode I (Opening)

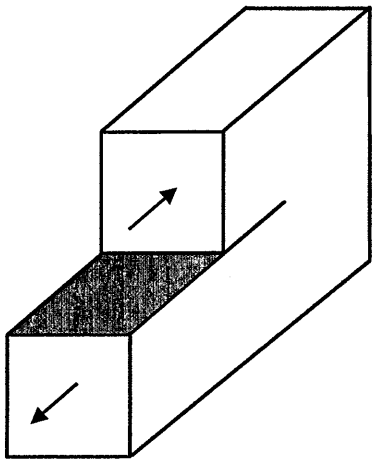

b) Mode II (In-Plane Shear)

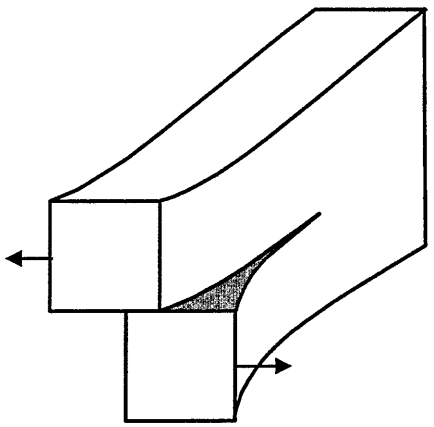

c) Mode III (Out-of-Plane Shear)

Figure 2.6: Three modes of loading applicable to a crack.

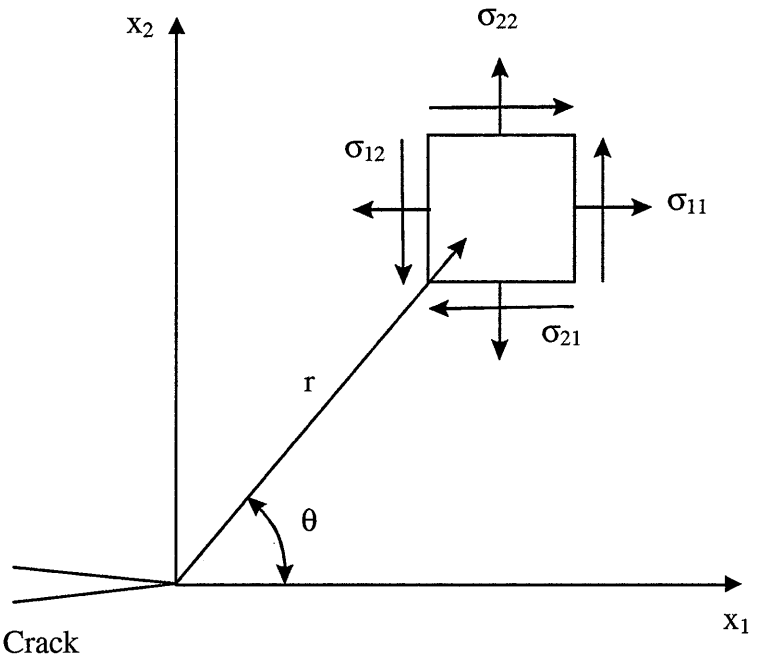

Figure 2.7: Stresses on an element near the crack tip in a linear elastic material.

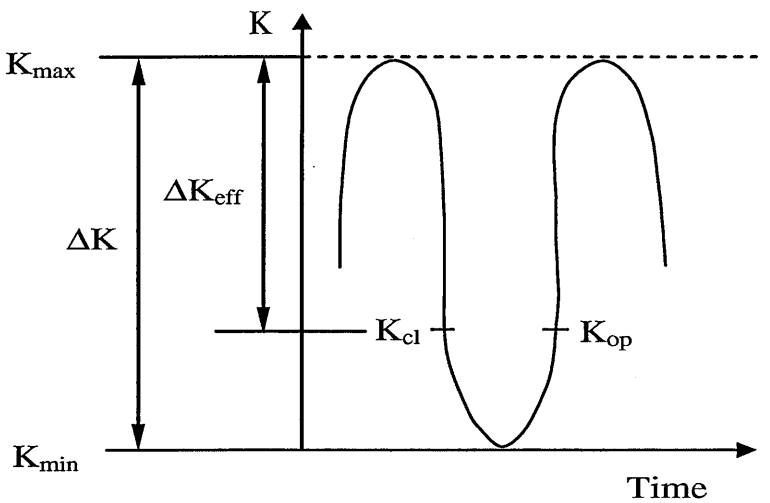

Figure 2.8: Schematic of fatigue loading defining effective stress intensity factor range.

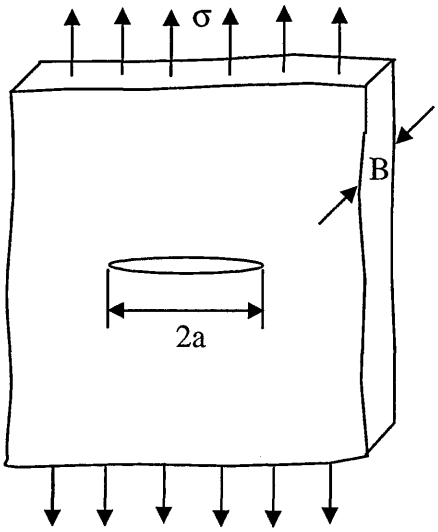

Figure 2.9: Central through cracked component under mode I loading.

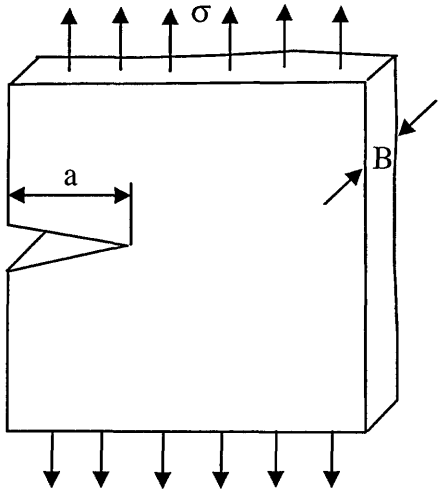

Figure 2.10: Edge cracked component under mode I loading.

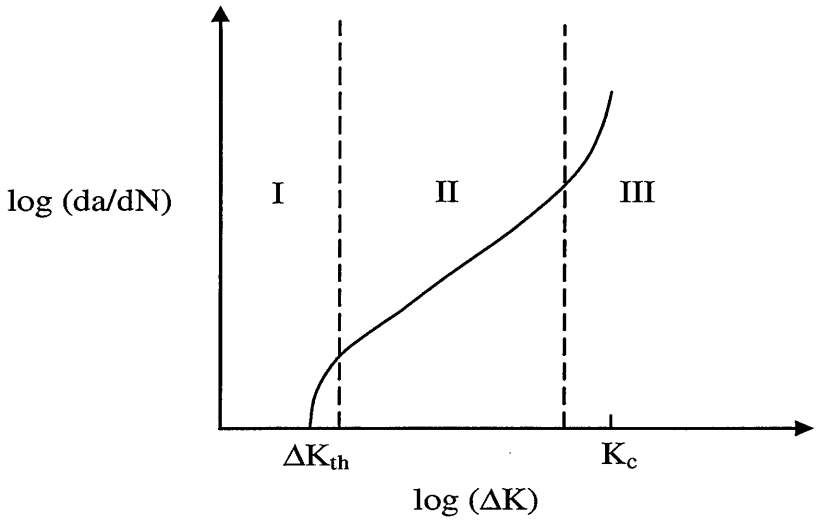

Figure 2.11: Variation of fatigue crack propagation rate with stress intensity factor range in a material.

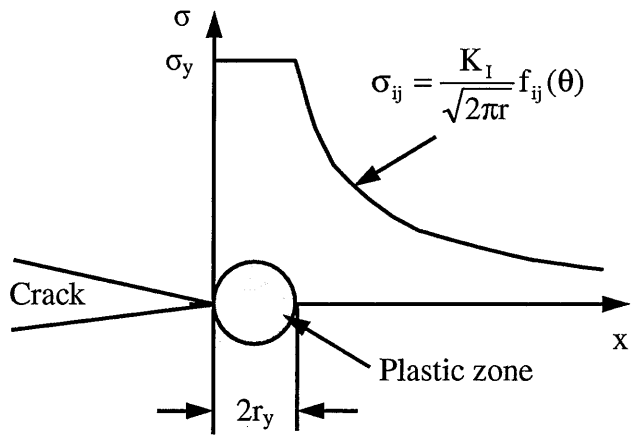

Figure 2.12: Crack tip stress field and plastic zone under monotonic loading for non-hardening material.

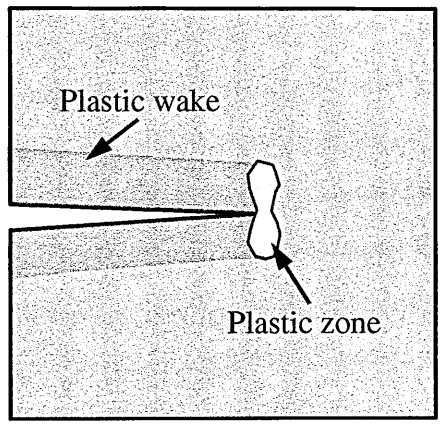

Figure 2.13: Growing fatigue crack leaving a plastic wake on the crack flanks behind the crack tip.

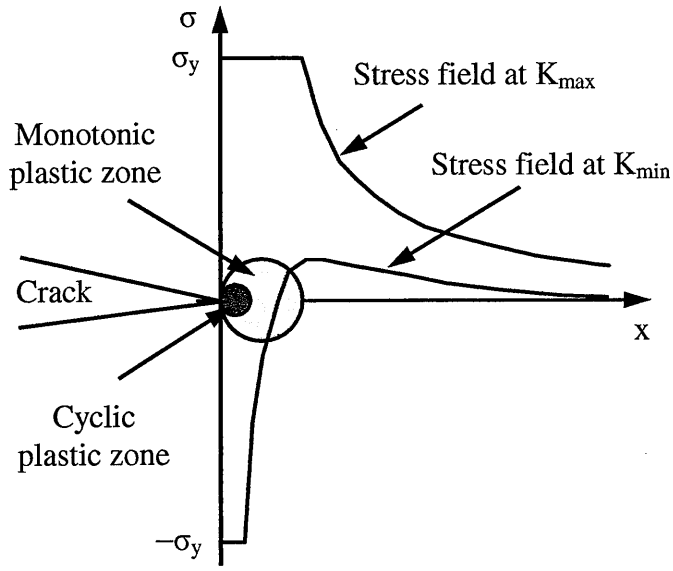

Figure 2.14: Crack tip stress fields and plastic zones under fatigue loading for non-hardening material.

Chapter 3 Diffraction techniques for strain measurement

3.1 Introduction

This chapter presents a discussion of the principle of strain measurement in engineering materials using diffraction techniques, and particularly the synchrotron X-ray diffraction technique, which has been employed in this work for investigation of the crack tip stress fields in aluminium alloy 5091 compact tension (CT) fatigued specimens. For completeness other diffraction techniques are also reviewed briefly.

3.2 Principle of diffraction techniques

Diffraction techniques have become well established as important non-destructive tools for measuring strains (residual or applied) within polycrystalline materials. Diffraction is an elastic scattering phenomenon, which occurs when X-ray, neutron or electron beams are incident on a crystalline material. The incident beam is scattered in all directions by the periodically arranged atoms in the crystal lying in the path of the incident beam. A diffracted beam comprises a number of scattered beams mutually reinforcing one another. The incident and the diffracted beams possess the same energy, as diffraction is an elastic scattering phenomenon. Figure 3.1a-d shows incident and diffracted beams on an un-deformed crystal, the Q-vector at the direction of strain measurement, the angular shifts of incident and diffracted beams on deformed geometry and the angular shift of a diffraction peak position. It should be mentioned that the Q-vector is known as the scattering vector, and can be defined as: $\vec{Q} = \vec{k}_d - \vec{k}_i$, where $\vec{k}_i$ is the incident beam wave vector and $\vec{k}_d$ is the

diffracted beam wave vector (Figure 3.1a&b). For elastic scattering the magnitudes of the incident and the diffracted beam wave vectors are equal, i.e., $\left|\vec{k}_i\right| = \left|\vec{k}_d\right|$.

In the diffraction technique the crystalline lattice is used as an atomic strain gauge, where increases or decreases in lattice spacing are recorded as angular shifts in the diffraction peak positions (Figure 3.1c&d). Since diffraction is primarily sensitive to the elastic component of strain, the stresses can be calculated from the measured strains using elastic stress-strain relations.

Consider the diffracting geometry shown in Figure 3.1a. The diffraction technique for determining changes in lattice spacing is based on Bragg's law:

$$\lambda = 2d\sin\theta \tag{3.1}$$

where λ is the wavelength of the incident beam, d is the inter-planar spacing in the direction of measurement, and θ is the angle of incidence, which is equal to half the scattering angle. Equation 3.1 shows that for diffraction, $\lambda \leq 2d$ as the maximum value of $\sin\theta \leq 1$. For electro-magnetic radiation λ can be given as:

$$\lambda = \frac{hc}{E} \tag{3.2}$$

where h is Planck's constant, c is the speed of light and E is the energy of the incident photons. Substituting Equation 3.2 in Equation 3.1 gives:

$$\frac{hc}{E} = 2d\sin\theta \qquad (3.3)$$

By measuring the energy peak, the inter-planar spacing, d can be calculated from Equation 3.3 for a constant diffraction angle, θ.

Strain in terms of lattice spacing can be given as:

$$\varepsilon = \frac{d - d_0}{d_0} = \frac{\Delta d}{d_0} \qquad (3.4)$$

where d is the inter-planar spacing in material with strain and d_0 is the inter-planer spacing without strain. Strain can also be given in terms of lattice parameter as:

$$\varepsilon = \frac{a - a_0}{a_0} \qquad (3.5)$$

where a is the lattice parameter with strain and a_0 is the lattice parameter without strain. As mentioned earlier, from the measured strain components stresses within the material can be calculated using the elastic stress-strain relations given in Chapter 2 (Equations 2.13).

3.3 Gauge volume

Like all other methods, a diffraction technique measures strain over a region of the material rather than at a point. The volume of this region is called the gauge volume.

Alternatively, the gauge volume can be defined as the volume captured by the intersection of the incident and the diffracted beams (Withers and Webster, 2001). In diffraction measurements, the size and the shape of the gauge volume can be controlled by the incident beam slit, the diffracted beam receiving slit (or the collimator) in front of the detector and the diffraction angle. Figure 3.2a schematically illustrates the gauge volume, the incident and the diffracted beams and the direction of measurement in the specimen. A typical shape of the gauge volume is a cube (Figure 3.2b), which occurs when the diffraction angle (2θ) is 90°, which is often the case with neutron diffraction measurement. However, in synchrotron X-ray diffraction measurement, the relatively high energy (low wavelength) incident beam results in a low diffraction angle that leads to a gauge volume of an elongated shape (Figure 3.2c) (Withers and Webster, 2001). Selection of an appropriate gauge volume during measurement is important. For measurement in a component with a high stress gradient, high spatial resolution (i.e., a small gauge volume) is required. A larger gauge volume ensures shorter counting time, but results in lower spatial resolution.

3.4 Synchrotron X-ray diffraction

Neutron, conventional X-ray and electron diffraction techniques have their own limitations. With neutrons spatial resolution of less than 1 mm is difficult to achieve, and requires long counting times due to the relatively low intensity. With conventional X-rays only near surface stress measurement is possible. Although high spatial resolution can be achieved with electron diffraction, it has very low penetrating power.

Synchrotron X-ray diffraction has been used as a new technique for measuring strain in bulk engineering materials in recent years. Synchrotron X-rays can be a million times more intense than conventional X-rays, and are capable of producing high energy (20-300 keV) photons, which are over a thousand times more penetrating than conventional X-rays (Withers and Bhadeshia, 2001). With synchrotron X-ray diffraction technique, very fast data acquisition (<1 s), small lateral gauge dimensions (>20 μm) and high sampling depths (about 50 mm in aluminium) can be possible (Lebrun et al., 1995, Daymond and Withers, 1996, Webster et al., 1996, Withers and Webster, 2001). Due to these essentially important characteristics, synchrotron X-ray diffraction technique is becoming popular for measuring strains in fatigue and fracture research.

Synchrotron radiation is generated by accelerating electrons or positrons to a very high speed, near to the speed of light (Riekel, 2003, Winick, 1980, Kunz, 1979). For producing synchrotron X-rays, bunches of electrons (or positrons) are accelerated initially by a linear accelerator (linac) and then by a racetrack-shaped booster ring to an energy level of 6 GeV. These high-energy electrons from the booster ring are then injected into a storage ring (844 meters in circumference at the European Synchrotron Radiation Facility) where they circulate with nearly the speed of light. Figure 3.3 shows a schematic diagram of a polygon shaped storage ring, which is a typical third generation synchrotron radiation source. In the storage ring the electrons are guided from one straight section to another by dipole magnets. The straight sections of the storage ring contain insertion devices as the principal sources of radiation inside the storage ring. The insertion devices consist of a periodic array of bending magnets, which guide the electrons to bend and oscillate in the magnetic

field, causing them to emit synchrotron radiation. The loss of energy by the electrons in the storage ring due to radiation is compensated by radio frequency (RF) cavities. The emitted synchrotron radiation covers a range of frequencies from infra-red to γ-rays. The selection of a wavelength (λ) or a bandwidth ($\Delta\lambda = \lambda_{max} - \lambda_{min}$) from the spectrum is accomplished with a monochromator made up of one or more silicon or germanium crystals. From the storage ring synchrotron X-rays are passed to the beam lines, where experiments are performed.

Figure 3.4 schematically illustrates strain measurement using synchrotron X-ray diffraction, showing the diffraction angle and gauge dimensions. The incident beam is collimated, and both the incident and the diffracted beams are passed through slit systems, which control the sizes of the beams. The diffracted beam is detected by a solid state detector. The incident and the diffracted beams are the same height ($h_i=h_d=h$); the small diffraction angle (2θ) results in a rhombus-shaped (elongated) gauge volume cross section (Figure 3.4). The lengths of the long diagonal, d_l and short diagonal, d_s of the rhombus in terms of beam height, h can be given as:

$$d_l = \frac{h}{\sin\theta} \text{ and } d_s = \frac{h}{\cos\theta} \tag{3.6}$$

For strain measurement with synchrotron X-rays (based on Bragg's law), both poly-chromatic (white) or monochromatic beams can be used. When a monochromatic beam of a fixed wavelength is used, the changes in lattice spacing (i.e., the strains) are recorded as the angular shifts, $\Delta\theta$ in a single diffraction peak according to following equation:

$$\varepsilon = \frac{\Delta d}{d_0} = -\Delta\theta \cot\theta \qquad (3.7)$$

A typical diffraction peak obtained by monochromatic synchrotron X-rays is shown in Figure 3.5. However, when a polychromatic (white) beam is used, the changes in lattice spacing, i.e., the strains are determined by the peak shifts of the photon energy, ΔE, for a fixed diffraction angle, 2θ:

$$\varepsilon = \frac{\Delta d}{d_0} = -\frac{\Delta E}{E} \qquad (3.8)$$

Here a full energy spectrum with multiple peaks is obtained as shown in Figure 3.6. Due to their increased penetration depth, synchrotron X-rays can be used both in transmission and reflection geometries (Figure 3.7). However, the low diffraction angle with this technique results in a much higher path length in reflection, which limits the strain measurement to the near surface region in reflection geometry.

Three different methods can be used for measuring strains with synchrotron X-ray diffraction: (i) traditional $\theta/2\theta$ scanning either in transmission or reflection geometry, with or without an analyser crystal, (ii) transmission method using high energy monochromatic photons with a two-dimensional detector, and (iii) energy dispersive method using white beam high energy photons (Withers, 2001). All three methods provide very low diffraction angles of the order of 4°-10° (Withers and Bhadeshia, 2001).

In $\theta/2\theta$ scanning a monochromatic beam of fixed wavelength is used to measure strains either in transmission or reflection geometry. In this method the changes in lattice spacing are recorded as the angular shifts, $\Delta\theta$ in a single diffraction peak according to Equation 3.7 (Figure 3.8a). Here near surface stress measurement can be influenced by the problem of partial filling of the gauge volume. However, this problem can be resolved by using an analyser crystal in front of the detector (Withers, 2003).

In the transmission method a high energy monochromatic beam is focussed on the specimen and CCD detectors are used to collect large two-dimensional diffraction patterns (rings) in transmission geometry (Withers, 2001). Here the small diffraction angle results in the Q-vector being almost perpendicular to the incident beam, so the strains in the horizontal and vertical in-plane directions can be given by the changes in the horizontal and vertical diameters of the diffraction rings respectively (Figure 3.8b). Difficulties in restricting the gauge dimension along the direction of the beam makes this method only suitable for a material in which the stress is largely invariant through the thickness.

In the energy dispersive method a high energy (from 40 keV to 300 keV) poly-chromatic (white) beam is incident on the specimen and the diffracted (transmitted) beam is detected by two solid state detectors placed at a small angle ($2\theta = 4°$ to $10°$) to the incident beam to measure strains in the horizontal and vertical in-plane directions. Here a whole diffraction spectrum is obtained as a function of photon energy (Figure 3.8c), where the strains are given by the peak shifts of the photon energy, ΔE, for a fixed diffraction angle, 2θ (Equation 3.8).

3.5 Laboratory X-ray diffraction

Laboratory X-ray diffraction is widely used in measuring stresses in the near surface region of a component due to its low penetrating depth (typically tens of micrometers) (Withers and Bhadeshia, 2001). Since the normal stress must be zero at the surface, for the near surface measurement plane stress condition can be assumed (Fitzpatrick et al., 2002). Information can be obtained at greater depths of up to 1mm by successively removing surface of the specimen using electro-polishing and measuring stresses (Withers, 2001). From the stress variation with depth, the original stress state in the specimen can be deduced by back calculating the effect of surface removal (Withers, 2001).

3.6 Neutron diffraction

Neutron diffraction is a valuable non-destructive strain measurement technique with a penetrating depth of several centimetres, which allows the technique to measure strain deep inside the bulk of a material (Withers and Bhadeshia, 2001). With neutron diffraction, the required diffracted intensity inside the material can be obtained from a gauge volume of just over 1 mm^3 (Withers and Bhadeshia, 2001).

Two kinds of neutron sources are available for neutron diffraction measurement, namely reactor sources (steady-state source) for continuous beams and spallation sources for pulsed beams. With reactor neutron sources, conventional $\theta/2\theta$ scanning method is usually employed, where the diffraction profile is recorded as a function of Bragg angle, θ (Withers and Bhadeshia, 2001). In this method a

monochromatic beam of a fixed wavelength is normally used in which the changes in lattice spacing are recorded as the angular shifts, $\Delta\theta$ in a single diffraction peak following Equation 3.7, which is identical in principle to the synchrotron X-ray $\theta/2\theta$ scanning method.

With a spallation neutron source a time-of-flight method is employed, where pulses (perhaps 50 times a second) of neutrons are incident on the specimen and diffracted with a fixed Bragg angle (usually $2\theta = 90°$) (Withers and Bhadeshia, 2001). Each pulse leaving the moderator contains neutrons with a large energy range as a polychromatic (white) beam is used. Although all the neutrons from one pulse leave the source almost at the same time, the time taken by an individual neutron to reach the detector from the moderator depends upon the energy of that neutron. The time taken by a neutron to travel from the moderator to the detector is called the time-of-flight. The wavelength, λ and hence the energy of each detected neutron (using Equation 3.2) can be deduced from the time-of-flight, t using de Broglie's relationship:

$$\lambda = \frac{ht}{ml} \tag{3.9}$$

where h is Planck's constant, m is the neutron mass and l is the flight path length. The changes in lattice spacing i.e., the strains are given by the peak shifts of the time-of-flight, Δt:

$$\varepsilon = \frac{\Delta d}{d_0} = \frac{\Delta t}{t} \tag{3.10}$$

Here a whole diffraction spectrum is obtained as a function of the time-of-flight (Figure 3.9). The strain resolution obtained is dependent on the accuracy of the measurement of the time-of-flight. However, high resolution instruments usually have large flight paths (>100 m) (Withers and Bhadeshia, 2001).

3.7 Electron diffraction

With electron diffraction a high lateral spatial resolution of as small as 10 nm, but only low penetrating depth (<100 nm) is possible (Withers and Bhadeshia, 2001). Therefore, electron diffraction can be used to measure type II and type III residual stresses in very thin samples (<100 nm), for example: measuring the stress fields between and within individual grains at precipitates, dislocations or defects.

3.8 Conclusion

As a part of the theoretical review the principle of diffraction strain measurement and different diffraction techniques have been discussed briefly. Synchrotron X-ray diffraction technique is of particular interest as the energy dispersive method has been used in this study for the investigation of stresses around fatigue cracks in aluminium alloy 5091 compact tension specimens. The results of the investigation will be presented in the following chapter.

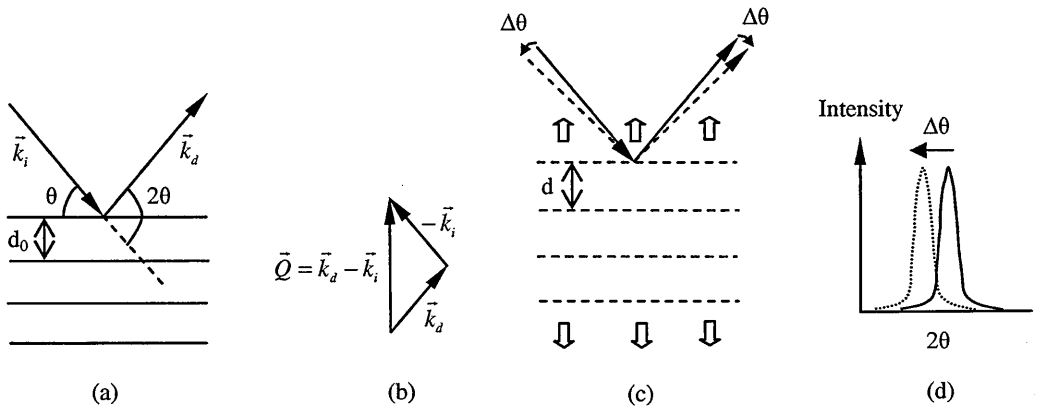

Figure 3.1: (a) Incident and diffracted beams on un-deformed geometry, (b) Q-vector at the direction of strain measurement, (c) angular shifts of incident and diffracted beams on deformed geometry, (d) angular shift of a diffraction peak position.

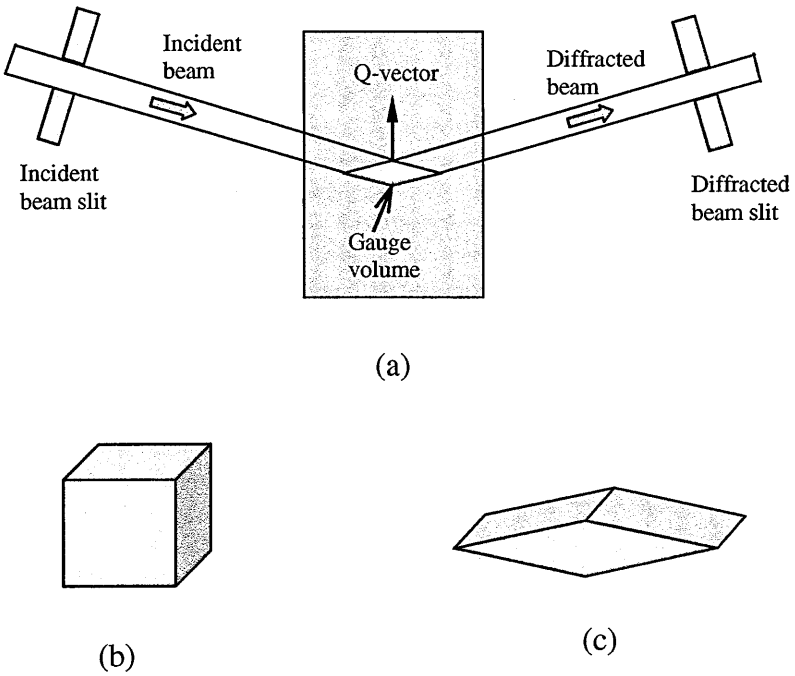

Figure 3.2: (a) Gauge volume showing the incident and the diffracted beams and the direction of measurement, (b) a cube gauge volume, (c) an elongated gauge volume.

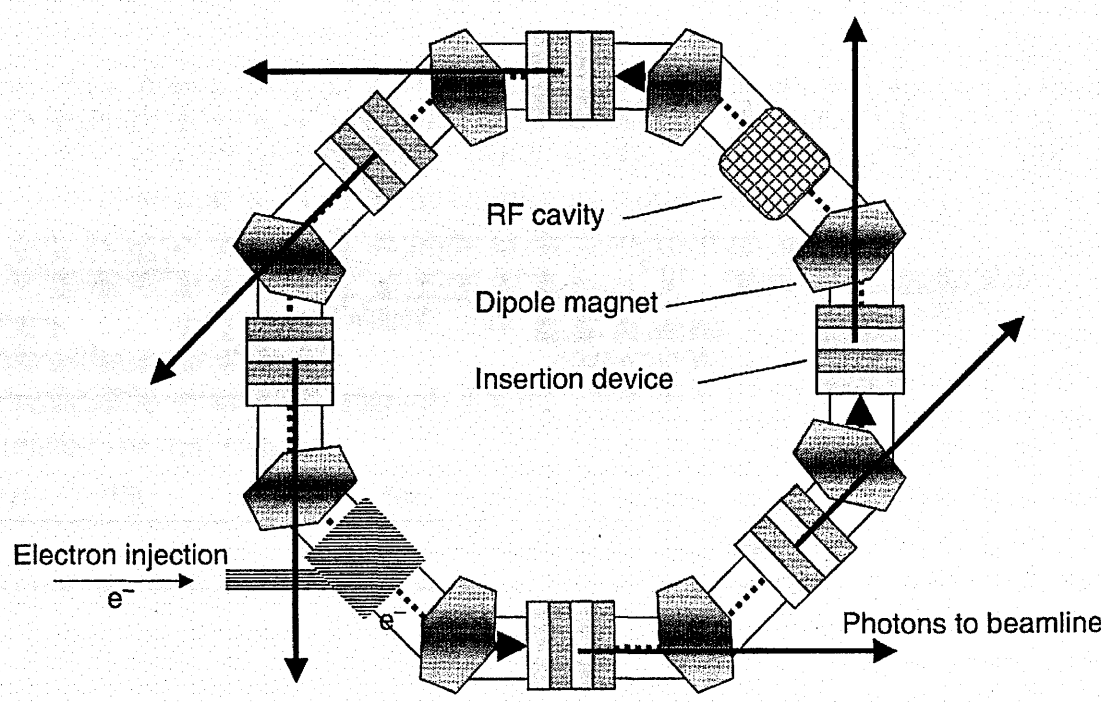

Figure 3.3: Schematic diagram of synchrotron X-ray storage ring (Riekel, 2003).

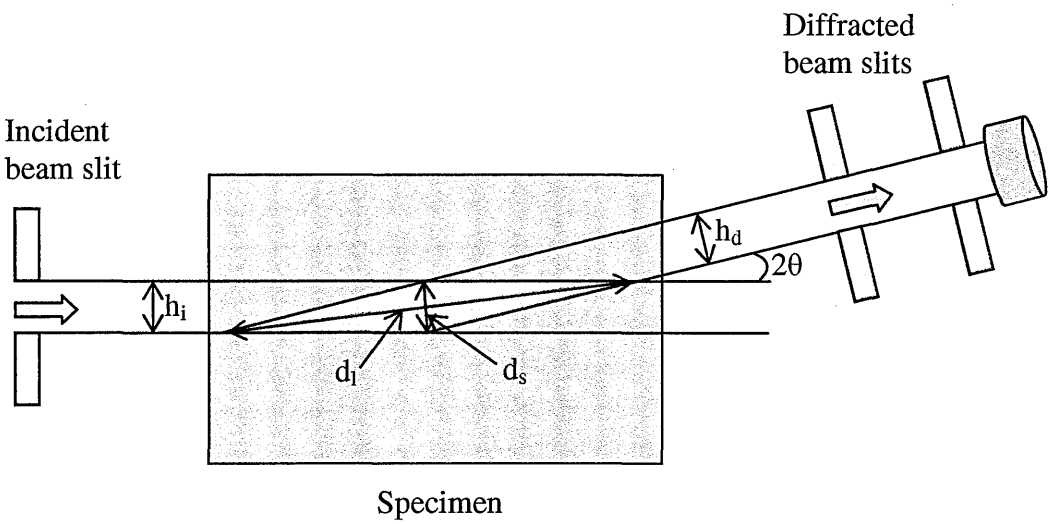

Figure 3.4: Schematic of synchrotron X-ray diffraction strain measurement, showing diffraction angle and gauge dimensions with rhombus-shaped gauge volume cross section (red).

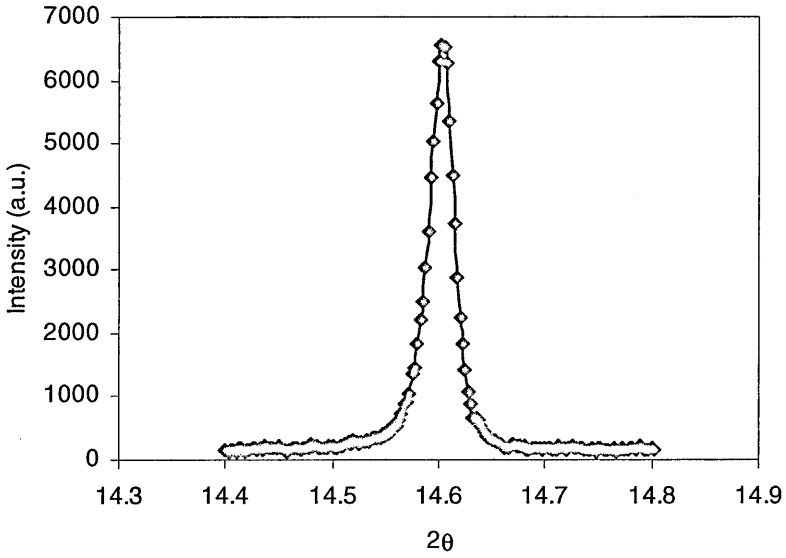

Figure 3.5: A typical diffraction peak obtained by monochromatic synchrotron X-ray diffraction.

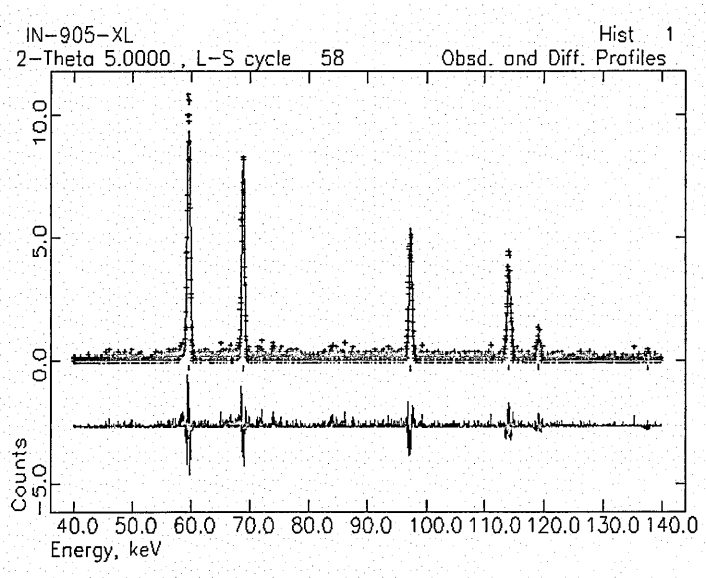

Figure 3.6: A typical diffraction spectrum obtained by polychromatic synchrotron X-rays showing data points (red pulses), its fitted curve (green) and the difference curve (pink).

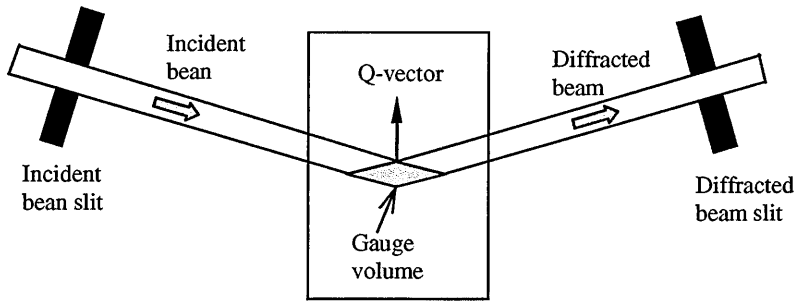

(a)

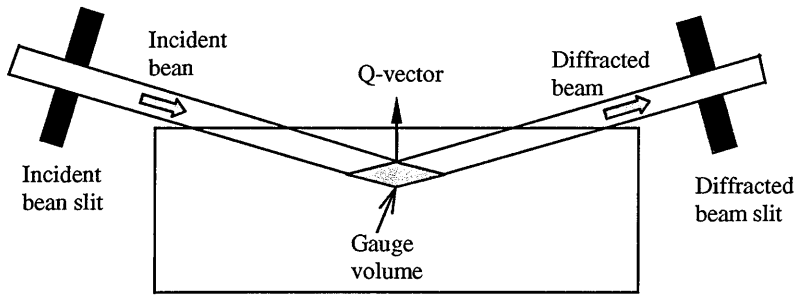

(b)

Figure 3.7: Schematic of strain measurement in (a) transmission and (b) reflection.

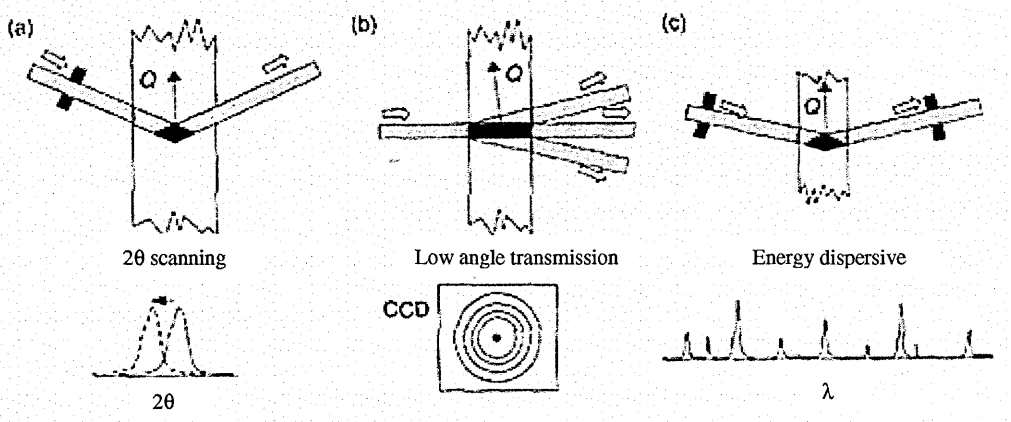

Figure 3.8: Schematic of three different synchrotron X-ray strain measurement methods showing the diffraction patterns they provide (Withers, 2003).

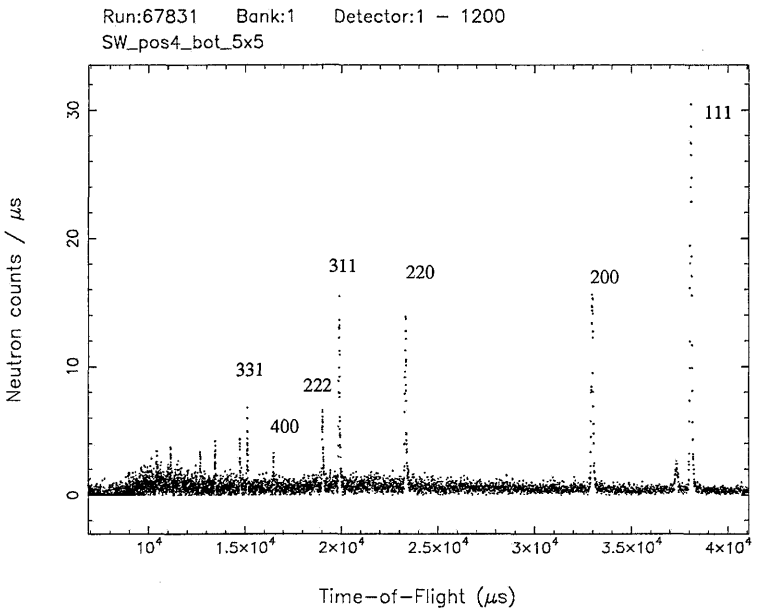

Figure 3.9: A typical time-of-flight diffraction pattern for stainless steel (Pratihar, 2006).

Chapter 4 Experimental investigation of the strain and stress fields around fatigue cracks in aluminium alloy 5091

4.1 Introduction

Paris and Erdogan (1963) employed fracture mechanics for characterizing fatigue crack propagation. Since then, a multitude of research has been undertaken to provide insight into the mechanisms of fatigue crack growth. Various empirical models/equations have been developed to describe crack growth rate as well as to predict/assess fatigue life under constant amplitude fatigue (Weertman, 1966, Forman et al., 1967, Elber, 1970, Klesnil and Lucas, 1972, Donahue et al., 1972, McEvily, 1988). However, a real structure or a component experiences a spectrum of stresses, i.e., variable amplitude fatigue, over its lifetime. Therefore, the crack growth rate depends not only on the current loading conditions, but also on the previous loading history. For example, an overload produces compressive residual stresses at the crack tip (Schijve, 1961, Ramos et al., 2003), which retard the crack growth rate by altering the local crack tip stresses under baseline loading following the overload. When the crack advances through the overload plastic zone, the compressive residual stresses in the element now just behind the crack tip are relaxed and the material in this element expands, thereby contributing to the crack closure on the crack flanks behind the crack tip (McEvily and Ishihara, 2001). Therefore, the compressive residual stresses at the crack tip resulting from an overload and the crack closure behind the crack tip on the crack flanks are intimately related. Plasticity-induced crack closure due to an overload reduces ΔK by

increasing K_{min} of the fatigue cycle, resulting in crack retardation.

Fatigue crack growth is caused by the local fracture of the material of a component. Consequently, understanding of the local internal stress and strain fields around the crack tip is crucial in constructing an effective fatigue life prediction model. X-ray and neutron diffraction are widely accepted non-destructive techniques, which can be employed in the direct measurement of the changes of lattice parameters so as to measure local strain fields in polycrystalline materials under stress.

Despite its high penetration depth (typically many centimetres), the application of neutron diffraction is limited to strain measurements in comparatively large components preferably with low strain gradients because of the limitation of using a large gauge volume with this technique. On the contrary, the low penetration depth of the conventional X-ray method, limits its use in measuring strain to the near surface region (typically tens of micrometres). Synchrotron X-ray diffraction is emerging as an appropriate technique for profiling local internal crack tip strain and stress fields, because high penetration and high spatial resolution are achievable with this technique.

Efforts have been made by many previous researchers to investigate stresses around fatigue cracks experimentally. Allison (1979) studied near surface crack tip stress fields using conventional X-ray diffraction in 1045 steel compact tension (CT) fatigued specimens. This study was focused on the crack plane stresses, where the influences of overload and crack extension on the crack tip stress fields were studied. He found that the overload has a strong effect on the subsequent applied and

residual stress profiles at the crack tip; however the effect of crack extension is small. The results showed that the size of the compressive residual stress zone at the crack tip due to an overload increases with increasing overload magnitude. He also investigated crack tip stresses under in-situ loading. Holloway (1979) investigated crack tip stresses in a 1020 steel compact tension specimen using X-ray diffraction. In his investigation a single overload was applied and the existing crack was extended past the overload-affected zone. The results show that compressive residual stresses develop in the vicinity of the point of overload. He observed that the effect of the overload on the applied and residual stresses had dissipated by the time the crack was propagated through a distance approximately equal to the plastic zone size caused by the overload.

Wang et al. (1999) numerically and experimentally investigated residual stress effects on fatigue crack growth under constant amplitude loading in a low alloy high strength structural steel of European grade S690QL1. X-ray diffraction was employed for surface strain measurement around the crack of a compact tension shear (CTS) specimen used in this investigation. Based on their initial finite element calculations, a combined hardening law was applied for further calculations. They showed that compressive residual stresses or crack closure effects along the crack surfaces behind the tip of a fatigue crack have hardly any influence on the residual stress distribution ahead of the crack tip and thus on further fatigue crack growth. Ramos et al. (2003) investigated the effects of single and multiple overloading on the fatigue life of low carbon structural steel. Using surface X-ray diffraction, residual stresses (σ_{yy}) acting along the direction perpendicular to the crack plane were measured in the crack plane region in compact tension specimens after

overloading to levels of 200% and 300%. The results revealed that with the increasing overload the compressive residual stresses in the vicinity of the crack tip increase in magnitude and spatial extent. It was also shown that a higher overload gives rise to a greater fatigue life extension.

James et al. (2004) applied synchrotron X-ray diffraction to investigate the distribution and influence of residual stresses in fatigue. Firstly, they studied the variation of the local residual stresses and diffraction peak intensities in as-welded 5083-H321 aluminium alloy friction-stir welded (FSW) and metal-inert gas (MIG) welded specimens. They also studied the change in the variation of the local residual stresses and diffraction peak intensities in those specimens during fatigue loading. Secondly, they applied the synchrotron X-ray diffraction technique for strain mapping around the crack tip of a standard 5083-O aluminium alloy compact tension fatigued specimen. Croft et al. (2005) employed energy dispersive X-ray diffraction (EDXRD) for profiling longitudinal strains (ε_{yy}) around fatigue cracks in single edge notched tension (SENT) and compact tension 4140 steel specimens with 4 mm thickness. They discussed a comparison of residual strain profiles in the x direction along and parallel to the crack planes and in the y direction crossing the crack in the region 2-4 mm behind the crack tip for fatigued, fatigued-overloaded and fatigued-overloaded-fatigued SENT specimens. They also discussed the variation of ε_{yy} along the y direction crossing the crack plane for various x positions relative to the crack tip (x=0) in fatigued-overloaded-fatigued CT specimen under tensile loading and unloading conditions. Steuwer et al. (2006) reported on the direct measurement and mapping of local residual strains around a fatigue crack in a 1 mm thick aluminium alloy 5091 SENT specimen using synchrotron X-ray diffraction.

They showed how a 100% overload affects the residual strain fields at the crack tip. Recently, Tsakalakos et al. (2006) measured residual stresses around the crack tip due to an overload in CT 4140 steel specimen in plane strain using EDXRD. Their experimental results show compressive longitudinal residual stresses on the crack flank behind the crack tip.

This chapter presents the results of an investigation of the strain and stress fields around fatigue cracks in fine-grained aluminium alloy 5091 compact tension specimens using energy dispersive X-ray diffraction. The measurements were carried out at the European Synchrotron Radiation Facility (ESRF), Grenoble, France.

4.2 Experimental details

4.2.1 Material

The material used in this investigation was aluminium alloy 5091 with the composition Al-4Mg-1.3Li-1.1C-0.4O, which contains a dispersion of very fine oxides (Al_2O_3) and carbides (Al_4C_3). The microstructure consists of uniform and equiaxed grains with an average diameter of about 0.6 μm (Blankenship et al., 1995). The oxide dispersoids are of approximately spherical shape with an average diameter of 40 nm and the carbides are cylindrical with average dimensions of 20 nm by 100 nm (Blankenship et al., 1995). Although the alloy is in principle precipitation hardenable, the combination of dispersion and very fine grain size permits high strength to be achieved without the utilization of precipitation

hardening. The alloy was manufactured by Inco Alloys International using mechanical alloying, a powder metallurgy process. The very small grain size of aluminium alloy 5091 makes it an ideal material for high resolution investigation by energy dispersive X-ray diffraction, since it allows very narrow slits to be used (while still providing a powder average). The mechanical properties of the material are: yield strength 448 MPa, ultimate tensile strength 517 MPa, modulus of elasticity 78 GPa, Poisson's ratio 0.345 and bulk fracture toughness 29.7 MPa$\sqrt{m}$ (Schelleng et al., 1985). The specimens were machined from a forged plate of 50 mm thickness.

4.2.2 Specimens

Three compact tension specimens were prepared as recommended in standard ASTM E647. Specimens investigated were fatigued (F), fatigued-overloaded (FO) and fatigued-overloaded-fatigued (FOF). The specimens were prepared: with constant amplitude fatigue (fatigued specimen), with constant amplitude fatigue followed by a single overload (fatigued-overloaded specimen), and finally with constant amplitude fatigue followed by a single overload then followed by further constant amplitude fatigue (fatigued-overloaded-fatigued specimen). For all three specimens, the specimen width, W and the initial crack length, a_o were 50 mm and 15.2 mm respectively. The thicknesses, B for the fatigued, fatigued-overloaded and fatigued-overloaded-fatigued specimens were 12.25 mm, 12.35 mm and 12 mm respectively. The specimens were fatigue cracked under a constant ΔK of 6 MPa$\sqrt{m}$ with K_{max}=6.6 MPa$\sqrt{m}$ and R=0.1 (K_{min}=0.66 MPa$\sqrt{m}$) in an MTS servo-hydraulic test system. During fatigue cracking of each specimen, the crack length was monitored by a travelling microscope and the specimen compliance was monitored

using a back face strain gauge. For the fatigued specimen the crack was grown to a length of 26.7 mm. For the fatigued-overloaded specimen the crack was grown to 27.5 mm and then an overload of 16.5 MPa$\sqrt{m}$ (150%) was applied. Finally, for the fatigued-overloaded-fatigued specimen the crack was grown to 26.6 mm, where an overload of 13.2 MPa$\sqrt{m}$ (100%) was applied, and following that overload the crack was extended a further 0.1 mm resulting in a final crack length of 26.7 mm. For each of the specimens, before stopping the test, the relationship between the applied load and the back face strain was noted for the final crack length, effectively calibrating the strain gauge as a load gauge for that crack length. The determination of the relationship between the applied load and the back face strain for all specimens was required in order to determine the applied in-situ loads in terms of back face strains, as the Hounsfield tensometer used for applying load during the experiments, did not have a load cell. For all three specimens, the final crack lengths were such that the crack length to the width ratio, a/W lies between 0.45 and 0.55. Figure 4.1 illustrates a compact tension specimen showing all characteristic dimensions.

4.2.3 Strain measurement and stress calculation

During the diffraction strain measurement experiment, the specimens were loaded using a modified Hounsfield tensometer mounted vertically on the mounting table as shown in Figure 4.2. The selected in-situ loads for each of the specimens were calculated from the relations between the loads and the back face strains obtained during preparation of the specimens. Two solid state X-ray detectors were used to measure strains inside the specimen both in the horizontal and vertical directions as shown schematically in Figure 4.3. The incident beam and the horizontal and the

vertical detectors were fixed to give a scattering angle of $2\theta=5°$ for both detectors. The incident beam slit gaps were 25 μm both in the horizontal and vertical directions. For the diffracted beams, near the specimen and near the detector the slit gaps were set to 40 μm in the horizontal and vertical directions. The detectors and the receiving slits were aligned precisely to within 20 μm.

In energy dispersive X-ray diffraction (EDXRD), a high energy white beam (of all wavelengths of up to 250 keV in this case) is incident on the specimen, and the energy of the resulting diffracted beams (photons) are analyzed by the detectors. In energy dispersive mode the diffraction profile is obtained as a function of energy rather than angle. The EDXRD spectrum (Multi-Channel Analyser data) is first transformed to an artificial pseudo-angular dispersive domain (Steuwer et al., 2004) and then refined and fitted using the software package GSAS (Larson and Von Dreele, 2000) in intensity extraction mode (LeBail et al., 1988), which fits all peak positions to the lattice parameter. A typical diffraction spectrum for Al 5091, its fitted curve using the software GSAS and the difference curve are shown in Figure 4.4.

The strains in the specimens were calculated from the stress free lattice parameter, a_0 obtained from a far field measurement in the unloaded state, and the measured point-to-point lattice parameters, a, using Equation 3.5. The strain measurements were carried out around the crack tip over a 2×2 mm^2 area along the mid-thickness of the specimen. Within this region an area of 0.5×0.5 mm^2 surrounding the crack tip was scanned with a pitch of 25 μm and the remaining area was scanned with a pitch

of 100 μm. The counting time for each point was set to 50 s for simultaneously measuring the strain components ε_{yy} (the longitudinal strain along the direction perpendicular to the crack plane) and ε_{xx} (the transverse strain along the direction of the crack). It is worth mentioning here that during strain measurement the position of the crack tip inside the specimen was difficult to identify as it may be displaced slightly compared to the apparent position on the specimen surface. Therefore, a low resolution map (1×1 mm^2 area with 50 μm pitch) was produced initially under each load in order to identify the crack tip inside the specimen before taking the final measurements.

Cartesian stresses σ_{yy} (the longitudinal stress along the direction perpendicular to the crack plane), σ_{xx} (the transverse stress along the direction of the crack) and σ_{zz} (the normal stress through the thickness), and the hydrostatic stress, σ_m around the crack tip were calculated from the measured strains using elastic stress-strain relations (Equations 2.13) and assuming plane strain conditions, since all three specimens satisfy the plane strain linear elastic fracture mechanics dimensional conditions recommended in ASTM E 399-90 (1990) as $a, B, (W-a) \geq 2.5\left(\frac{K_{IC}}{\sigma_y}\right)^2$. The thickness, B ensures plane strain conditions, while (in-plane dimensions) the crack length, a and the width, W ensure linear elastic behaviour. Validity for the small scale yielding approximation was checked by calculating the crack tip plastic zone radius, r_y using Equation 2.49. For small scale yielding r_y must be $\leq \frac{1}{50}\{a, (W-a)\}$ (Anderson, 1995).

4.3 Results

Experimental results are presented for the fatigued (F), fatigued-overloaded (FO) and fatigue-overloaded-fatigued (FOF) specimens. It should be mentioned here that throughout the thesis the load is presented in terms of stress intensity factor (K). Strain and stress fields have been investigated under applied K=6.6 (K_{max}) MPa$\sqrt{m}$ in the fatigued specimen; under K=16.5 (K_{ol}), 3.6 and 0.66 (K_{min}) MPa$\sqrt{m}$ in the fatigued-overloaded specimen; and finally under K=6.6 (K_{max}), 3.6, and 2.6 MPa$\sqrt{m}$ in the fatigued-overloaded-fatigued specimen. The analysis is based on both Cartesian (x,y) and cylindrical (r,θ) coordinate systems centred at the crack tip.

Strain and stress maps for the fatigued, fatigued-overloaded and fatigued-overloaded-fatigued specimens have been constructed from the experimental data for the whole range of loading. Experimental strain and stress profiles around the crack tips in the specimens have also been determined for all applied loads. The strain and stress profiles have been compared for the different load cases in each specimen and for the different specimens under the same applied load.

A detailed discussion of the theoretical strain and stress distributions around the crack tip for a stationary crack is presented first in order to provide a benchmark for the experimental results. The theoretical stress calculations have been performed for an applied load of 6.6 MPa$\sqrt{m}$ (K_{max}) using the linear elastic fracture mechanics (LEFM) solution (Equations 2.36) given by Westergaard (1939). From the stresses, the strains have been calculated using elastic stress-strain relations (Equations 2.10). The theoretical stresses and strains around the crack tip have been determined using

the coordinates of all 730 points used in experimental measurement in order to construct maps as well as line plots of the theoretical strains and stresses. Calculations were performed using Microsoft Excel and assuming plane strain conditions. The experimental crack tip stresses for the fatigued specimen at K=6.6 MPa$\sqrt{m}$ have been compared with the theoretically determined results.

4.3.1 Stationary crack results

Figures 4.5 and 4.6 present crack tip strain and stress maps respectively for a stationary crack for K=6.6 MPa$\sqrt{m}$. Figure 4.5a shows a region of two strain lobes on either side of the crack plane with a maximum longitudinal strain of about 2800 με just ahead of the crack tip, where the two strain lobes appear to swing forward. Figure 4.5b shows an area with a maximum transverse strain of about 1400 με just ahead of the crack tip in the crack plane region accompanied by two compressive strain lobes (upward and downward) along the y direction. In the region behind the crack tip, starting at zero in the crack plane, the longitudinal and transverse strains change to compressive and tensile respectively along the y direction near the crack plane. The corresponding stress maps in Figure 4.6 show significant Cartesian stresses just ahead of the crack tip resulting in high stress triaxiality as well as high hydrostatic stress at the crack tip, which is expected in plane strain at K_{max}. Like the strains the stresses in the crack plane behind the crack tip appear to be zero and they increase along the y direction from the crack plane. The nature of the strain and stress distributions around the crack tip for a stationary crack will become clear from the subsequent strain and stress profiling.

Figures 4.7 and 4.8 illustrate the strain and stress variations respectively along the x direction in the crack plane. It is shown in Figure 4.7 that in the crack plane ahead of the crack tip, the longitudinal and transverse strains show identical x variations, which results in identical longitudinal and transverse stress variations with lower normal and hence lower hydrostatic stresses as shown in Figure 4.8. It should be mentioned here that for linear elastic fields both strains and stresses are infinite at the crack tip, therefore the crack tip is omitted as a data point in the graphs. In the crack plane ahead of the crack tip, both the strain and stress starts with a minimum value (tensile) in the far field, and then continues to increase to a maximum value (tensile) as x moves towards the crack tip as shown in Figures 4.7 and 4.8. Behind the crack tip along the crack plane the strains and stresses appear to be zero.

Figures 4.9 and 4.10 show the variation of the strains and stresses respectively along the y direction crossing the crack plane at three different x positions ahead of the crack tip. It is seen from Figure 4.9a that in the crack plane, the longitudinal strain appears to have relatively low tensile values, and starting from the crack plane this strain continues to increase to a maximum value at a certain distance along the y direction and then decreases gradually to a minimum value (tensile) as y moves away from the crack plane. However, as the distance x ahead of the crack tip increases, the slope of the strain variation curve decreases as in Figure 4.9a. Ahead of the crack tip the transverse strains appear to be maximum (tensile) along the crack plane as shown in Figure 4.9b. Near to the crack tip (with smaller x values) this strain decreases sharply along the y direction and becomes compressive, reaching a maximum compressive value at a certain distance from the crack plane, and then starts decreasing (becomes less compressive) as y moves away from the crack plane.

However, as the distance x ahead of the crack tip increases, the slope of the strain variation curve as well as the magnitude of the maximum compressive strain decreases as in Figure 4.9b. Figure 4.10a shows that the y variation of the longitudinal stress ahead of the crack tip is reasonably similar to that of the longitudinal strain. Figure 4.10b shows that in and near the crack plane the y variation of the transverse stress is also similar to that of the transverse strain, but unlike the transverse strain, the transverse stress does not become compressive with y moving further away from the crack plane. The normal and hydrostatic stresses show y variations similar to the transverse stress with slight differences in stress variation slope as shown in Figure 4.10c&d. It should be mentioned here that unlike the transverse strain, none of the stresses appears to be compressive ahead of the crack tip regardless of positions x and y.

Figures 4.11 and 4.12 illustrate the distributions of strains and stresses respectively along the y direction crossing the crack plane at three different x positions behind the crack tip. Figure 4.11 shows that for a stationary crack, behind the crack tip along the crack plane both the longitudinal and transverse strains appear to be zero. As shown in Figure 4.11a, starting at zero in the crack plane, the longitudinal strain becomes compressive along the y direction and reaches a maximum value at a certain distance from the crack plane. However, as y moves further away from the crack plane, the compressive strain decreases and finally becomes tensile, then continues to increase with y and reaches a maximum value, and then decreases in the far field. It is further apparent from Figure 4.11a that as the distance x from the crack tip increases, the slope of the strain variation curve and the magnitudes of the maximum compressive and tensile strains decrease although the span of the

compressive strain region (along the y direction) widens. Figure 4.11b shows that starting at zero in the crack plane, the transverse strain becomes tensile along the y direction and reaches a maximum value at a certain distance from the crack plane, and then starts decreasing as y moves further away from the crack plane. It is also seen from Figure 4.11b that as the distance x from the crack tip increases, the slope of the strain variation curve and the magnitude of the maximum strain (tensile) decreases. Moreover, with increasing x the position of the maximum strain moves away from the crack plane. Figure 4.12a shows that starting from zero in the crack plane, the longitudinal stress increases to a maximum value (tensile) at a certain y position and then decreases as y moves away from the crack plane. Near the crack tip (for smaller x values) the stress variation follows a steeper curve and it becomes flatter with increasing distance x. Figure 4.12b shows that the y variation of the transverse stress behind the crack tip follows a similar variation to the longitudinal strain, except that it follows a steeper curve. The normal and hydrostatic stresses in Figure 4.12c&d also start from zero in the crack plane, and both follow trends in between the longitudinal and transverse stresses.

4.3.2 The fatigued specimen results

Figures 4.13 and 4.14 show the experimentally-determined crack tip strain and stress maps respectively for the fatigued specimen for an applied K=6.6 MPa$\sqrt{m}$ (K_{max}). Figure 4.13a shows that a region with a maximum longitudinal strain of about 2400 $\mu\varepsilon$ develops just ahead of the crack tip and two strain lobes appear to swing forward, which is reasonably similar to the modelled crack results discussed earlier. However, behind the crack tip a band of relatively high compressive strains (about

–800 to –1200 με) is apparent along the crack surface region, which was not evident for a stationary crack. Figure 4.13b shows a high transverse strain area of about 1600 με in the crack tip region, forming two horizontal lobes. As in the modelled crack tip map, above and below the crack tip two compressive transverse strain regions are also apparent in Figure 4.13b. However, the maximum compressive strain is much less here (less than –200 με), which may be due to plastic deformation at the crack tip. Behind the crack tip, along the crack plane region the transverse strain appears to be noticeably tensile (about 600 to 1500 με), which was not evident for a stationary (modelled) crack. The corresponding stress maps in Figure 4.14 show high longitudinal, transverse and normal stresses (about 375, 300 and 225 MPa respectively) just ahead of the crack tip resulting in high stress triaxiality as well as high hydrostatic stress (about 300 MPa), which is expected in plane strain. Ahead of the crack tip the experimentally determined stress fields in Figure 4.14 are quite similar to that for a stationary (modelled) crack in Figure 4.6 except that the theoretical fields show relatively high maximum stresses ahead of the crack tip due to the absence of crack tip plasticity. Figure 4.14a shows a longitudinal compressive stress region behind the crack tip, where the stresses appear to be more compressive (about –75 MPa) along the crack plane region which is in contrast to the modelled crack where the longitudinal stresses are zero along the crack surface. Figure 4.14b shows a transverse tensile stress region behind the crack tip. Here, the transverse stresses along the crack surface region are apparently higher than for the modelled crack. Behind the crack tip along the crack plane region both the normal and hydrostatic stresses appear to be compressive as in Figure 4.14c&d.

Figures 4.15 and 4.16 show the variation of the strains and stresses along the x direction in the crack plane for the fatigued specimen. Figure 4.15 shows that the far field longitudinal strain (about 300 με at x =+0.95 mm) increases as x approaches the crack tip. It can be noticed here that the longitudinal strain variation rate increases significantly as x moves closer to the crack tip. Near the crack tip the longitudinal strain reaches a maximum value (about 2900 με at x=+0.025 mm). Then it shows a discontinuity in the crack tip region, where the strain changes rapidly from tensile to compressive values. Behind the crack tip the longitudinal strain appears to be compressive (about −1300 με at x=−0.075 mm) in the crack plane, showing a slight variation with x along the crack plane (about −650 με at x=−1.1 mm). Similar longitudinal strain variations were observed by Croft et al. (2005) using relatively thin (4 mm thick) SENT (single edge notched tension) specimens (i.e., in plane stress) with energy dispersive synchrotron X-ray diffraction measurements.

Figure 4.15 shows that ahead of the crack tip (except close to the crack tip) the transverse strain appears to show higher values than the longitudinal strain and a relatively small variation along the x direction. Starting with a value of about 950 με at x=+0.95 mm ahead of the crack tip the transverse strain increases gradually as x moves towards the crack tip. At x=+0.1 mm the transverse strain shows a maximum value of about 1570 με. Then it exhibits a sharp decrease to about 950 με at x=+0.025 mm, where the longitudinal strain exhibits its maximum value. Following the sharp decrement at x=+0.025 mm, the transverse strain appears to show an instant sharp increment near the crack tip. This sharp change of transverse

strain distribution near the crack tip is possibly due to equilibrating the rapidly increasing stresses near the crack tip. Behind the crack tip the transverse strain appears to be tensile with a slight variation with x along the crack plane (about 1300 με at x=–0.05 mm and 460 με at x=–1.1 mm). Figure 4.16 shows the x variation of Cartesian and hydrostatic stresses along the crack plane. The longitudinal and transverse stresses show quite similar x variations along the crack plane ahead of the crack tip with slight differences in magnitudes. Starting in the far field both stresses increase as x moves towards the crack tip. However, the transverse stress continues to maintain higher values for most of the distance except in the region close to the crack tip, where the longitudinal stress exhibits a sharp increase. At x=+0.025 mm the longitudinal and transverse stresses are 426 and 320 MPa respectively as in Figure 4.16. Theoretically (Westergaard, 1939) along the crack plane ahead of the crack tip both the longitudinal and transverse strains and hence both the longitudinal and transverse stresses are expected to show identical x variations as discussed in the previous section. The observed differences in strain and stress variations are possibly due to the effect of the specimen geometry under an applied load, which will be discussed later.

The normal and hydrostatic stresses show crack plane variations ahead of the crack tip similar to the longitudinal and transverse stresses, but with lower stress values as shown in Figure 4.16. Behind the crack tip along the crack plane the longitudinal and transverse stresses appear to be compressive and tensile respectively as shown in Figure 4.16. It is seen that at x=–0.075 mm behind the crack tip the longitudinal and transverse stresses are –80 and 74 MPa respectively, and the stresses show small

variations over the distance behind the crack tip (at x=–1.1 mm the longitudinal and transverse stresses are –50 MPa and 15 MPa respectively).

Wang et al. (1999) found compressive longitudinal residual stresses near the crack plane region behind the crack tip using surface X-ray diffraction measurements and finite element calculations. Zhao et al. (2004) found compressive residual stresses along the crack plane behind the crack tip both in plane stress and plane strain using finite element analysis, where the compressive stress magnitudes were much higher in plane stress. Tsakalakos et al. (2006) also observed compressive residual longitudinal stresses on the crack flank behind the crack tip in plane strain for a fatigued-overloaded specimen using EDXRD measurements. They mentioned two possible causes of the crack flank compressive longitudinal stresses as: the probing volumes for ε_{xx} and ε_{yy} in the EDXRD measurements are different, and the precise location of the same point of measurement is very difficult. Compressive longitudinal stresses are expected on the crack flank when the crack is closed. At K_{max} (6.6 MPa$\sqrt{m}$) the longitudinal stresses on the crack flank are expected to be zero as the crack is open under this load. In the present work the compressive longitudinal stresses on the crack flank at K_{max} could possibly be due to the two different gauge volumes (in terms of diffraction gauge volume geometry and positioning) for measuring the two strain components ε_{xx} and ε_{yy} in a region with a high compressive longitudinal strain gradient along the y direction from the crack plane. The present results are in contrast to Allison (1979) and Holloway (1979), who found tensile longitudinal stresses on the crack flank behind the crack tip using surface X-ray diffraction measurements in loaded specimens when the crack was open. Allison (1979) attributed the cause of the nonzero (tensile) stresses on the

crack flank to the size of the X-ray beam, which was much larger than the crack opening, and thus stresses were measured in the material on both sides of the open crack. The normal and hydrostatic stresses appear to be very small along the crack surface as shown in Figure 4.16.

Figures 4.17 and 4.18 illustrate the y variations of the strains and stresses respectively at three different x positions (x=+0.025, +0.1 and +0.3 mm) ahead of the crack tip crossing the crack plane for the fatigued specimen at K_{max}. In Figure 4.17 both the longitudinal and transverse strains demonstrate reasonably similar variations to the theoretical results shown in Figure 4.9. However, it can be mentioned here that in the experimental results at x=+0.025 mm, the longitudinal strain does not appear to show a sharp decrement at the crack plane as in the theoretical results. On the other hand the transverse strain at that position (x=+0.025 mm) in the crack plane shows a relatively lower value than predicted by theoretical calculations. Moreover, unlike the theoretical prediction the experimental results show little or no compressive transverse strains at all x positions when y moves away from the crack plane. There could be two possible causes of these differences. One cause of the differences between the theoretical and experimental results is possibly the presence of plasticity at the crack tip in the specimen, which was not considered in the theoretical calculations based on linear-elastic fracture mechanics. Another possible cause could be associated with the averaging in the gauge volume during measurement in that small region of high strain gradient. The corresponding stress distributions in Figure 4.18a-d appear to be reasonably similar to those for theoretical stresses in Figure 4.10a-d. Figure 4.18a-d shows that at x=+0.025 mm ahead of the crack tip in the crack plane the longitudinal, transverse, normal and

hydrostatic stresses are 426, 320, 257 and 334 MPa respectively and all of them continue to decease with y moving away from the crack plane. It can be noticed that like the longitudinal strain, the longitudinal stress at x=+0.025 mm shows a slightly different variation in the crack plane region (no decrease in the crack plane) from the theoretical field, where starting from the crack plane the longitudinal stress initially increases slightly and then decreases along the y direction (Figure 4.10a). As mentioned earlier, this difference may be due to the crack tip plasticity and averaging in the gauge volume during measurement, associated with the experimental field. For other x positions (x=+0.1 and +0.3 mm), the y variations of the experimentally measured longitudinal stress are similar to the theoretical distributions.

Figures 4.19 and 4.20 show the strain and stress distributions respectively along the y direction crossing the crack plane for two different x positions (x=–0.1 and –0.3 mm) behind the crack tip. Figure 4.19 shows that at both x positions in the crack plane (y=0) the longitudinal and transverse strains appear to be compressive and tensile respectively (at x=–0.1 mm the longitudinal and transverse strains are –1367 and 1263 με respectively). With y moving away from the crack plane, the compressive longitudinal strain decreases and finally becomes tensile (Figure 4.19a). However, as x moves away from the crack tip (with increasing negative x), the extent of the compressive longitudinal strain region along the y direction increases. On the other hand the transverse strain appears to be relatively constant over a distance along the y direction starting from the crack plane and then decreases as y moves away from the crack plane for both x positions (Figure 4.19b). The span of the relatively constant strain region increases with increasing x.

Although behind the crack tip the experimental strain distributions show similarities with the stationary (modelled) crack results in the region away from the crack plane, they differ in the crack plane region. In the crack plane the stationary crack exhibits zero longitudinal and transverse strains for both x positions. In contrast the experimental results show compressive longitudinal and tensile transverse strains in the crack plane. The corresponding stress distributions in Figure 4.20 show that behind the crack tip in the crack plane the longitudinal and transverse stresses are compressive and tensile respectively regardless of distance x from the crack tip (at x=–0.1 mm in the crack plane the longitudinal and transverse stresses are –86 and 67 MPa respectively). Behind the crack tip the longitudinal stress (Figure 4.20a) shows a y variation similar to the longitudinal strain (Figure 4.19a). On the other hand, for both x positions, starting with a tensile background in the crack plane the transverse stress appears to increase to a maximum value and then decreases as y moves away from the crack plane as shown in Figure 4.20b. The transverse stress variation appears to be flatter with increasing x behind the crack tip. The normal and hydrostatic stresses appear to be compressive in the crack plane and show similar y variations to the longitudinal stress (Figure 4.20c&d). Like the experimental strain distributions behind the crack tip, the experimental stress distributions show similarities with the stationary crack results in the region away from the crack plane, but they differ in the crack plane region. For a modelled stationary crack in plane strain, the stresses in the crack plane behind the crack tip are zero and the normal stresses are not compressive anywhere around the crack tip.

Figure 4.21 shows a comparison of the experimental (left) and theoretical (right) stress maps for the fatigued specimen for applied K=6.6 MPa$\sqrt{m}$. As the theoretical

maps are constructed for a stationary crack, they are expected to show similarities with the experimental maps ahead of the crack tip region. The experimental and theoretical results show good agreement. However, immediately ahead of the crack tip the theoretical maps appear to show a very small region of relatively higher stresses because of using the LEFM equations (Westergaard, 1939) in the theoretical stress calculations, where the stresses are singular at the crack tip.

Figures 4.22 and 4.23 show a comparison of the experimental and theoretical stresses along the x direction in the crack plane ahead of the crack tip and along the y direction crossing the crack plane at x=+0.1 mm ahead of the crack tip respectively for the fatigued specimen for applied K=6.6 MPa$\sqrt{m}$. The experimental stresses show good overall agreement with the analytical results. However, it can be noticed from Figures 4.22b and 4.23b that the experimental transverse stresses show slightly higher values than the theoretical results. This is possibly due to the effect of T-stress. T-stress is a uniaxial stress working parallel to the crack flanks (Rice, 1974). T-stress is dependent on the geometry of the specimen and the applied load. For the compact tension specimen geometry T-stress is tensile. The Westergaard equations (Westergaard, 1939) used in the theoretical calculations do not account for T-stress. One of the possible causes of the slight overall variations between the experimental and analytical stresses can be addressed to the fact that the gauge volumes for measuring two strain components ε_{xx} and ε_{yy} in EDXRD measurement are different because of the diffraction gauge volume geometry and positioning. Another possible cause may be that the crack may not be straight inside the specimen measured. Finally, it should be mentioned here that the theoretical stresses

are for a purely elastic material, whilst there is plasticity at the crack tip of the specimen measured.

4.3.3 The fatigued-overloaded specimen results

Figures 4.24 and 4.25 show longitudinal and transverse strain maps respectively for the fatigued-overloaded specimen under three different applied loads of 16.5 (K_{ol}), 3.6 and 0.66 (K_{min}) MPa$\sqrt{m}$. Figure 4.24a shows that a high tensile longitudinal strain region of about 6000 με develops just ahead of the crack tip under an applied load of 16.5 MPa$\sqrt{m}$. The tensile strains ahead of the crack tip decrease with decreasing applied load, and the strains in the crack tip region become compressive at K=3.6 and 0.66 MPa$\sqrt{m}$ as shown in Figure 4.24b&c. It can be noticed that the compressive longitudinal strains in the crack tip region increase in magnitude and spatial extent with decreasing applied load. Behind the crack tip, compressive longitudinal strains develop along the crack plane region for all load cases as seen in the fatigued specimen. Figure 4.25a shows that a higher transverse strain (about 2900 to 3400 με) region develops in the crack tip region under K_{ol} (16.5 MPa$\sqrt{m}$) splitting into two horizontal lobes. The transverse strains ahead of the crack tip appear to decrease with decreasing applied load as shown in Figure 4.25b&c. Like in the fatigued specimen, compressive transverse strain regions above and below the crack plane are evident here for all load cases. Behind the crack tip a relatively high tensile transverse strain region is apparent along the crack plane for K=3.6 and 0.66 MPa$\sqrt{m}$.

Figures 4.26 to 4.29 illustrate stress maps for the fatigued-overloaded specimen. At overload (16.5 MPa$\sqrt{m}$) the Cartesian stresses (the longitudinal, transverse and normal stresses in Figures 4.26a, 4.27a and 4.28a respectively) just ahead of the crack tip appear to be of significantly high magnitudes (about 800, 650 and 500 MPa respectively) resulting in high stress triaxiality and hydrostatic stresses (about 650 MPa in Figure 4.29a) ahead of the crack tip, which are expected at overload in plane strain. As the load is reduced from the maximum, the stresses (both the Cartesian and hydrostatic) ahead of the crack tip decrease and compressive residual stresses are produced in the crack tip region (Figures 4.26b&c, 4.27b&c, 4.28b&c and 4.29b&c). The compressive residual stresses in the crack tip region are considered to be the result of compression (by the surrounding material during load reduction) of the monotonic tensile plastic zone created during overloading. With the decreasing applied loading, the compressive residual stresses at the crack tip region increase in magnitude and spatial extent as a result of the increasing compression. Like in the fatigued specimen, the compressive longitudinal stresses along the crack plane behind the crack tip are also evident in the fatigued-overloaded specimen under the entire range of loading as shown in Figure 4.26.

Figures 4.30 and 4.31 illustrate the strain and stress distributions along the x direction in the crack plane for the fatigued-overloaded specimen under applied loads of 16.5, 3.6 and 0.66 MPa$\sqrt{m}$. It is seen from Figure 4.30a&b that high longitudinal and transverse strains ahead of the crack tip region at overload (16.5 MPa$\sqrt{m}$) appear to decrease with load reduction (to 3.6 and 0.66 MPa$\sqrt{m}$). It is seen from Figure 4.30a that compressive longitudinal strains develop at the crack tip at 3.6 and 0.66 MPa$\sqrt{m}$. Similar results were found by Croft et al. (2005) in their

energy dispersive X-ray diffraction measurement in thin specimens (plane stress). Figure 4.30a shows that the magnitude of the maximum compressive longitudinal strain at the crack tip increases with decreasing applied load. For the applied loads of 3.6 and 0.66 MPa$\sqrt{m}$ in Figure 4.30a the maximum compressive longitudinal strains at the crack tip appear to be –2941 and –3648 με respectively. However, like in the fatigued specimen behind the crack tip along the crack plane the longitudinal and transverse strains (Figure 4.30b) appear to be compressive and tensile respectively for all load cases. Croft et al. (2005) also found compressive longitudinal strain distributions along the crack plane behind the crack tip for a fatigued-overloaded specimen. The corresponding stress profiles in Figure 4.31a-d show that at overload (16.5 MPa$\sqrt{m}$) all the stresses ahead of the crack tip increase uniformly as x approaches the crack tip from the positive x direction. At x=+0.025 mm ahead of the crack tip the maximum longitudinal, transverse, normal and hydrostatic stresses at overload are 913, 682, 550 and 715 MPa respectively. However under lower applied loads (3.6 and 0.66 MPa$\sqrt{m}$) the stresses ahead of the crack tip decrease and compressive residual stresses (particularly the longitudinal stress) develop at the crack tip as shown in Figure 4.31a-d. It can be noticed that the span of the compressive longitudinal stress region and the magnitude of the maximum compressive stress at the crack tip increase with decreasing applied load. These results are consistent with Allison (1979), Holloway (1979) and Ramos et al. (2003), who found compressive residual stresses at the crack tip region as a result of overloads using surface X-ray diffraction measurements. Tsakalakos et al. (2006) also found compressive residual stresses at the crack tip inside a CT steel specimen (in plane strain) after an overload, using energy dispersive X-ray diffraction measurement. For applied K=3.6 and 0.66 MPa$\sqrt{m}$ in Figure 4.31a the maximum

compressive longitudinal stresses at the crack tip are –269 and –397 MPa respectively. Like the fatigued specimen, the fatigued-overloaded specimen exhibits compressive longitudinal stresses along the crack plane behind the crack tip for all load cases, which is in contrast to Allison (1979) and Holloway (1979) who found tensile longitudinal stresses behind the crack tip as discussed earlier.

Figures 4.32 and 4.33 illustrate strain and stress profiles respectively along the y direction crossing the crack plane at x=+0.15 mm ahead of the crack tip for the fatigued-overloaded specimen under the three applied loads. For K=16.5 and 3.6 MPa$\sqrt{m}$ the measured strains and stresses exhibit reasonably similar distributions to theoretical results. However, the applied load of 0.66 MPa$\sqrt{m}$ exhibits negligible strains and stresses at x =+0.15 mm, possibly as a result of the overload.

4.3.4 The fatigued-overloaded-fatigued specimen results

Figures 4.34 and 4.35 show longitudinal and transverse strain maps respectively for the fatigued-overloaded-fatigued specimen under applied K=6.6 (K_{max}), 3.6 and 2.6 MPa$\sqrt{m}$. It should be mentioned here that experimental measurements at K_{min} (0.66 MPa$\sqrt{m}$) were planned for all specimens in order to investigate crack closure phenomenon. However, for the fatigued-overloaded-fatigued specimen the data of the first measurement at K=0.66 MPa$\sqrt{m}$ were not good enough, and the experiment would have needed to repeat. But, due to the time constraint associated with beam time, the repeat experiment had not been possible. Figure 4.34a shows that a tensile longitudinal strain region of about 2400 με develops just ahead of the crack tip

under applied K=6.6 MPa$\sqrt{m}$. The tensile longitudinal strain ahead of the crack tip decreases with decreasing applied load as shown in Figure 4.34b&c. Like in the fatigued and fatigued-overloaded specimens, a higher compressive longitudinal strain region develops along the crack plane behind the crack tip for all load cases. Figure 4.35a shows that a higher transverse strain (1200 to 1500 $\mu\varepsilon$) region develops in the vicinity of the crack tip under K_{max} (6.6 MPa$\sqrt{m}$) splitting into two horizontal lobes. The transverse strain ahead of the crack tip appears to decrease with decreasing applied load as shown in Figure 4.35b&c. Like the fatigued and fatigued-overloaded specimens, compressive transverse strain regions above and below the crack plane are evident here for all load cases. Behind the crack tip, relatively high tensile transverse strains are apparent along the crack plane region under K=3.6 and 2.6 MPa$\sqrt{m}$. Although an overload of 13.2 MPa$\sqrt{m}$ (100%) was applied at –0.1 mm behind the current crack tip, its position is not evident on the strain maps.

The stress maps for the fatigued-overloaded-fatigued specimen are presented in Figures 4.36 to 4.39 for applied K=6.6 (K_{max}), 3.6 and 2.6 MPa$\sqrt{m}$. At K_{max} all stress maps (longitudinal, transverse, normal and hydrostatic) appear to show a high stress region ahead of the crack tip (Figures 4.36a, 4.37a, 4.38a and 4.39a). With decreasing applied load, the stresses ahead of the crack tip decrease in magnitude (Figures 4.36b&c, 4.37b&c, 4.38b&c and 4.39b&c), but unlike in the fatigued-overloaded specimen, the stresses at the crack tip region still remain tensile. Like in the fatigued and fatigued-overloaded specimens, the compressive longitudinal stresses along the crack plane behind the crack tip are also evident in the fatigued-overloaded-fatigued specimen under the entire range of applied loading. However, like in the strain maps, the overload position is not evident in the stress maps.

Figures 4.40 and 4.41 illustrate the strain and stress distributions respectively along the x direction in the crack plane for the fatigued-overloaded-fatigued specimen under applied K= 6.6 (K_{max}), 3.6 and 2.6 MPa$\sqrt{m}$. It is seen from Figure 4.40a&b that like in the fatigued specimen, starting in the far field both the longitudinal and transverse strains ahead of the crack tip increase under the whole range of loading as x approaches the crack tip. However, for all the load cases just ahead of the crack tip the transverse strains exhibit a sharp drop in magnitude, where the longitudinal strains exhibit the maximum values. Like in the fatigued specimen, following the sharp decrement the transverse strains show a sharp increase in the crack tip region. On the other hand following the maximum values just ahead of the crack tip, the longitudinal strains show a discontinuity in the crack tip region, where the strains cross over rapidly from tensile to compressive values. Here, the magnitudes of both the longitudinal and transverse strains in the region ahead of the crack tip decrease with decreasing applied load, but unlike in the fatigued-overloaded specimen no compressive longitudinal strain region develops around the crack tip. Like in the fatigued and fatigued-overloaded specimens, behind the crack tip along the crack plane the longitudinal and transverse strains are compressive and tensile respectively for all load cases as in Figure 4.40a&b. Here, the overload position is not clear in the strain distributions. The corresponding stress distributions in Figure 4.41a-d show that all stresses ahead of the crack tip region increase uniformly as x approaches the crack tip from the positive x direction regardless of applied loading. Under K=6.6 MPa$\sqrt{m}$ just ahead of the crack tip the maximum longitudinal, transverse, normal and hydrostatic stresses are 396, 313, 244 and 317 MPa respectively. However, with decreasing applied load (for K=3.6 and 2.6 MPa$\sqrt{m}$) the stresses ahead of the crack tip region appear to decrease as expected. Like the fatigued and fatigued-overloaded

specimens, the fatigued-overloaded-fatigued specimen also shows compressive longitudinal stresses along the crack plane behind the crack tip. However, the overload position (x=–0.1 mm) behind the crack tip does not appear to be identifiable from the stress distributions. In order to find out the reason why the overload position is not well-defined, the sizes of the overload plastic zone and the reverse plastic zone due to the overload have been estimated (Equations 2.51 & 2.52), which are 46 and 11.5 μm respectively. One possible reason may be that as the overload plastic zone is very small it might have been wiped out during the additional 0.1 mm of crack growth. Another possible cause may have been associated with the averaging in the gauge volume during strain measurement in the small overload-affected region.

Figures 4.42 and 4.43 illustrate the strain and stress profiles respectively along the y direction crossing the crack plane at x=+0.025 mm ahead of the crack tip for the fatigued-overloaded-fatigued specimen under applied K=6.6, 3.6 and 2.6 MPa$\sqrt{m}$. Here, the strains and stresses for all three loads exhibit reasonably similar distributions to those from LEFM results.

4.3.5 Comparison of the fatigued and fatigued-overloaded-fatigued specimen results

Figures 4.44 and 4.45 show a comparison of the strain and stress distributions respectively along the x direction in the crack plane for the fatigued (F) and fatigued-overloaded-fatigued (FOF) specimens at K_{max} (6.6 MPa$\sqrt{m}$). Moreover, Figures 4.46 and 4.47 show a comparison of the strain and stress distributions

respectively along the y direction crossing the crack plane at x=+0.025 mm ahead of the crack tip for the fatigued and fatigued-overloaded-fatigued specimens at K_{max}. The two specimens show very good agreement in the strain and stress distributions in both planes.

4.3.6 Comparison of the fatigued-overloaded and fatigued-overloaded-fatigued specimen results

Figures 4.48 and 4.49 show a comparison of the strain and stress distributions respectively along the x direction in the crack plane for the fatigued-overloaded (FO) and fatigued-overloaded-fatigued (FOF) specimens at K=3.6 MPa$\sqrt{m}$. Figure 4.48a&b shows that the two specimens exhibit slightly different longitudinal and transverse strain profiles. For both specimens, starting in the far field ahead of the crack tip, both the longitudinal and transverse strains increase as x moves towards the crack tip and then exhibit a sharp decrease but at different x positions ahead of the crack tip. For the fatigued-overloaded specimen, the strains start decreasing relatively far ahead of the crack tip as a result of the overload. Moreover, in the fatigued-overloaded specimen, high compressive longitudinal strain develops at the crack tip, and the strains remain compressive along the crack plane behind the crack tip. On the other hand, in the fatigued-overloaded-fatigued specimen the longitudinal strain is tensile at the crack tip, and compressive longitudinal strains develop behind the crack tip along the crack plane. Behind the crack tip along the crack plane the transverse strains are tensile for both specimens. Just behind the crack tip both specimens exhibit higher transverse strains, which decrease as x moves away from the crack tip. However, as a result of the overload the fatigued-overloaded specimen

shows quite large tensile transverse strains behind the crack tip. The corresponding stress distributions in Figure 4.49a-d show that starting in the far field ahead of the crack tip all stresses for the two specimens increase as x approaches the crack tip. Here both specimens exhibit good agreement in stress distributions over a considerable distance towards the crack tip. Then both specimens exhibit a sharp decrease in stresses, but at different x positions ahead of the crack tip. Due to the presence of the overload plastic zone at the crack tip the fatigued-overloaded specimen shows a peak stress at a greater distance from the crack tip. Besides, in the fatigued-overloaded specimen compressive longitudinal stresses appear to develop at the crack tip region as well as behind the crack tip along the crack plane, where the fatigued-overloaded-fatigued specimen shows compressive longitudinal stresses only behind the crack tip along the crack plane.

Figures 4.50 and 4.51 show a comparison of the strain and stress distributions respectively along the y direction crossing the crack plane at x=+0.15 mm ahead of the crack tip for the fatigued-overloaded and fatigued-overloaded-fatigued specimens. It is seen from Figure 4.50a that the fatigued-overloaded specimen shows significantly lower longitudinal strains than the fatigued-overloaded-fatigued specimen in the far field although it exhibits higher strains in and near the crack plane region. The transverse strains in the fatigued-overloaded specimen also appear to be lower than in the fatigued-overloaded specimen particularly in and near the crack plane region as in Figure 4.50b. The corresponding stress fields in Figure 4.51a-d show that all the stresses are significantly lower in the fatigued-overloaded specimen than in the fatigued-overloaded-fatigued specimen particularly in the region away from the crack plane. The lower strain and stress levels in the fatigued-

overloaded specimen may be due to the loss of crack tip constraint resulting from the overload plastic deformation at the crack tip.

4.4 Discussion

Strain and stress fields around fatigued, fatigued-overloaded and fatigued-overloaded-fatigued crack tips in aluminium alloy 5091 compact tension specimens have been presented and discussed. All specimens exhibit similarities in the strain and stress distributions ahead of the crack tip region with theoretical results for a stationary crack (Westergaard, 1939). Behind the crack tip the experimental results show significantly different strain and stress distributions from a stationary crack. For a stationary crack, along the x direction in the crack plane behind the crack tip, both the longitudinal and transverse strains, and all the stresses (longitudinal, transverse, normal and hydrostatic) are zero. Besides, no compressive stresses are found anywhere around a stationary crack tip. On the other hand, behind the crack tip the experimental results exhibit compressive longitudinal strains and stresses along the x direction in the crack plane in all specimens and under all applied loads. The longitudinal strain distributions behind the crack tip along the crack plane in the present work are consistent with Croft et al. (2005), who found compressive longitudinal strains on the crack flank in their EDXRD measurements in plane stress regardless of applied loading. Wang et al. (1999) found compressive longitudinal residual stresses near the crack plane region behind the crack tip using surface X-ray diffraction measurements and finite element calculations. Zhao et al. (2004) also observed compressive residual stresses along the crack plane behind the crack tip both in plane stress and plane strain using finite element analysis. Tsakalakos et al.

(2006) found compressive residual longitudinal stresses on the crack flank behind the crack tip in plane strain for a fatigued-overloaded specimen using EDXTD measurements in plane strain. They mentioned two possible causes of the crack flank compressive longitudinal stresses as: the probing volumes for ε_{xx} and ε_{yy} in the EDXRD measurements are different, and the precise location of the same point of measurement is very difficult.

The compressive longitudinal stresses are expected on the crack flank when the crack is closed. However, in the present work the compressive longitudinal stresses on the crack flank are found in all specimens regardless of the applied loading. According to the Westergaard linear elastic equations (Westergaard, 1939) the strains ε_{xx} and ε_{yy} along the crack plane behind the crack tip are zero, although there are high strain gradients along the y direction near the crack plane. Croft et al. (2005) observed compressive longitudinal strains (ε_{yy}) on the crack flank in EDXRD measurements even for a crack with separated crack faces, which possibly would have resulted in compressive longitudinal stresses on the crack flank, had the investigation been extended further, as obtained by Tsakalakos et al. (2006) and in the present work. However, Croft et al. (2005) attributed the compressive longitudinal strains on the crack flank to a strain anisotropy in the plastic wake, as their investigation was based on single diffraction peak (321) analysis. As a possible cause of the compressive longitudinal stresses on the crack flank in the present work, an error in the stress free lattice parameters (a_o) can be ruled out, as the experimental stresses ahead of the crack tip for K_{max} (6.6 MPa$\sqrt{m}$) in the fatigued specimen show good agreement with the analytical results. Therefore, the compressive longitudinal stresses on the crack flank could possibly be due to the

two different gauge volumes (in terms of diffraction gauge volume geometry and positioning) for measuring the two strain components ε_{xx} and ε_{yy} in a region with a high compressive longitudinal strain gradient along the y direction from the crack plane. However, the present results are in contrast to Allison (1979) and Holloway (1979), who found tensile longitudinal stresses on the crack flank behind the crack tip using surface X-ray diffraction measurements in loaded specimens when the crack was open. Allison (1979) attributed the cause of the nonzero (tensile) stresses on the crack flank to the size of the X-ray beam, which was much larger than the crack opening, and thus stresses were measured in the material on both sides of the open crack.

For the fatigued-overloaded specimen, compressive longitudinal stresses develop in the crack tip region when the load is reduced from the overload. The area of the compressive longitudinal stress region and the magnitude of the maximum compressive stress at the crack tip increase with decreasing applied load. These results are consistent with Allison (1979), Holloway (1979) and Ramos et al. (2003), who found compressive residual stresses in the crack tip region as a result of overloads using surface X-ray diffraction measurements. Tsakalakos et al. (2006) also found compressive residual stresses at the crack tip inside a CT steel specimen (in plane strain) after an overload, using energy dispersive X-ray diffraction measurement.

For the fatigued-overloaded-fatigued specimen the overload position has not been identified in the strain and stress fields. From further finite element investigations in the subsequent chapters, it has been predicted that the fatigued-overloaded-fatigued

crack remains open inside the specimen (in plane strain) even at K=2.6 MPa$\sqrt{m}$, the minimum applied load discussed here. Therefore, the overload position for the range of loading (K=6.6, 3.6 and 2.6 MPa$\sqrt{m}$) discussed here, cannot be identifiable from the longitudinal stress fields, as there is no contact between the crack surfaces. However, it can be identifiable from the strains as well as the transverse, normal and hydrostatic stress distributions. The reason why the overload position is not evident from the strain and stress distributions could be attributed to the small overload plastic zone (46 μm in plane strain) in this case. One possibility is that the plastic zone might have been wiped out during the additional 0.1 mm of crack growth. Another possibility could be, even if the plastic zone exists after crack growth, its effect may have disappeared with the averaging in the gauge volume during strain measurement.

Finally, the experimental stresses for the fatigued specimen ahead of the crack tip show good overall agreement with the analytical results obtained by employing the Westergaard equations (Westergaard, 1939). These results demonstrate the significance of energy dispersive X-ray diffraction for the stress field investigations inside the components in structural integrity assessment.

4.5 Conclusion

This chapter discusses the strain and stress fields around fatigued, fatigued-over-loaded and fatigued-overloaded-fatigued crack tips in aluminium alloy 5091 compact tension specimens under various levels of in-situ loading. The results provide a clear picture of the strain and stress distributions around fatigue cracks in

the interior of the specimens with different loading history. The effect of the overload is to produce highly compressive longitudinal residual stresses in the crack tip region, and this is clearly evident from the stress maps and stress profiles for the fatigued-overloaded specimen. However, the overload effect is not clear from the stress maps and stress profiles for the fatigued-overloaded-fatigued specimen.

For all three specimens, compressive longitudinal stresses along the crack plane behind the crack tip are apparent from the stress maps and stress profiles regardless of loading history and applied loading. These results are consistent with Tsakalakos et al. (2006), who employed EDXRD in their measurements.

This investigation provides a clear insight into the local crack tip strain and stress fields in the interior of fatigued, fatigued-overloaded and fatigued-overloaded-fatigued specimens using energy dispersive X-ray diffraction, which is essential in constructing fatigue life prediction/assessment models. Moreover, through this work energy dispersive X-ray diffraction clearly offers the opportunity for investigating local strain and stress fields in the interior of the safety critical engineering components.

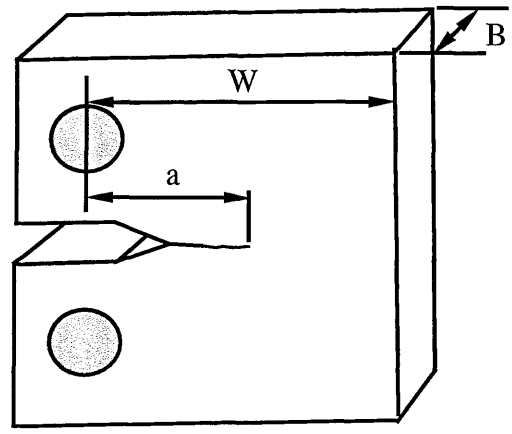

Figure 4.1: Compact tension specimen showing all characteristic dimensions.

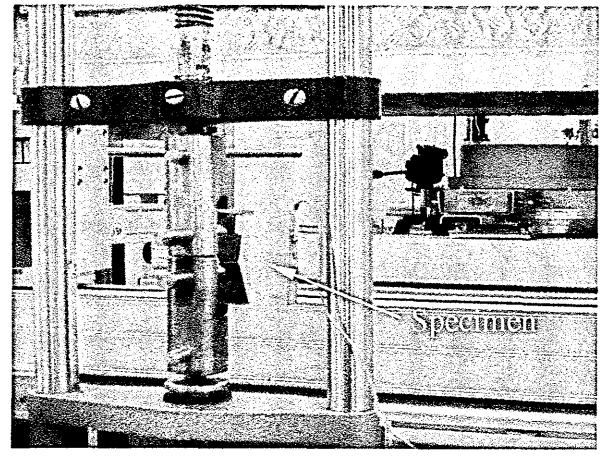

Figure 4.2: Compact tension specimen on the loading rig for strain measurement.

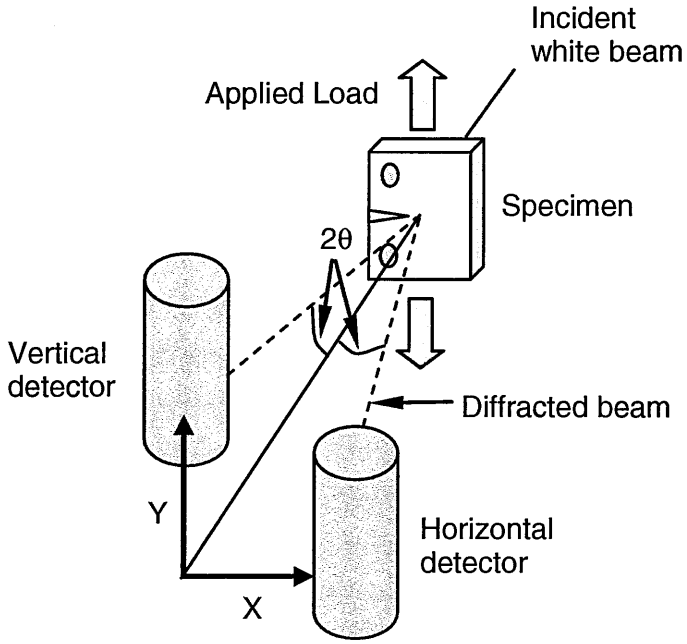

Figure 4.3: Schematic of the diffraction strain measurement technique.

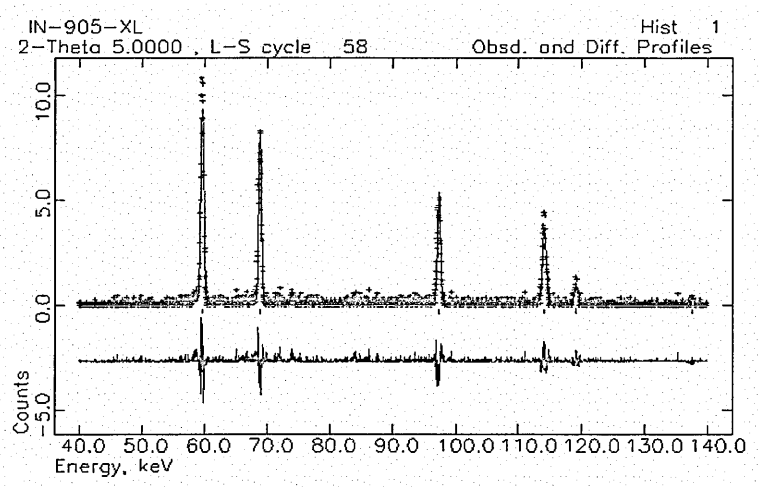

Figure 4.4: A diffraction spectrum for Al 5091 showing data points (red points), its fitted curve (green) and the difference curve (pink).

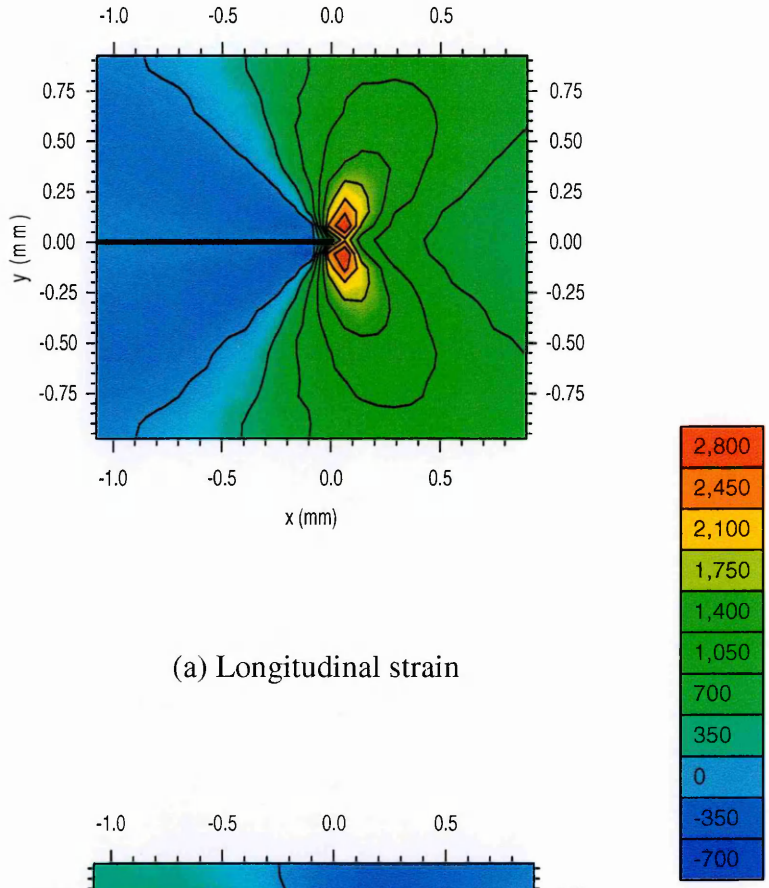

(a) Longitudinal strain

(b) Transverse strain

Figure 4.5: Theoretical strain (με) maps for a stationary crack for applied K=6.6 MPa√m.

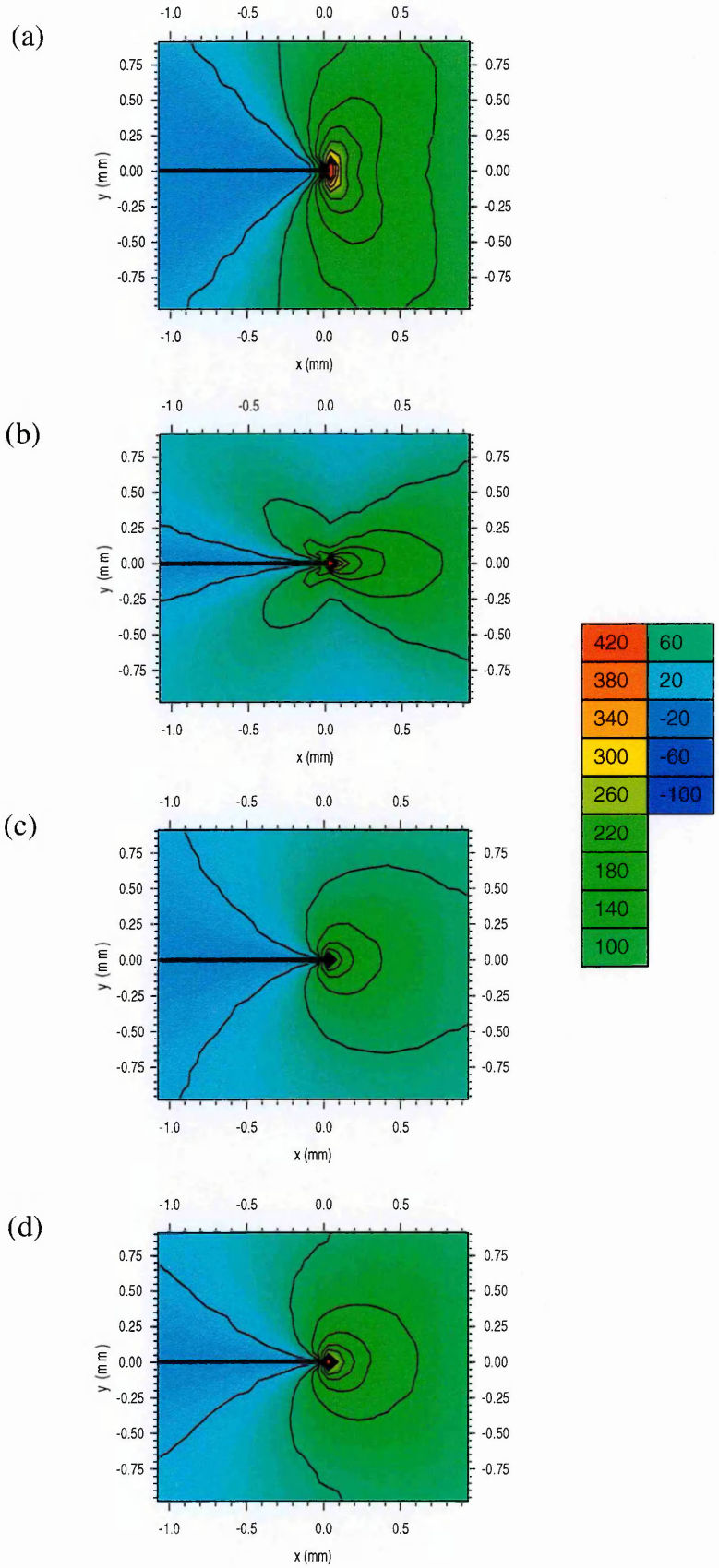

Figure 4.6: Theoretical stress (MPa) maps for a stationary crack for applied K=6.6 MPa$\sqrt{m}$: (a) longitudinal, (b) transverse, (c) normal and (d) hydrostatic stresses.

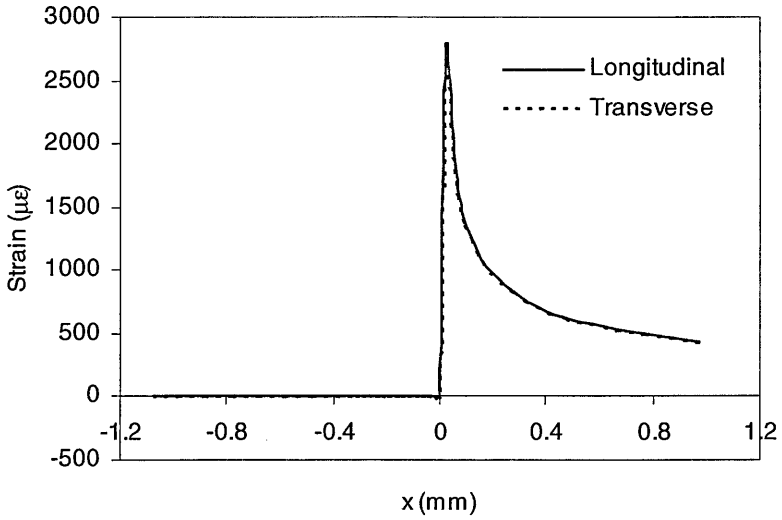

Figure 4.7: Variation of theoretical strains along the x direction in the crack plane (y=0) for a stationary crack under applied K=6.6 MPa$\sqrt{m}$.

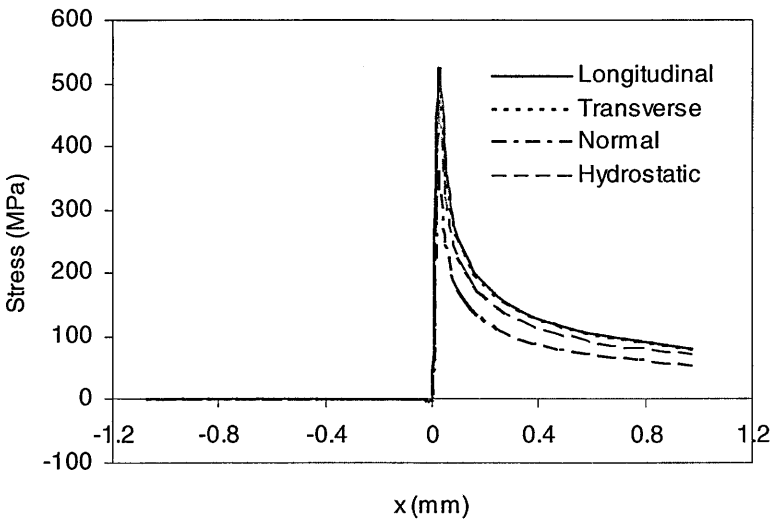

Figure 4.8: Variation of theoretical stresses along the x direction in the crack plane (y=0) for a stationary crack under applied K=6.6 MPa$\sqrt{m}$.

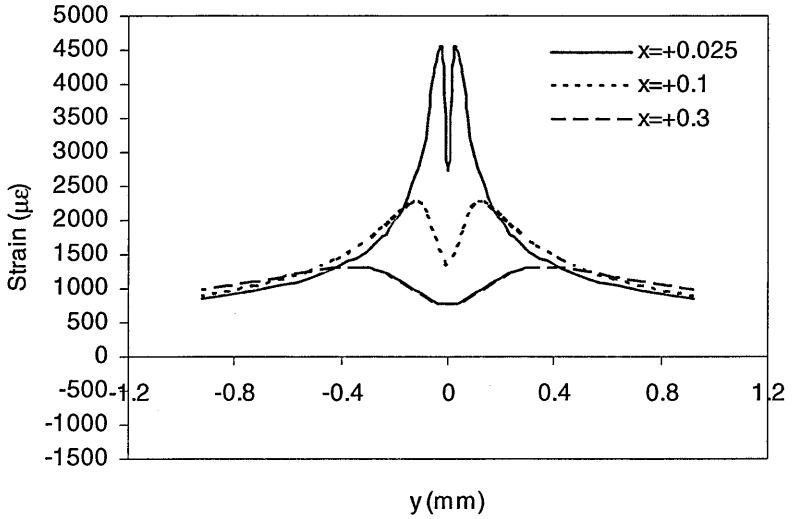

(a) Longitudinal strain

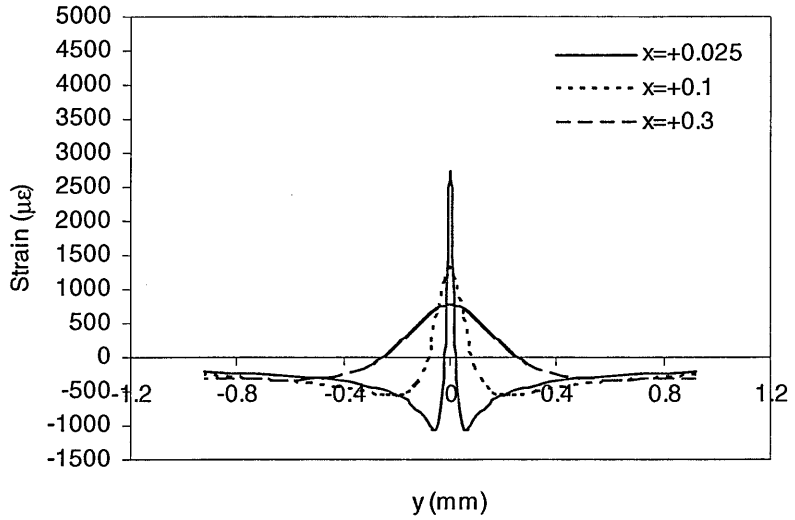

(b) Transverse strain

Figure 4.9: Variation of theoretical strains along the y direction (crossing the crack plane) at different x (mm) positions ahead of the crack tip of a stationary crack for applied K=6.6 MPa$\sqrt{m}$.

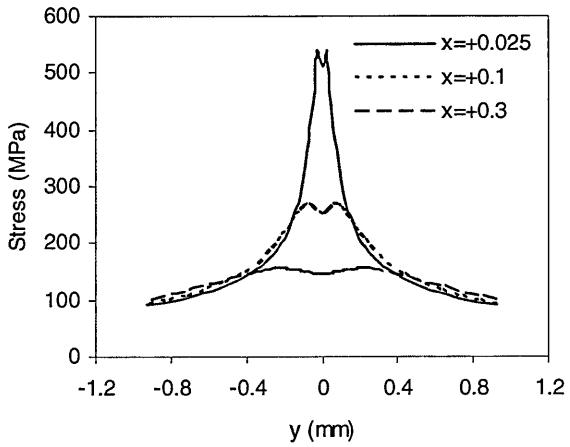

(a) Longitudinal stress

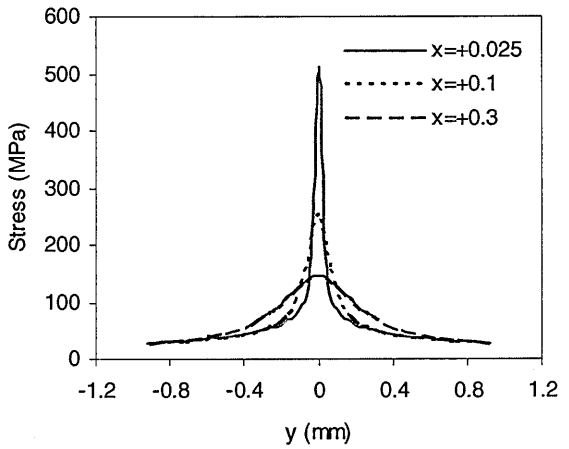

(b) Transverse stress

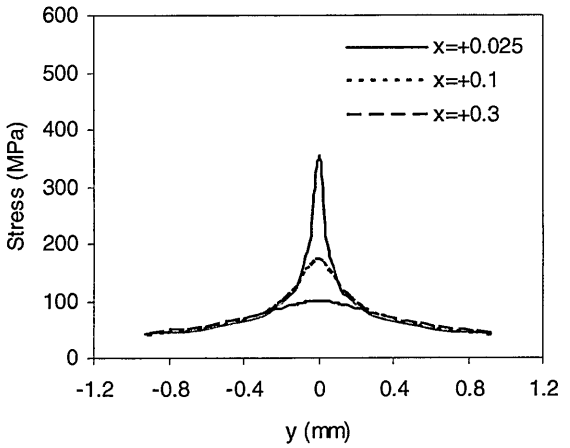

(c) Normal stress

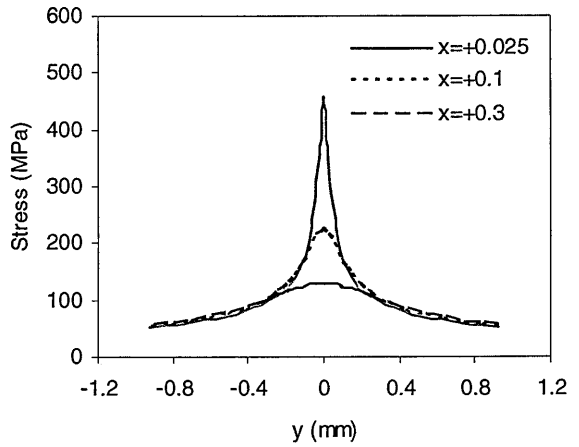

(d) Hydrostatic stress

Figure 4.10: Variation of theoretical stresses along the y direction (crossing the crack plane) at different x (mm) positions ahead of the crack tip of a stationary crack for applied K=6.6 MPa$\sqrt{m}$.

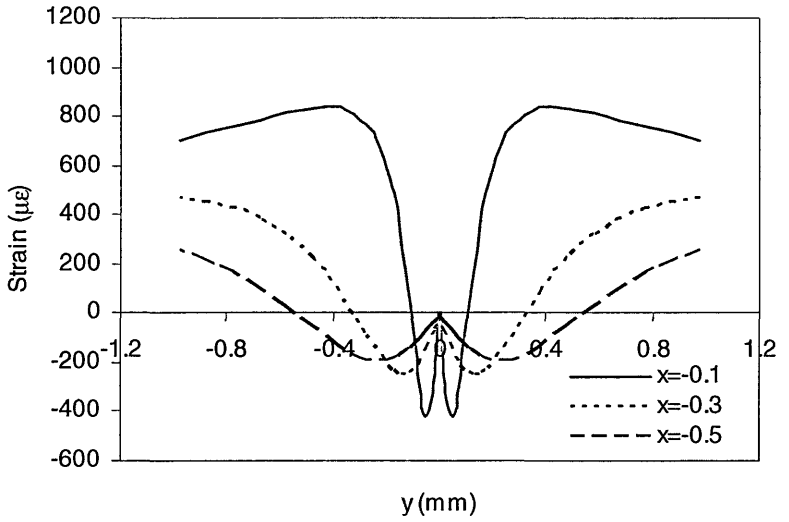

(a) Longitudinal strain

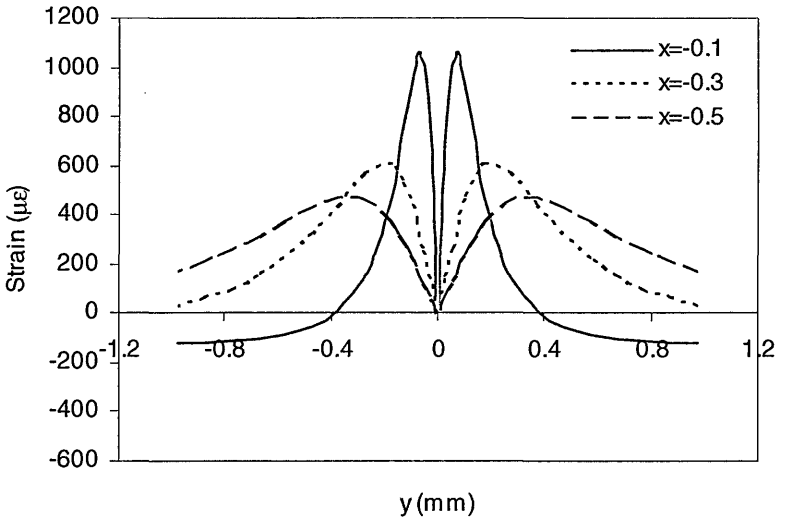

(b) Transverse strain

Figure 4.11: Variation of theoretical strains along the y direction (crossing the crack plane) at different x (mm) positions behind the crack tip of a stationary crack for applied K=6.6 MPa$\sqrt{m}$.

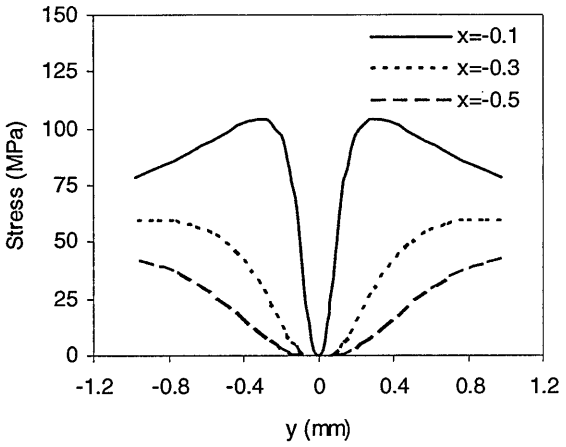

(a) Longitudinal stress

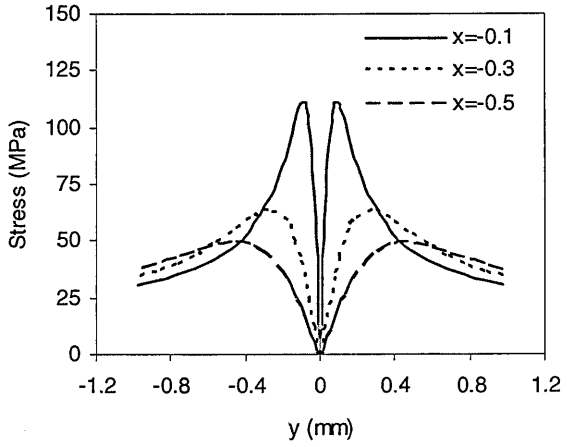

(b) Transverse stress

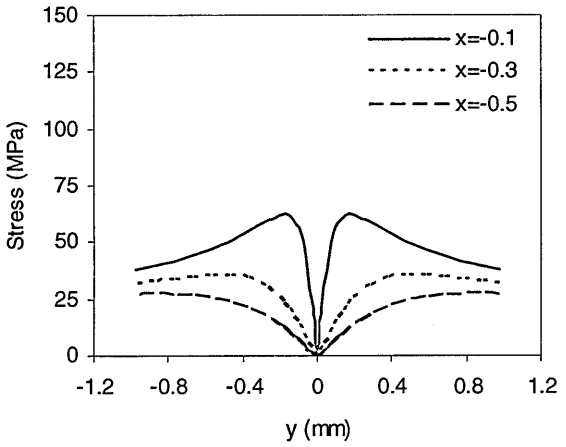

(c) Normal stress

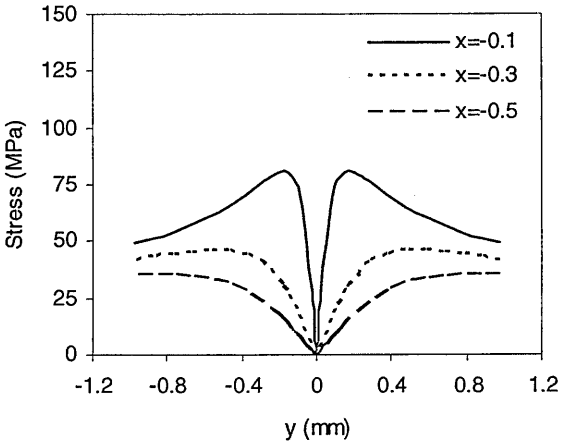

(d) Hydrostatic stress

Figure 4.12: Variation of theoretical stresses along the y direction (crossing the crack plane) at different x (mm) positions behind the crack tip of a stationary crack for applied K=6.6 MPa$\sqrt{m}$.

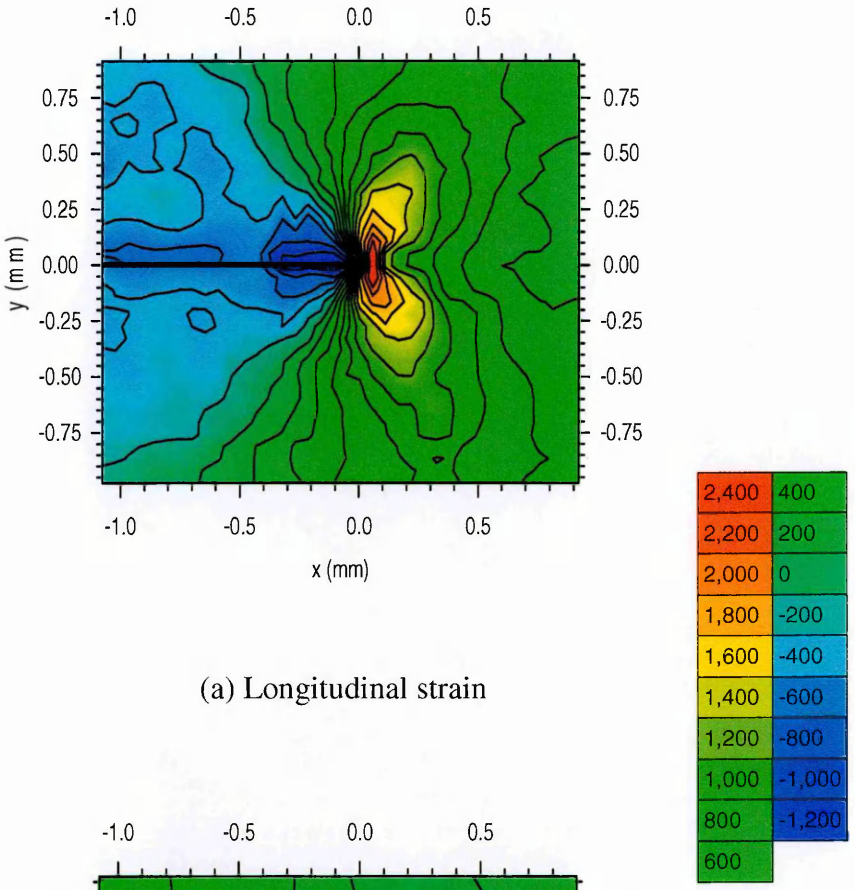

(a) Longitudinal strain

(b) Transverse strain

Figure 4.13: Strain (με) maps around the crack tip of the fatigued specimen for applied K=6.6 MPa√m.

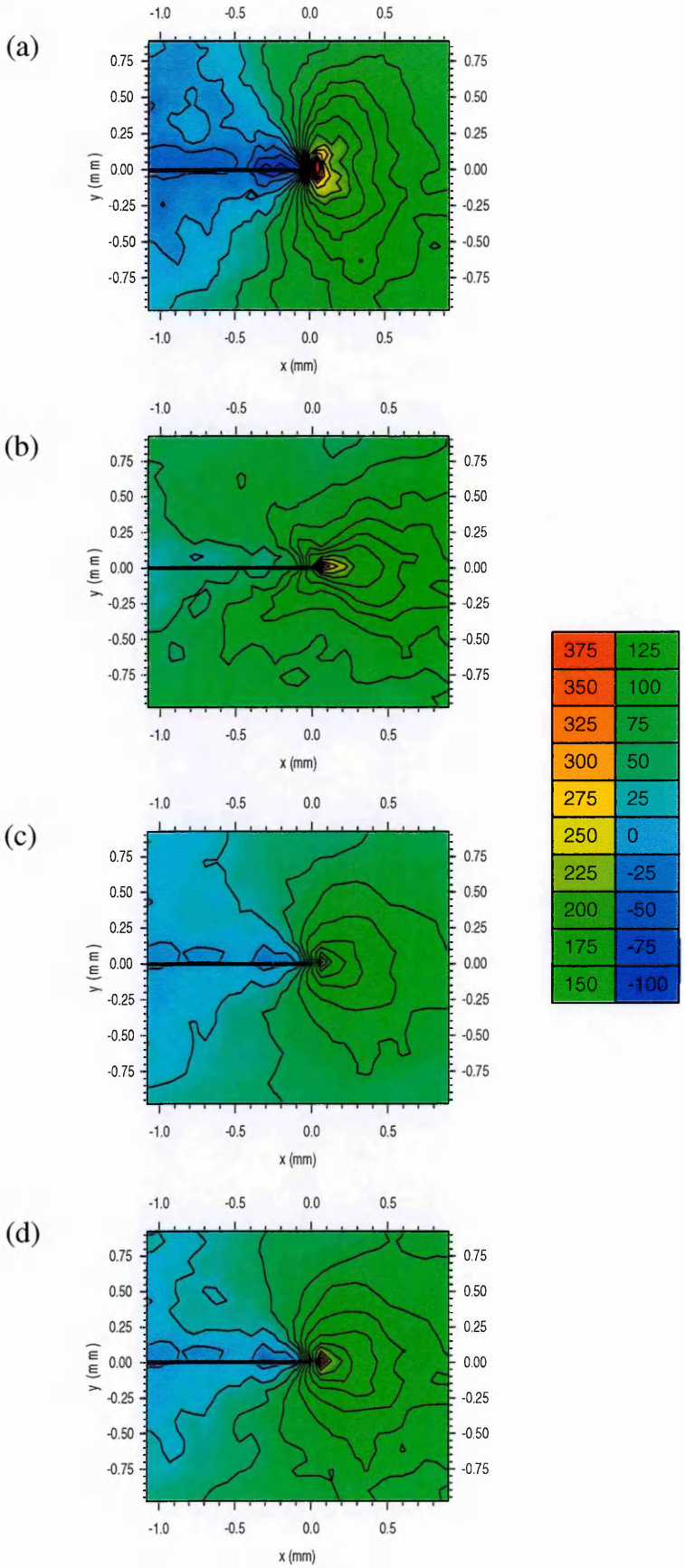

Figure 4.14: Stress (MPa) maps around the crack tip of the fatigued specimen for applied K=6.6 MPa√m: (a) longitudinal, (b) transverse, (c) normal and (d) hydrostatic stresses.

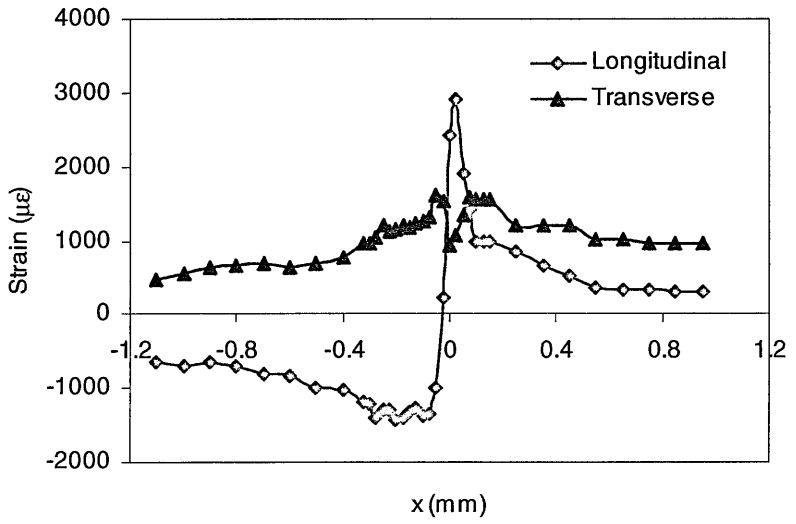

Figure 4.15: Variation of strains along the x direction in the crack plane (y=0) in the fatigued specimen for applied K=6.6 MPa√m.

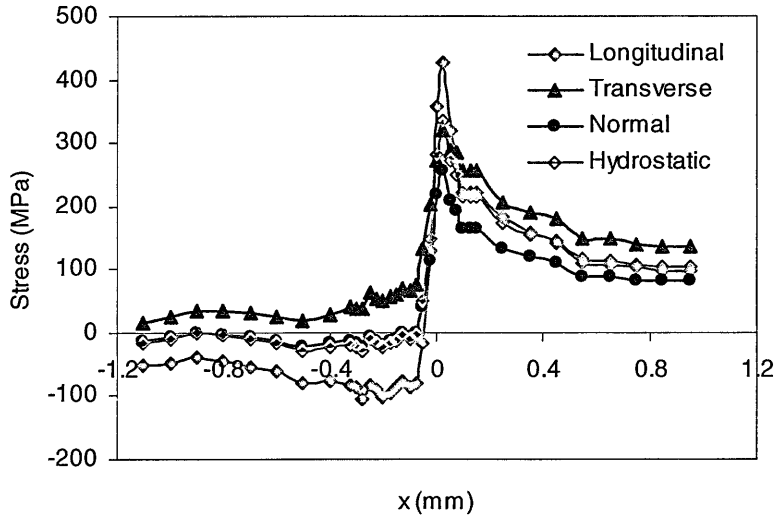

Figure 4.16: Variation of stresses along the x direction in the crack plane (y=0) in the fatigued specimen for applied K=6.6 MPa√m.

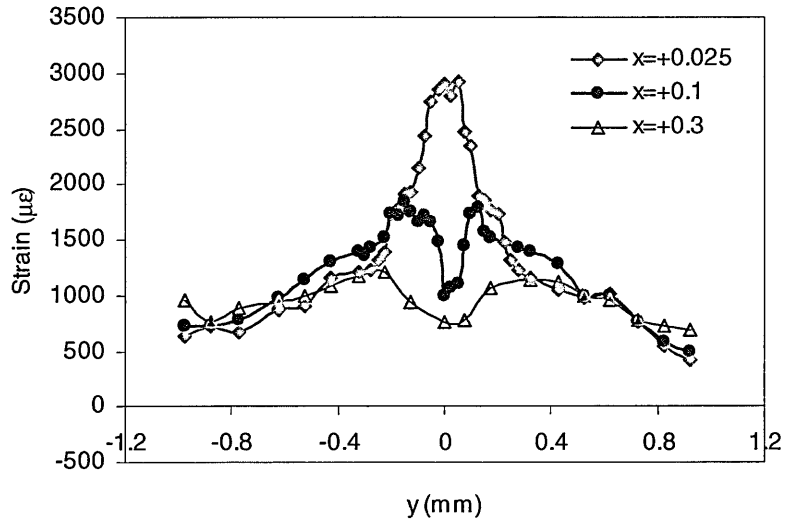

(a) Longitudinal strain

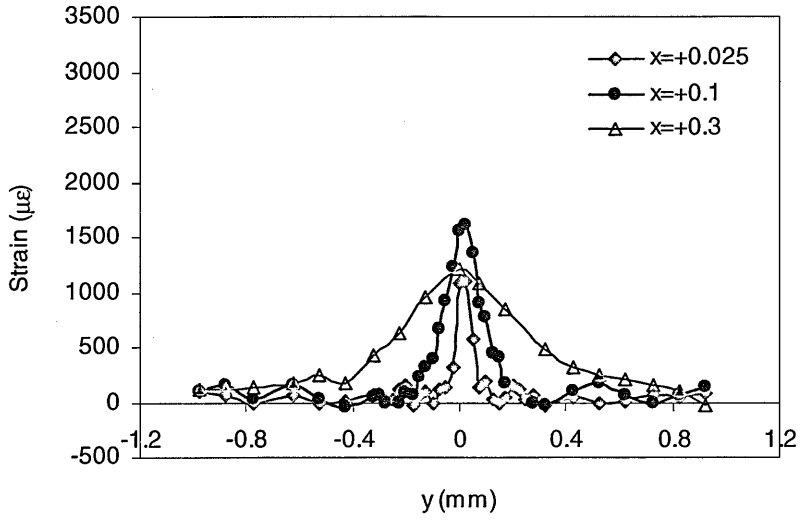

(b) Transverse strain

Figure 4.17: Variation of strains along the y direction (crossing the crack plane) at different x (mm) positions ahead of the crack tip in the fatigued specimen for applied K=6.6 MPa$\sqrt{m}$.

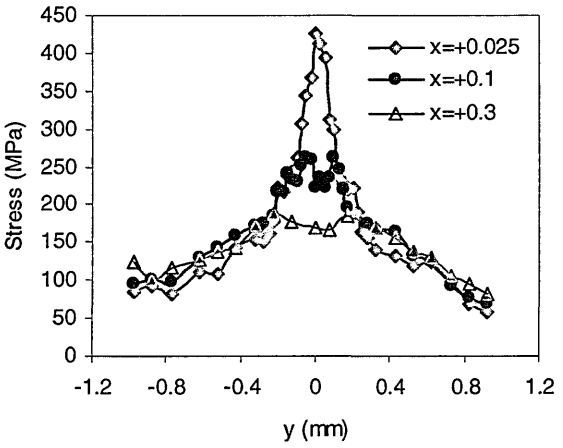

(a) Longitudinal stress

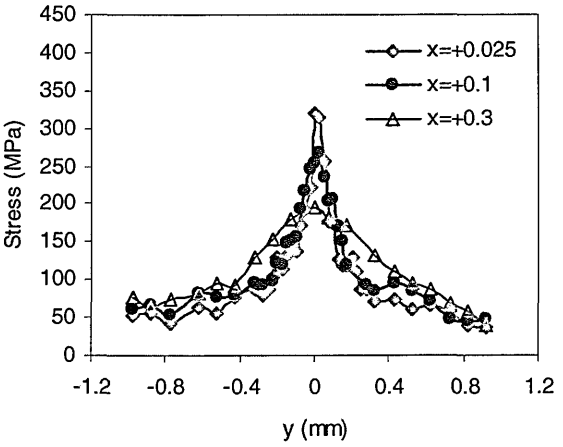

(b) Transverse stress

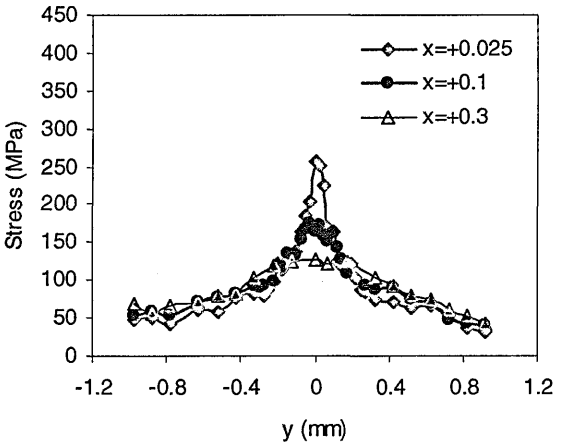

(c) Normal stress

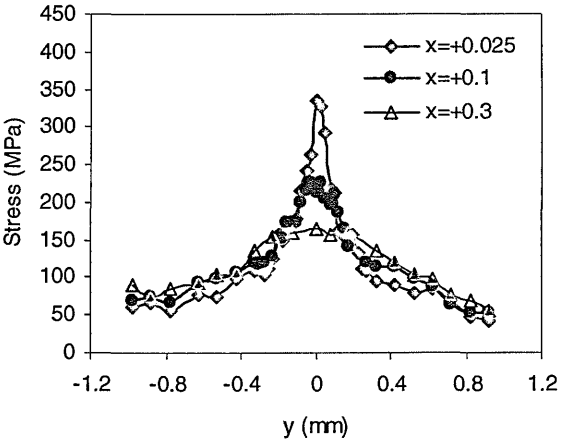

(d) Hydrostatic stress

Figure 4.18: Variation of stresses along the y direction (crossing the crack plane) at different x (mm) positions ahead of the crack tip in the fatigued specimen for applied K=6.6 MPa$\sqrt{m}$.

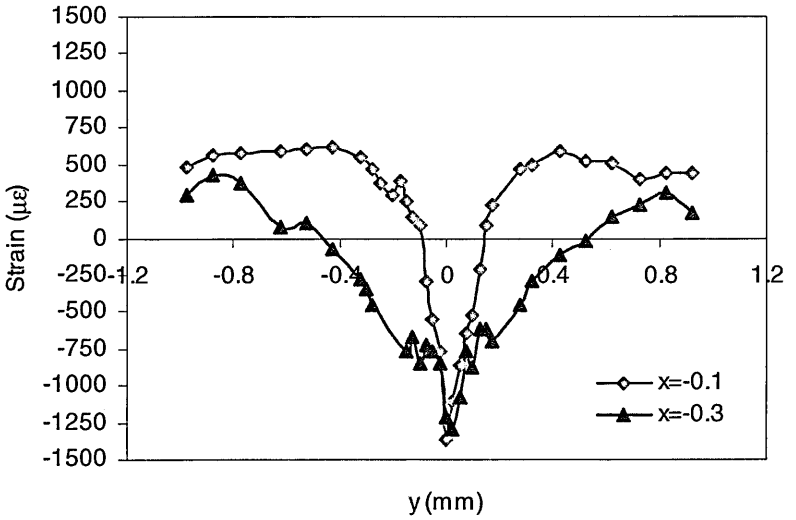

(a) Longitudinal strain

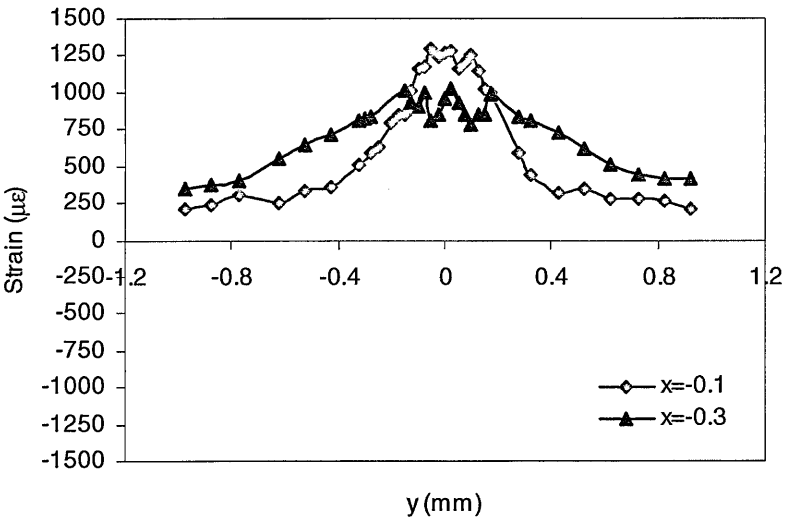

(b) Transverse strain

Figure 4.19: Variation of strains along the y direction (crossing the crack plane) at different x (mm) positions behind the crack tip in the fatigued specimen for applied K=6.6 MPa$\sqrt{m}$.

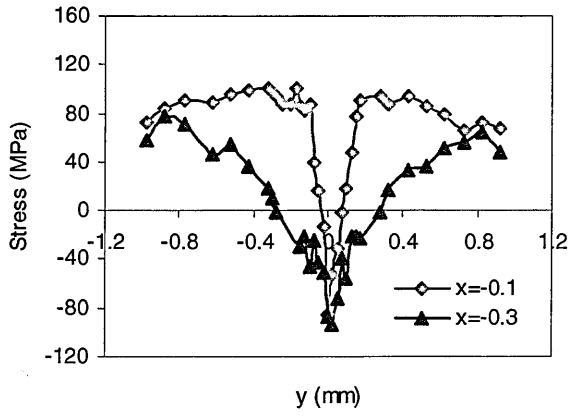

(a) Longitudinal stress

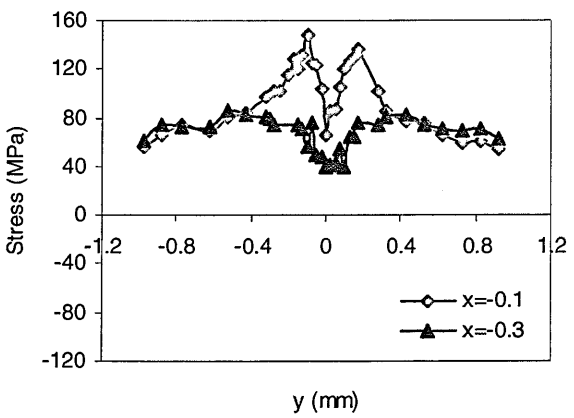

(b) Transverse stress

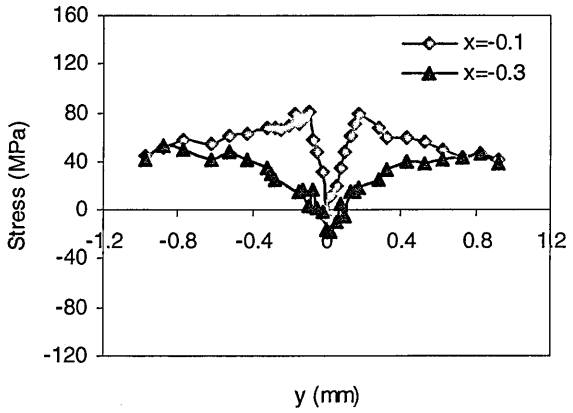

(c) Normal stress

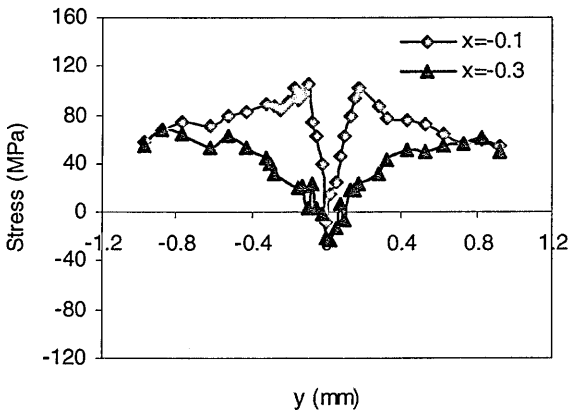

(d) Hydrostatic stress

Figure 4.20: Variation of stresses along the y direction (crossing the crack plane) at different x (mm) positions behind the crack tip in the fatigued specimen for applied K=6.6 MPa$\sqrt{m}$.

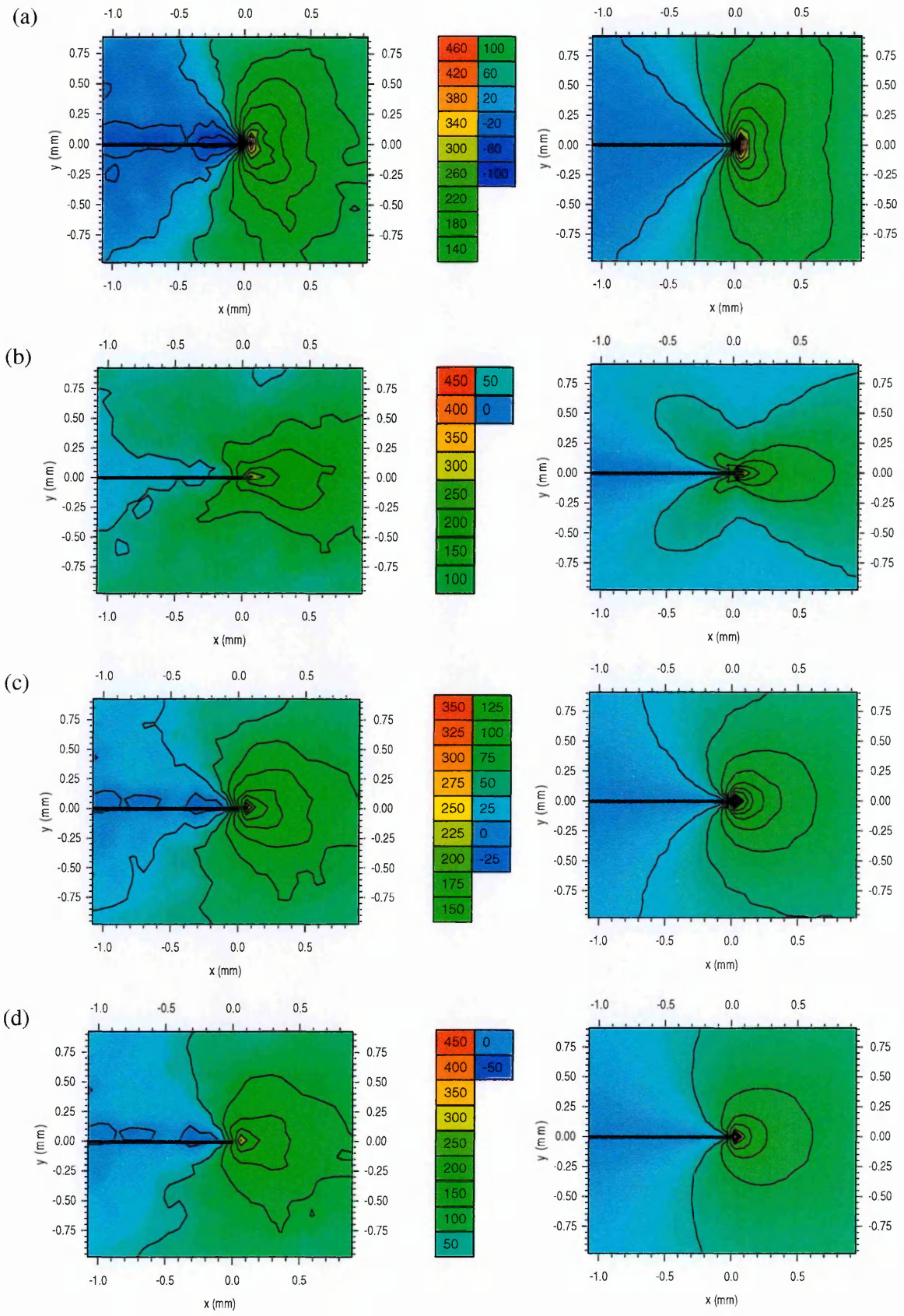

Figure 4.21: Comparison of experimental (left) and theoretical (right) stress (MPa) maps for the fatigued specimen for applied K=6.6 MPa$\sqrt{m}$:
(a) longitudinal, (b) transverse, (c) normal and (d) hydrostatic stresses.

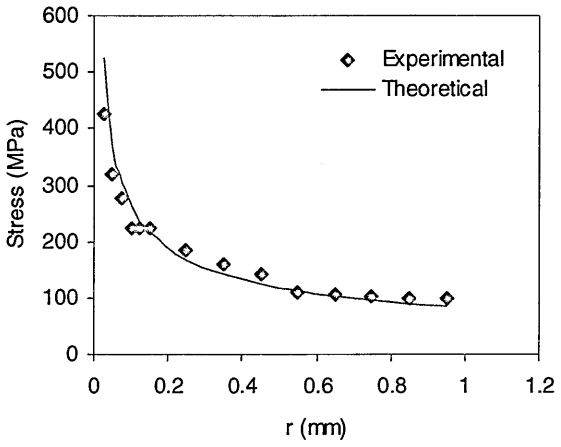

(a) Longitudinal stress

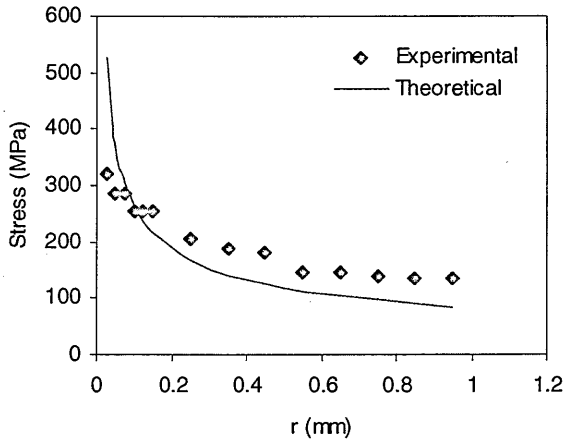

(b) Transverse stress

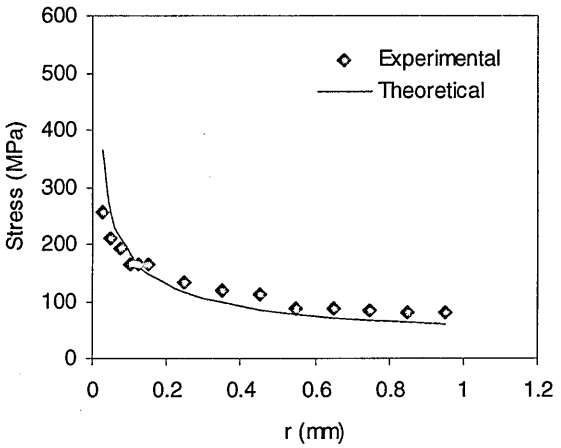

(c) Normal stress

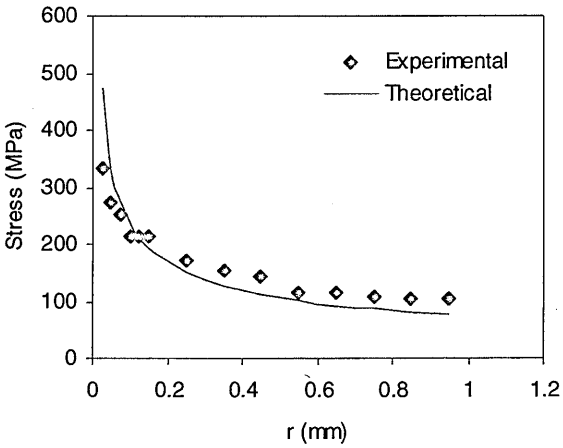

(d) Hydrostatic stress

Figure 4.22: Comparison of experimental and theoretical stresses along the x direction in the crack plane (y=0) ahead of the crack tip in the fatigued specimen for applied K=6.6 MPa$\sqrt{m}$.

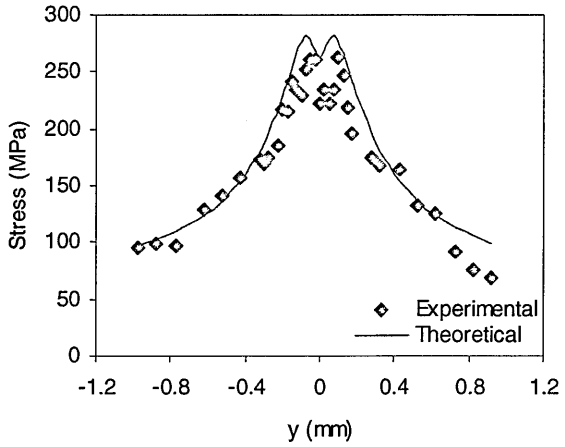

(a) Longitudinal stress

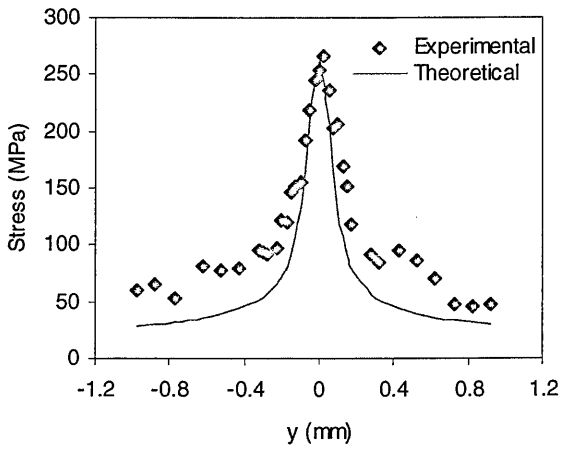

(b) Transverse stress

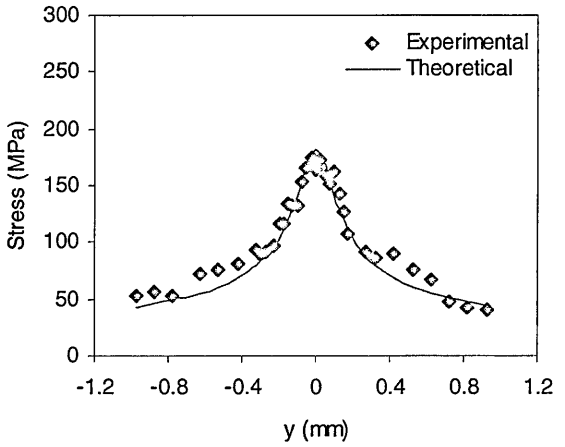

(c) Normal stress

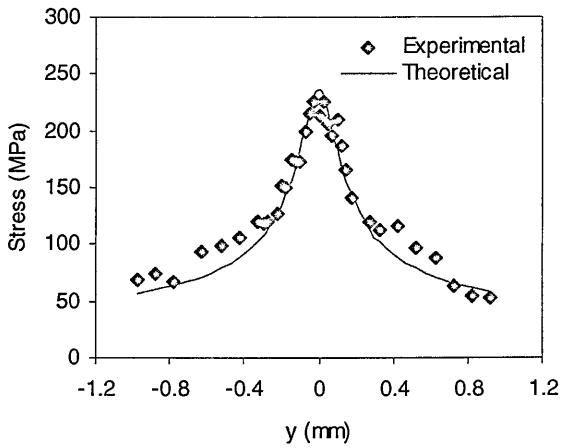

(d) Hydrostatic stress

Figure 4.23: Comparison of experimental and theoretical stresses at x=+0.1 mm ahead of the crack tip along the y direction crossing the crack plane in the fatigued specimen for applied K=6.6 MPa$\sqrt{m}$.

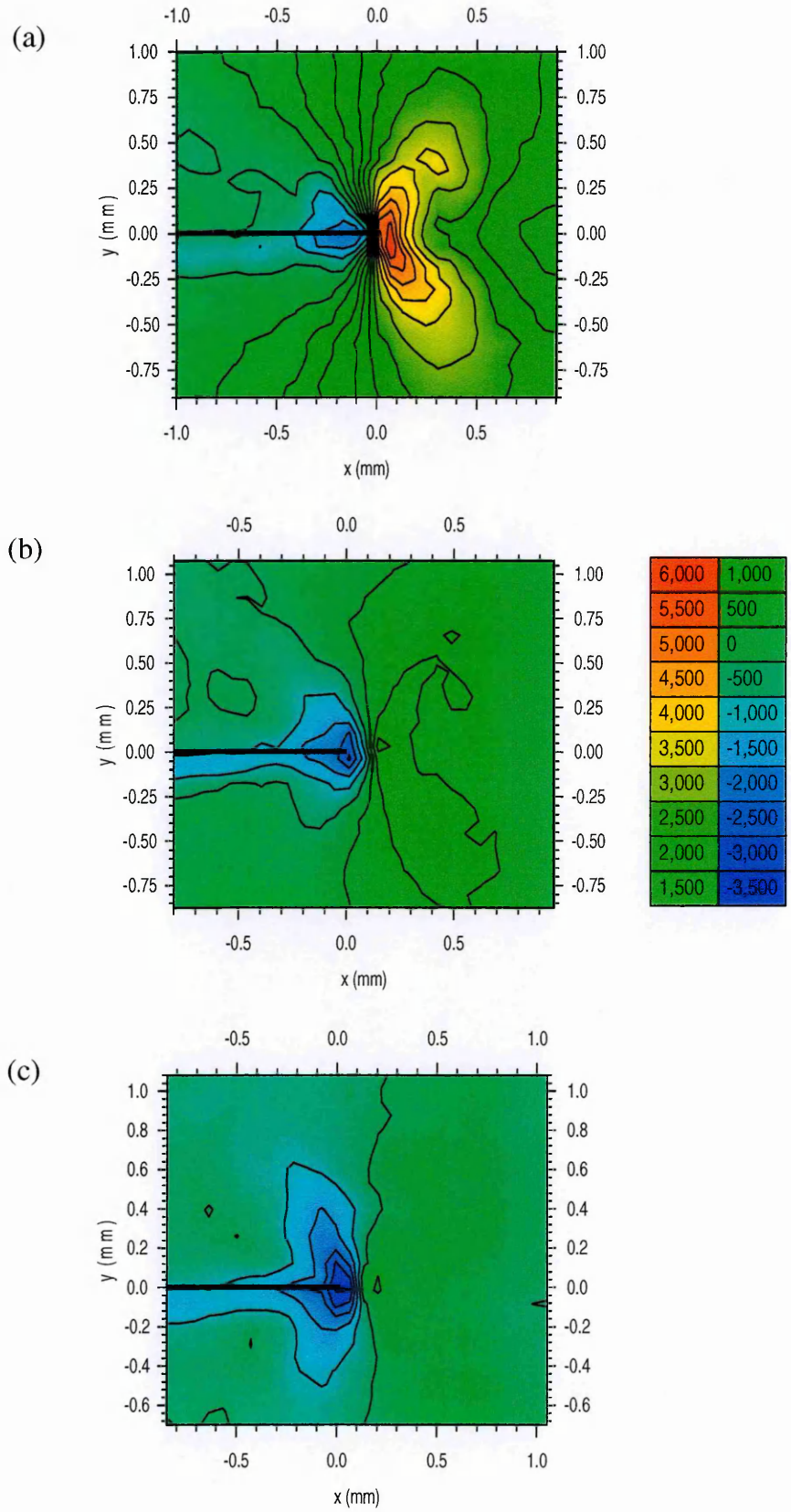

Figure 4.24: Longitudinal strain (με) maps around the crack tip of the fatigued-overloaded specimen: (a) K=16.5 MPa√m, (b) K=3.6 MPa√m and (c) K=0.66 MPa√m.

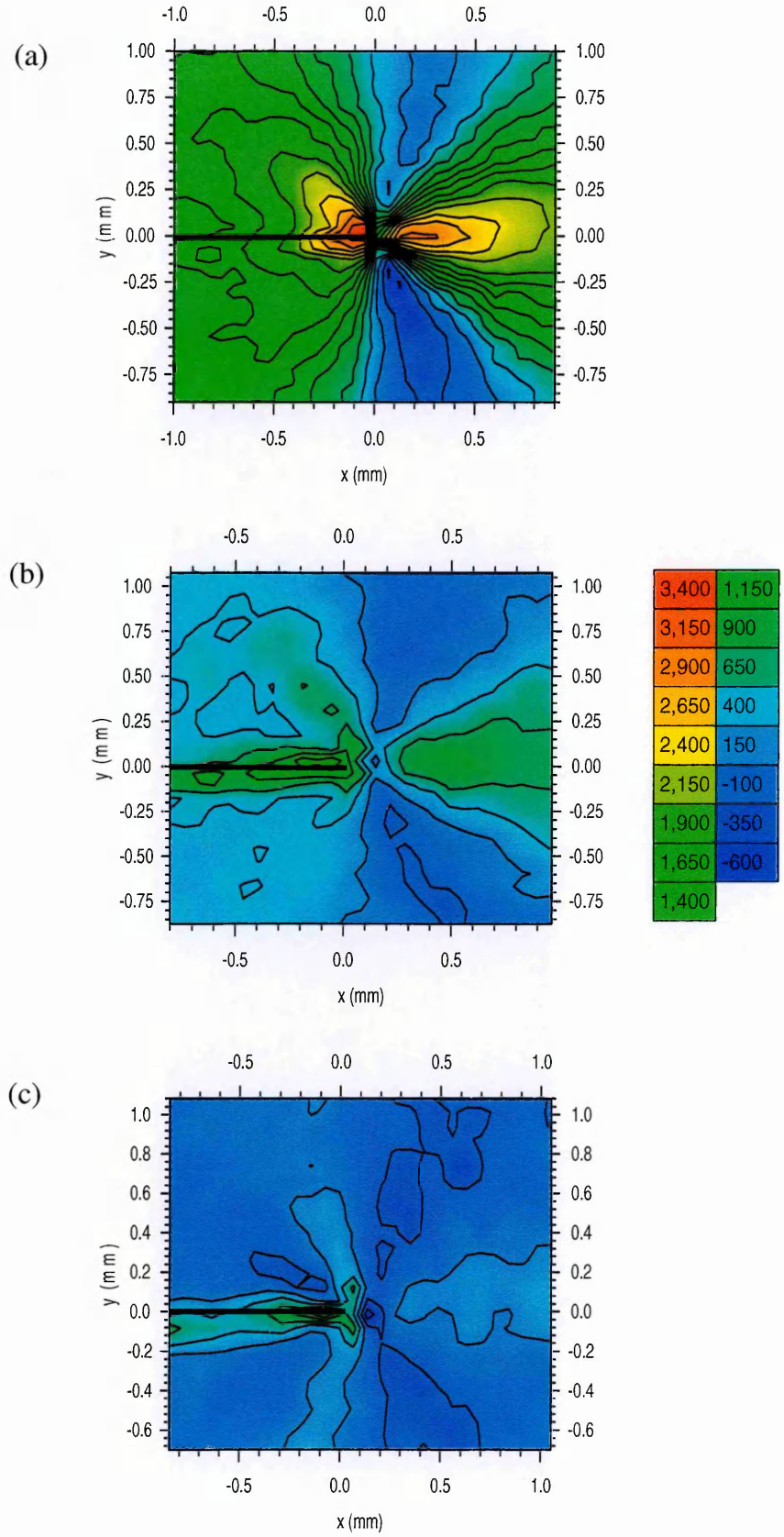

Figure 4.25: Transverse strain (με) maps around the crack tip of the fatigued-overloaded specimen: (a) K=16.5 MPa√m, (b) K=3.6 MPa√m and (c) K=0.66 MPa√m.

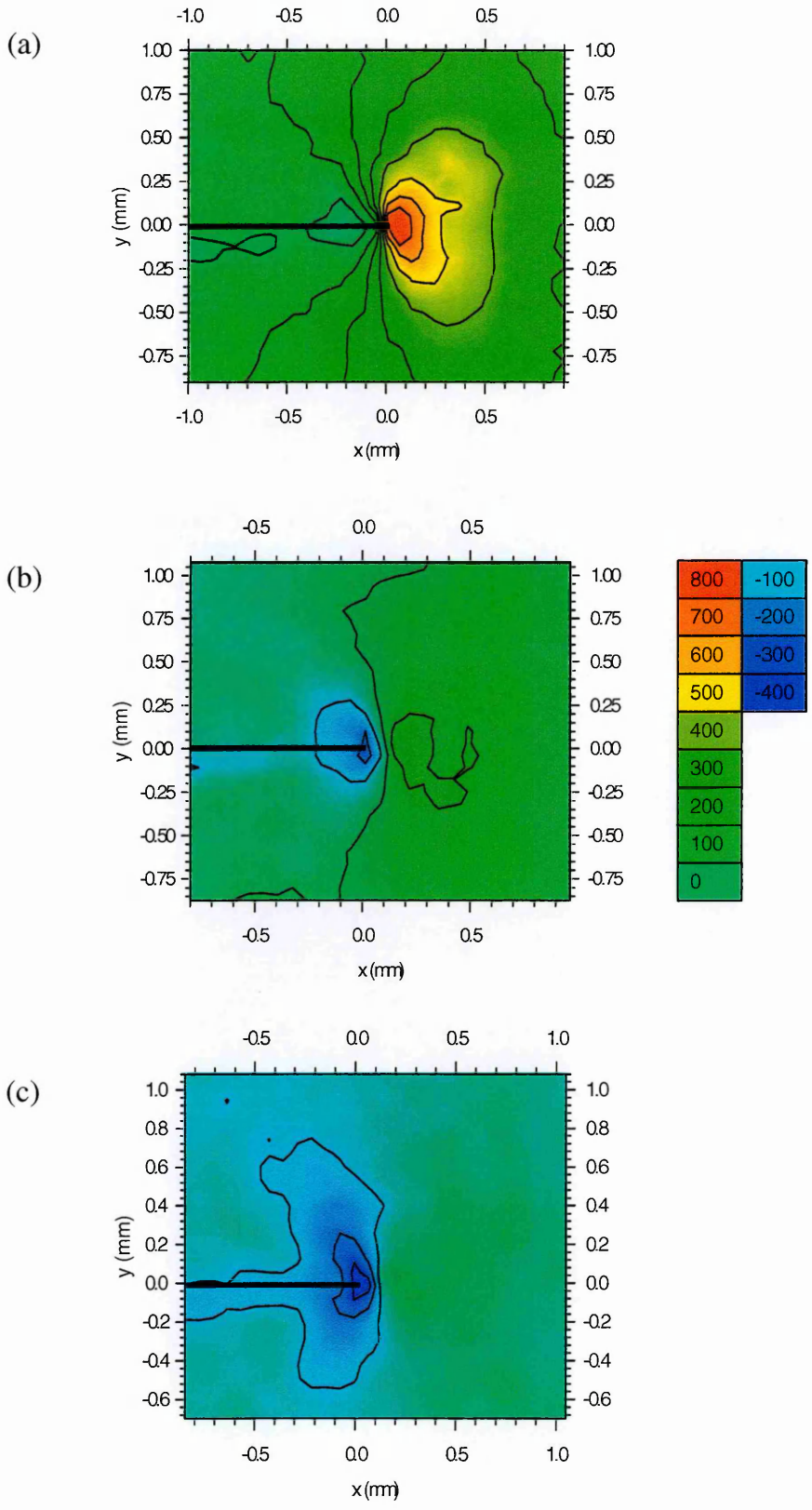

Figure 4.26: Longitudinal stress (MPa) maps around the crack tip of the fatigued-overloaded specimen: (a) K=16.5 MPa√m, (b) K=3.6 MPa√m and (c) K=0.66 MPa√m.

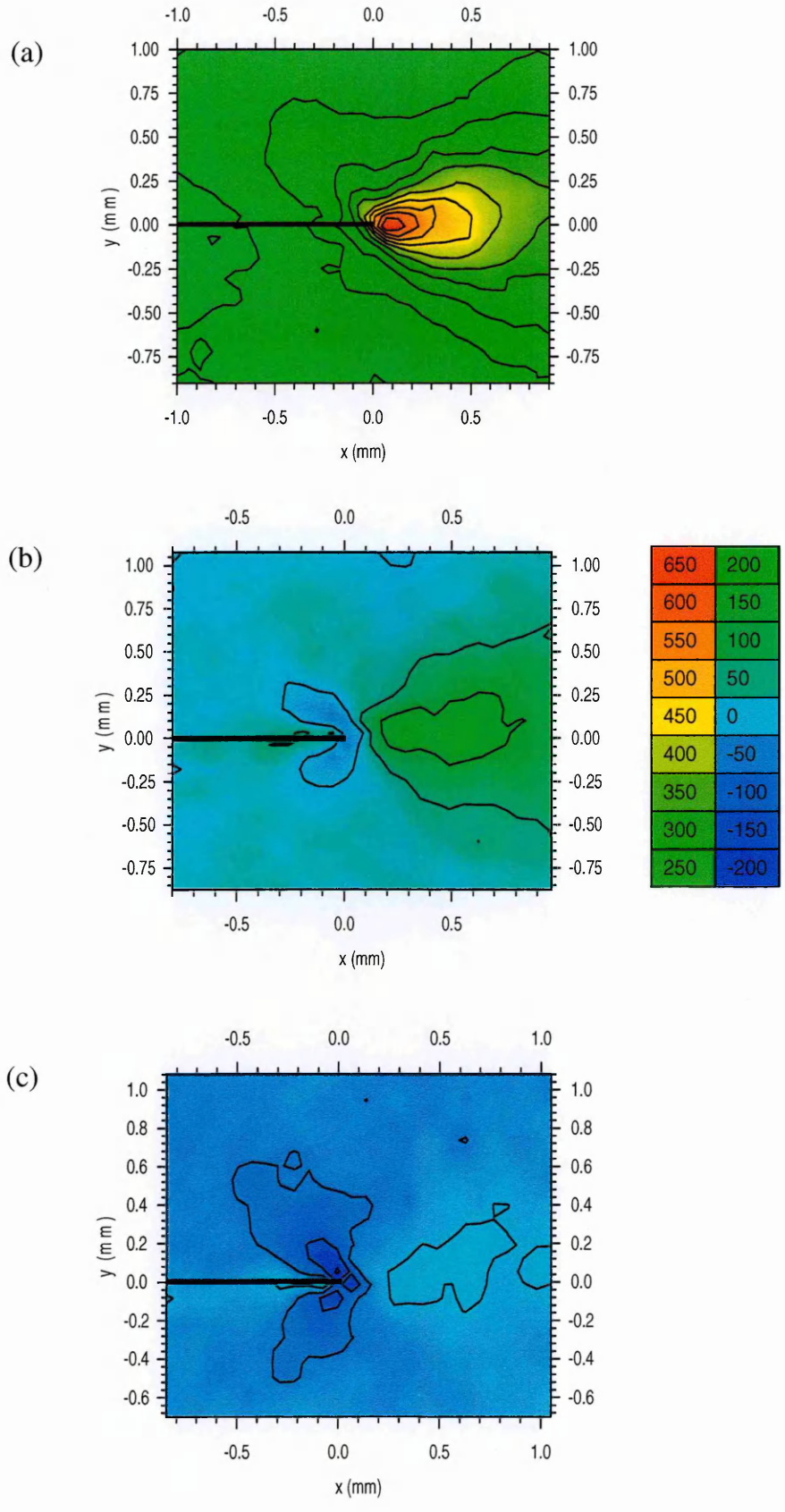

Figure 4.27: Transverse stress (MPa) maps around the crack tip of the fatigued-overloaded specimen: (a) K=16.5 MPa√m, (b) K=3.6 MPa√m and (c) K=0.66 MPa√m.

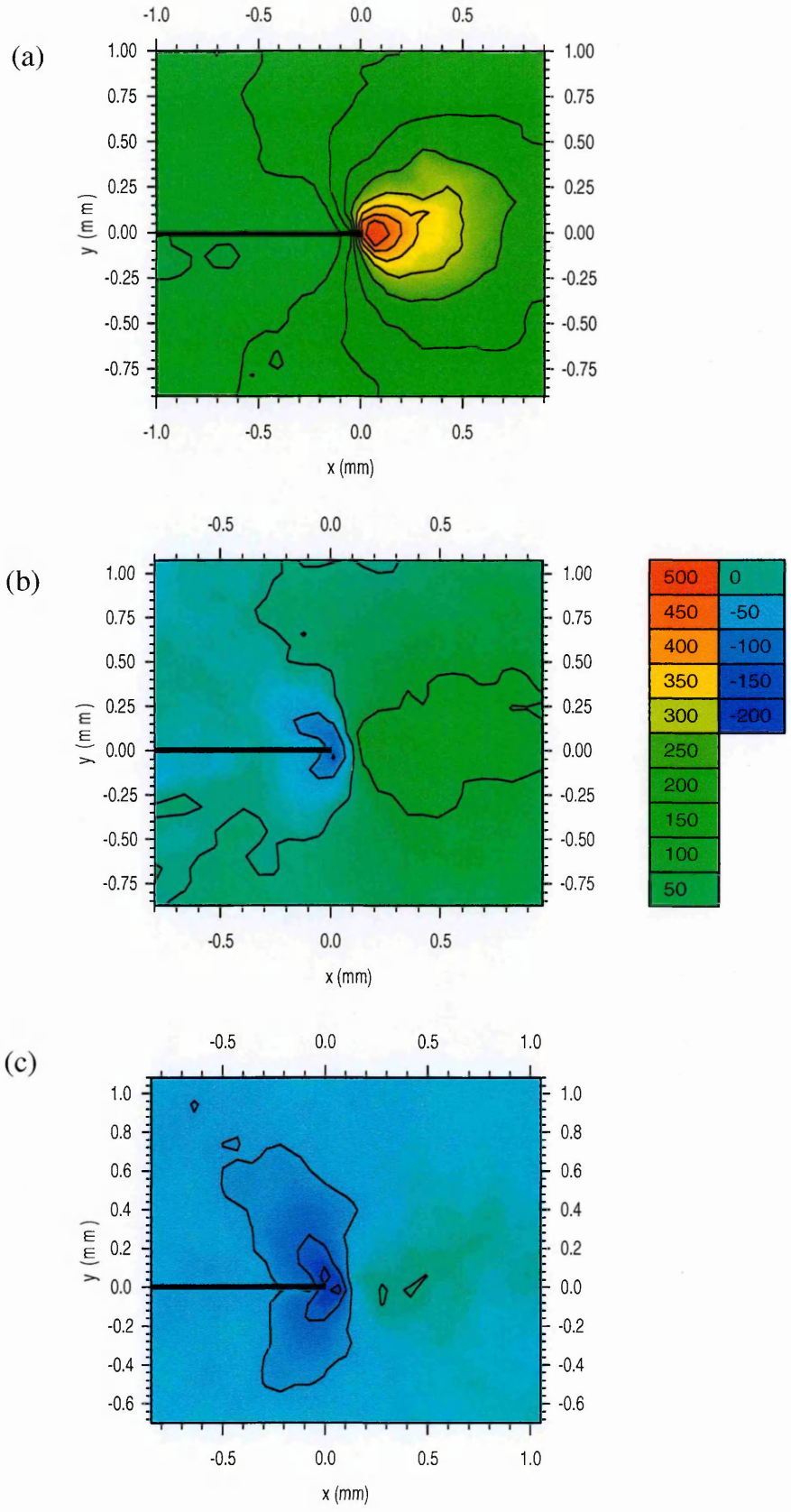

Figure 4.28: Normal stress (MPa) maps around the crack tip of the fatigued-overloaded specimen: (a) K=16.5 MPa√m, (b) K=3.6 MPa√m and (c) K=0.66 MPa√m.

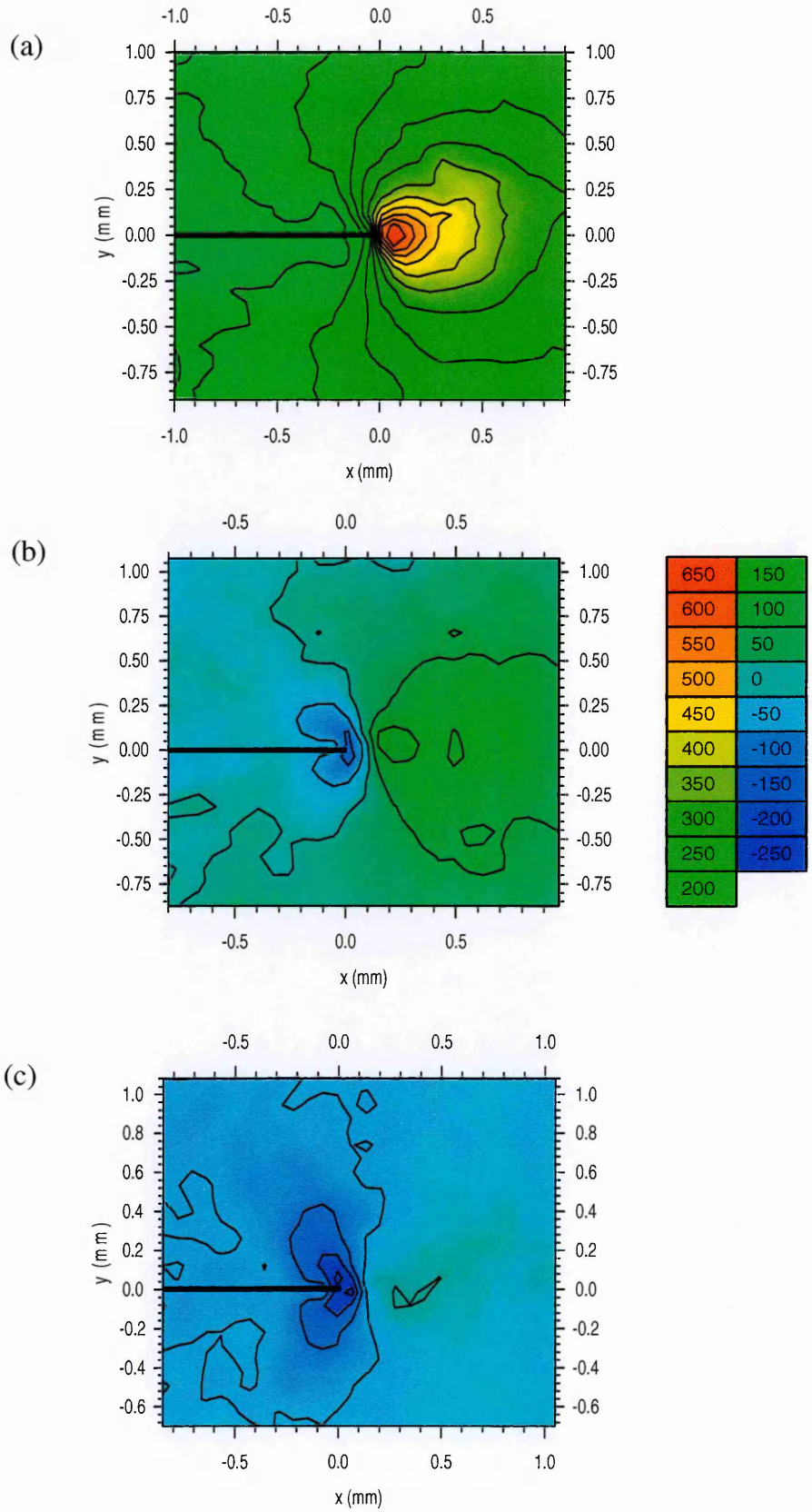

Figure 4.29: Hydrostatic stress (MPa) maps around the crack tip of the fatigued-overloaded specimen: (a) K=16.5 MPa√m, (b) K=3.6 MPa√m and (c) K=0.66 MPa√m.

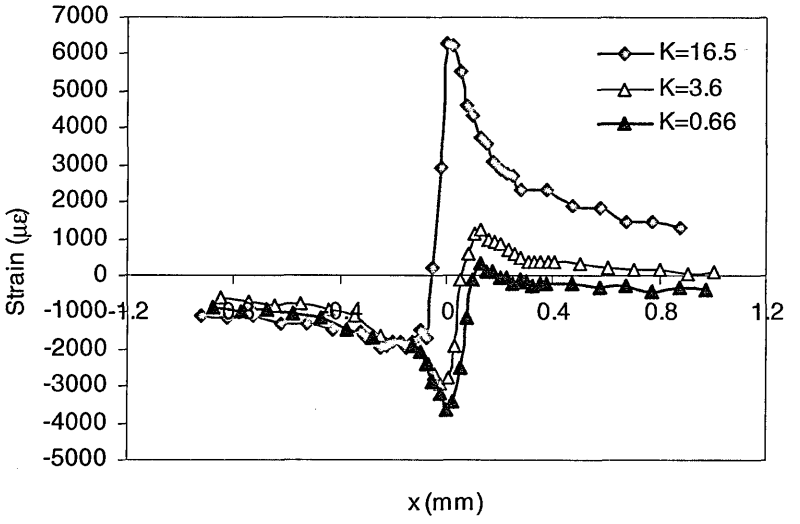

(a) Longitudinal strain

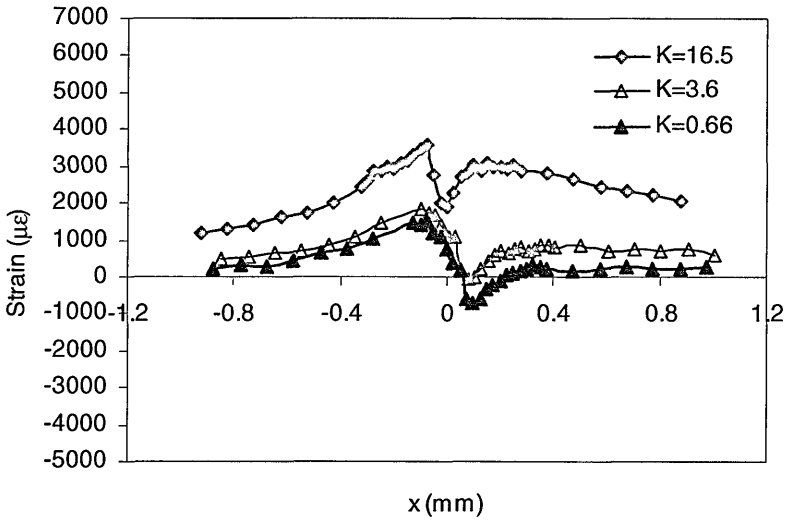

(b) Transverse strain

Figure 4.30: Variation of strains along the x direction in the crack plane (y=0) in the fatigued-overloaded specimen for different applied K (MPa$\sqrt{m}$).

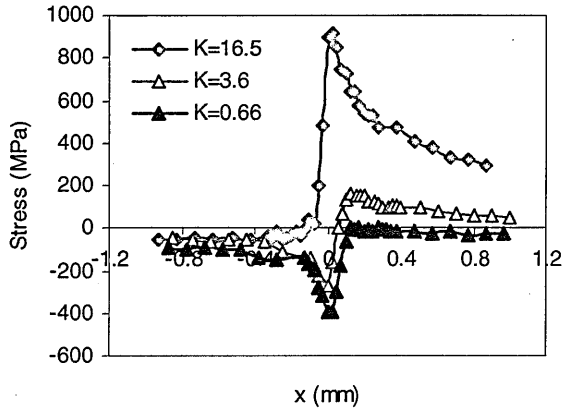

(a) Longitudinal stress

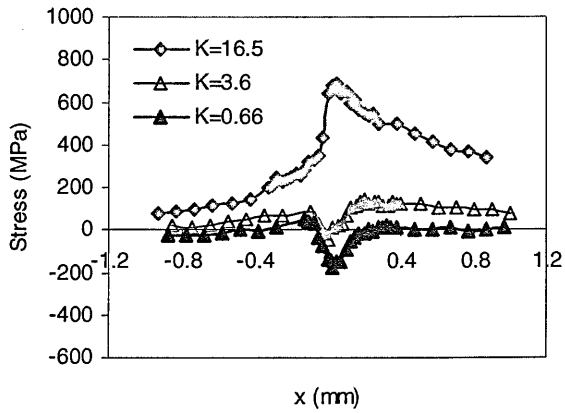

(b) Transverse stress

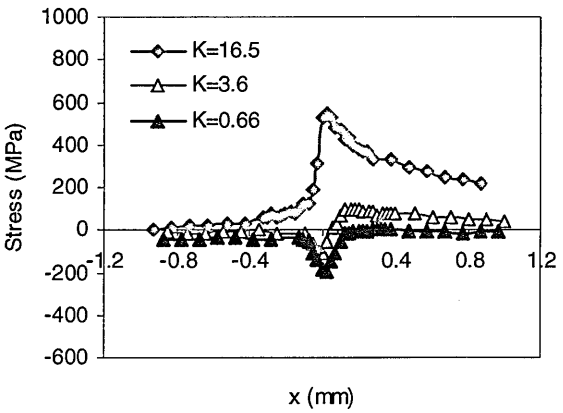

(c) Normal stress

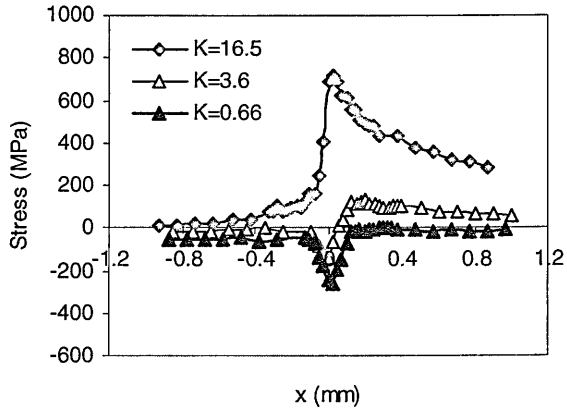

(d) Hydrostatic stress

Figure 4.31: Variation of stresses along the x direction in the crack plane (y=0) in the fatigued-overloaded specimen for different applied K (MPa$\sqrt{m}$).

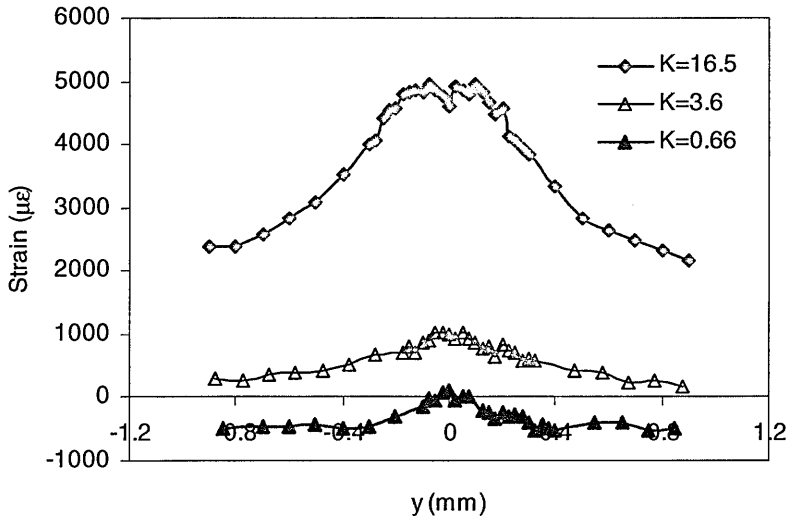

(a) Longitudinal strain

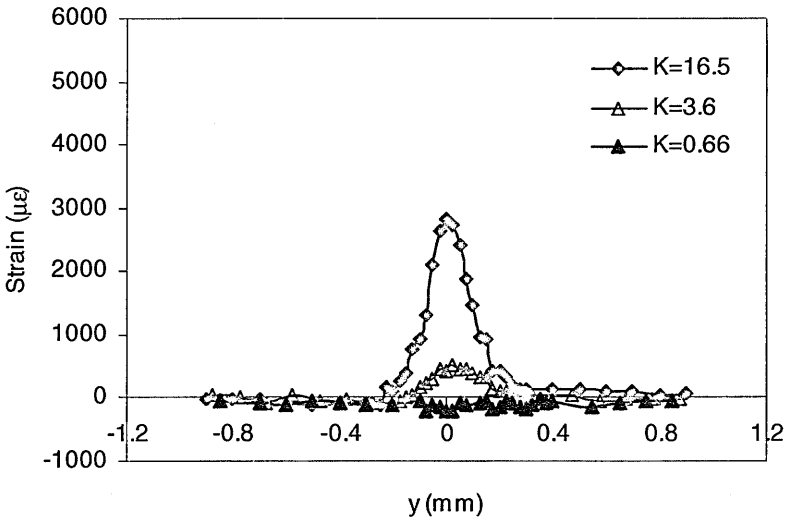

(b) Transverse strain

Figure 4.32: Variation of strains along the y direction (crossing the crack plane) at +0.15 mm ahead of the crack tip in the fatigued-overloaded specimen for different applied K (MPa$\sqrt{m}$).

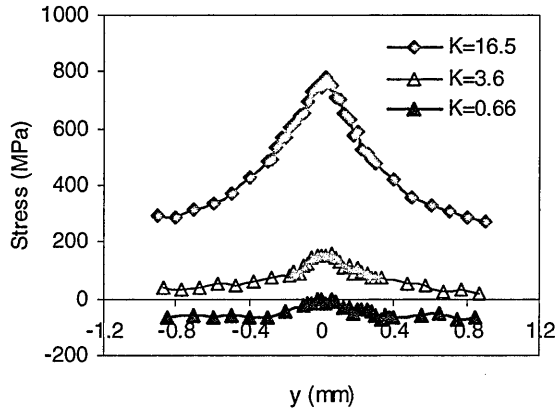

(a) Longitudinal stress

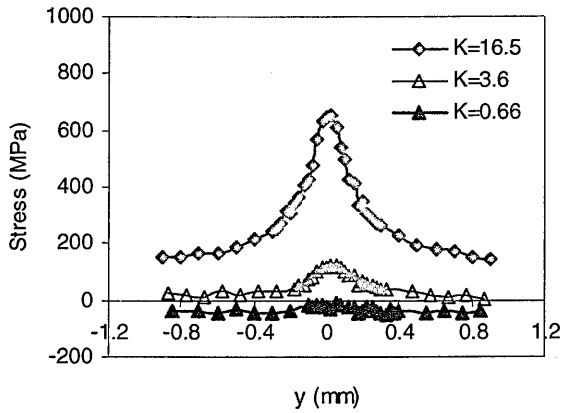

(b) Transverse stress

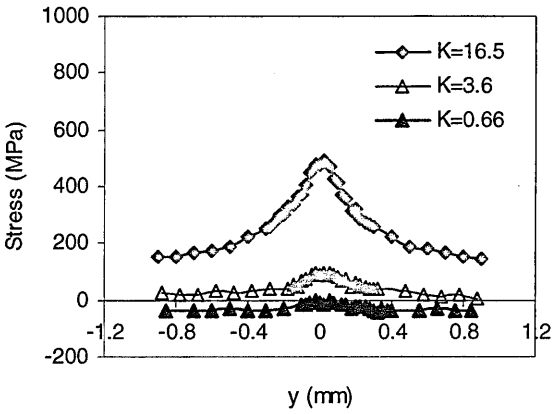

(c) Normal stress

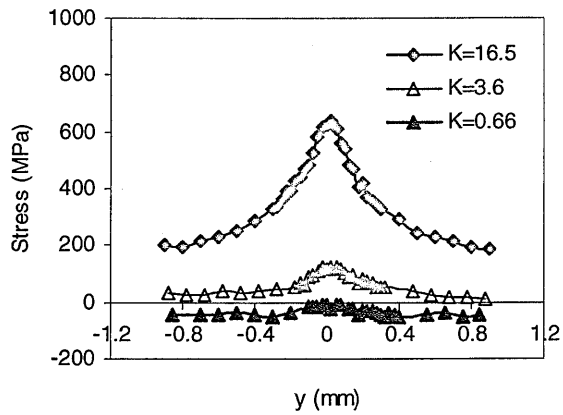

(d) Hydrostatic stress

Figure 4.33: Variation of stresses along the y direction (crossing the crack plane) at +0.15 mm ahead of the crack tip in the fatigued-overloaded specimen for different applied K (MPa$\sqrt{m}$).

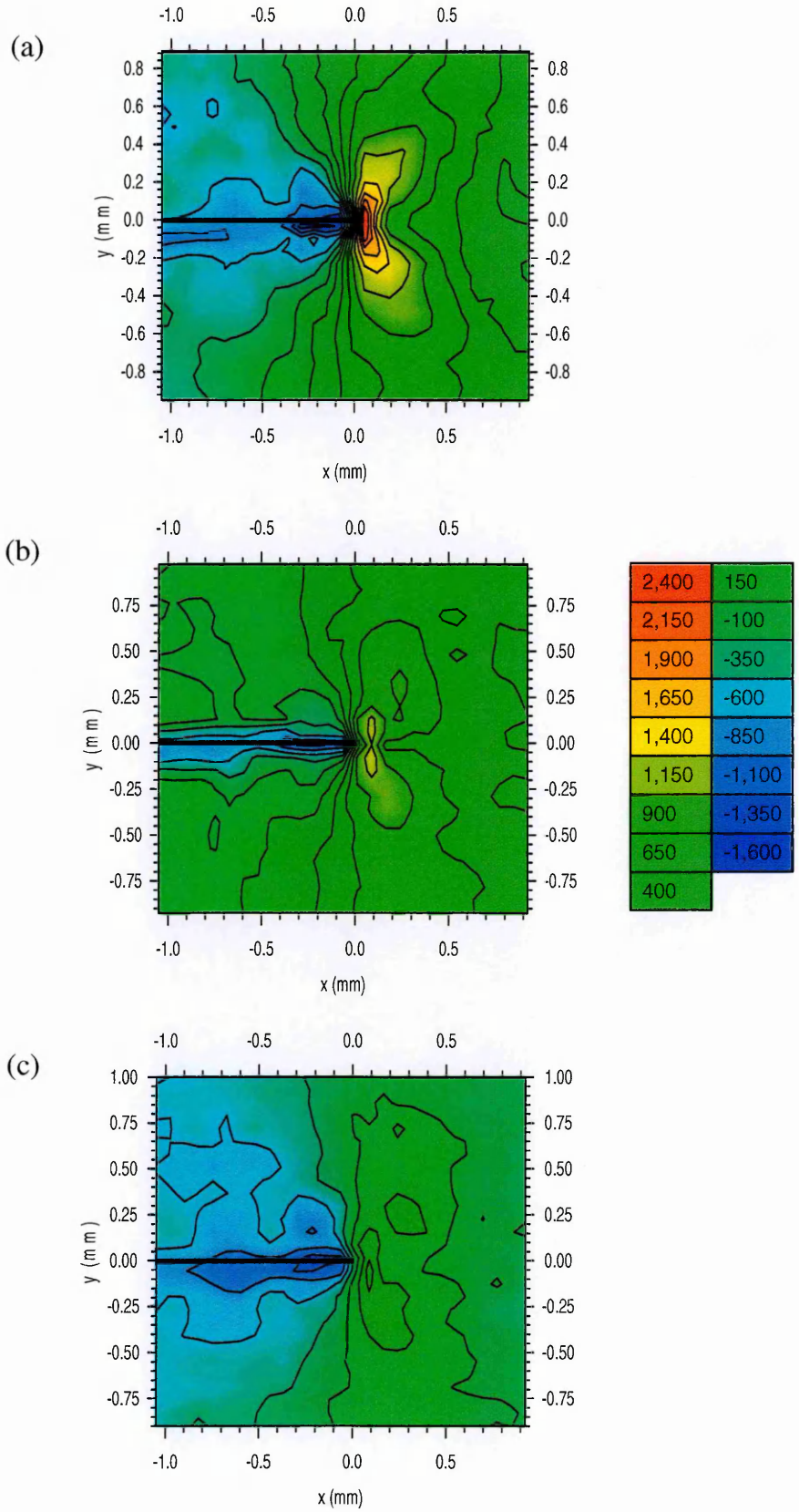

Figure 4.34: Longitudinal strain (με) maps around the crack tip of the fatigued-overloaded-fatigued specimen: (a) K=6.6 MPa√m, (b) K=3.6 MPa√m and (c) K=2.6 MPa√m.

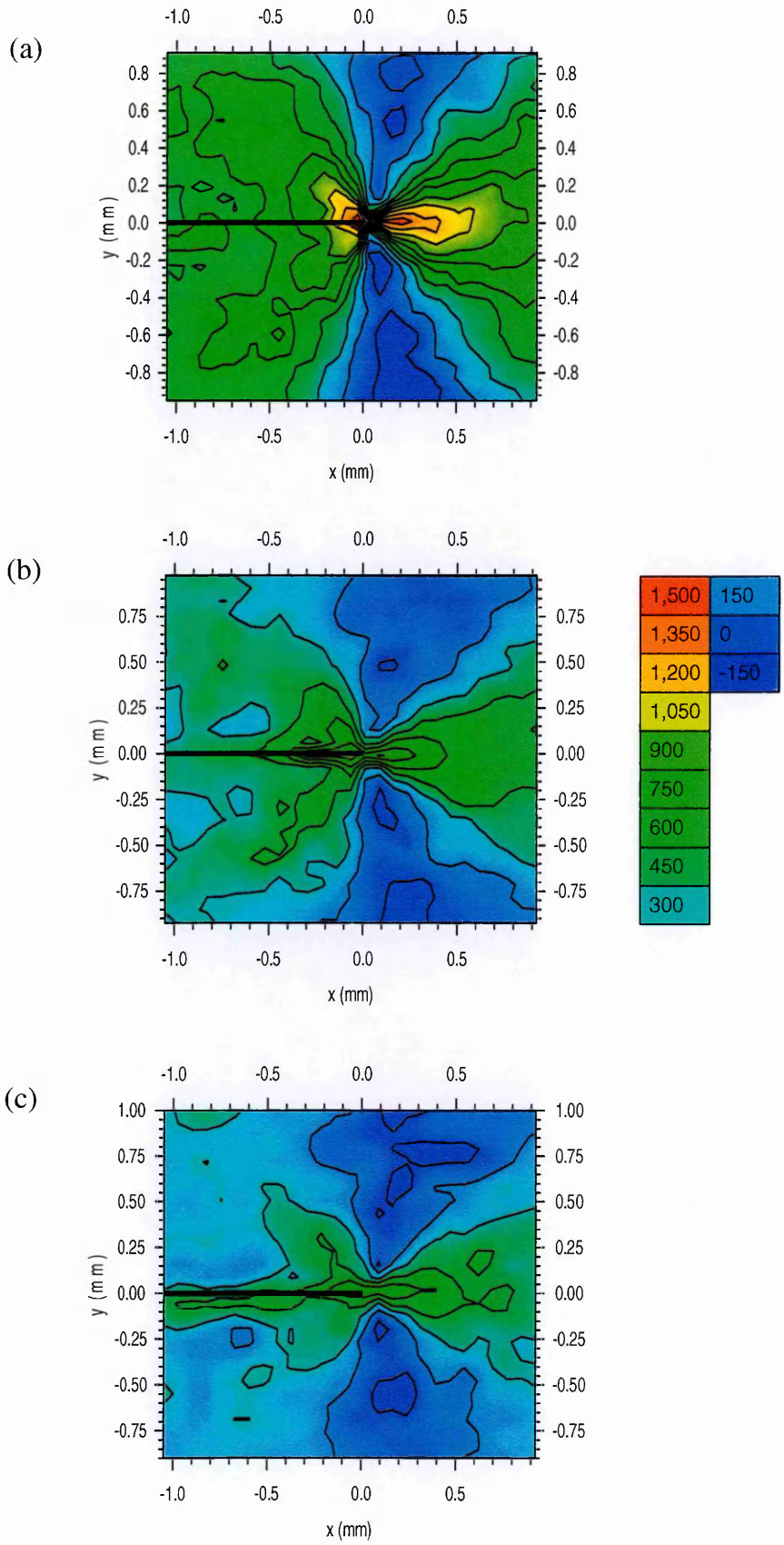

Figure 4.35: Transverse strain (με) maps around the crack tip of the fatigued-overloaded-fatigued specimen: (a) K=6.6 MPa√m, (b) K=3.6 MPa√m and (c) K=2.6 MPa√m.

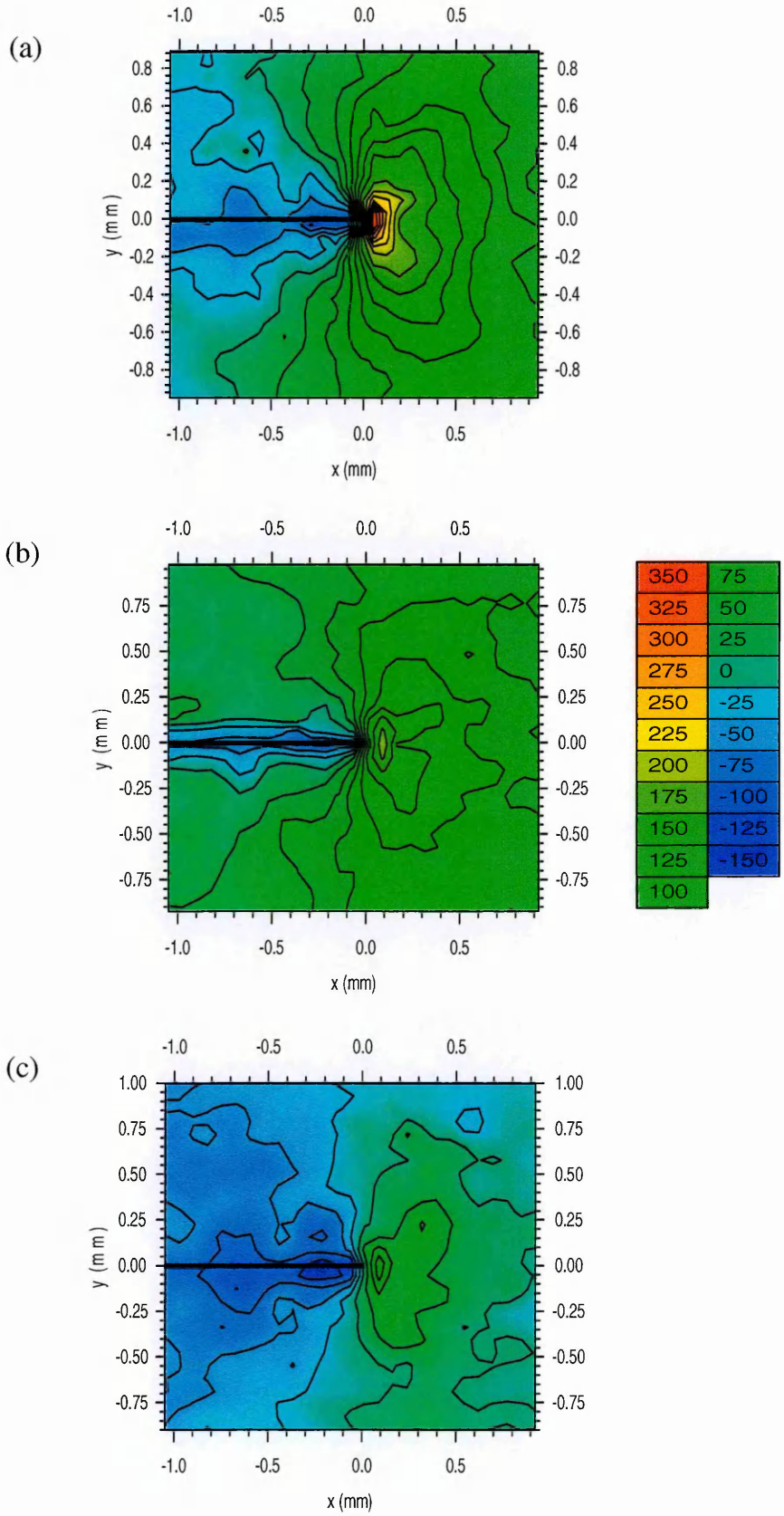

Figure 4.36: Longitudinal stress (MPa) maps around the crack tip of the fatigued-overloaded-fatigued specimen: (a) K=6.6 MPa√m, (b) K=3.6 MPa√m and (c) K=2.6 MPa√m.

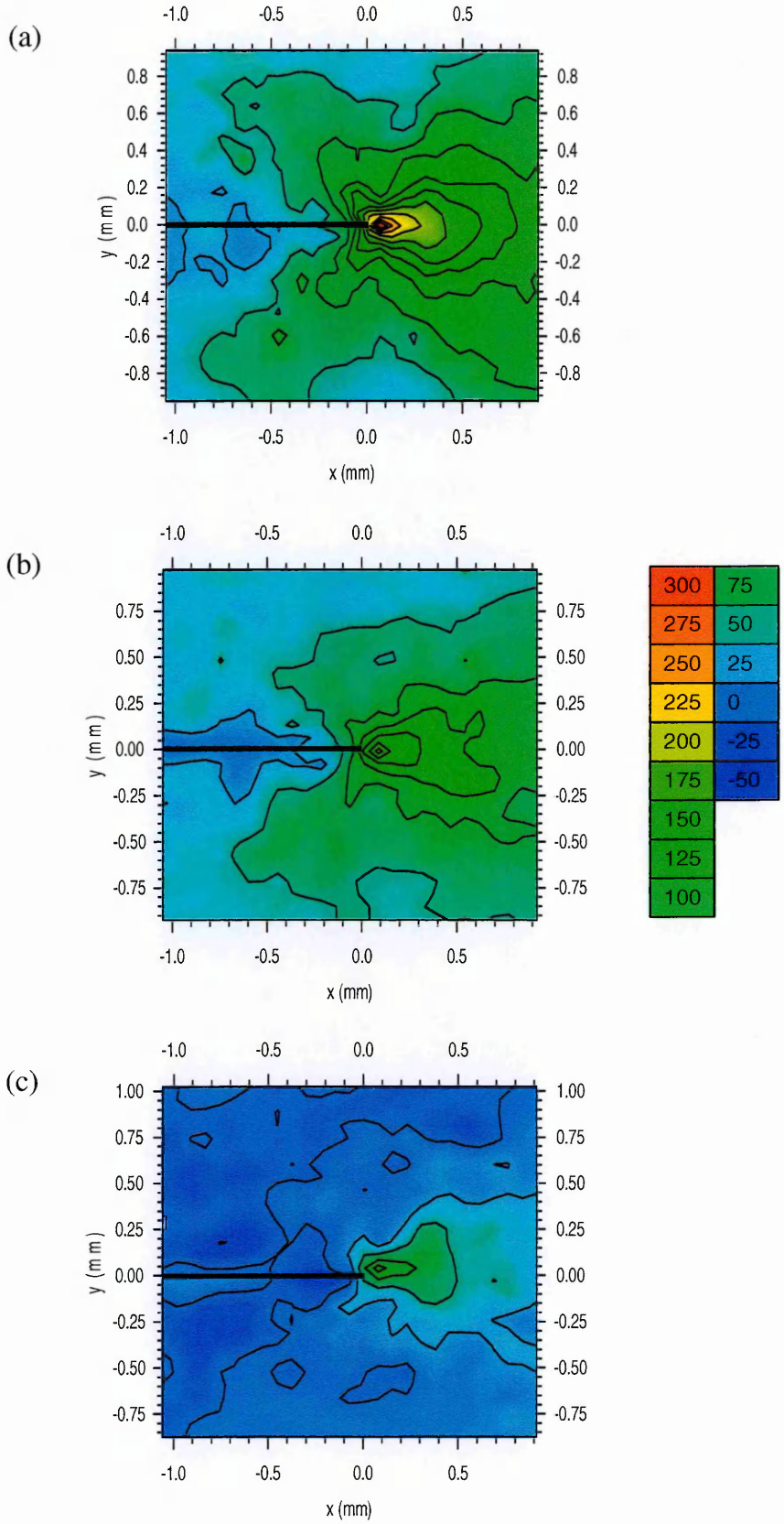

Figure 4.37: Transverse stress (MPa) maps around the crack tip of the fatigued-overloaded-fatigued specimen: (a) K=6.6 MPa√m, (b) K=3.6 MPa√m and (c) K=2.6 MPa√m.

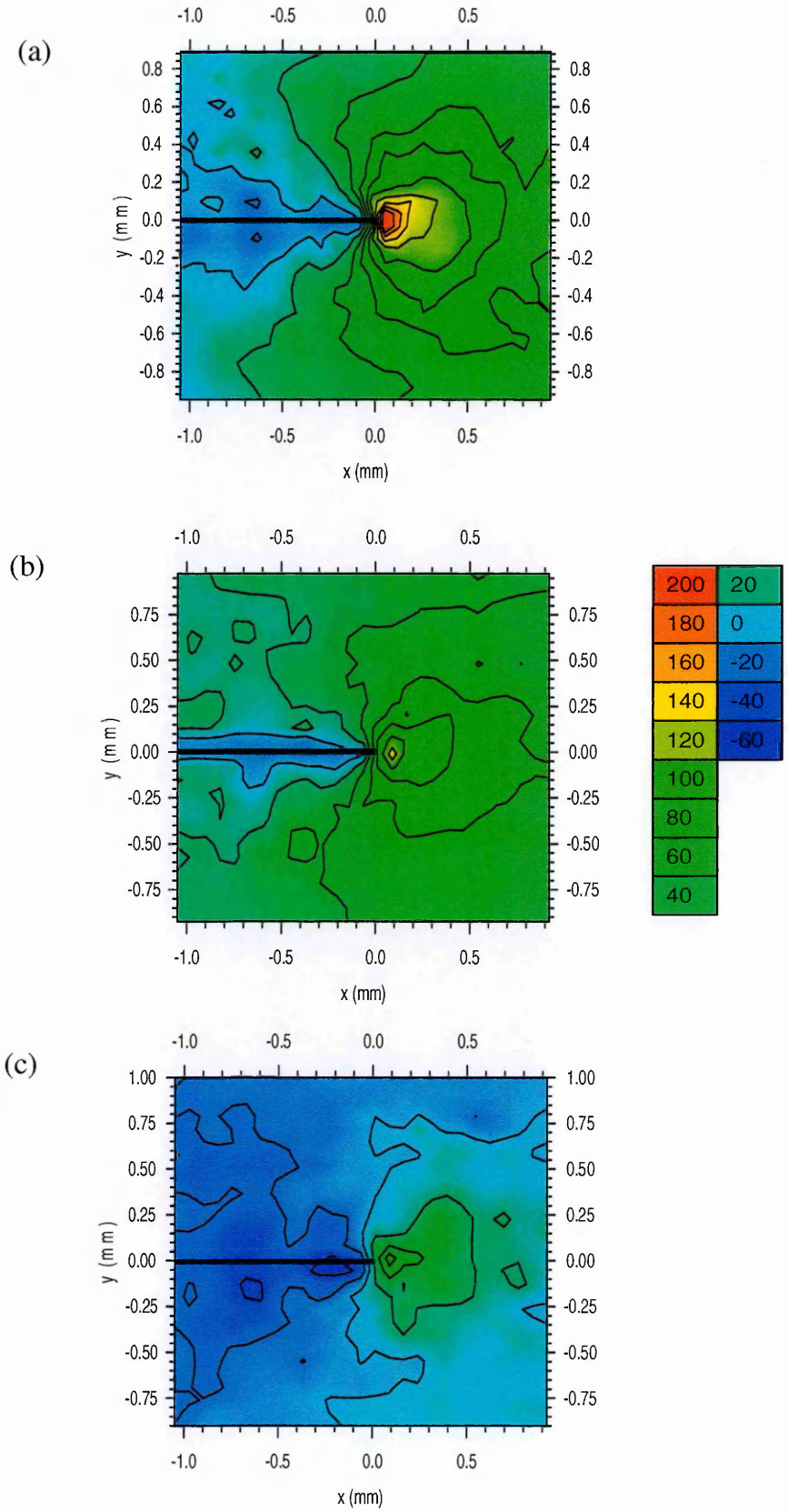

Figure 4.38: Normal stress (MPa) maps around the crack tip of the fatigued-overloaded-fatigued specimen: (a) K=6.6 MPa√m, (b) K=3.6 MPa√m and (c) K=2.6 MPa√m.

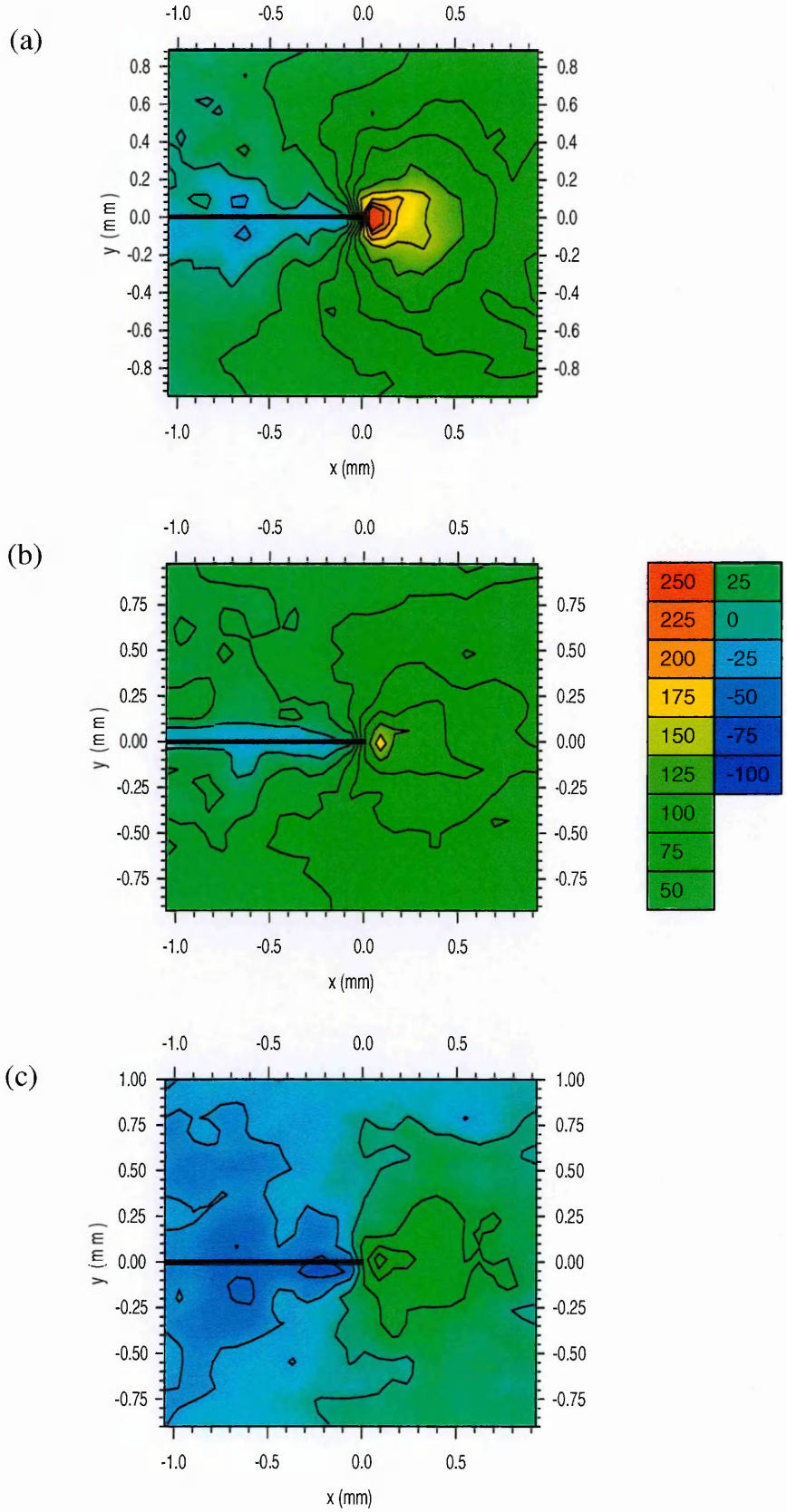

Figure 4.39: Hydrostatic stress (MPa) maps around the crack tip of the fatigued-overloaded-fatigued specimen: (a) K=6.6 MPa√m, (b) K=3.6 MPa√m and (c) K=2.6 MPa√m.

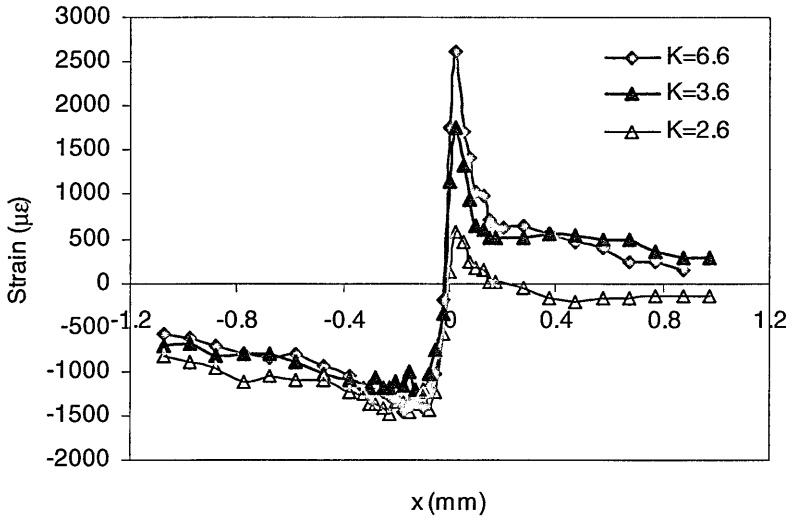

(a) Longitudinal strain

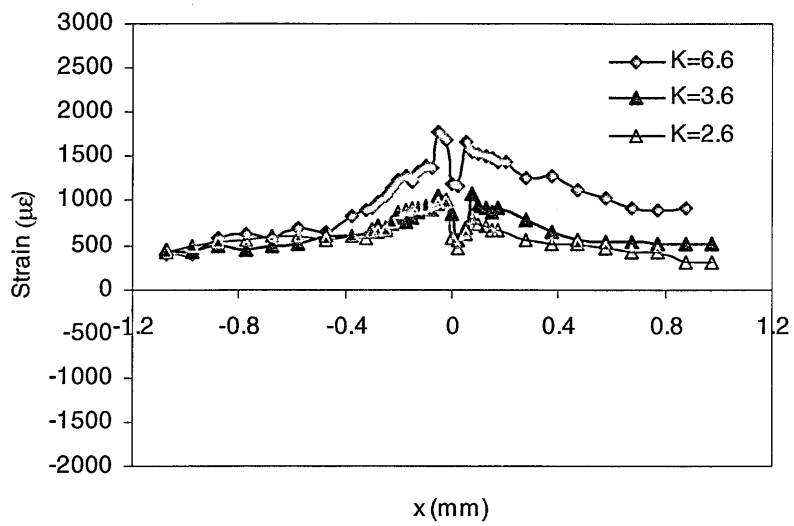

(b) Transverse strain

Figure 4.40: Variation of strains along the x direction in the crack plane (y=0) in the fatigued-overloaded-fatigued specimen for different applied K (MPa$\sqrt{m}$).

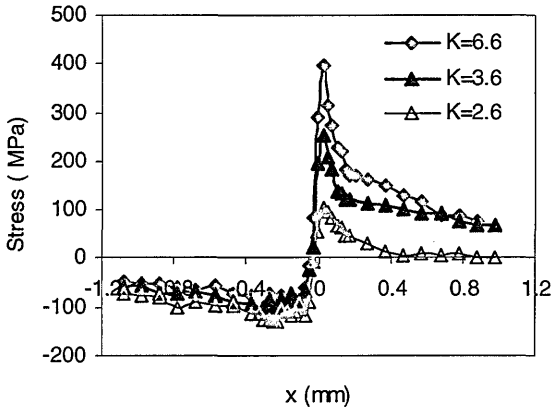

(a) Longitudinal stress

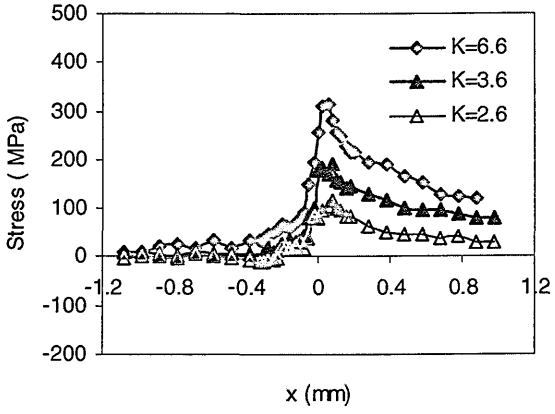

(b) Transverse stress

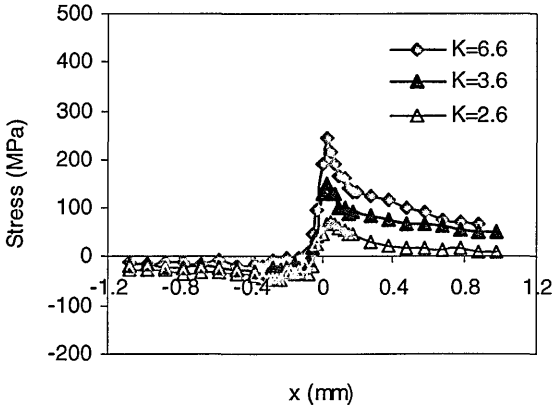

(c) Normal stress

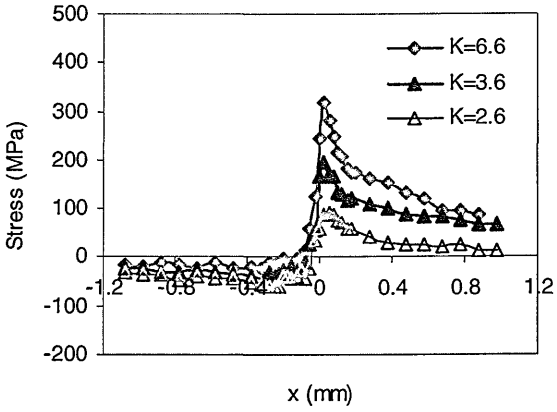

(d) Hydrostatic stress

Figure 4.41: Variation of stresses along the x direction in the crack plane (y=0) in the fatigued-overloaded-fatigued specimen for different applied K (MPa$\sqrt{m}$).

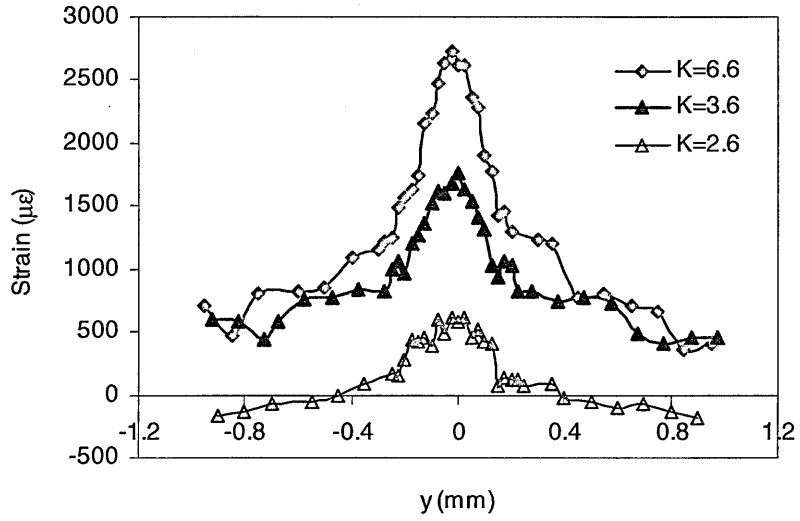

(a) Longitudinal strain

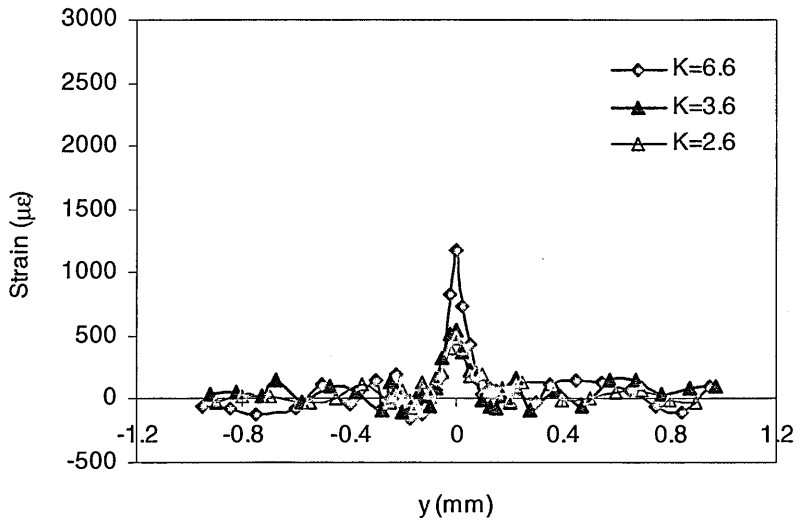

(b) Transverse strain

Figure 4.42: Variation of strains along the y direction (crossing the crack plane) at +0.025 mm ahead of the crack tip in the fatigued-overloaded-fatigued specimen for different applied K (MPa$\sqrt{m}$).

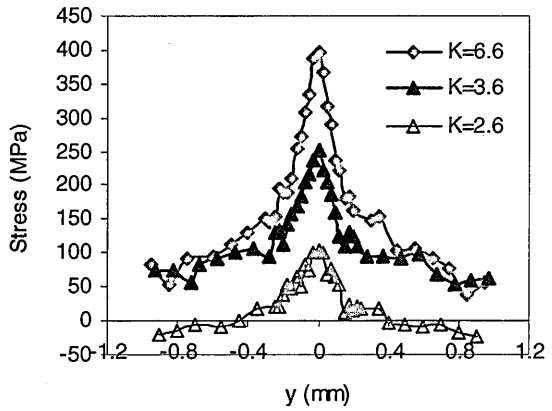

(a) Longitudinal stress

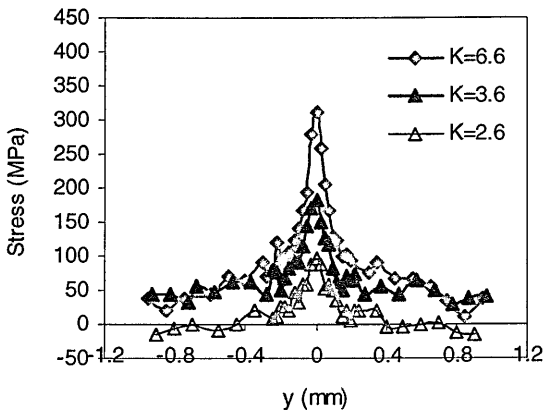

(b) Transverse stress

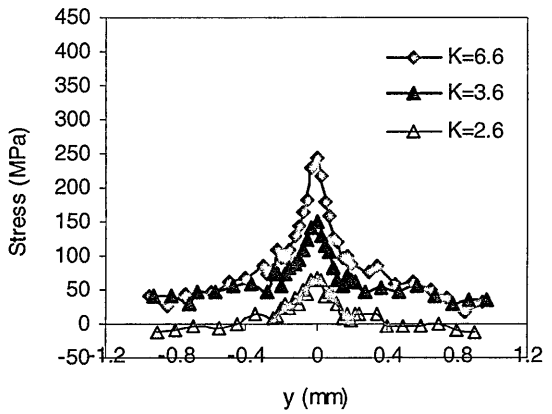

(c) Normal stress

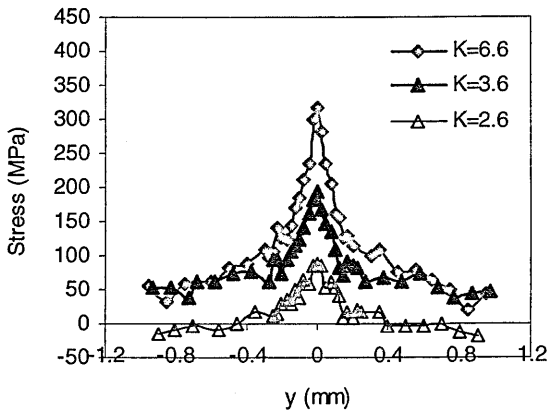

(d) Hydrostatic stress

Figure 4.43: Variation of stresses along the y direction (crossing the crack plane) at +0.025 mm ahead of the crack tip in the fatigued-overloaded-fatigued specimen for different applied K (MPa$\sqrt{m}$).

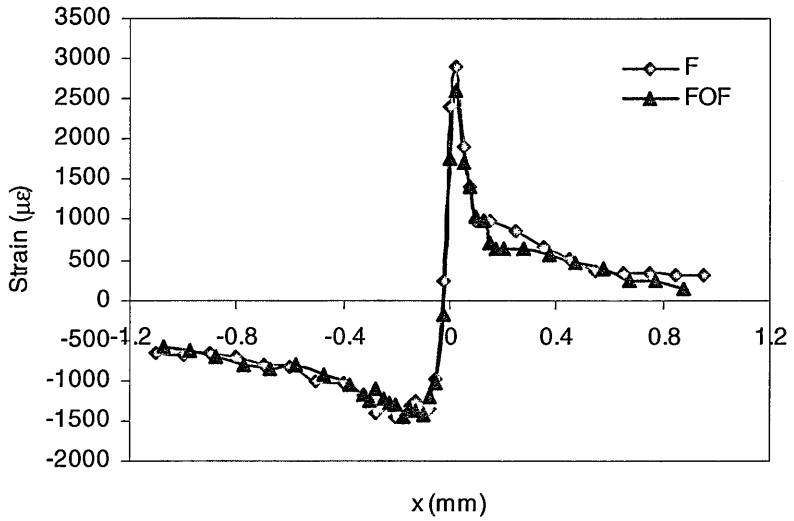

(a) Longitudinal strain

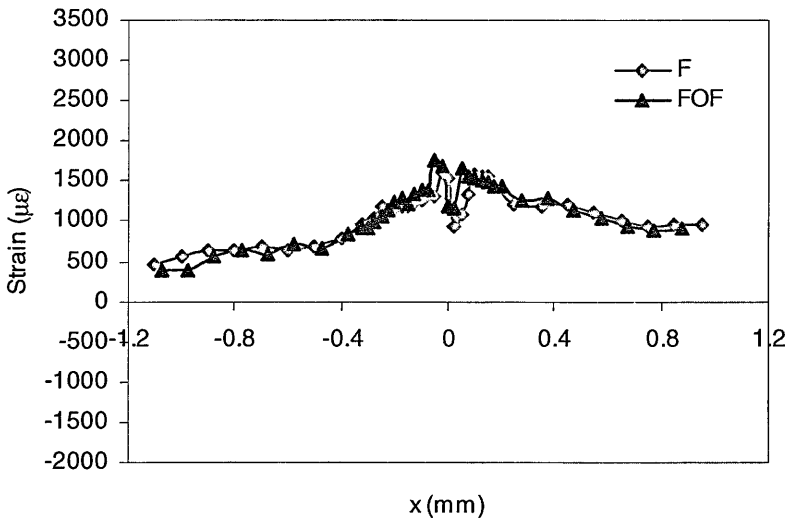

(b) Transverse strain

Figure 4.44: Variation of strains along the x direction in the crack plane (y=0) in the fatigued (F) and fatigued-overloaded-fatigued (FOF) specimens for applied K=6.6 MPa$\sqrt{m}$.

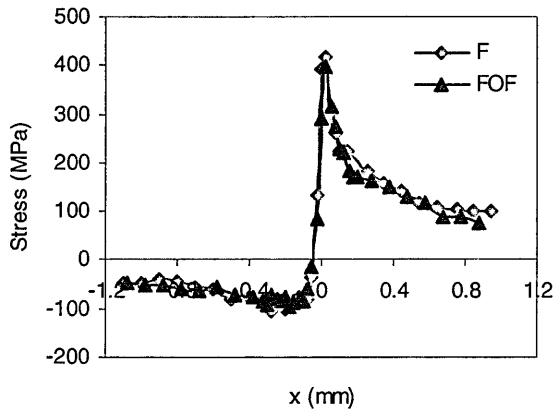

(a) Longitudinal stress

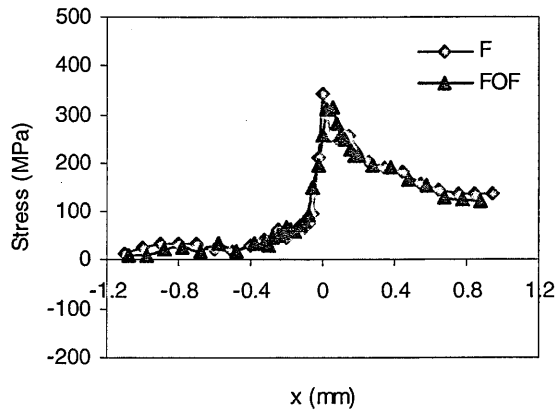

(b) Transverse stress

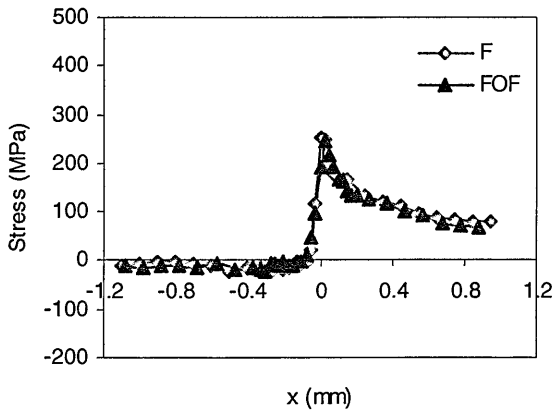

(c) Normal stress

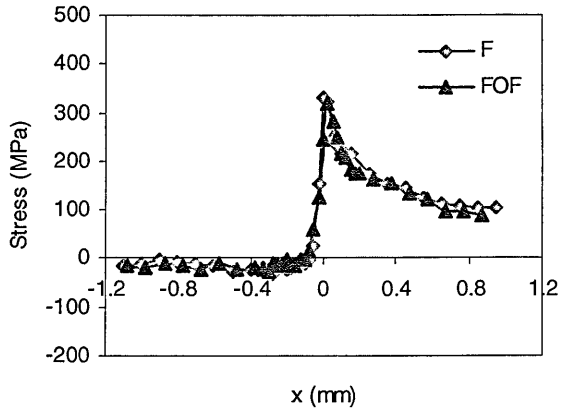

(d) Hydrostatic stress

Figure 4.45: Variation of stresses along the x direction in the crack plane (y=0) in the fatigued (F) and fatigued-overloaded-fatigued (FOF) specimens for applied K=6.6 MPa$\sqrt{m}$.

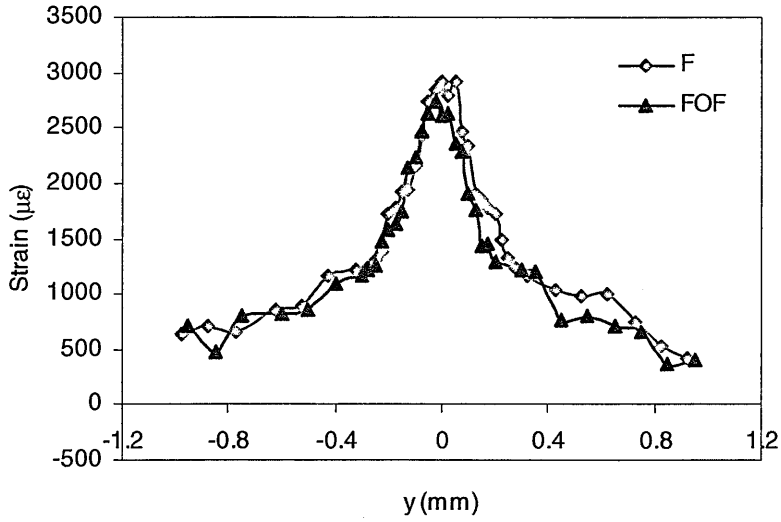

(a) Longitudinal strain

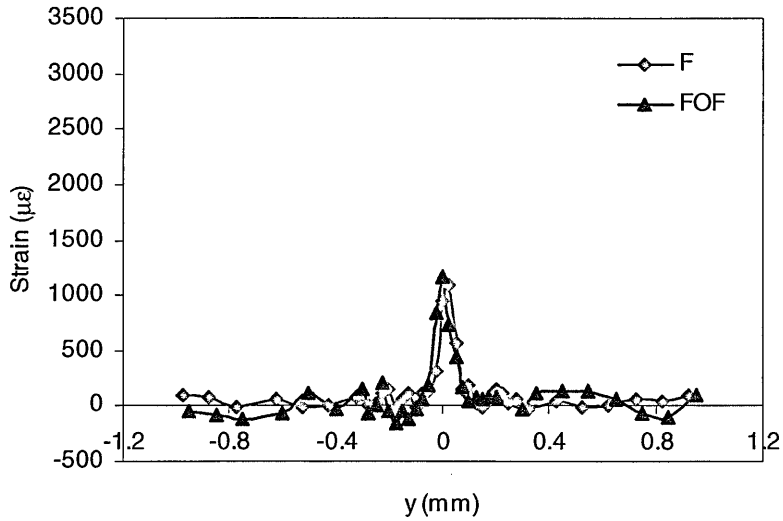

(b) Transverse strain

Figure 4.46: Variation of strains along the y direction (crossing the crack plane) at +0.025 mm ahead of the crack tip in the fatigued (F) and fatigued-overloaded-fatigued (FOF) specimens for applied K=6.6 MPa$\sqrt{m}$.

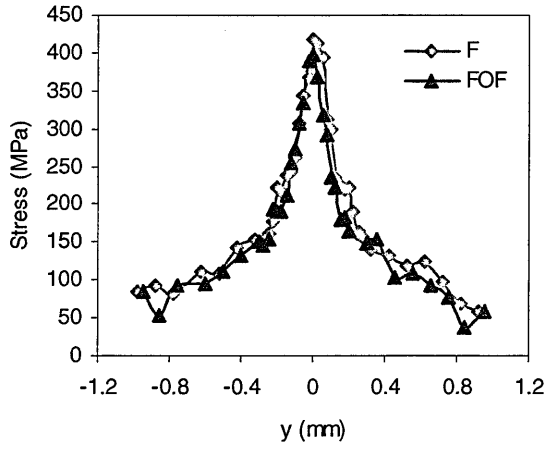

(a) Longitudinal stress

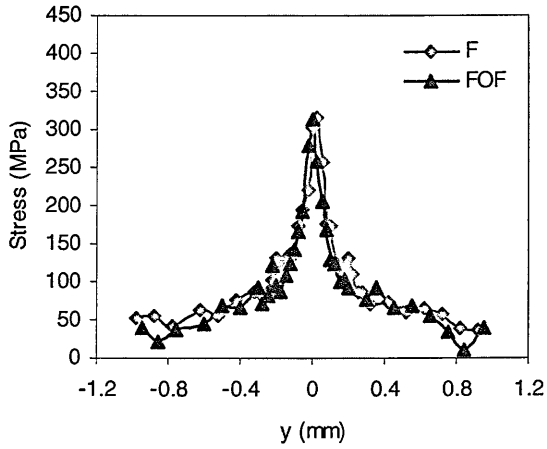

(b) Transverse stress

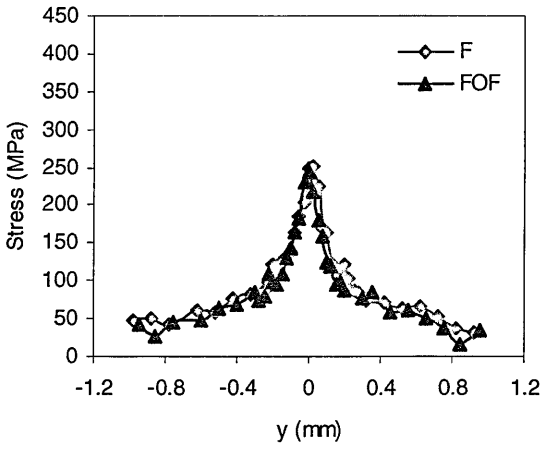

(c) Normal stress

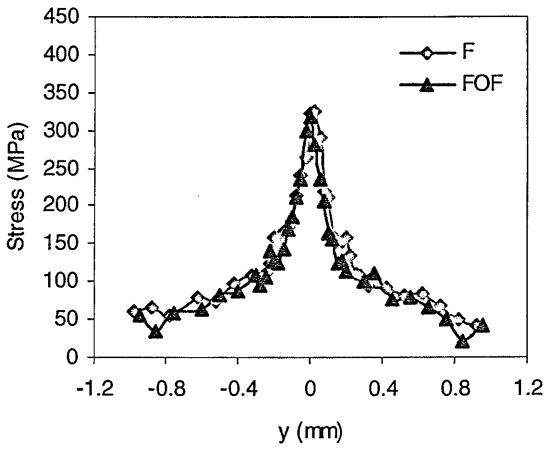

(d) Hydrostatic stress

Figure 4.47: Variation of stresses along the y direction (crossing the crack plane) at +0.025 mm ahead of the crack tip in the fatigued (F) and fatigued-overloaded-fatigued (FOF) specimens for applied K=6.6 MPa$\sqrt{m}$.

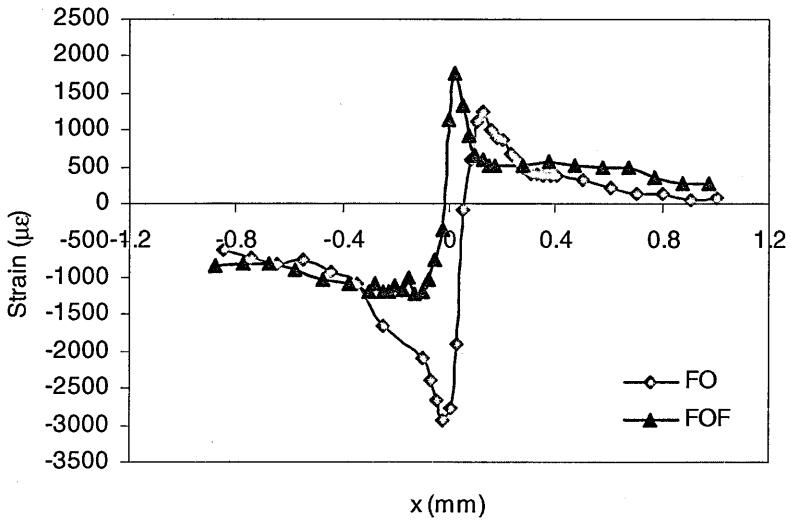

(a) Longitudinal strain

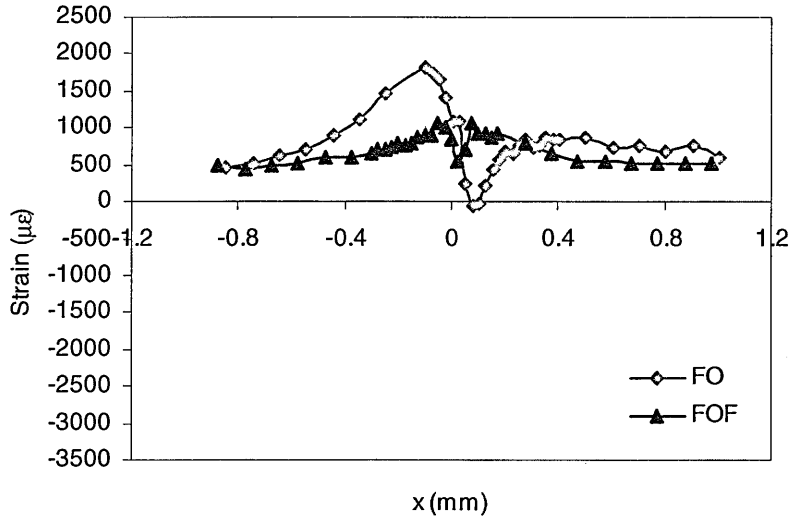

(b) Transverse strain

Figure 4.48: Variation of strains along the x direction in the crack plane (y=0) in the fatigued-overloaded (FO) and fatigued-overloaded-fatigued (FOF) specimens for applied K=3.6 MPa$\sqrt{m}$.

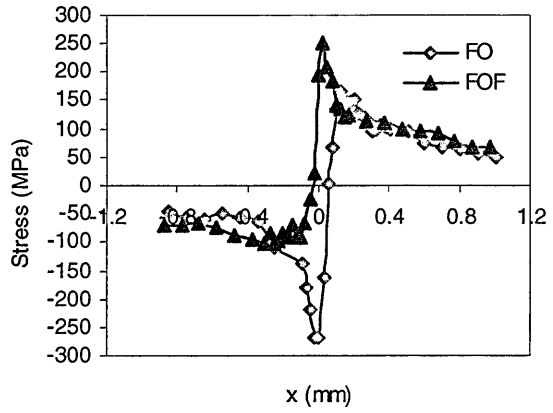

(a) Longitudinal stress

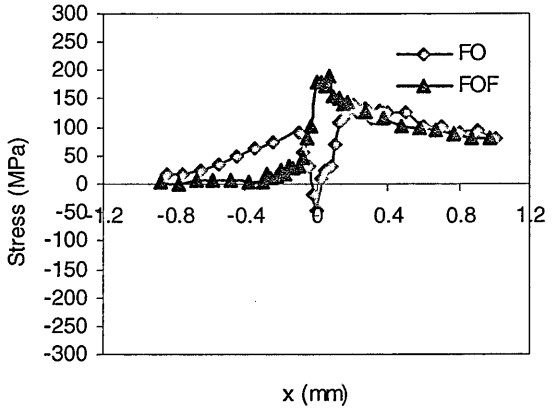

(b) Transverse stress

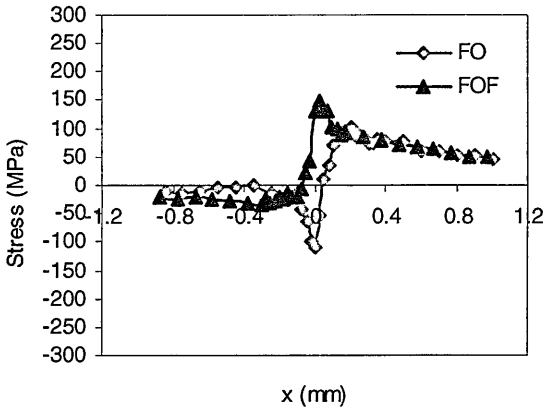

(c) Normal stress

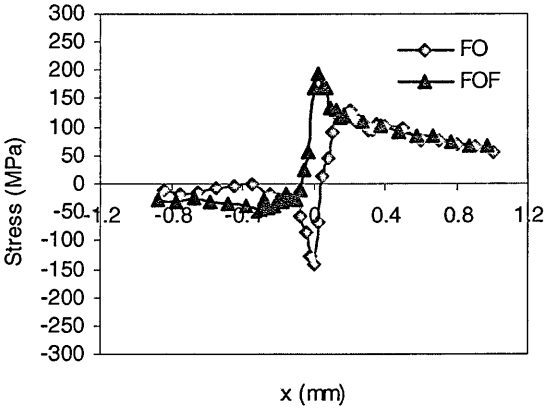

(d) Hydrostatic stress

Figure 4.49: Variation of stresses along the x direction in the crack plane (y=0) in the fatigued-overloaded (FO) and fatigued-overloaded-fatigued (FOF) specimens for applied K=3.6 MPa$\sqrt{m}$.

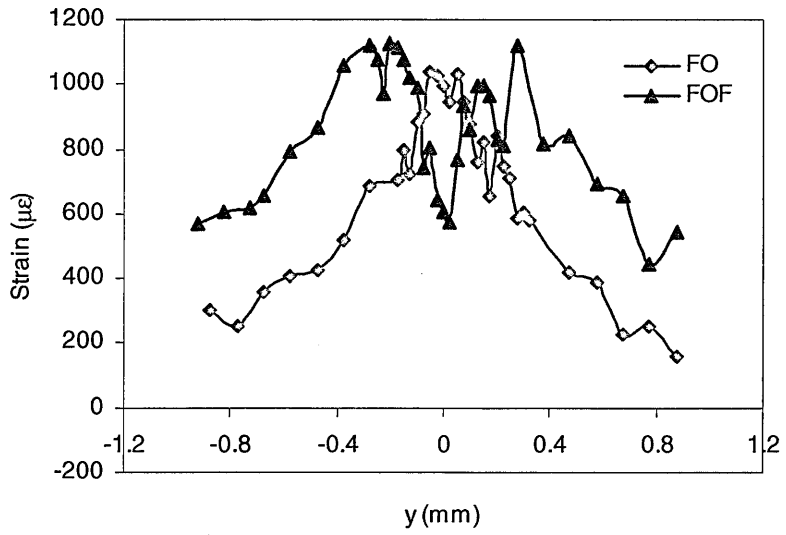

(a) Longitudinal strain

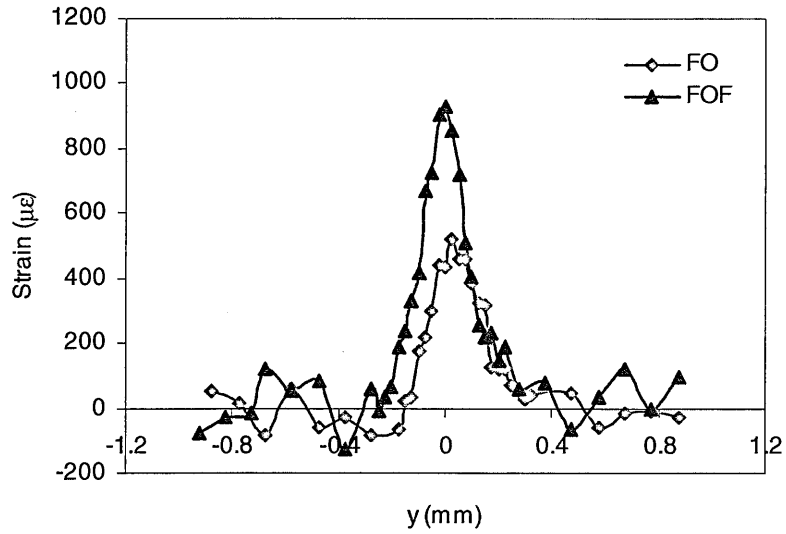

(b) Transverse strain

Figure 4.50: Variation of strains along the y direction (crossing the crack plane) at +0.15 mm ahead of the crack tip in the fatigued-overloaded (FO) and fatigued-overloaded-fatigued (FOF) specimens for applied K=3.6 MPa$\sqrt{m}$.

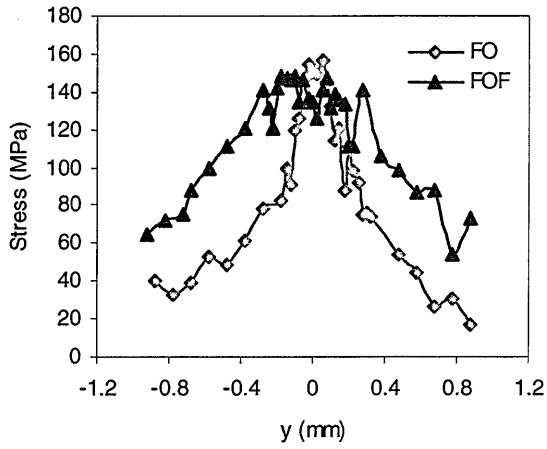

(a) Longitudinal stress

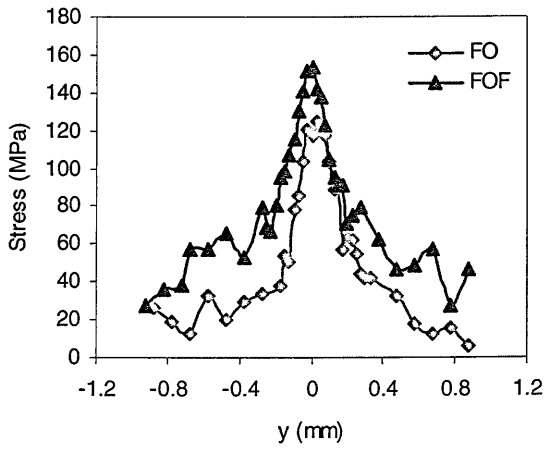

(b) Transverse stress

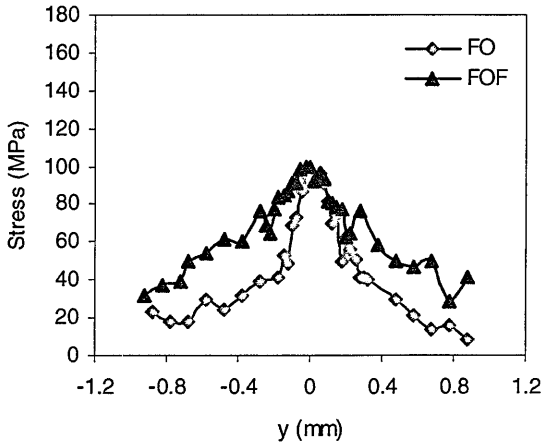

(c) Normal stress

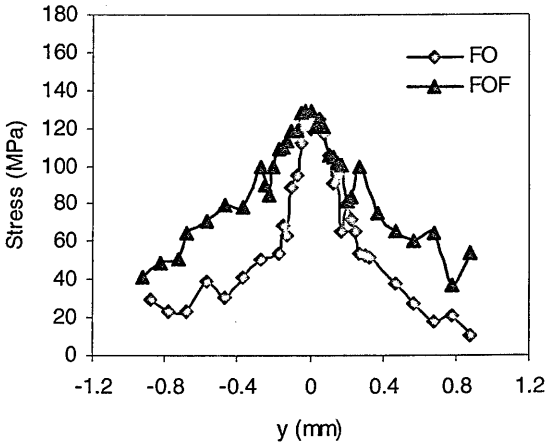

(d) Hydrostatic stress

Figure 4.51: Variation of stresses along the y direction (crossing the crack plane) at +0.15 mm ahead of the crack tip in the fatigued-overloaded (FO) and fatigued-overloaded-fatigued (FOF) specimens for applied K=3.6 MPa$\sqrt{m}$.

Chapter 5 Numerical investigation of the stress fields around fatigue cracks in aluminium alloy 5091

5.1 Introduction

Parallel to the experimental investigations using surface X-ray diffraction and recently using synchrotron X-ray diffraction (discussed in the previous chapter), numerical (finite element) investigations have also been carried out in order to provide insight into the local stress fields around the fatigue cracks. Newman (1976) and Ogura and Ohji (1977) conducted finite element analysis to investigate crack tip stress fields in fatigue in plane stress. Newman considered a centre-cracked panel with elastic perfectly-plastic material under constant amplitude fatigue. He presented longitudinal stress (σ_{yy}) distributions near the crack tip at different stages of unloading. He observed that at the maximum applied stress the near tip (ahead of the crack tip) stresses reach a plateau, and during unloading compressive stresses begin to develop on the crack surfaces as the surfaces contact. Ogura and Ohji studied a double-edge-notched plate with strain-hardening steel. They investigated residual stress distributions around the crack tip for constant and variable amplitude loading including single overloads and block loads to explain plasticity-induced crack closure. They observed that compressive residual stresses develop behind the crack tip as the crack propagates under constant amplitude loading. They also found that the increasing overload level causes the compressive residual stress region in the vicinity of the crack tip to become larger. Sun and Sehitoglu (1992) investigated residual stresses at an ideal crack tip, undergoing reverse deformation in the absence of crack closure, and residual stresses generated due to plasticity-induced crack

closure upon fatigue crack growth, using finite element analysis. They studied centre-cracked tension (CCT) and compact tension geometries in plane stress and plane strain. They observed that residual stresses resulting from reverse deformation are higher in plane strain than in plane stress, whilst residual stresses generated behind the crack tip are more significant in plane stress than in plane strain.

Wang et al. (1999) numerically and experimentally investigated the residual stress effects on fatigue crack growth under constant amplitude loading in a low alloy high strength structural steel of European grade S690QL1. A compact tension shear (CTS) specimen was used in this investigation. Based on their initial finite element calculations, a combined hardening law was applied for further calculations, where residual stress distributions around the crack tip were investigated. They showed that compressive residual stresses or crack closure effects along the crack surfaces behind the fatigue crack tip have hardly any influence on the residual stresses ahead of the crack tip and thus on further fatigue crack growth. Zhao et al. (2004) studied the residual stress and strain fields near a fatigue crack tip in a nickel base super alloy compact tension specimen in plane stress and plane strain, using finite element analysis. They found high compressive residual stresses over a large distance behind the crack tip in plane stress. Hou (2004) presented longitudinal stress (σ_{yy}) distributions on the crack flanks at minimum applied stress for R=0 and −1, from a three-dimensional finite element analysis of fatigue semi-circular surface cracks. They observed significant compressive stresses behind the current crack front both for R=0 and −1 due to the contact between the crack surfaces. Roychowdhury and Dodds (2005) discussed the effect of a single overload on the residual stress distributions along the crack plane of a fatigue crack using a three-dimensional finite

element model. In this investigation the stresses on the crack plane were presented for various thickness positions. The results show that stresses near the centre plane (mid-thickness) behind the crack front are zero, indicating no crack closure in this region. The results also show that other planes experience compressive stresses behind the crack front, where the larger compressive stresses in planes near the outside surface indicate that closure occurs first at the outside surface. Sander and Richard (2005, 2006) performed plane stress finite element analysis to investigate overload and mixed mode I/II effects on the crack tip stress fields in aluminium alloy EN AW-7075-T651 compact tension shear (CTS) specimen. They showed that due to an overload high compressive stresses are generated in the vicinity of the crack tip at K_{min}, and the compressive stresses increase in magnitude and spatial extent with an increasing overload ratio. They also observed that at K_{max} the stress maximum at the crack tip is not influenced by variation of the overload ratio, but the characteristics of the stresses ahead of the crack tip are strongly affected. Their finite element results show compressive longitudinal stresses (σ_{yy}) on the crack flanks regardless of the applied load, although the stresses are expected to be zero when the crack is open. Toribio and Kharin (2006) investigated the influence of the load range, load ratio and overload on the crack tip stress-strain field during cyclic loading by plane strain finite element analysis. They showed that the cyclic loading parameters ΔK and K_{max} largely affect the near tip evaluations of cyclic stresses and plastic strains, which govern the behaviour of a crack.

The experimental and analytical investigations in Chapter 4 were not sufficient themselves for making a conclusion on crack closure phenomenon, as there were no experimental data for K_{min} for the fatigued and fatigued-overloaded-fatigued

specimens. Moreover, the analytical model was based on linear elastic solution, which does not account for plasticity. Besides, the analytical model was developed to provide a benchmark for the experimental results, particularly for K=6.6 MPa$\sqrt{m}$ for the fatigued specimen. Therefore, to provide a clearer understanding of the stress fields around the crack tips, to validate experimental results, and to investigate crack closure for constant amplitude fatigue as well as after a single overload, elastic-plastic finite element analysis was essential. This chapter numerically investigates the stress fields around the fatigue cracks in aluminium alloy 5091 compact tension (CT) specimens. Fatigued (F), fatigued-overloaded (FO) and fatigued-overloaded-fatigued (FOF) specimens have been modelled in plane stress and plane strain and the stress fields have been investigated under different loading conditions. The finite element results are compared to and validated by the synchrotron X-ray diffraction results.

5.2 Finite element modelling

A standard compact tension (CT) specimen with width W=50 mm, thickness B=12.25 mm and initial crack length a_o=25 mm has been considered to simulate the fatigued (F), fatigued-overloaded (FO) and fatigued-overloaded-fatigued (FOF) specimens, using the finite element code ABAQUS. Due to the geometric and load symmetry, one half of the specimen has been modelled. The finite element mesh is shown in Figure 5.1. Four-noded first-order reduced integration elements (CPS4R, CPE4R) have been used in plane stress and plane strain. An element size of 25 μm in the crack plane region has been chosen for comparing the stresses from finite element analysis with the stresses obtained by the synchrotron X-ray measurement

using lateral gauge dimensions of 25×25 μm and a measuring interval of 25 μm. A crack growth of 1 mm has been simulated with an initial crack length of 25 mm to a final crack length of 26 mm. The surfaces along the crack line are defined as contact surfaces using the master-slave algorithm of ABAQUS, where the master surface is a rigid surface introduced along the symmetry axis and the specimen surface is defined as the slave surface. Initially the nodes at and ahead of the crack tip are bonded to the rigid surface. The surfaces behind the crack tip behave like regular contact surfaces as the nodes in that region are unconnected.

The cyclic load has been applied in terms of amplitude as a function of total time to a rigid pin fitted into the hole of the specimen, where the rigid pin and the hole surfaces are treated as contact surfaces. The cracks have been grown under constant amplitude loading with K_{max}=6.6 MPa$\sqrt{m}$ and K_{min}=0.66 MPa$\sqrt{m}$ (i.e., R=0.1). The crack propagation is simulated by debonding the crack tip node at the minimum load of every third cycle by specifying the crack growth with respect to a reference point (initial crack tip) as a function of total time. Debonding of the crack tip node at the minimum load has been chosen following McClung and Sehitoglu (1989), who found no significant influence of the debonding load on the crack opening stress. Each time the crack extends over a distance of 25 μm, corresponding to the size of one element. For simulating a fatigued-overloaded-fatigued crack a 100% (13.2 MPa$\sqrt{m}$) overload was introduced in the amplitude data at a crack length of 25.9 mm. To simulate a fatigued-overloaded crack the overloads (100% and 150%) were applied in separate steps at the end of 1 mm crack growth i.e., at the final crack length of 26 mm.

The material response of aluminium alloy 5091 is modelled to be elastic-plastic by a separate definition of the elastic and the plastic part of the uniaxial true stress-strain curve (Figure 5.2), which allows the incremental plasticity theory implemented in ABAQUS to be employed in the analysis. The uniaxial stress-strain relations for the elastic and the plastic parts can be given as:

$$\sigma = E\varepsilon \quad \text{for } \varepsilon < \frac{\sigma_y}{E} \tag{5.1}$$

$$\sigma = \sigma_y \left(1 + \frac{\varepsilon_p E}{\sigma_y}\right)^n \quad \text{for } \varepsilon \geq \frac{\sigma_y}{E} \tag{5.2}$$

where σ is the true stress, ε is the true strain, E is the modulus of elasticity, σ_y is the uniaxial yield strength, ε_p is the true plastic strain and n is the strain hardening exponent. Equation 5.2 represents the Ramberg-Osgood power hardening law. To generalise the uniaxial material response to multiaxial states of stress the von Mises yield criterion is used with an associated flow rule implemented in ABAQUS. The mechanical properties of the material are: yield strength 448 MPa, ultimate tensile strength 517 MPa, modulus of elasticity 78 GPa, Poisson's ratio 0.345 and bulk fracture toughness 29.7 MPa$\sqrt{m}$ (Schelleng et al., 1985).

The cyclic plasticity was taken into account by using a combined (nonlinear isotropic/ kinematic) hardening model implemented in ABAQUS. To consider expected large deformations in the material near the crack tip, geometric nonlinearity was taken into account.

5.3 Results

Numerical stresses along the x direction in the crack plane for the fatigued, fatigued-overloaded and fatigued-overloaded-fatigued cracks are presented for applied K=6.6 (K_{max}), 3.6 and 0.66 (K_{min}) MPa$\sqrt{m}$ in plane stress and plane strain. Figures 5.3 to 5.5 show a comparison of the longitudinal (σ_{yy}), transverse (σ_{xx}) and hydrostatic (σ_m) stresses separately under three different applied loads for the fatigued crack in plane stress and plane strain. At higher loads (K=6.6 and 3.6 MPa$\sqrt{m}$) higher longitudinal stresses are predicted ahead of the crack tip in plane strain than in plane stress (Figure 5.3a&b). The stress triaxiality in plane strain restricts the crack tip deformation, resulting in higher stresses ahead of the crack tip at higher loads. However, at K_{min} (0.66 MPa$\sqrt{m}$) slightly higher stresses ahead of the crack tip are predicted in plane stress due to residual stresses resulting from tensile plastic deformation at K_{max}. Behind the crack tip longitudinal stresses are expected to be zero along the crack surfaces both in plane stress and plane strain as the crack flanks are traction free. However, compressive longitudinal stresses develop on the crack flank at K_{min} in plane stress indicating the presence of crack closure, which is not apparent in plane strain (Figure 5.3a&b). Like the longitudinal stress, the transverse and hydrostatic stresses also show higher values ahead of the crack tip in plane strain than in plane stress at K=6.6 and 3.6 MPa$\sqrt{m}$ (Figures 5.4&5.5). At K_{min} the levels of both transverse and hydrostatic stresses ahead of the crack tip in plane stress and plane strain appear to be comparable. Behind the crack tip along the crack flank, both the transverse and hydrostatic stresses are compressive in plane stress but tensile in plane strain regardless of the level of applied loading. Besides, the stresses

are relatively constant over the entire distance on the crack flank. The level of compression in plane stress slightly decreases and the level of tension in plane strain slightly increases with increasing applied loading. This can be explained as the effect of tensile T-stress acting in the x direction parallel to the crack flanks (Rice, 1974). This T-stress depends on the applied load and the geometry of the specimen. Figures 5.6 to 5.8 show a comparison of the Cartesian and hydrostatic stresses under three different levels of loading in plane stress and plane strain. The effect of T-stress can be noticed from the comparison of the longitudinal and transverse stresses on the ligament well ahead of the crack tip, where the transverse stress shows slightly higher values than that of the longitudinal stress (Figures 5.6a&b, 5.7a&b and 5.8b). This is because the transverse stress is affected by T-stress, where the longitudinal stress remains unaffected. However, for K_{min} in plane stress the effect of T-stress is not apparent because of the development of longitudinal residual stresses at the crack tip due to plastic deformation at K_{max} (Figure 5.8a).

Figures 5.9 to 5.11 show a comparison of the longitudinal, transverse and hydrostatic stresses separately under three different applied loads for the fatigued-overloaded crack in plane stress and plane strain. For K=6.6 and 3.6 MPa$\sqrt{m}$ the maxima (peaks) of all stresses ahead of the crack tip appear to be higher in plane strain than in plane stress as a result of the higher overload plastic deformation at the crack tip in plane stress. However, this effect is not evident at K_{min} due to the relatively high tensile residual stresses resulting from the overload in plane stress. It can be noticed that due to the higher overload plastic deformation at the crack tip, the tensile peaks of all stresses ahead of the crack tip move forward more in plane stress than in plane strain and all stresses become compressive at the crack tip in

plane stress regardless of the applied load. These compressive stresses at the crack tip increase with decreasing applied load. In plane strain the crack tip stresses appear to be compressive only at K_{min} with smaller magnitudes as a result of relatively small overload plastic deformation. At K_{min} the compressive longitudinal stresses developed on the crack flank of the fatigued crack in plane stress disappear here as a result of 100% overload (Figure 5.9a). Also, no compressive stresses are found on the crack flank in plane strain at K_{min} (Figure 5.9b). Figures 5.12 to 5.14 show a comparison of the Cartesian and hydrostatic stresses under a single load and then for three different levels of loading in plane stress and plane strain. Here the effect of T-stress (slightly higher transverse stresses than longitudinal stresses on the ligament well ahead of the crack tip) is clearly evident at K=6.6 and 3.6 MPa$\sqrt{m}$ in plane strain (Figures 5.12b and 5.13b).

Figures 5.15 to 5.17 show a comparison of the longitudinal, transverse and hydrostatic stresses independently under three different applied loads for the fatigued-overloaded-fatigued crack in plane stress and plane strain. The overload position here is 0.1 mm behind the crack tip position. The stresses ahead of the crack tip show a trend reasonably similar to that for the fatigued-overloaded crack. Figure 5.15 shows that at the overload position on the crack flank behind the crack tip, compressive longitudinal stresses develop at K_{min} and K=3.6 MPa$\sqrt{m}$ in plane stress and at K_{min} in plane strain. The results indicate that a 100% overload results in crack closure both in plane stress and plane strain as the crack passes through the overload position, although the closure level is higher in plane stress. The transverse stresses appear to decrease in magnitude in the overload-affected region under all loads both in plane stress and plane strain (Figure 5.16). The hydrostatic stresses show a trend

similar to the transverse stresses both in plane stress and plane strain (Figure 5.17). Figures 5.18 to 5.20 show a comparison of the Cartesian and hydrostatic stresses under a single load and then for three different applied loads in plane stress and plane strain. At K_{max} the overload position on the crack flank can be identified by the sharp decrease in the transverse stresses in plane stress and plane strain as shown in Figure 5.18a&b. For K=3.6 MPa$\sqrt{m}$ all stresses change sharply to compressive at the overload position in plane stress, however in plane strain the overload position is more identifiable by following the transverse stress profile, which decreases sharply in the overload-affected region on the crack flank (Figure 5.19a&b). At K_{min} all stresses decrease sharply to compressive in the overload-affected region both in plane stress and plane strain as shown in Figure 5.20a&b.

The effect of overloading on the crack tip stresses at K_{max} and K_{min} is shown in Figures 5.21 to 5.24. Two overloads of 100% and 150% have been applied in plane stress and plane strain. In plane stress a 100% overload causes the stresses at the crack tip to become compressive at K_{max} (Figure 5.21). The stresses at the crack tip appear to be more compressive as the overload increases to 150%. It can be noticed that the tensile peaks of the stresses ahead of the crack tip decrease with increasing overload and the positions of the peaks move away from the crack tip. These results are consistent with Allison (1979), who has shown by X-ray diffraction measurement that a single overload decreases the stresses ahead of the crack tip at K_{max}. In plane strain at K_{max} the crack tip stresses also appear to decrease with the application of overload (Figure 5.22). Here the reduction of stresses at the crack tip is relatively small and they do not appear to be compressive even after 150% overloading. At K_{min} in plane stress all stresses at the crack tip are compressive before the application

of an overload (Figure 5.23), and the development of compressive longitudinal stresses along the crack flank indicates the presence of crack closure (Figure 5.23a). The crack tip stresses become more compressive and the compressive stress regions increase in size with the application of overloads, but the crack closure disappears with overloading. In plane strain the crack tip stresses are tensile at K_{min} before the application of the overload (Figure 5.24). Upon the application of 100% overload the stresses at the tip become compressive. The stresses appear to be more compressive as the overload increases to 150%. However, the magnitudes of the compressive stresses and the sizes of the compressive stress zones are smaller in plane strain than in plane stress.

Figures 5.25 to 5.30 show the comparison of the stresses for the fatigued (F), fatigued-overloaded (FO) and fatigued-overloaded-fatigued (FOF) cracks at different loads in plane stress and plane strain. Here the overload levels are 100% for the fatigued-overloaded and fatigued-overloaded-fatigued cracks. Figures 5.25 and 5.26 show the stress distributions under K_{max} in plane stress and plane strain respectively. As discussed earlier, the overload reduces all the stresses (denoted by FO) ahead of the crack tip from the baseline levels (denoted by F) both in plane stress and plane strain. In plane stress all stresses at the crack tip become compressive as a result of the overload (Figure 5.25). However, with a 0.1 mm crack growth from the overload point the stresses (denoted by FOF) appear to be gradually restoring their baseline levels at the crack tip as the crack grows through the overload-affected zone. In plane strain the stresses have almost restored their baseline levels at the crack tip in 0.1 mm crack growth (Figure 5.26). This is because the overloaded-affected zone is smaller in plane strain. Using finite element analysis in plane stress for aluminium

alloy 7075-T651 CT specimen, Sander and Richard (2005) observed a similar trend as the crack extends from the overload point. For the fatigued-overloaded-fatigued crack in plane stress the stresses appear to be disturbed slightly in the overload-affected zone behind the crack tip (Figure 5.25). In plane strain the effect of the overload behind the crack tip on the crack flank is more prominent in the transverse stress profile for the fatigued-overloaded-fatigued crack (Figure 5.26). The overload produces high tensile stresses at the crack tip as a result of which the crack tip deforms plastically. Upon the load reduction during the fatigue cycle the material in the overload-affected zone is compressed resulting in a sharp decrement of the stresses and the crack propagates leaving residual stresses on the crack flanks.

Figures 5.27 and 5.28 show the stress distributions for the three different cracks under K=3.6 MPa$\sqrt{m}$ in plane stress and plane strain respectively. Under this load in plane stress the stresses at the crack tip still remain tensile for the fatigued crack (Figure 5.27). However, for the fatigued-overloaded crack the compressive stresses at the crack tip largely increase with load reduction from K_{max}. With further crack growth (fatigued-overloaded-fatigued crack) the compressive stresses in the over-load affected region on the crack flank appear to decrease but do not disappear. The presence of the compressive longitudinal stresses on the crack flank indicates a partial crack closure at K=3.6 MPa$\sqrt{m}$ in plane stress. In plane strain due to an overload, a reduction of the stresses at and ahead of the crack tip from the baseline level is also apparent, although the crack tip stresses remain tensile (Figure 5.28). With a further 0.1 mm crack growth from the overload point the stresses have almost recovered their baseline levels at the crack tip, but in the overload-affected region the transverse and hydrostatic stresses become compressive (Figure 5.28).

Figures 5.29 and 5.30 show the stress distributions for the three different cracks under K_{min} in plane stress and plane strain respectively. Here the stresses at the crack tip in plane stress appear to be compressive for the fatigued crack (Figure 5.29). The overload causes the compressive stresses at the tip to become even higher than that for K=3.6 MPa$\sqrt{m}$. With 0.1 mm crack extension from the overload point, the crack leaves the compressive stresses on the crack flank with almost no change in magnitude. The results indicate that level of crack closure observed at the overload region at K=3.6 MPa$\sqrt{m}$ increases with the decrease of load to K_{min}. These results are consistent with Allison (1979) and Holloway (1979), who found by X-ray diffraction measurements that the residual stress profiles caused by the overloads were essentially undisturbed by crack extension. In plane strain the stresses at the crack tip in fatigue remain tensile at K_{min} (Figure 5.30). This is due to the lower plasticity incurred at K_{max} in plane strain. An overload causes compressive stresses at the crack tip. With 0.1 mm crack extension from the overload point, the crack leaves the compressive stresses on the crack flank. Here the compressive longitudinal stresses on the crack flank indicate the presence of crack closure occurring in plane strain at K_{min} as the crack extends from the overload point.

Figures 5.31 to 5.37 show a comparison of the stresses from the finite element analysis with the results from the synchrotron X-ray diffraction measurements. The stress profiles are presented along the x direction in the crack plane. The experimental stresses have been calculated assuming plane strain conditions, whilst the finite element results are presented both for plane stress and plane strain. Figure 5.31 shows the stress profiles for the fatigued specimen at applied K=6.6 MPa$\sqrt{m}$ (K_{max}). The experimental stresses show generally good agreement with the finite

element results. It can be noticed that the finite element results in plane strain are in better agreement with the experimental results than in plane stress as expected. However, the longitudinal stresses on the crack flank behind the crack tip from the experiment appear to be compressive, which are expected to be zero as the crack is open at K_{max} (Figure 5.31a). Tsakalakos et al. (2006) also found compressive longitudinal residual stresses on the crack flank by the energy dispersive X-ray diffraction measurement in a CT steel specimen assuming plane strain conditions. They pointed out two possible causes of the observed compressive longitudinal stresses. Firstly, in energy dispersive X-ray diffraction measurement the gauge volumes are different for measuring the two strain components (ε_{xx}, ε_{yy}) and secondly, precisely locating the same point of measurement for the two components is very difficult. Elastic stress-strain relations show that the longitudinal stress component cannot be negative unless one or both of the strain components (ε_{xx}, ε_{yy}) is negative in plane strain. For a stationary crack in plane strain, the longitudinal strain behind the crack tip sharply decreases to compressive along the y direction near the crack plane starting at zero in the crack plane. Therefore, the compressive longitudinal stresses on the crack flank could possibly be due to the two different gauge volumes (in terms of diffraction gauge volume geometry and positioning) for measuring the two strain components ε_{xx} and ε_{yy} in a region with a high strain gradient along the y direction from the crack plane.

Figures 5.32 to 5.34 show the comparison of the stresses for the fatigued-overloaded specimen for applied stress intensity factors of 16.5 (K_{ol}), 3.6 and 0.66 MPa$\sqrt{m}$. The experimental results show good agreement with the plane strain finite element results. The effect of the overload is apparent in both the experimental and finite

element results under applied K=3.6 and 0.66 MPa√m, where compressive stresses develop at the crack tip (Figures 5.33 & 5.34).

Figures 5.35 to 5.37 show the comparison of the stresses for the fatigued-overloaded-fatigued specimen for applied stress intensity factors of 6.6 (K_{max}), 3.6 and 2.6 MPa√m. Here a 100% (13.2 MPa√m) overload was applied at a position 0.1 mm behind the current crack tip. As for the fatigued and fatigued-overloaded specimens the experimental results show generally good agreement with the plane strain finite element results. However, in the experimental stresses the effect of the overload on the crack flank behind the crack tip is not evident. One possible reason of this may be that as the overload plastic zone is very small (46 μm in this case) it might have been wiped out during the additional 0.1 mm of crack growth. Another possible cause may have been associated with the averaging in the gauge volume during strain measurement in the small overload-affected region.

5.4 Discussion

The stress fields around the fatigued, fatigued-overloaded and fatigued-overloaded-fatigued crack tips in aluminium alloy 5091 compact tension specimens have been presented in detail in plane stress and plane strain using finite element analysis. Moreover, the finite element results have been compared with the experimental results from the synchrotron X-ray diffraction measurements to validate the results. At K_{max} all the stresses show their highest magnitudes at the crack tip for the fatigued crack both in plane stress and plane strain, although the stresses are higher in plane strain than in plane stress. A 100% overload reduces the crack tip stresses

significantly both in plane stress and plane strain at K_{max}, and in plane stress the stresses appear to be compressive at the crack tip. With a further 0.1 mm crack growth from the overload point the stresses appear to restore their baseline levels at K_{max}. The distance taken by the crack for restoring the baseline level is shorter in plane strain as in this case the overload plastic zone is smaller. For the fatigued crack, behind the crack tip on the crack flanks the longitudinal stresses appear to be zero both in plane stress and plane strain at K_{max}. The transverse, normal (in plane strain only) and hydrostatic stresses at K_{max} appear to be compressive in plane stress and tensile in plane strain on the crack flanks. These results appear to be different from the linear elastic solution for a stationary crack where all stresses are zero on the crack flanks (Westergaard, 1939).

At K_{min} for the fatigued crack, the crack tip stresses are tensile in plane strain, but compressive in plane stress. Compressive longitudinal stresses develop on the crack flank behind the crack tip in plane stress but not in plane strain. The development of the compressive longitudinal stresses on the crack flank indicates the presence of crack closure at K_{min} in plane stress. Zhao et al. (2004) also observed crack closure in plane stress but not in plane strain in compact tension geometry, using finite element analysis. In their investigation, the lack of crack closure in plane strain was found to be independent of the material studied. With the application of a 100% overload the compressive stresses ahead of the crack tip in plane stress increase in magnitude and spatial extent, but the compressive longitudinal stresses behind the crack tip on the crack flank disappear. These results indicate that although an overload increases the compressive residual stresses at the crack tip it causes the near field closure to decrease as a result of tensile deformation at the crack tip.

These results are consistent with Bichler and Pippan (1999), who argued that the application of an overload results in crack tip blunting, which causes a decrease in near field closure. Therefore, crack growth acceleration occurs immediately following a single overload up to about 20-50 cycles and then the growth rate decreases below the steady state level as the crack passes through the overload-affected zone. At K_{min} in plane strain a 100% overload causes the crack tip stresses to become compressive from their tensile values before overloading, although the level of compression is much lower here than in plane stress. The lower compressive stresses at the crack tip are due to the smaller overload plastic zone developed in plane strain.

With increasing overload the crack tip stresses decrease both at K_{max} and K_{min} both in plane stress and plane strain. In plane stress, with 150% overload the stresses become more compressive and extend over a larger area both at K_{max} and K_{min}. In plane strain, with 150% overload the crack tip stresses decrease but remain tensile at K_{max}, whilst at K_{min} the compressive stresses at the crack tip resulting from 100% overload become more compressive. However, no compressive longitudinal stresses develop on the crack flank behind the crack tip at K_{min} in either plane stress and plane strain, which indicates the absence of crack closure.

With a 0.1 mm crack extension from the overload point, compressive longitudinal stresses develop in the overload-affected region behind the crack tip on the crack flank at K=3.6 and 0.66 MPa$\sqrt{m}$ in plane stress and at K=0.66 MPa$\sqrt{m}$ in plane strain. The results indicate that crack closure occurs both in plane stress and plane strain as the crack grows through the overload-affected zone following a 100%

overload, although the level of closure is much higher in plane stress than in plane strain.

Schijve (1961) postulated and Ramos et al. (2003) experimentally showed that the crack growth retardation as a result of overloading occurs due to the generation of compressive residual stresses in the vicinity of the crack tip. The present work shows that at K_{min} compressive longitudinal stresses exist both on the crack flank and at the crack tip under constant amplitude fatigue in plane stress but not in plane strain. An overload causes the crack tip to be under more compression at K_{min} in plane stress, but removes the compressive longitudinal stresses from the crack flank. In plane strain the crack tip also appears to be under compression at K_{min} as a result of an overload, where the tip was under tension before the application of overload. As the crack grows through the overload-affected zone, compressive longitudinal stresses develop on the crack flank both in plane stress and plane strain at K_{min}. McEvily and Ishihara (2001) concluded that the compressive residual stresses ahead of the crack tip due to an overload, and the crack closure occurring behind the crack tip as the crack extends through the overload plastic zone, are intimately related, and contribute to the crack retardation. The present work seems to support the argument of McEvily and Ishihara (2001) and concludes that this argument is also applicable for the crack under constant amplitude fatigue.

Finally, the finite element results in plane strain show good overall agreement with the synchrotron X-ray diffraction results. However, the slight overall variations between the experimental and finite element results can be addressed by the fact that the gauge volumes for measuring two strain components ε_{xx} and ε_{yy} in EDXRD

measurement are different because of the diffraction gauge volume geometry and positioning, and secondly in finite element analysis straight fatigue cracks have been modelled, which is just an approximation of the real cracks that may not be straight inside the specimens.

5.5 Conclusion

This chapter investigates the stress fields around fatigue cracks, with and without the application of overloading, in aluminium alloy 5091 compact tension specimens in plane stress and plane strain using finite element analysis. The finite element results are compared to and validated by the synchrotron X-ray diffraction results. The results show that compressive longitudinal stresses appear to develop at the crack tip and on the crack flank at K_{min} in plane stress but not in plane strain under constant amplitude fatigue. An overload reduces the crack tip stresses subsequently from the constant amplitude values both at K_{max} and K_{min} both in plane stress and plane strain, and the compressive longitudinal stresses on the crack flank at K_{min} in plane stress disappear, although the crack tip appears to be under more compression. As a result of overloading compressive longitudinal stresses also develop at the crack tip at K_{min} in plane strain. With further crack growth following an overload, compressive longitudinal stresses develop on the crack flank in the overload-affected zone behind the crack tip at K_{min} both in plane stress and plane strain. The results suggest that crack closure occurs in plane stress but not in plane strain under constant amplitude fatigue in the compact tension geometry. In finite element analysis, Zhao et al. (2004) also observed crack closure in plane stress but not in plane strain using compact tension geometry. With the application of an overload the crack closure

disappears in plane stress. With further crack growth after an overload crack closure occurs both in plane stress and plane strain. Compressive residual stresses in the vicinity of the crack tip and the crack closure behind the crack tip are related to each other, and contribute to crack retardation.

Finally, it can be concluded that the finite element results show good overall agreement with the experimental results from the synchrotron X-ray diffraction measurements. Therefore, this investigation appears to justify the applicability of the synchrotron X-ray diffraction technique for the local stress measurements in the interior of the engineering components with high stress gradient.

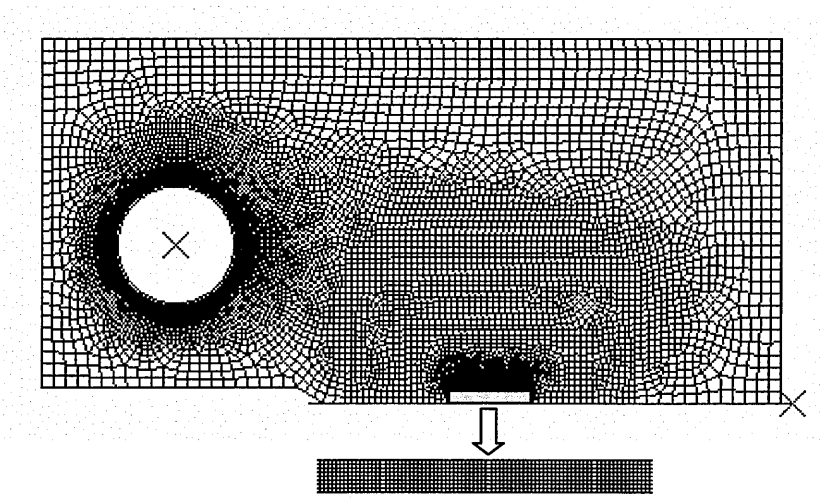

Figure 5.1: Finite element mesh used in fatigue crack growth modelling.

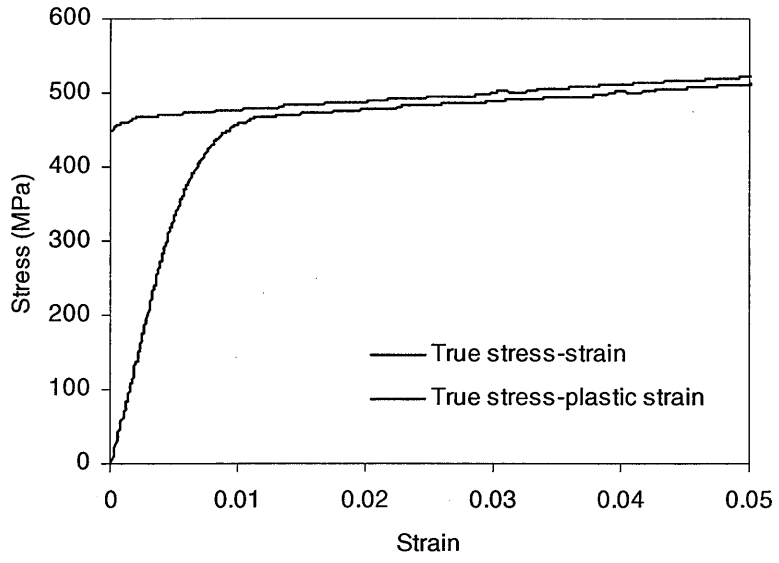

Figure 5.2: Uniaxial true stress-strain curve and the plastic part of the curve for aluminium alloy 5091.

(a)

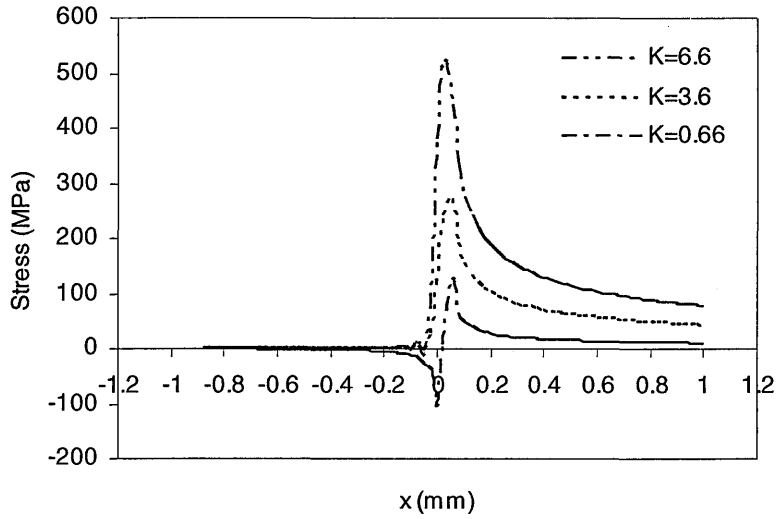

(b)

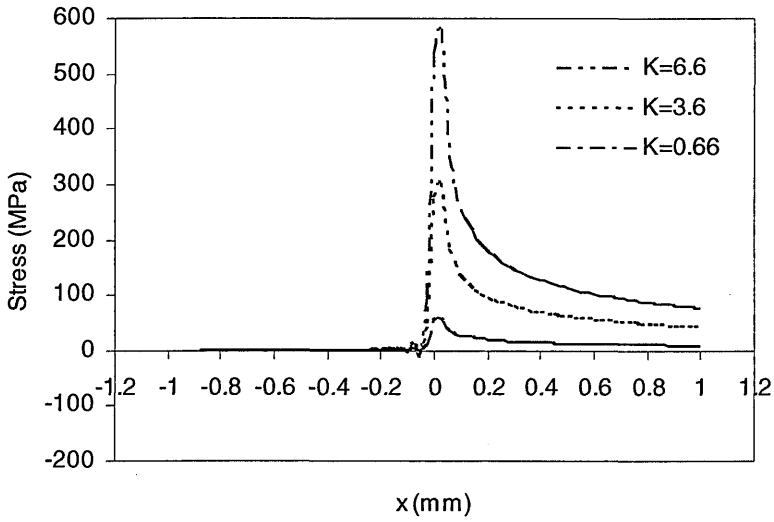

Figure 5.3: Variation of longitudinal stresses along the x direction in the crack plane (y=0) for the fatigued crack for different applied K (MPa$\sqrt{m}$): (a) plane stress, (b) plane strain.

(a)

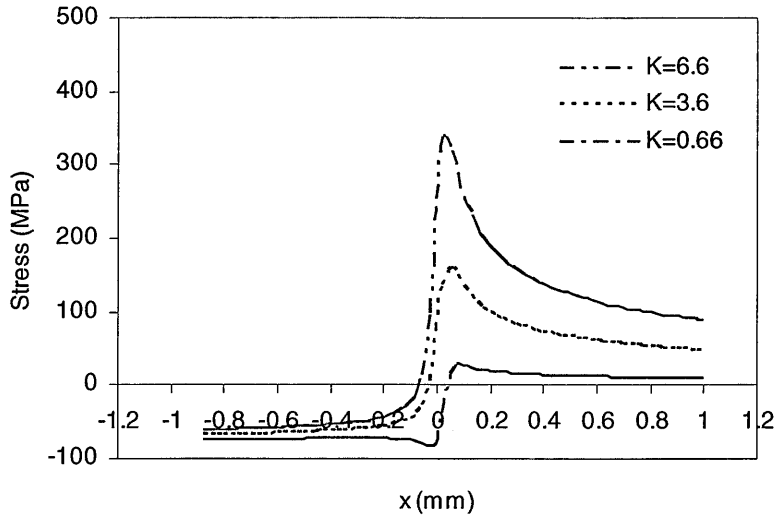

(b)

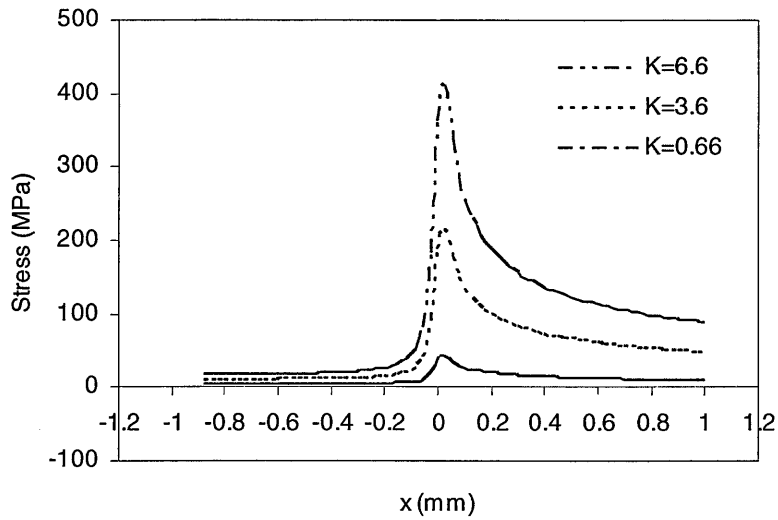

Figure 5.4: Variation of transverse stresses along the x direction in the crack plane (y=0) for the fatigued crack for different applied K (MPa$\sqrt{m}$): (a) plane stress, (b) plane strain.

(a)

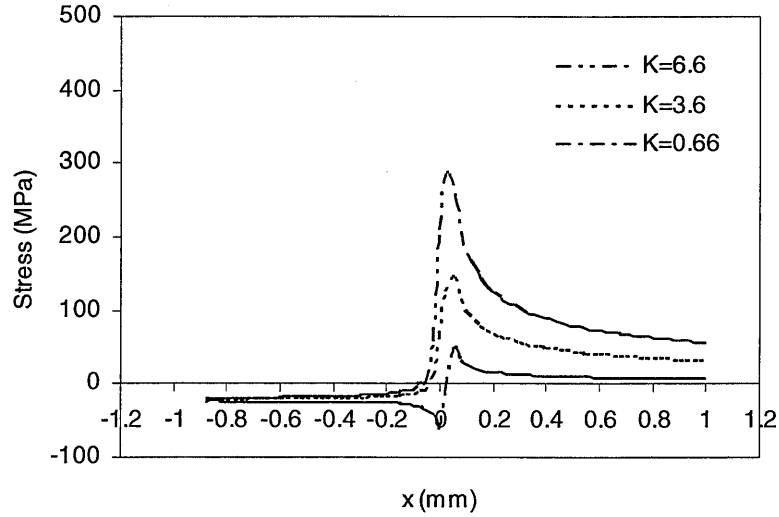

(b)

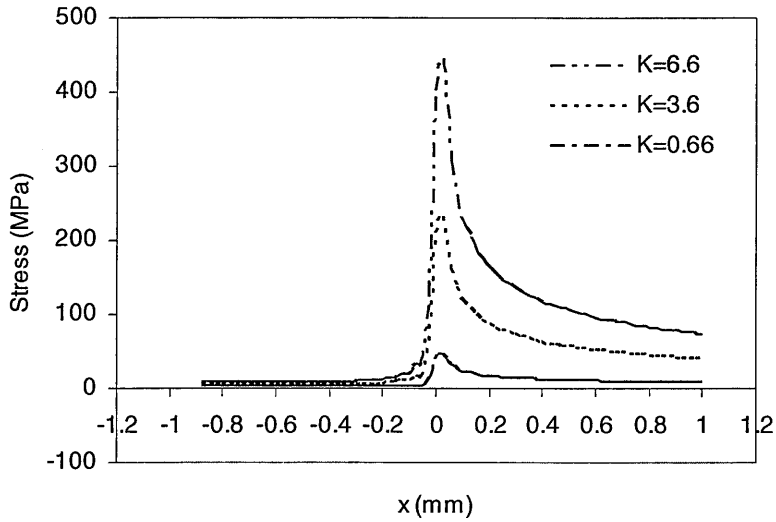

Figure 5.5: Variation of hydrostatic stresses along the x direction in the crack plane (y=0) for the fatigued crack for different applied K (MPa$\sqrt{m}$): (a) plane stress, (b) plane strain.

(a)

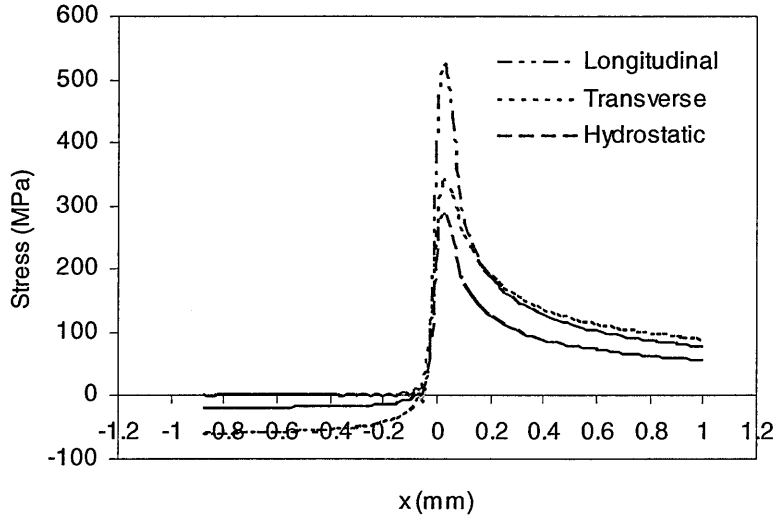

(b)

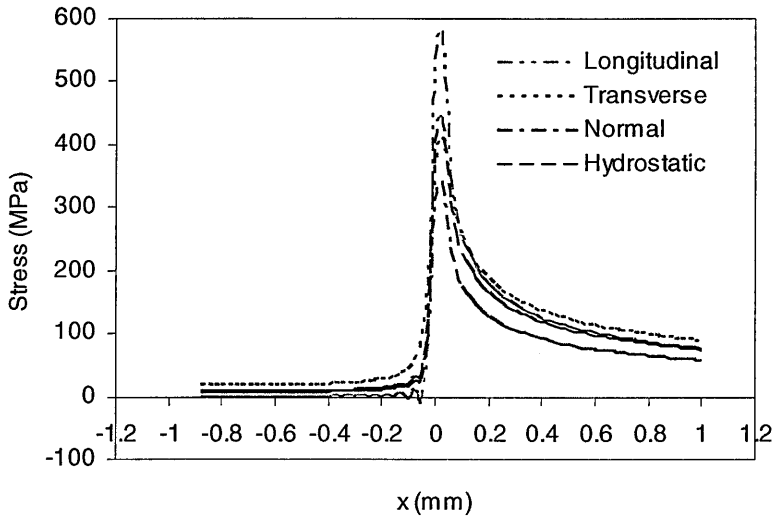

Figure 5.6: Variation of stresses along the x direction in the crack plane (y=0) for the fatigued crack for applied K=6.6 MPa$\sqrt{m}$: (a) plane stress, (b) plane strain.

(a)

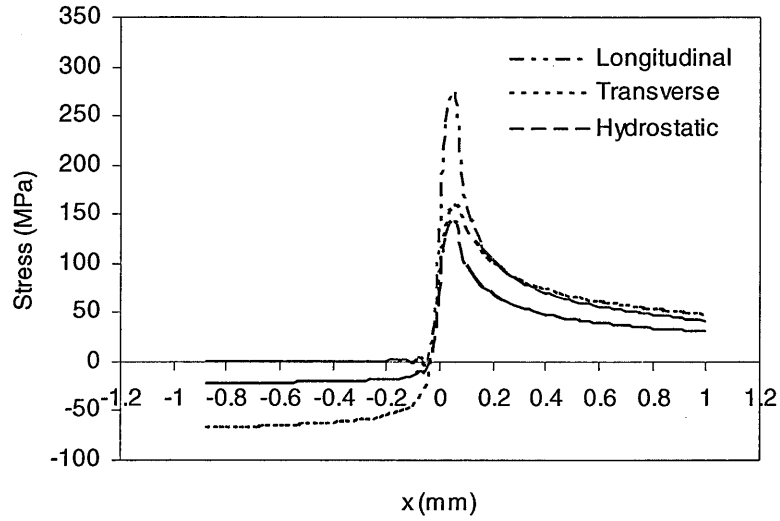

(b)

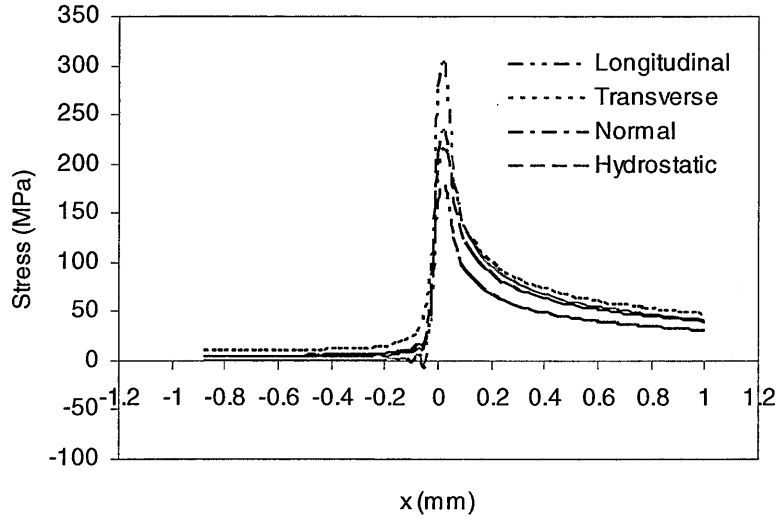

Figure 5.7: Variation of stresses along the x direction in the crack plane (y=0) for the fatigued crack for applied K=3.6 MPa$\sqrt{m}$: (a) plane stress, (b) plane strain.

(a)

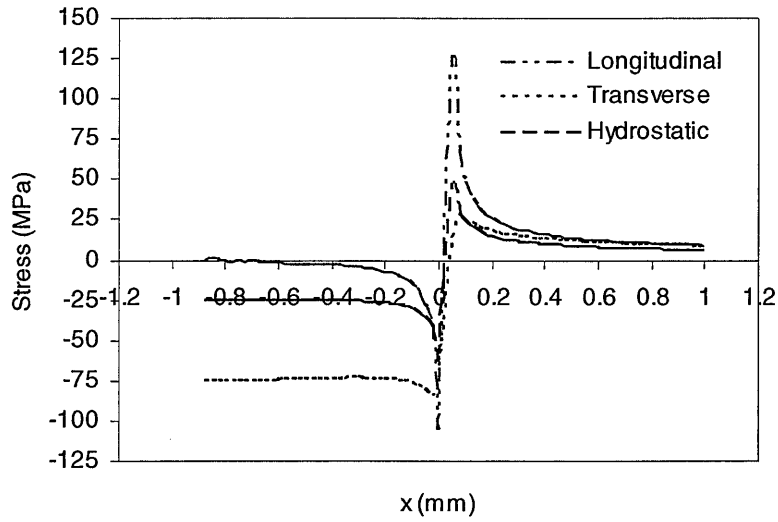

(b)

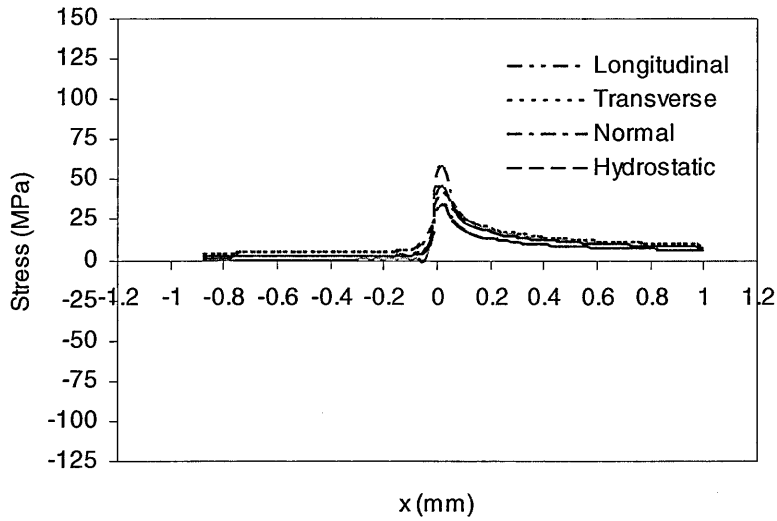

Figure 5.8: Variation of stresses along the x direction in the crack plane (y=0) for the fatigued crack for applied K=0.66 MPa$\sqrt{m}$: (a) plane stress, (b) plane strain.

(a)

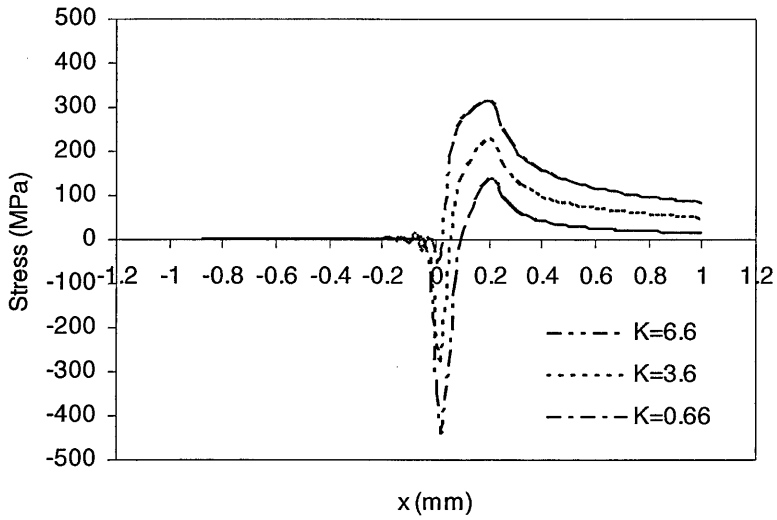

(b)

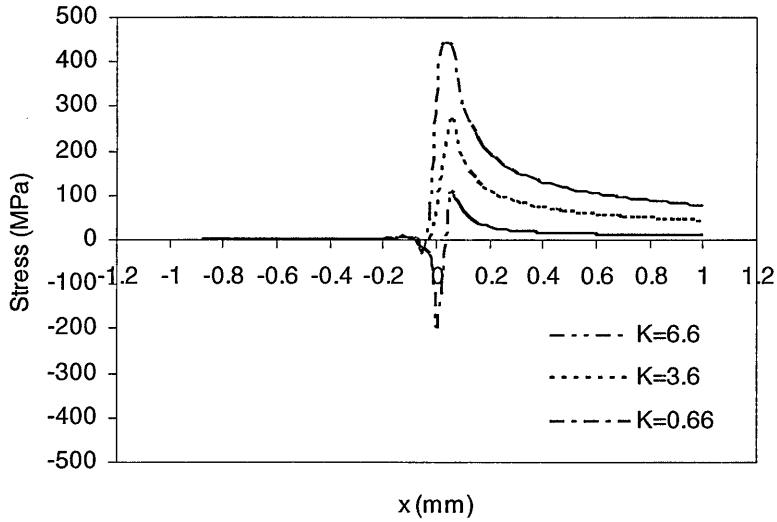

Figure 5.9: Variation of longitudinal stresses along the x direction in the crack plane (y=0) for the fatigued-overloaded crack for different applied K (MPa$\sqrt{m}$): (a) plane stress, (b) plane strain.

(a)

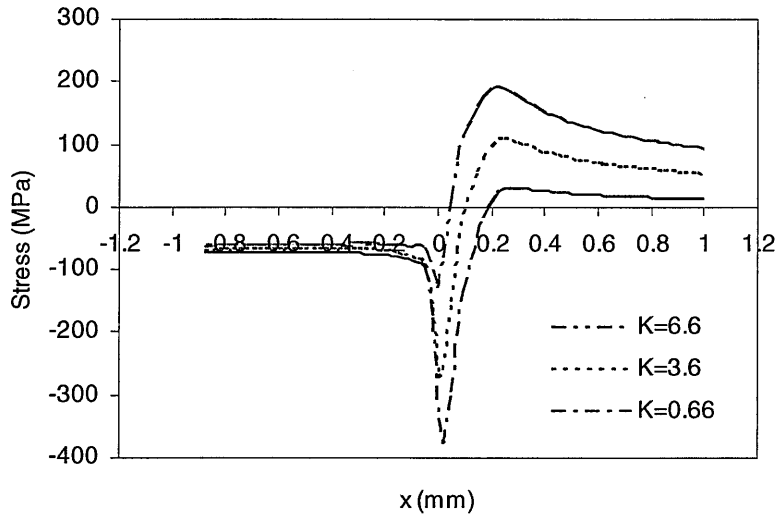

(b)

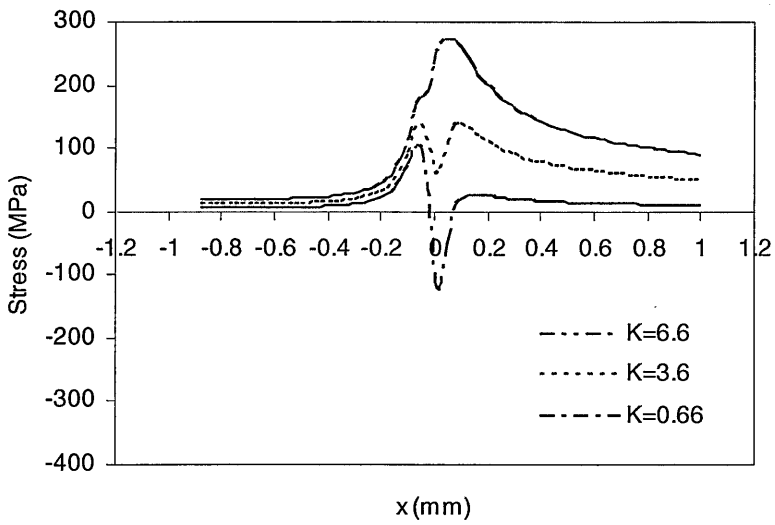

Figure 5.10: Variation of transverse stresses along the x direction in the crack plane (y=0) for the fatigued-overloaded crack for different applied K (MPa$\sqrt{m}$): (a) plane stress, (b) plane strain.

(a)

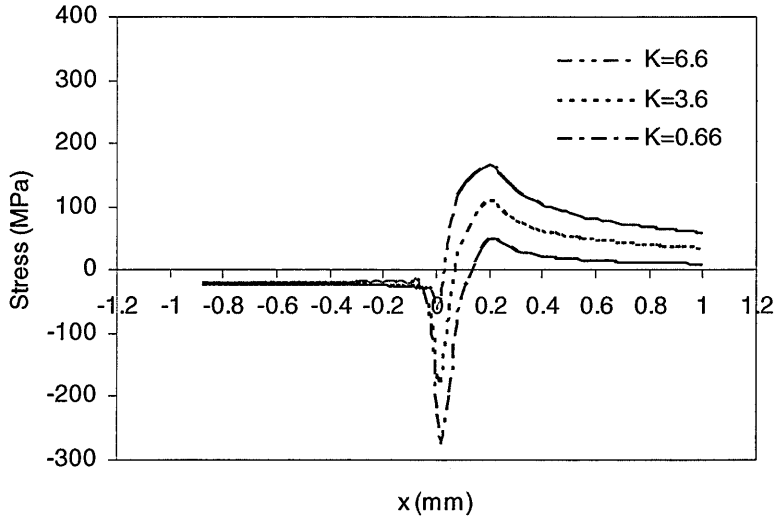

(b)

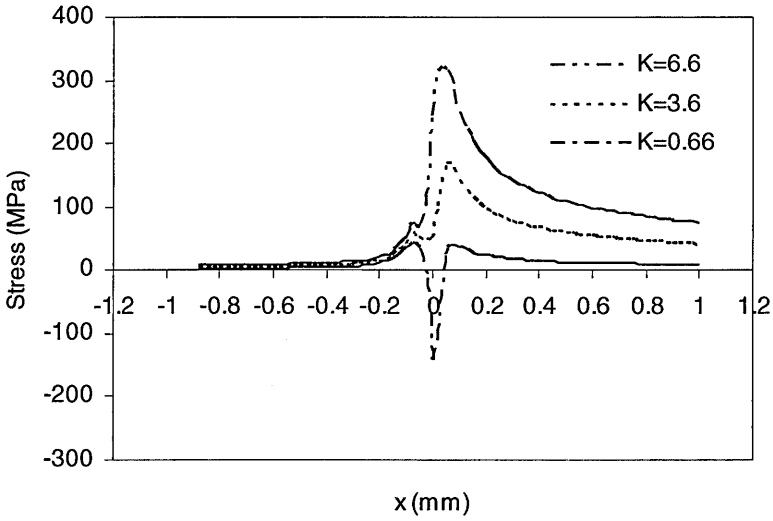

Figure 5.11: Variation of hydrostatic stresses along the x direction in the crack plane (y=0) for the fatigued-overloaded crack for different applied K (MPa$\sqrt{m}$): (a) plane stress, (b) plane strain.

(a)

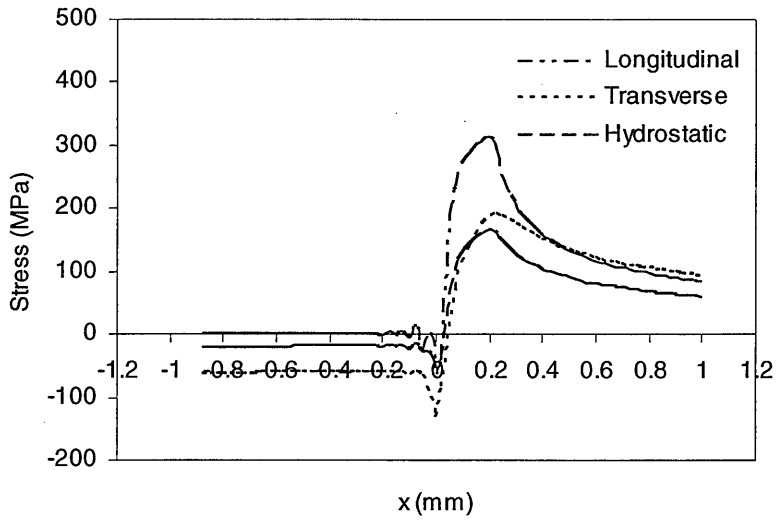

(b)

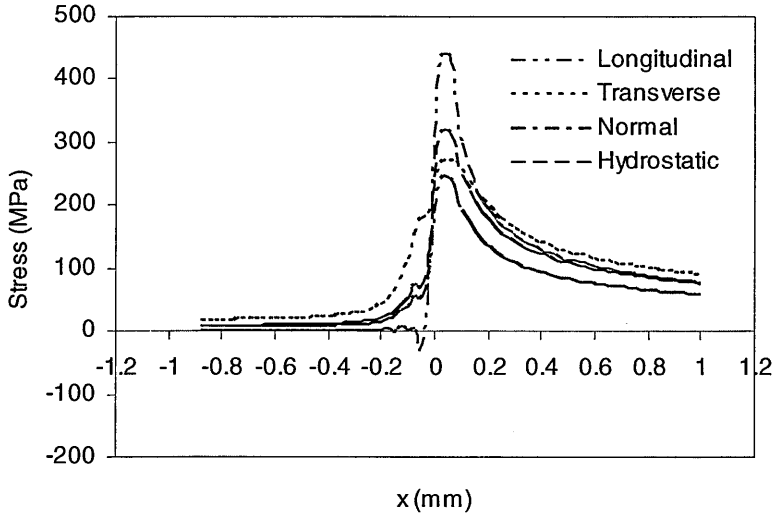

Figure 5.12: Variation of stresses along the x direction in the crack plane (y=0) for the fatigued-overloaded crack for applied K=6.6 MPa$\sqrt{m}$: (a) plane stress, (b) plane strain.

(a)

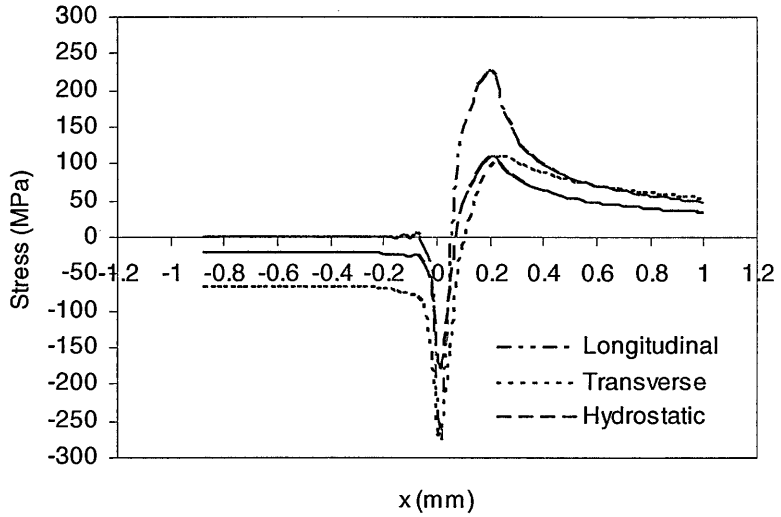

(b)

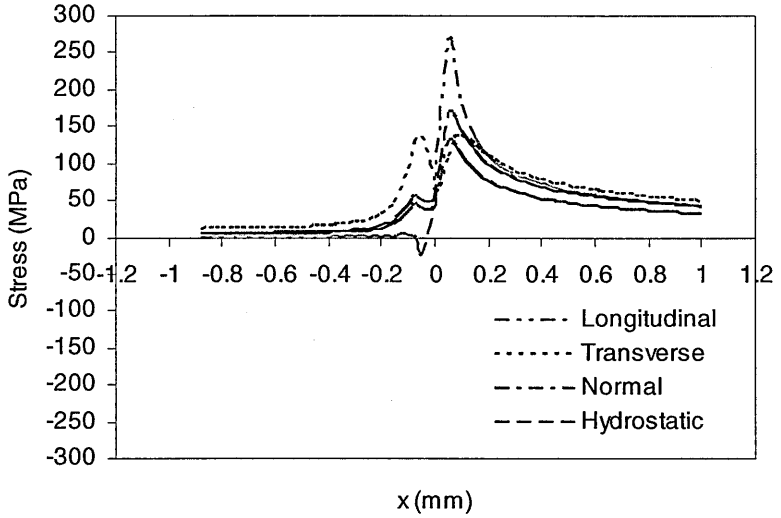

Figure 5.13: Variation of stresses along the x direction in the crack plane (y=0) for the fatigued-overloaded crack for applied K=3.6 MPa$\sqrt{m}$: (a) plane stress, (b) plane strain.

(a)

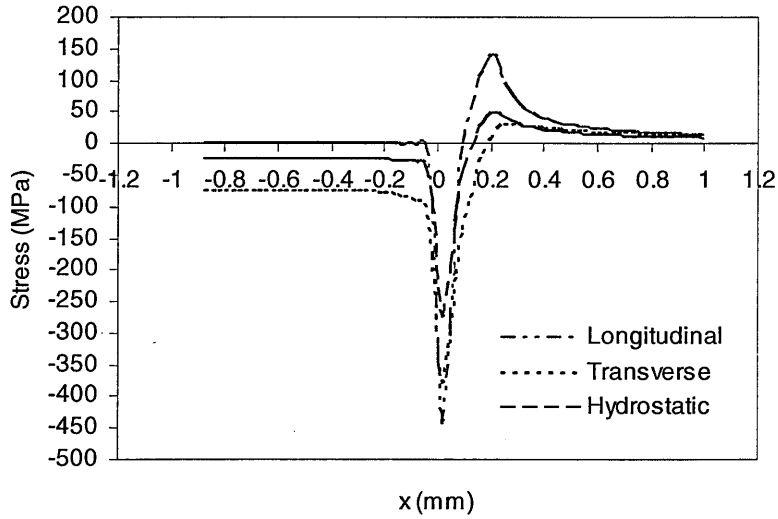

(b)

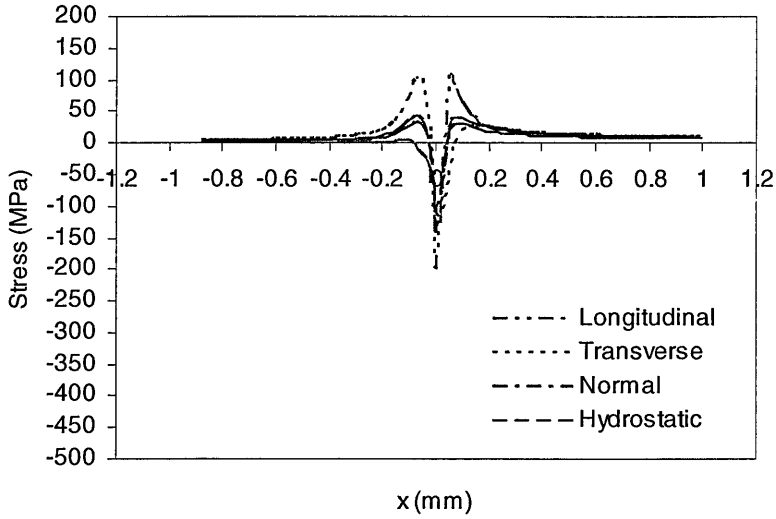

Figure 5.14: Variation of stresses along the x direction in the crack plane (y=0) for the fatigued-overloaded crack for applied K=0.66 MPa$\sqrt{m}$: (a) plane stress, (b) plane strain.

(a)

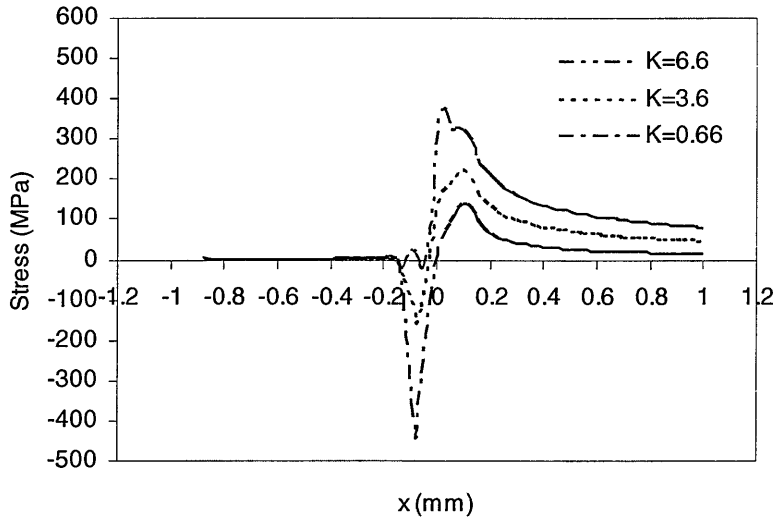

(b)

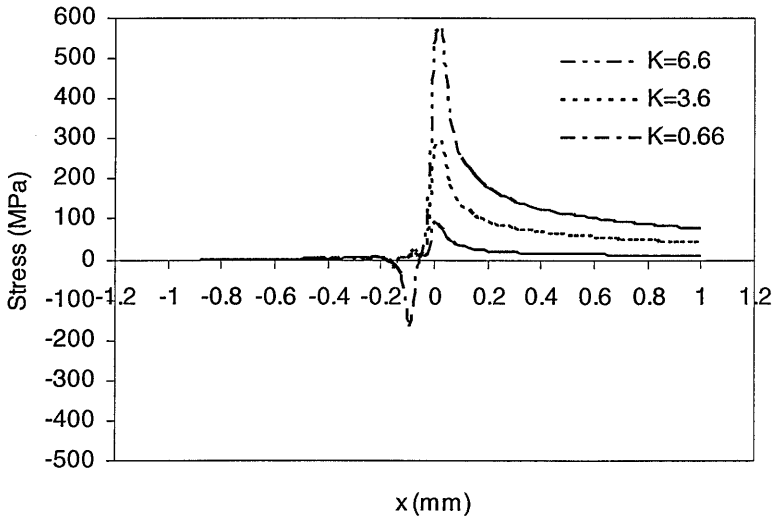

Figure 5.15: Variation of longitudinal stresses along the x direction in the crack plane (y=0) for the fatigued-overloaded-fatigued crack for different applied K (MPa$\sqrt{m}$): (a) plane stress, (b) plane strain.

(a)

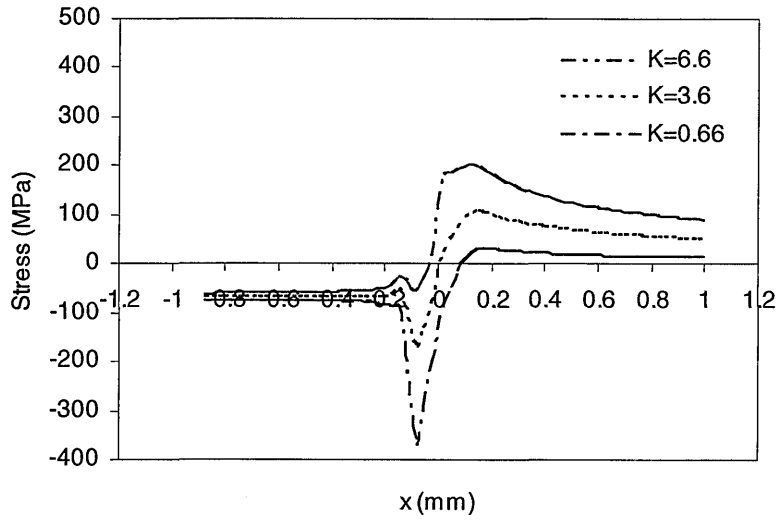

(b)

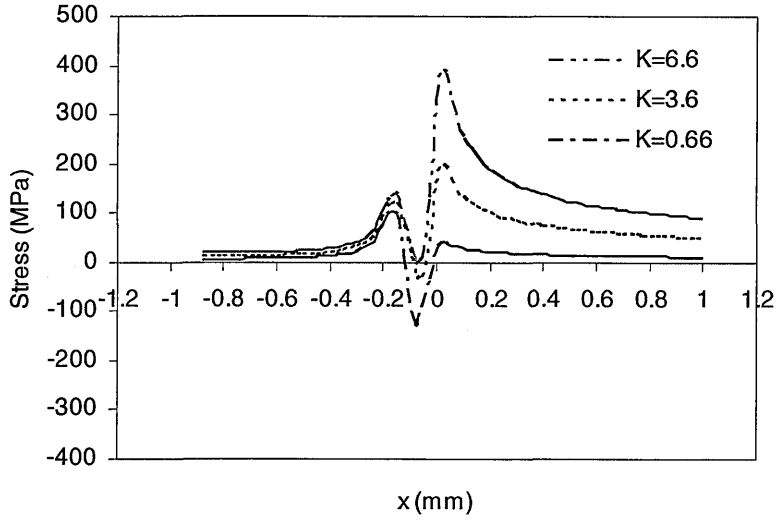

Figure 5.16: Variation of transverse stresses along the x direction in the crack plane (y=0) for the fatigued-overloaded-fatigued crack for different applied K (MPa$\sqrt{m}$): (a) plane stress, (b) plane strain.

(a)

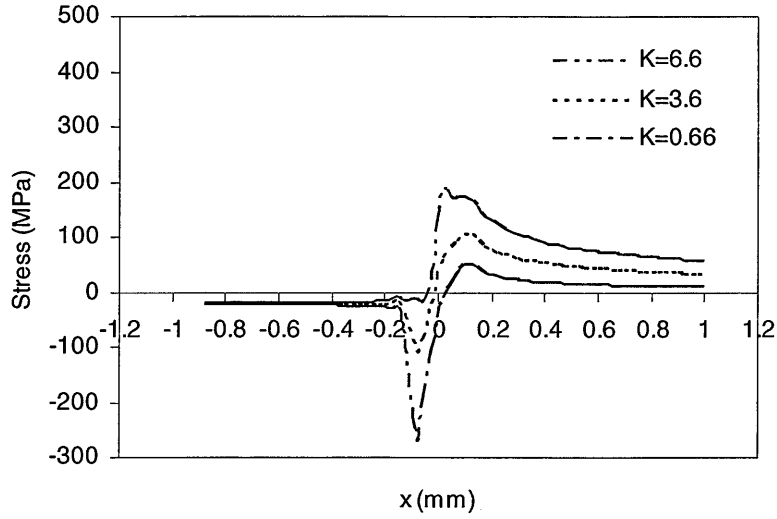

(b)

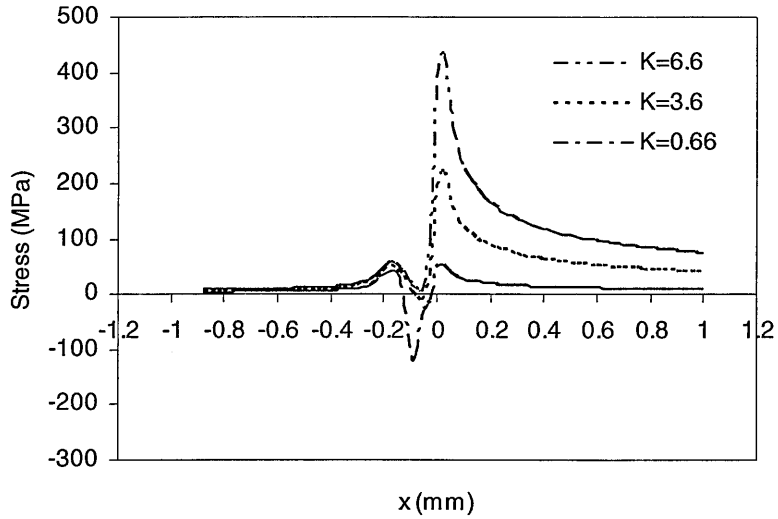

Figure 5.17: Variation of hydrostatic stresses along the x direction in the crack plane (y=0) for the fatigued-overloaded-fatigued crack for different applied K (MPa$\sqrt{m}$): (a) plane stress, (b) plane strain.

(a)

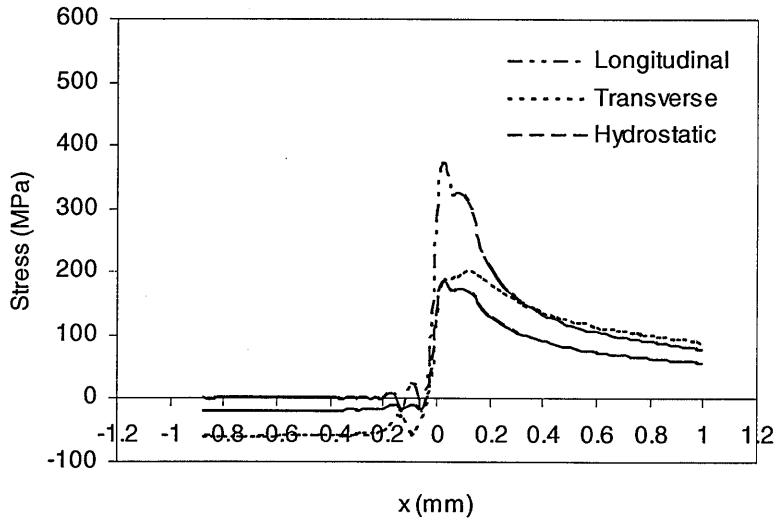

(b)

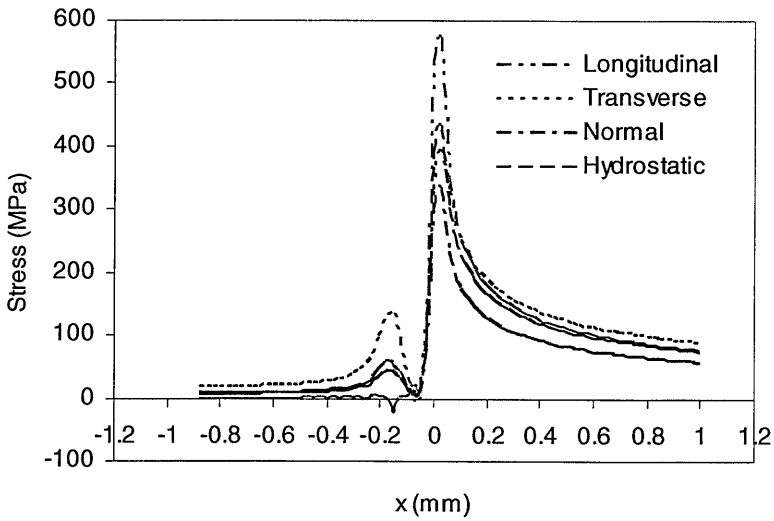

Figure 5.18: Variation of stresses along the x direction in the crack plane (y=0) for the fatigued-overloaded-fatigued crack for applied K=6.6 MPa$\sqrt{m}$: (a) plane stress, (b) plane strain.

(a)

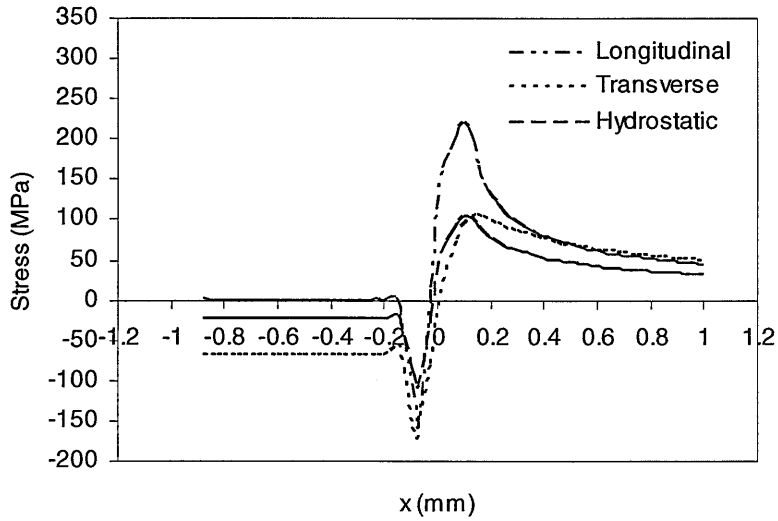

(b)

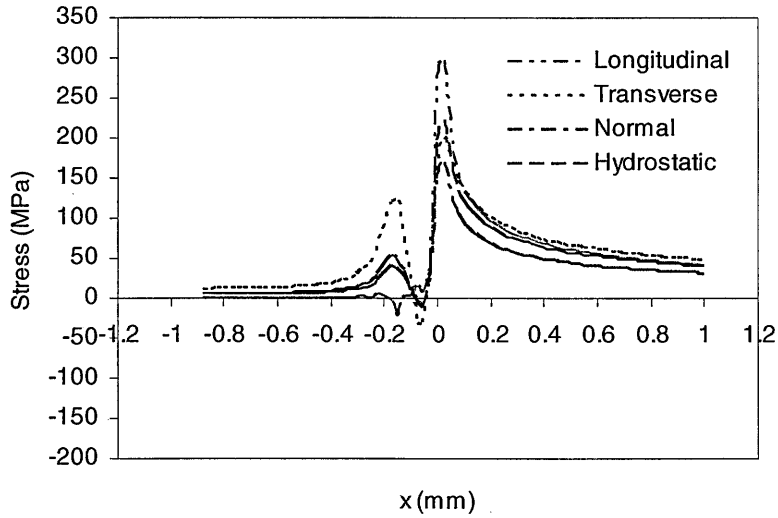

Figure 5.19: Variation of stresses along the x direction in the crack plane (y=0) for the fatigued-overloaded-fatigued crack for applied K=3.6 MPa$\sqrt{m}$: (a) plane stress, (b) plane strain.

(a)

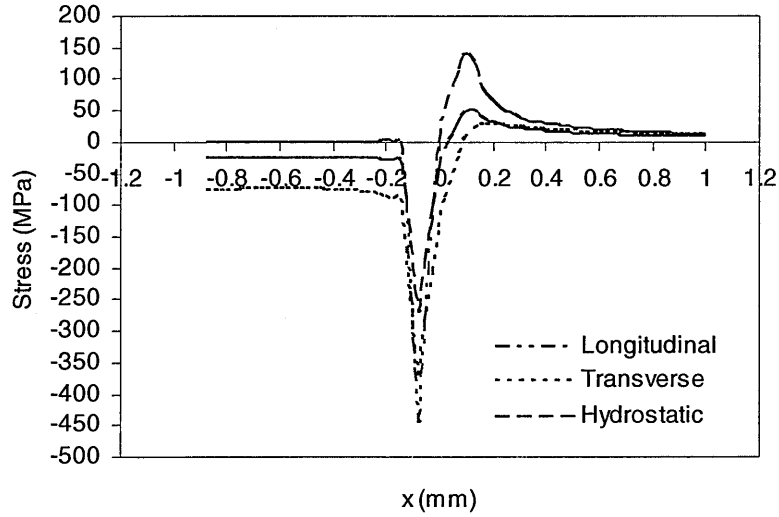

(b)

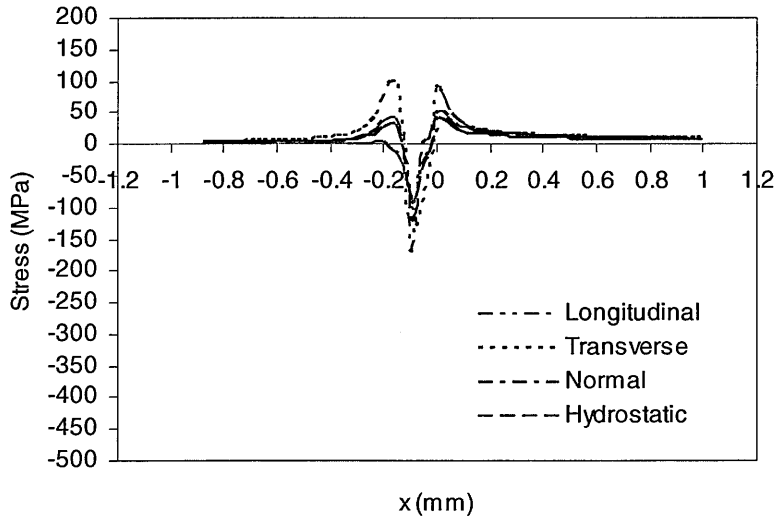

Figure 5.20: Variation of stresses along the x direction in the crack plane (y=0) for the fatigued-overloaded-fatigued crack for applied K=0.66 MPa$\sqrt{m}$: (a) plane stress, (b) plane strain.

(a)

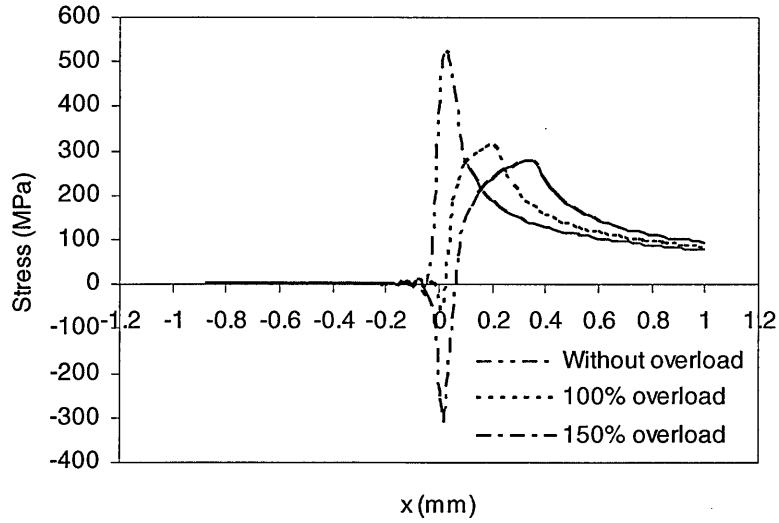

(b)

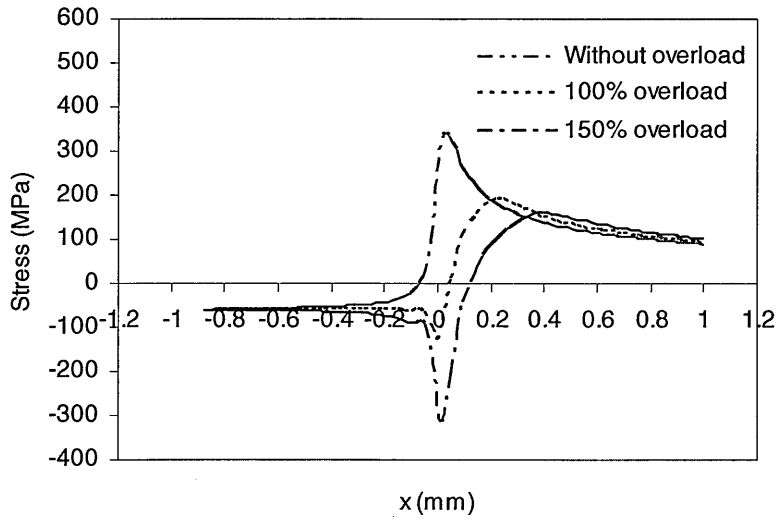

(c)

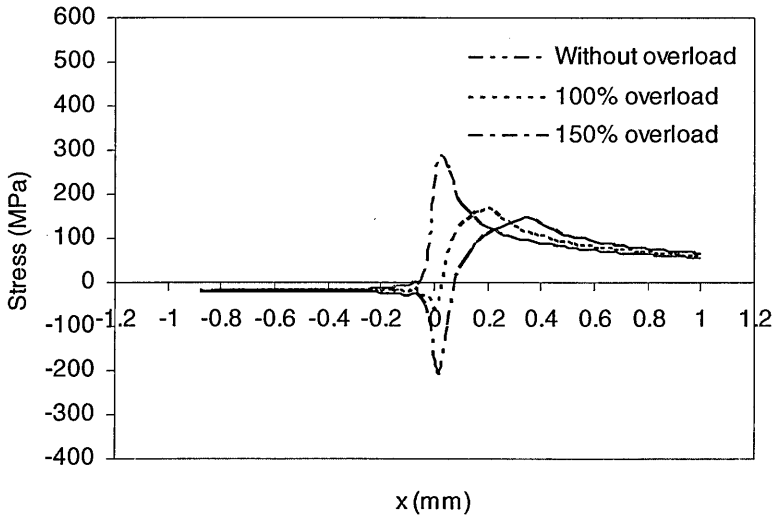

Figure 5.21: Comparison of stresses along the x direction in the crack plane (y=0) at K_{max} (6.6 MPa$\sqrt{m}$) before and after overloading in plane stress: (a) longitudinal, (b) transverse and (c) hydrostatic stresses.

(a)

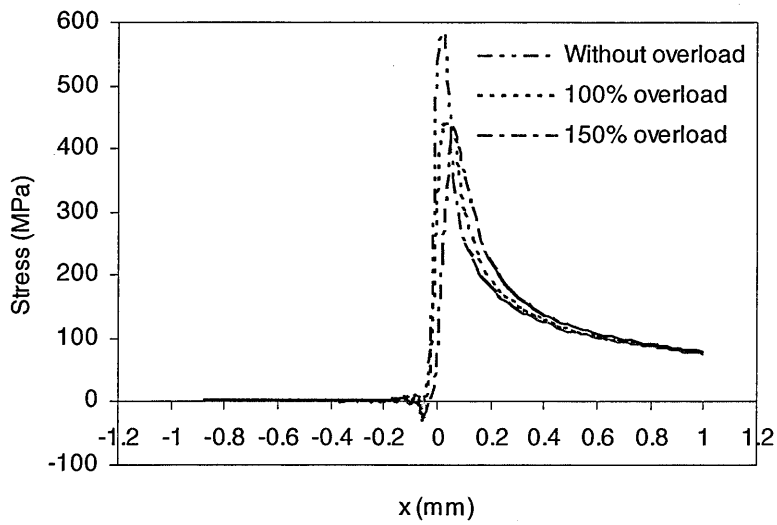

(b)

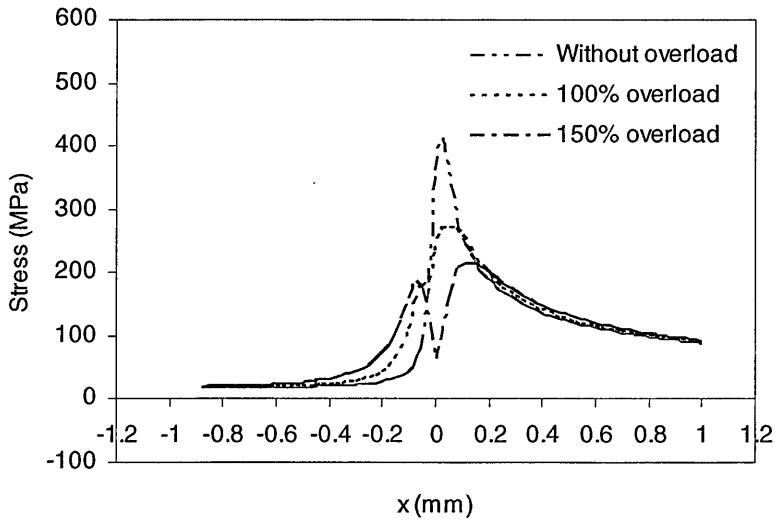

(c)

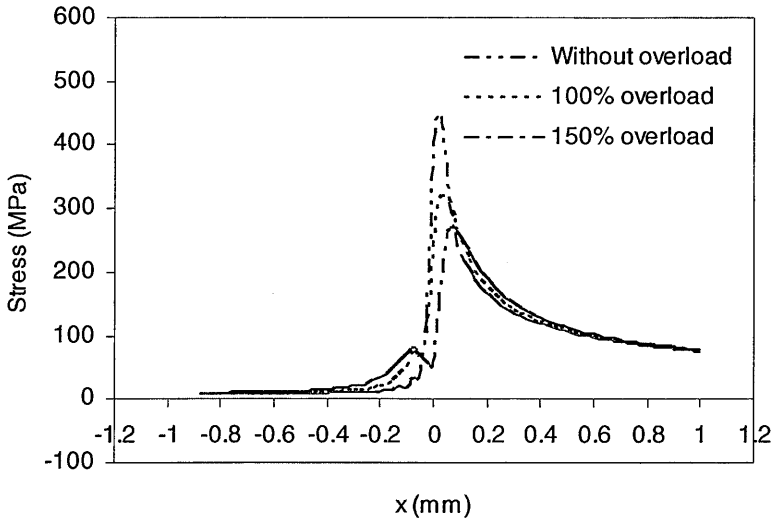

Figure 5.22: Comparison of stresses along the x direction in the crack plane (y=0) at K_{max} (6.6 MPa$\sqrt{m}$) before and after overloading in plane strain: (a) longitudinal, (b) transverse and (c) hydrostatic stresses.

(a)

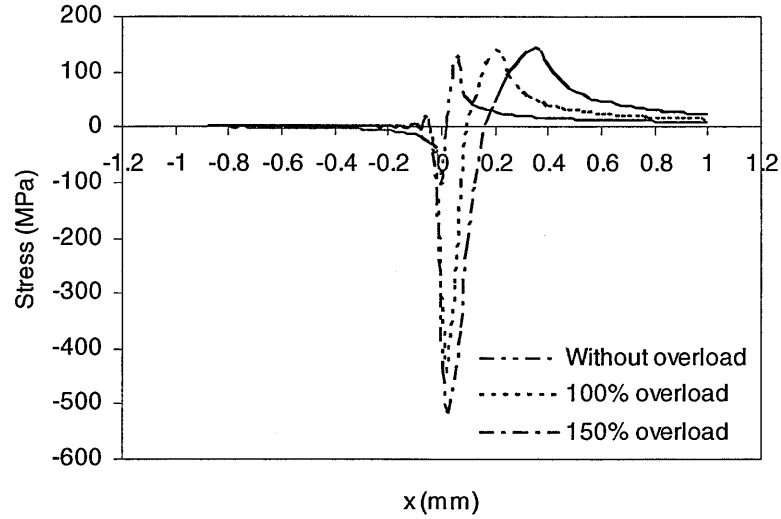

(b)

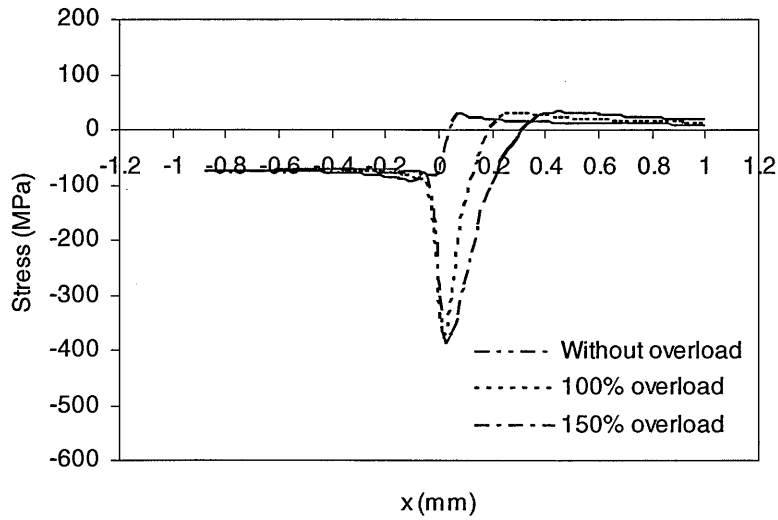

(c)

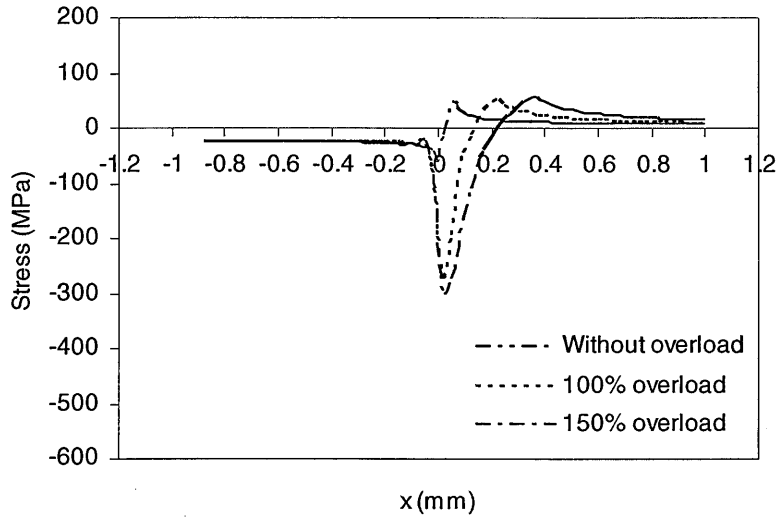

Figure 5.23: Comparison of stresses along the x direction in the crack plane (y=0) at K_{min} (0.66 MPa$\sqrt{m}$) before and after overloading in plane stress: (a) longitudinal, (b) transverse and (c) hydrostatic stresses.

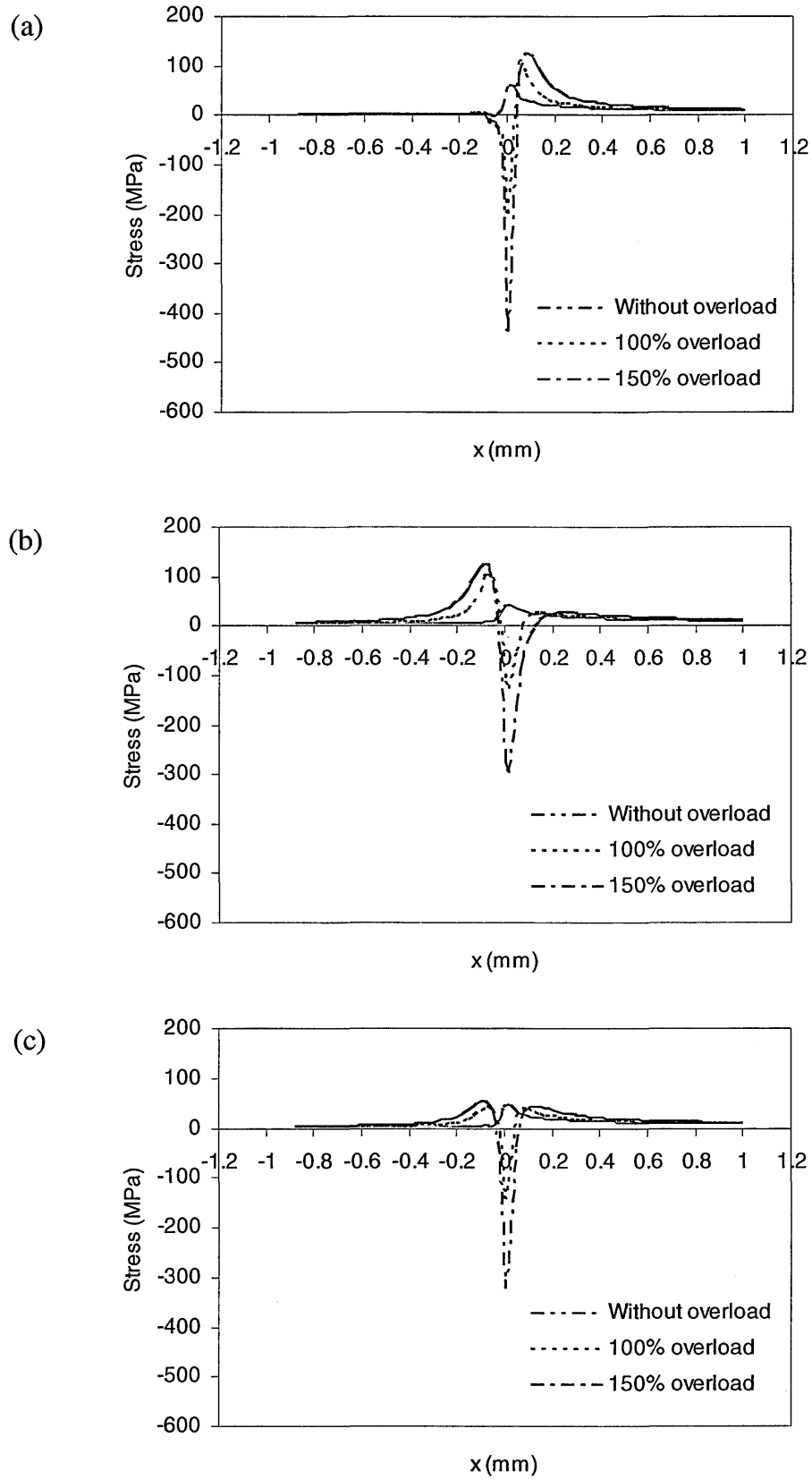

Figure 5.24: Comparison of stresses along the x direction in the crack plane (y=0) at K_{min} (0.66 MPa$\sqrt{m}$) before and after overloading in plane strain: (a) longitudinal, (b) transverse and (c) hydrostatic stresses.

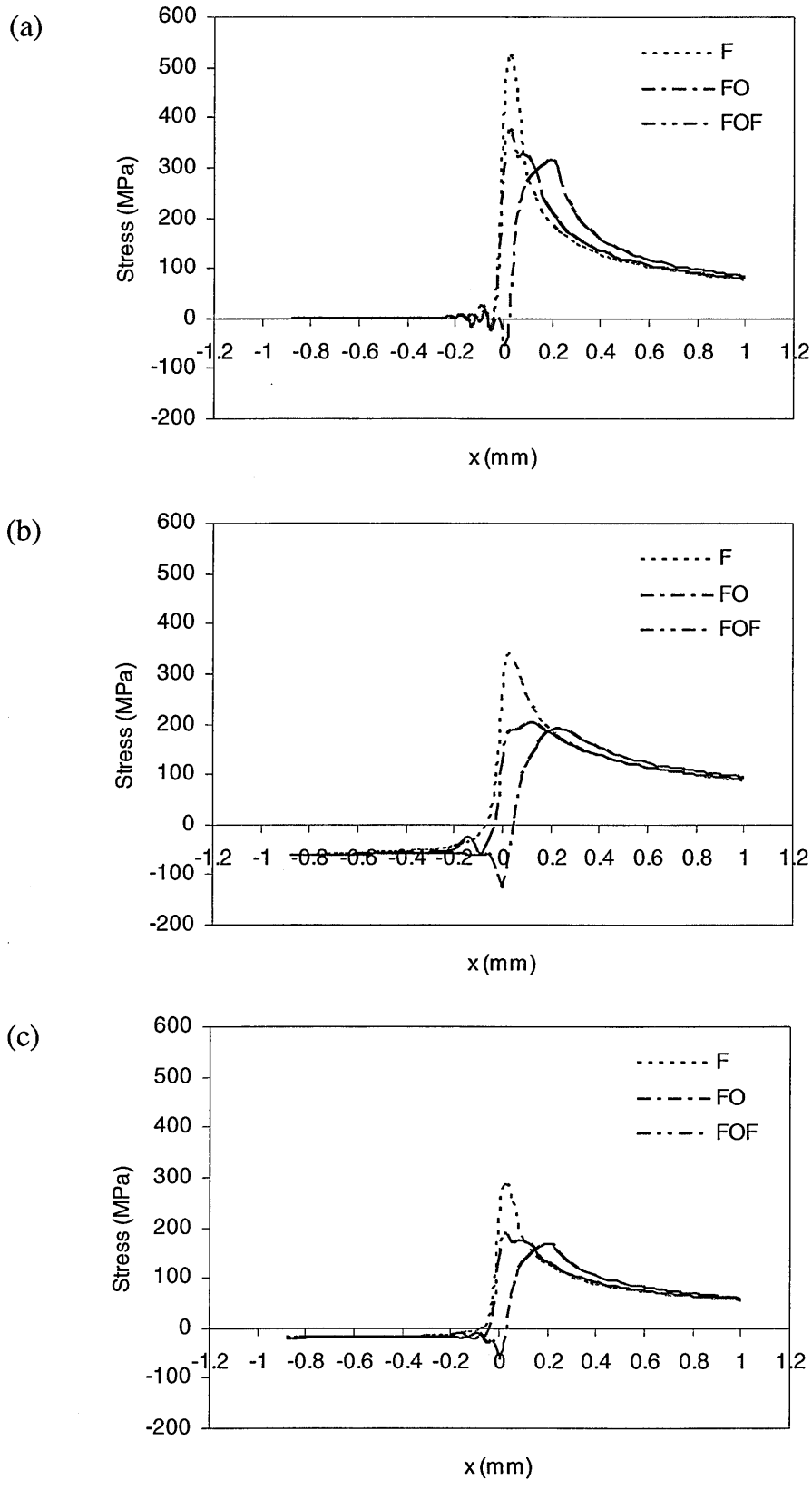

Figure 5.25: Variation of stresses along the x direction in the crack plane (y=0) for the fatigued, fatigued-overloaded and fatigued-overloaded-fatigued cracks for applied K=6.6 MPa$\sqrt{m}$ in plane stress: (a) longitudinal, (b) transverse and (c) hydrostatic stresses.

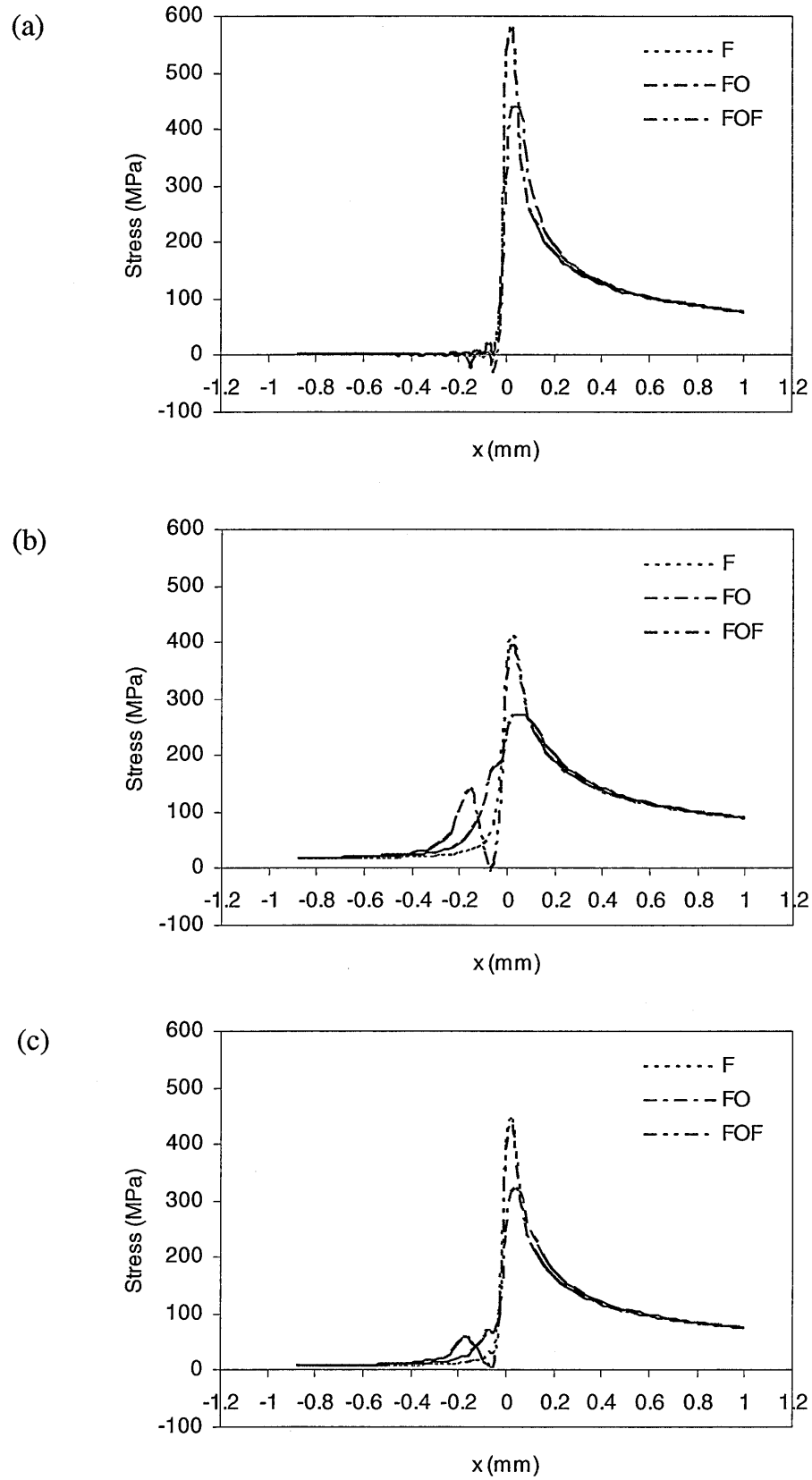

Figure 5.26: Variation of stresses along the x direction in the crack plane (y=0) for the fatigued, fatigued-overloaded and fatigued-overloaded-fatigued cracks for applied K=6.6 MPa$\sqrt{m}$ in plane strain: (a) longitudinal, (b) transverse and (c) hydrostatic stresses.

(a)

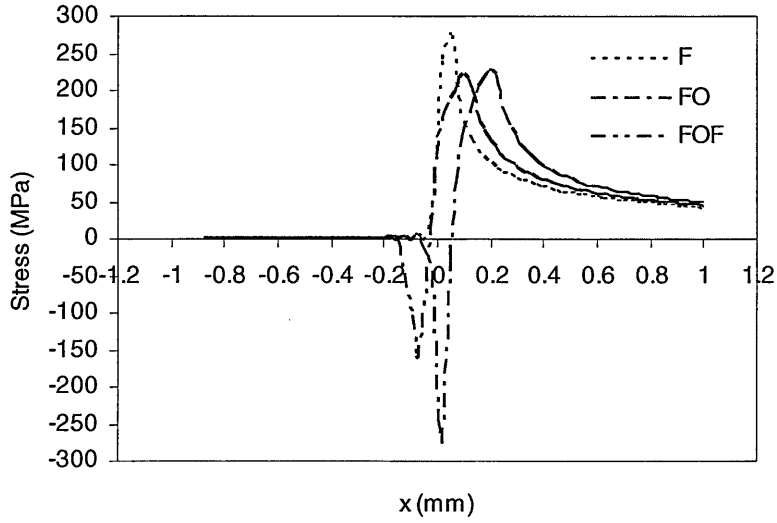

(b)

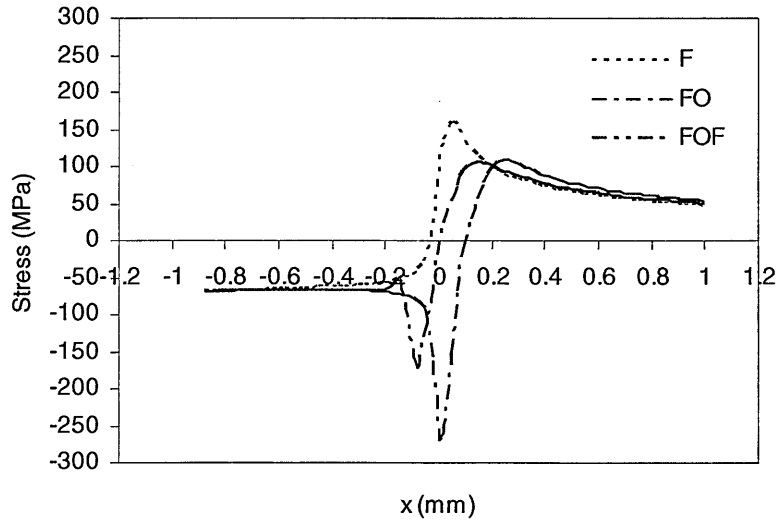

(c)

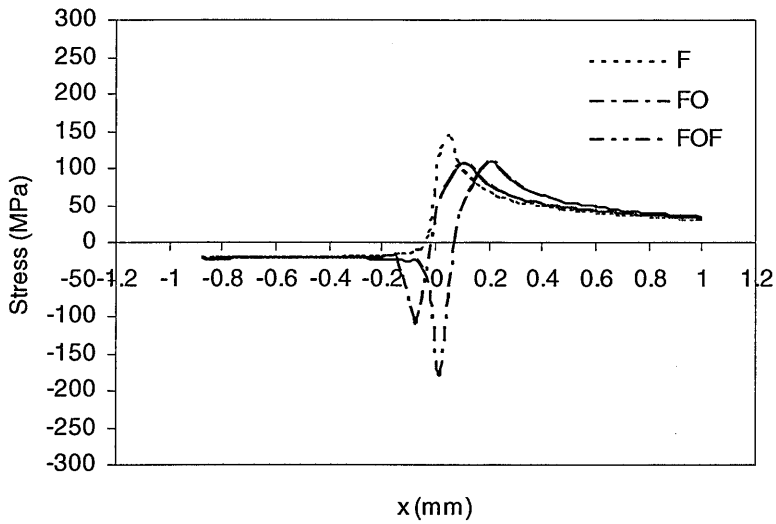

Figure 5.27: Variation of stresses along the x direction in the crack plane (y=0) for the fatigued, fatigued-overloaded and fatigued-overloaded-fatigued cracks for applied K=3.6 MPa$\sqrt{m}$ in plane stress: (a) longitudinal, (b) transverse and (c) hydrostatic stresses.

(a)

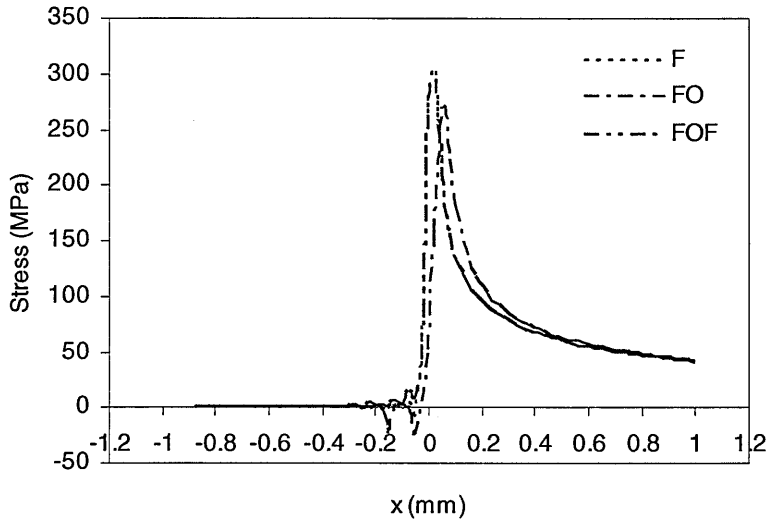

(b)

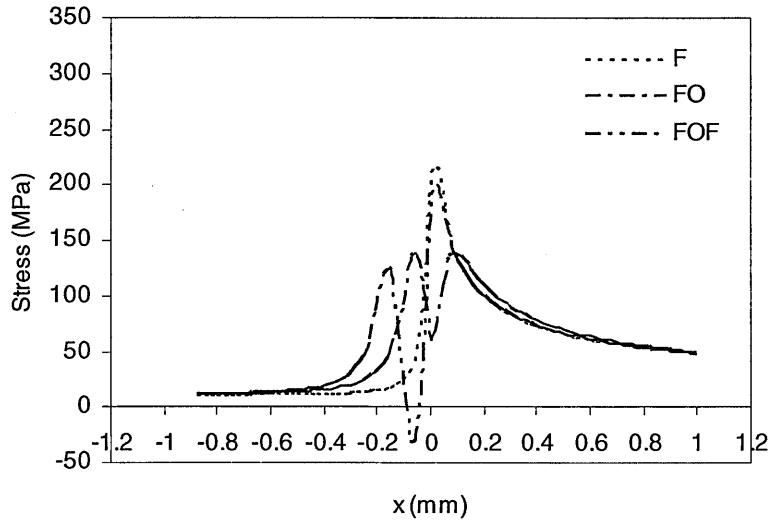

(c)

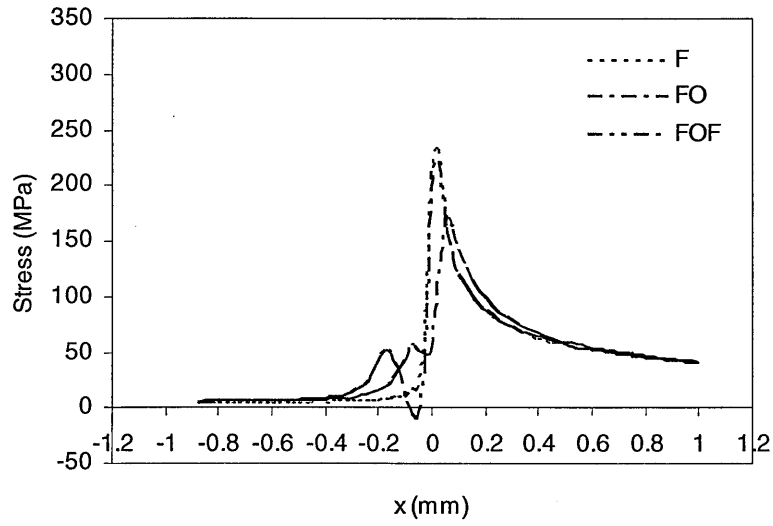

Figure 5.28: Variation of stresses along the x direction in the crack plane (y=0) for the fatigued, fatigued-overloaded and fatigued-overloaded-fatigued cracks for applied K=3.6 MPa$\sqrt{m}$ in plane strain: (a) longitudinal, (b) transverse and (c) hydrostatic stresses.

(a)

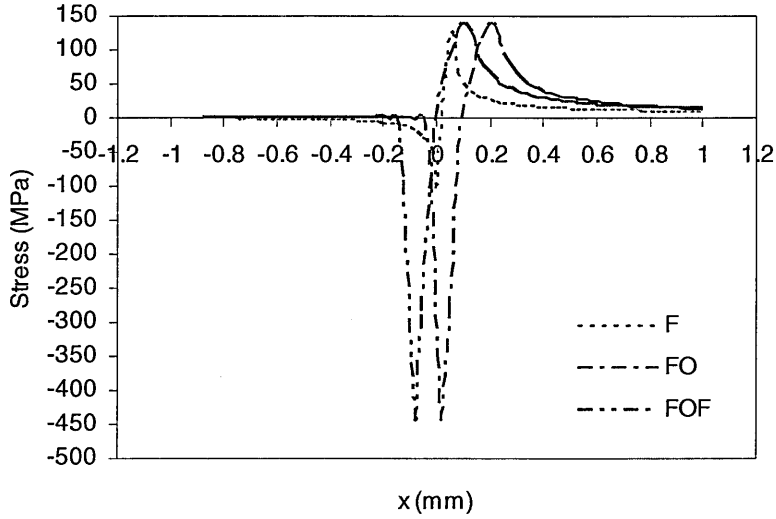

(b)

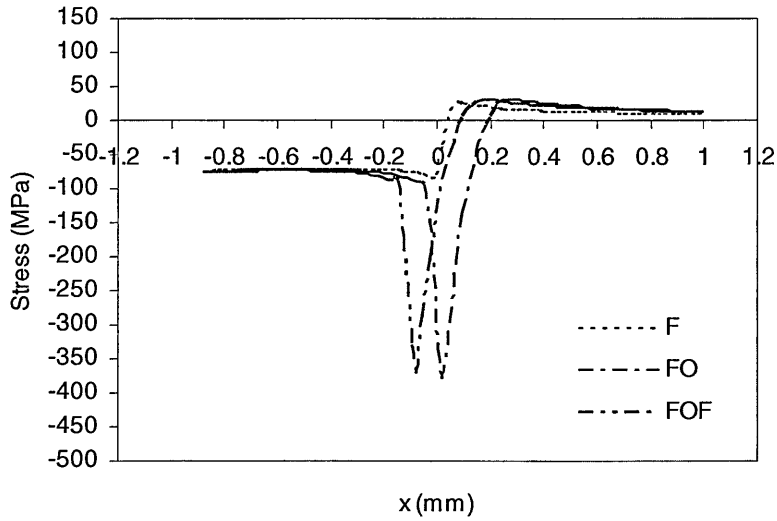

(c)

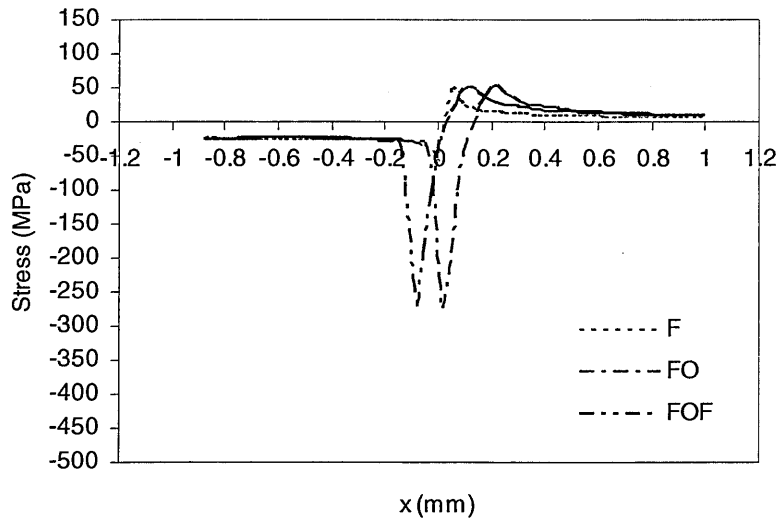

Figure 5.29: Variation of stresses along the x direction in the crack plane (y=0) for the fatigued, fatigued-overloaded and fatigued-overloaded-fatigued cracks for applied K=0.66 MPa$\sqrt{m}$ in plane stress: (a) longitudinal, (b) transverse and (c) hydrostatic stresses.

(a)

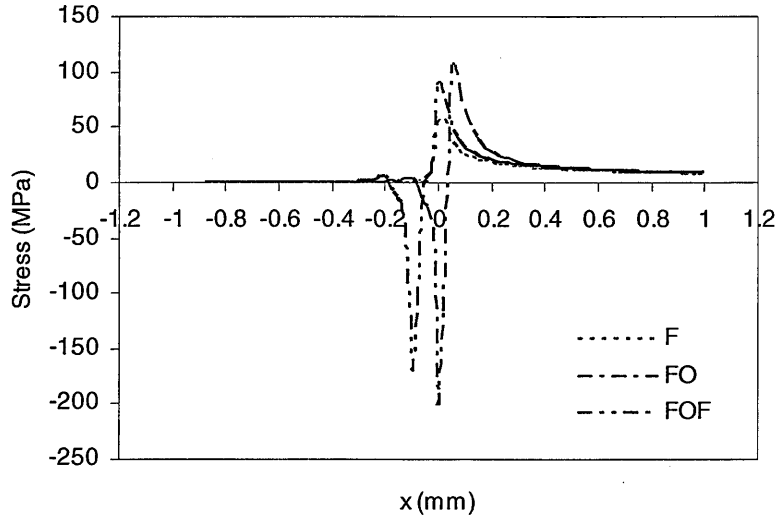

(b)

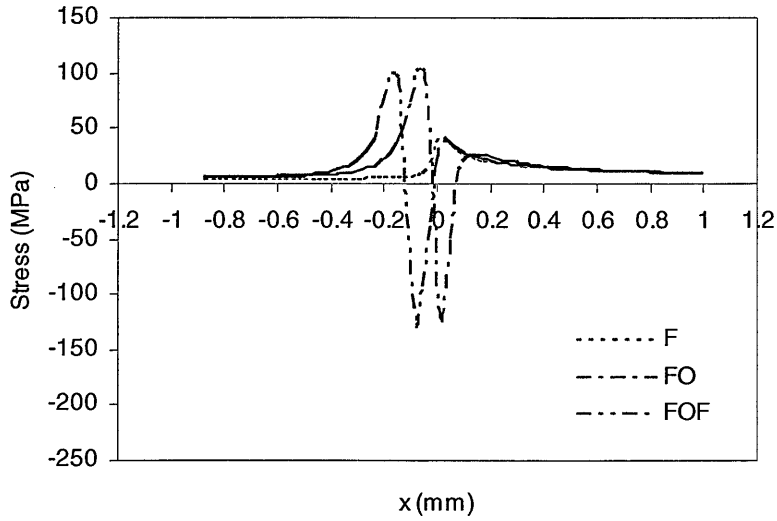

(c)

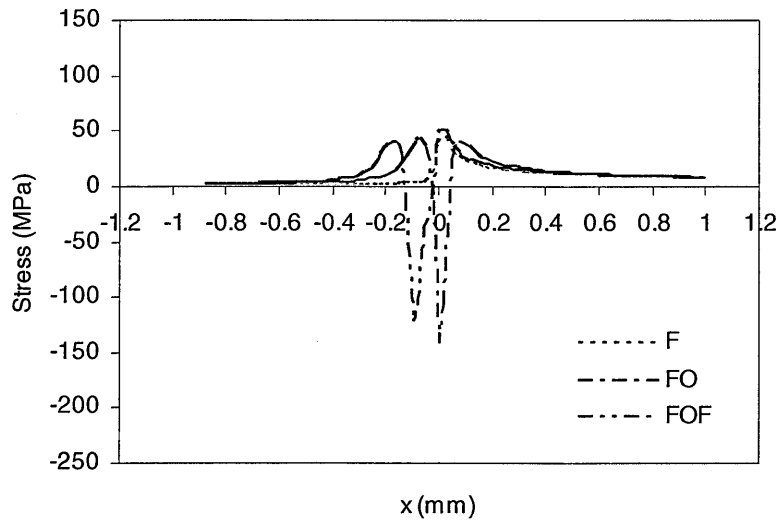

Figure 5.30: Variation of stresses along the x direction in the crack plane (y=0) for the fatigued, fatigued-overloaded and fatigued-overloaded-fatigued cracks for applied K=0.66 MPa$\sqrt{m}$ in plane strain: (a) longitudinal, (b) transverse and (c) hydrostatic stresses.

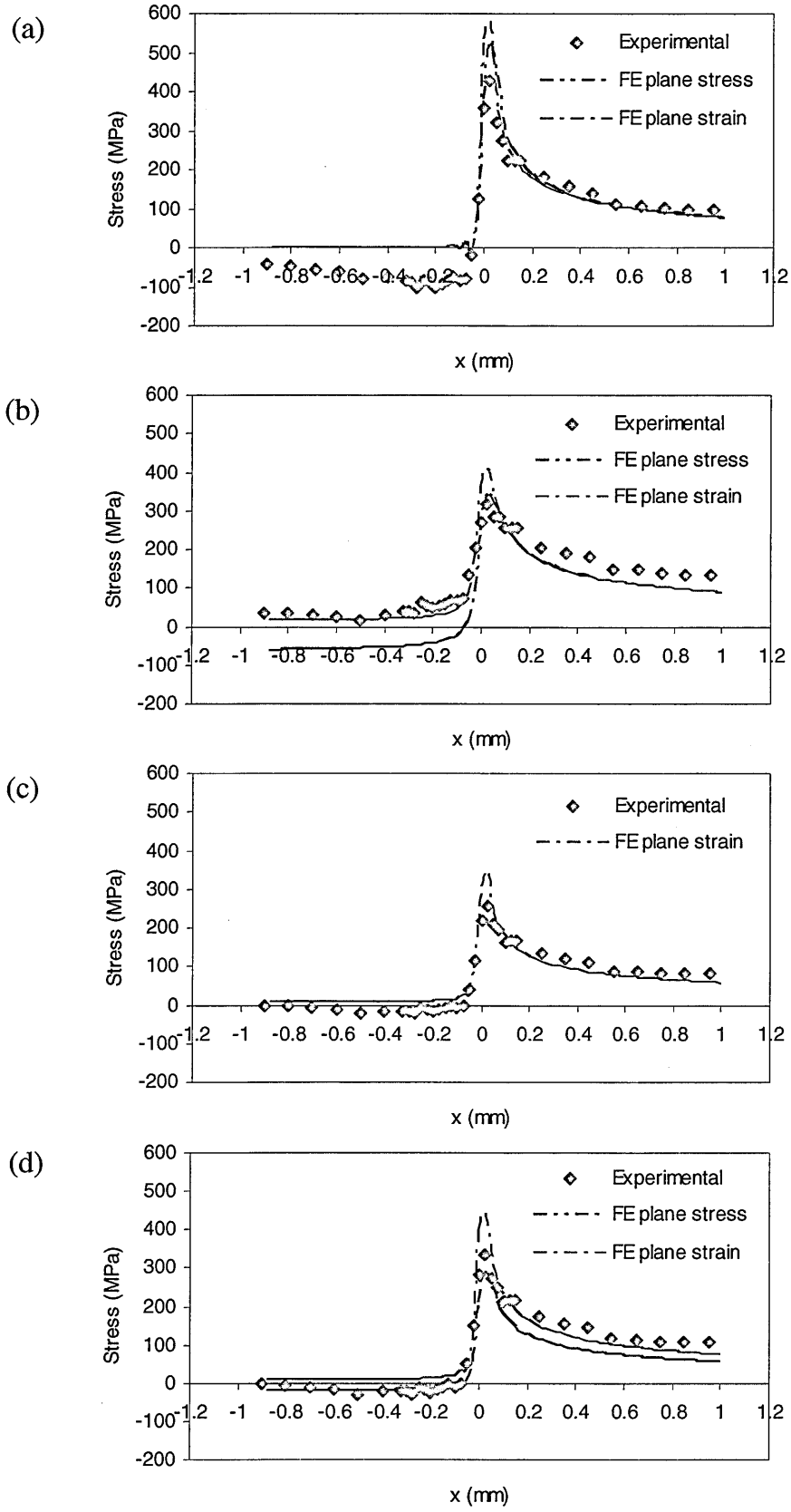

Figure 5.31: Comparison of experimental and numerical (FE) stresses along the x direction in the crack plane (y=0) for the fatigued specimen for applied K=6.6 MPa$\sqrt{m}$: (a) longitudinal, (b) transverse, (c) normal and (d) hydrostatic stresses.

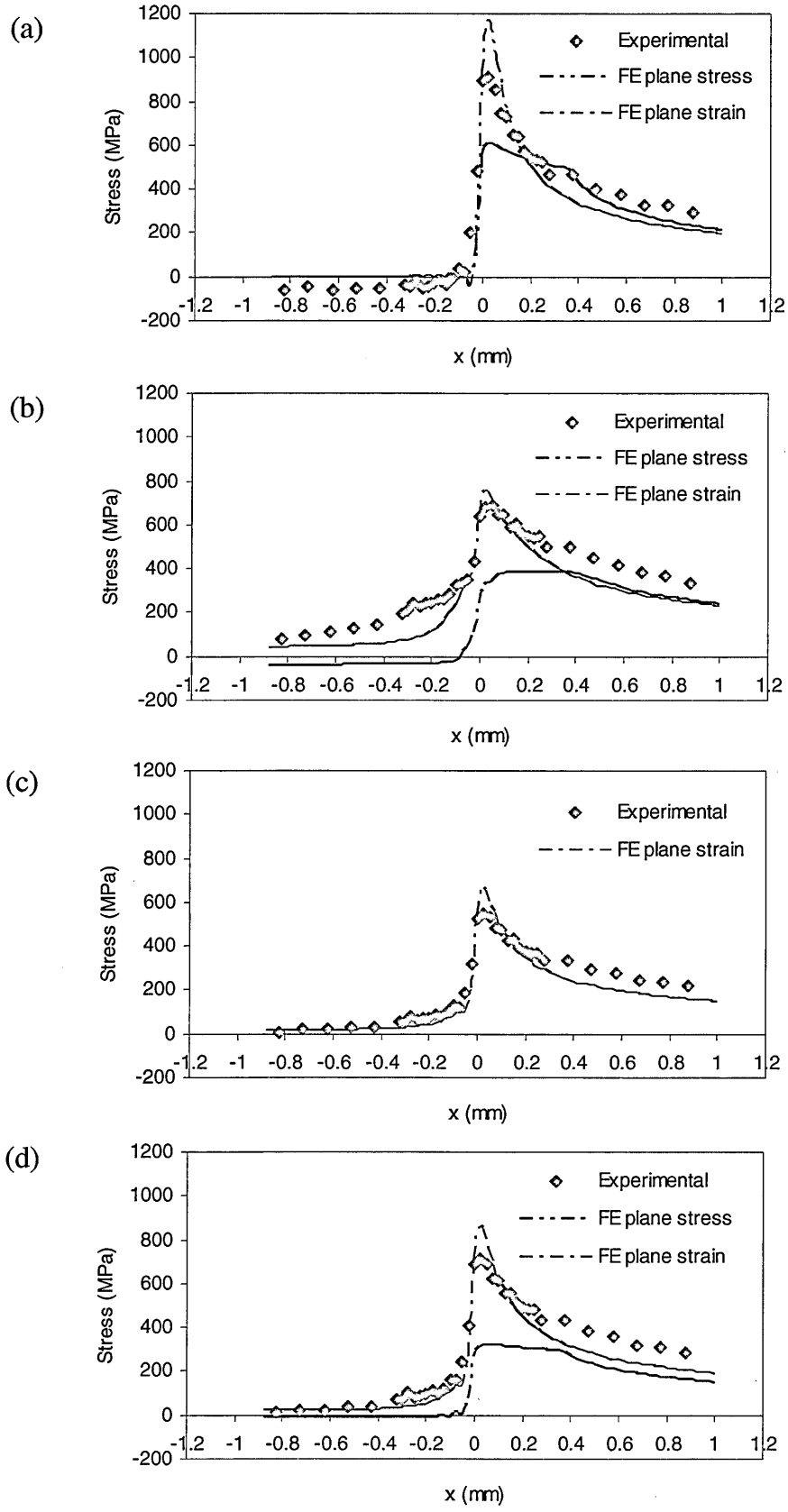

Figure 5.32: Comparison of experimental and numerical (FE) stresses along the x direction in the crack plane (y=0) for the fatigued-overloaded specimen for applied overload K_{ol}=16.5 MPa$\sqrt{m}$: (a) longitudinal, (b) transverse, (c) normal and (d) hydrostatic stresses.

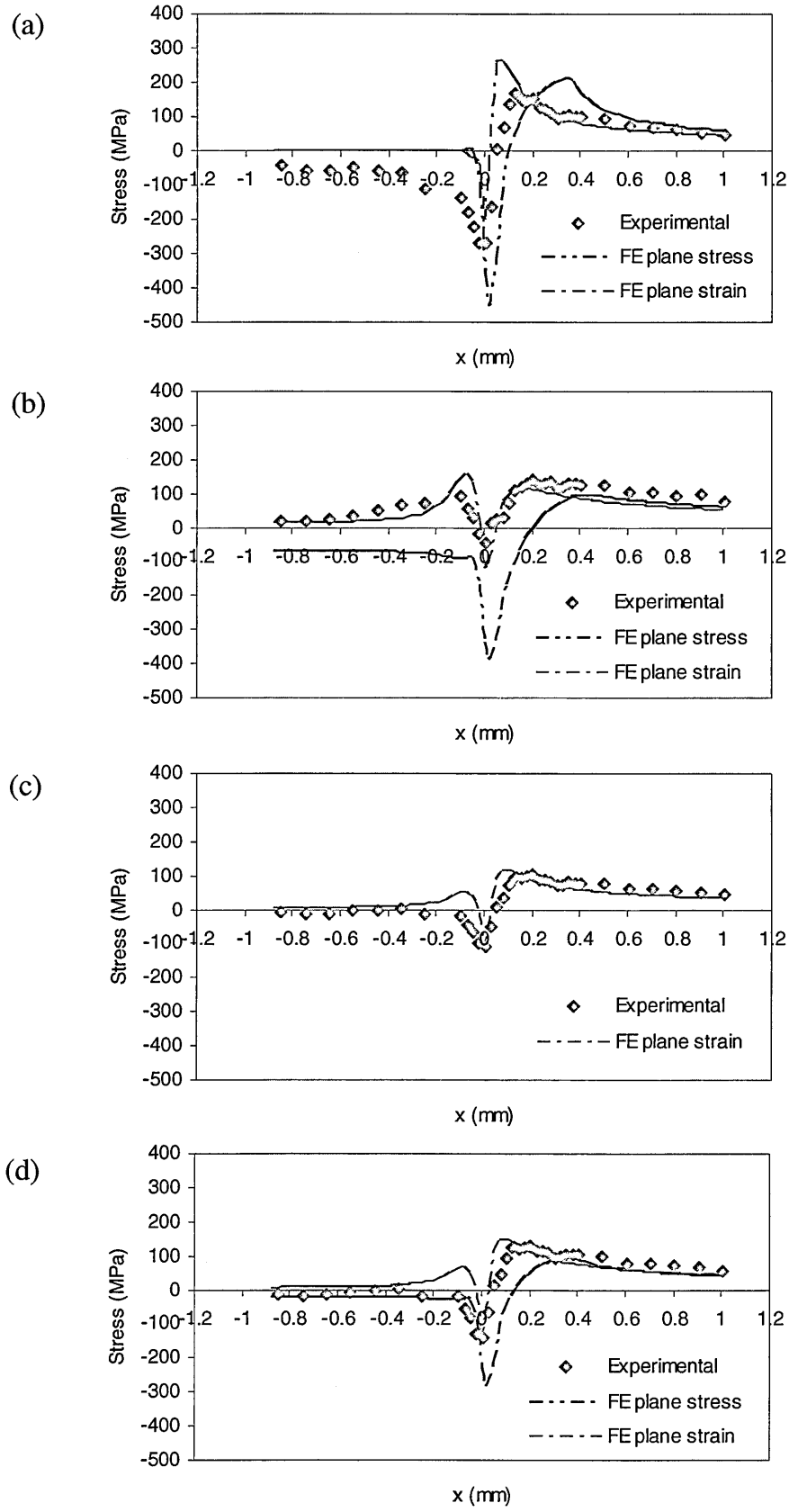

Figure 5.33: Comparison of experimental and numerical (FE) stresses along the x direction in the crack plane (y=0) for the fatigued-overloaded specimen for applied K=3.6 MPa$\sqrt{m}$: (a) longitudinal, (b) transverse, (c) normal and (d) hydrostatic stresses.

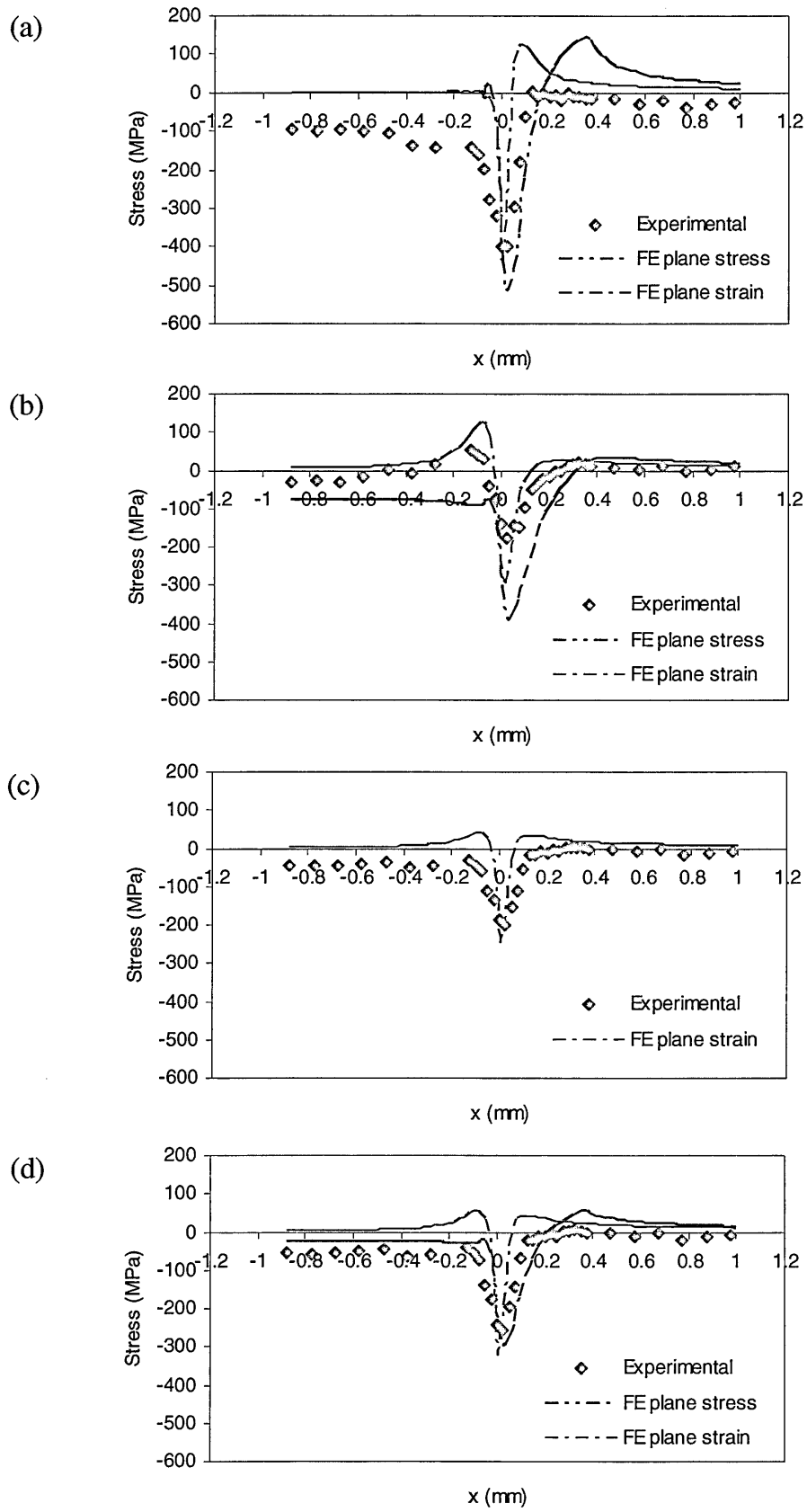

Figure 5.34: Comparison of experimental and numerical (FE) stresses along the x direction in the crack plane (y=0) for the fatigued-overloaded specimen for applied K=0.66 MPa$\sqrt{m}$: (a) longitudinal, (b) transverse, (c) normal and (d) hydrostatic stresses.

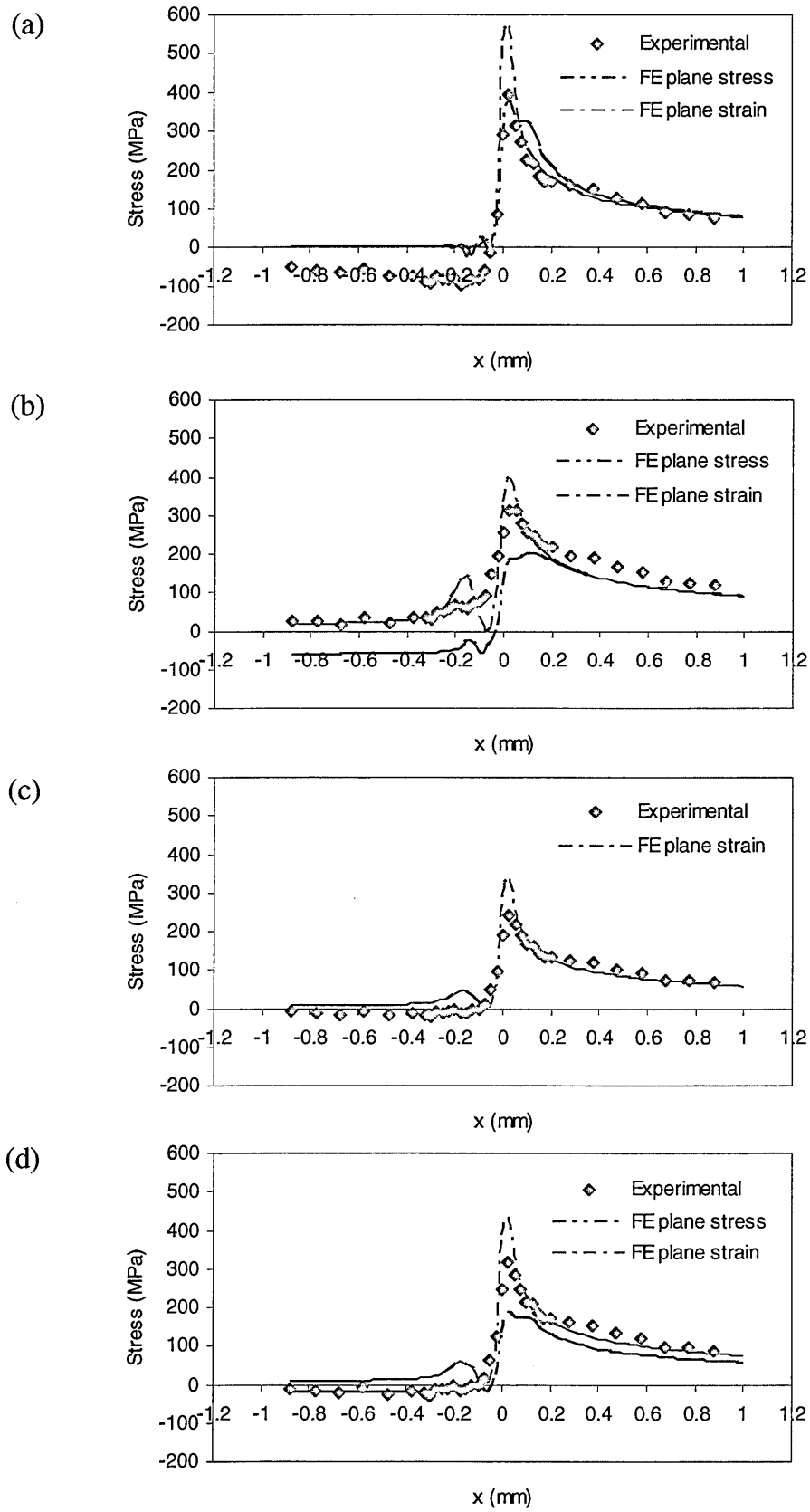

Figure 5.35: Comparison of experimental and numerical (FE) stresses along the x direction in the crack plane (y=0) for the fatigued-overloaded-fatigued specimen for applied K=6.6 MPa$\sqrt{m}$: (a) longitudinal, (b) transverse, (c) normal and (d) hydrostatic stresses.

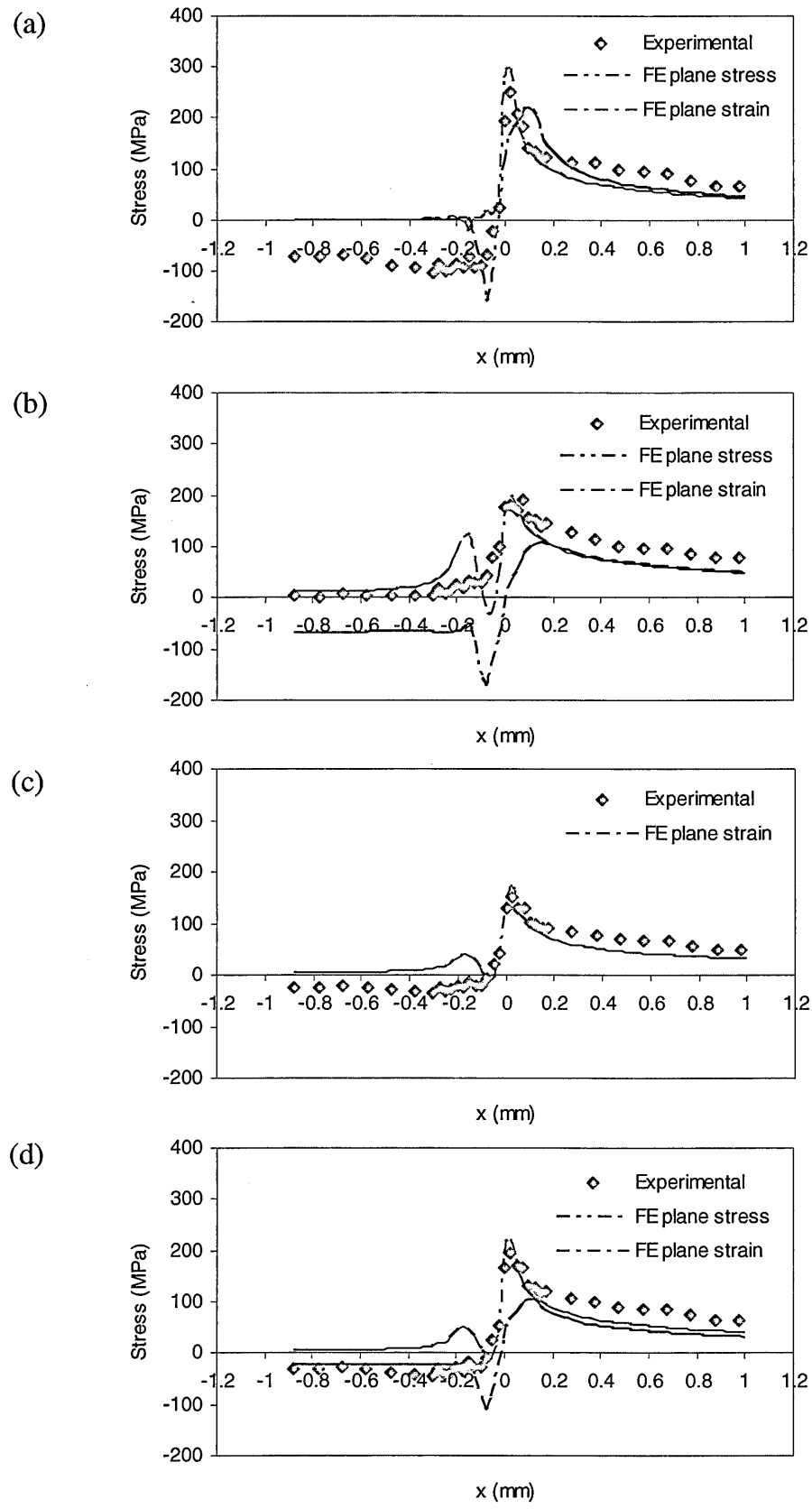

Figure 5.36: Comparison of experimental and numerical (FE) stresses along the x direction in the crack plane (y=0) for the fatigued-overloaded-fatigued specimen for applied K=3.6 MPa$\sqrt{m}$: (a) longitudinal, (b) transverse, (c) normal and (d) hydrostatic stresses.

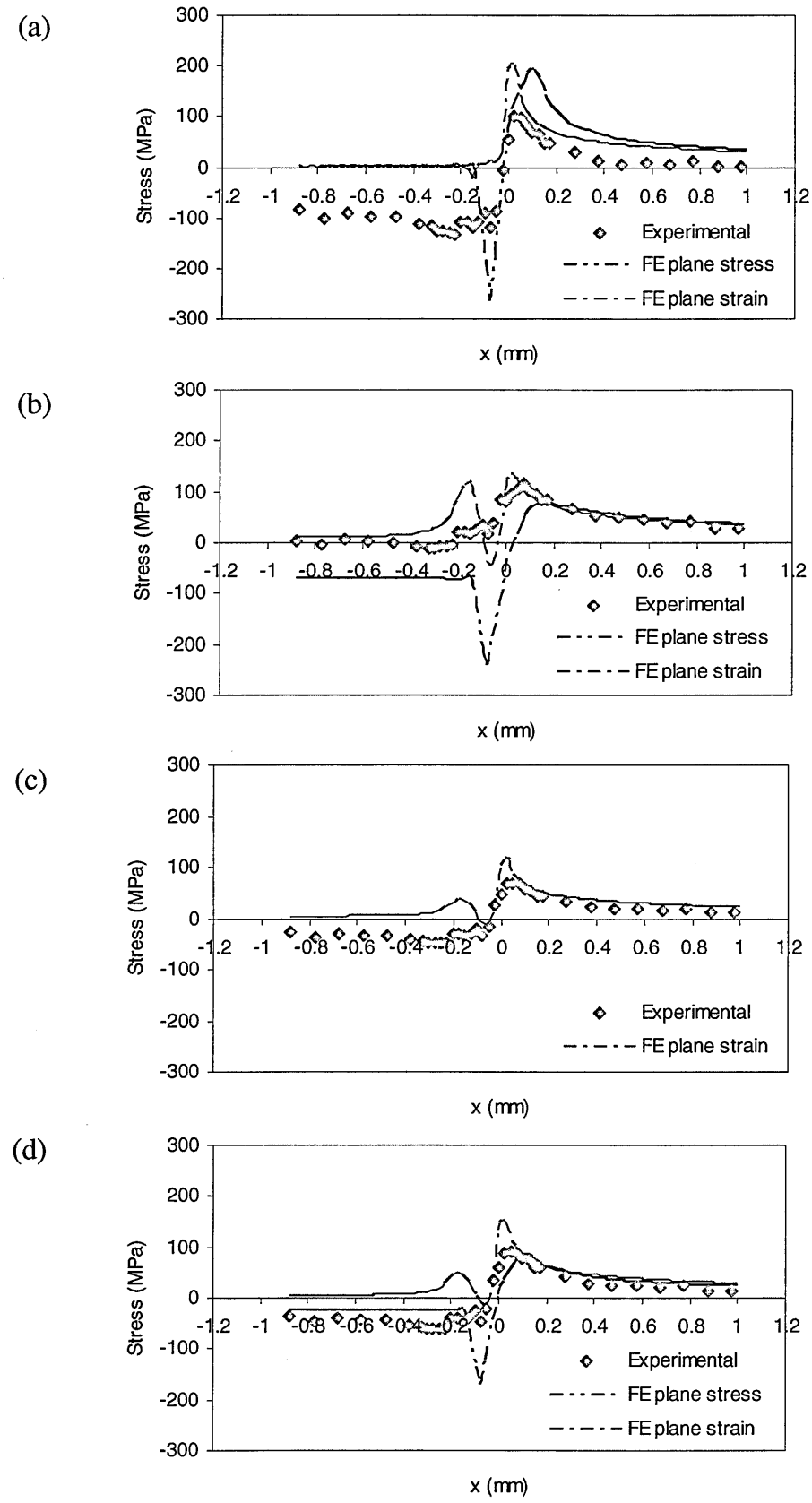

Figure 5.37: Comparison of experimental and numerical (FE) stresses along the x direction in the crack plane (y=0) for the fatigued-overloaded-fatigued specimen for applied K=2.6 MPa$\sqrt{m}$: (a) longitudinal, (b) transverse, (c) normal and (d) hydrostatic stresses.

Chapter 6 Numerical and experimental investigations of plasticity-induced crack closure in aluminium alloy 5091

6.1 Introduction

Elber (1970) was the first to propose plasticity-induced crack closure as a crack growth retardation mechanism. Since then a multitude of research has been carried out to investigate crack closure mechanisms numerically and experimentally.

An overload retards crack growth rate under baseline loading following the overload, as the crack grows through the overload plastic zone. The crack growth retardation occurs due to the generation of compressive residual stresses in the vicinity of the crack tip as a result of overloading (Schijve, 1961, Ramos et al., 2003). When the crack advances through the overload plastic zone, the compressive residual stresses in the element just behind the crack tip are relaxed and the material in this element expands, contributing to the crack closure on the crack flanks behind the crack tip (McEvily and Ishihara, 2001). Therefore, the compressive residual stresses at the crack tip resulting from an overload and the crack closure behind the crack tip on the crack flanks are intimately related. However, the crack growth retardation does not occur immediately after the application of the overload (Bichler and Pippan, 1999, Sadananda et al., 1999). Instead crack growth acceleration occurs immediately following a single tensile overload. This immediate acceleration is due to a decrease in near field closure associated with the crack tip blunting (Bichler and Pippan, 1999). Following the crack growth acceleration for up to about 20-50 cycles, the growth rate decreases below the steady state level as the crack passes

through the overload-affected zone. Lang and Marci (1999) argued that the crack closure has a secondary effect on the crack growth rate, which is so small that it can even be neglected.

Fleck and Smith (1982) discussed that crack closure can occur both on the surface (plane stress region) and in the interior (plane strain region) of a CT specimen. Because of the higher plasticity at the crack tip in plane stress, plasticity-induced crack closure is expected to be more significant in plane stress than in plane strain. To satisfy the incompressibility requirement during plastic deformation at the crack tip, material transfer to the crack tip is required from somewhere in the cracked body (McClung et al., 1991). Since the out-of-plane deformation is not constrained in plane stress, material can be transferred from the thickness direction to the axial direction (McClung et al., 1991). However, in plane strain no net out-of-plane contraction can occur. Therefore, it has been suggested that there can be no net axial stretch of material in the plastic wake behind the crack tip in plane strain (Fleck, 1986). This implies that plasticity-induced crack closure is unlikely in plane strain.

Many researchers have performed finite element analyses to investigate plasticity-induced crack closure in plane stress and plane strain using different specimen configurations. Although plasticity-induced crack closure in plane stress is well recognised, its existence in plane strain has been a topic of debate. Fleck and Newman (1988) showed that in plane strain, closure does not occur in a bend specimen, but closure does occur in a middle crack tension geometry. This may be due to the fact that the middle crack tension geometry has a compressive T-stress, which helps the material to flow parallel to the crack flanks towards the crack tip

during plastic deformation (Sherry et al., 1995). On the other hand the bend specimen has a tensile T-stress, which retards the material flow parallel to the crack flanks towards the crack tip. Using a middle crack tension geometry in finite element analysis, McClung et al. (1991) found crack closure to occur both in plane stress and plane strain. Ashbaugh et al. (1997) observed in their finite element analysis that crack closure occurs in plane strain in a compact tension geometry. However, due to using a relatively coarse mesh in the finite element analysis, these results are questionable. Zhao et al. (2004) investigated crack closure in a compact tension geometry in plane strain and plane stress using finite element analysis. Crack closure was observed in plane stress but not in plane strain. Here the lack of crack closure in plane strain was found to be independent of the material studied. Recently, Sander and Richard (2005) investigated crack closure and overload effects in aluminium alloy 7075-T651 compact tension shear (CTS) specimen in plane stress using finite element analysis. They found that an overload (R_{ol}=2.5) removes the previously occurred crack closure under baseline loading. However, as the crack grows further from the overload point through the overload plastic zone, crack closure occurs even at K_{max}.

This chapter numerically and experimentally investigates the plasticity-induced crack closure in the fatigued (F), fatigued-overloaded (FO) and fatigued-overloaded-fatigued (FOF) aluminium alloy 5091 compact tension (CT) specimens. The fatigued (F), fatigued-overloaded (FO) and fatigued-overloaded-fatigued (FOF) cracks have been modelled in plane stress and plane strain. Experimental compliance technique has been used in crack closure measurements. It should be mentioned here that as a fine-grained material, aluminium alloy 5091 has low levels

of fracture surface roughness and consequently reduced levels of roughness-induced crack closure, which results in relatively high crack growth rate in this material (Venning et al., 2006). However, plasticity-induced crack closure and crack retardation effects are observed in this material, and the retardation effect is found to be through-thickness in nature (Bray et al., 1992).

6.2 Finite element modelling

A standard compact tension specimen (CT) with width W=50 mm, thickness B=12.25 mm, and initial crack length a_0=25 mm has been considered to simulate the fatigued (F), fatigued-overloaded (FO) and fatigued-overloaded-fatigued (FOF) specimens using the finite element code ABAQUS. Due to the geometric and load symmetry, one half of the specimen has been modelled. The finite element mesh is shown in Figure 6.1. Four-noded first-order full integration elements (CPS4, CPE4) have been used in plane stress and plane strain. Element sizes of 2.5 and 1 μm in the crack plane region have been chosen in plane stress and plane strain respectively following the recommendation of McClung and Sehitoglu (1989) to consider at least 10 elements in the monotonic plastic zone radius, r_y (34.5 and 11.5 μm in plane stress and plane strain respectively in the present work). A crack growth of 0.3 mm has been simulated with an initial crack length of 25 mm to a final crack length of 25.3 mm. The surfaces along the crack line are defined as contact surfaces using the master-slave algorithm of ABAQUS, where the master surface is a rigid surface introduced along the symmetry axis and the specimen surface is defined as the slave surface. Initially the nodes at and ahead of the crack tip are bonded to the rigid surface. The surfaces behind the crack tip behave like regular contact surfaces as the

nodes in that region are unconnected.

The cyclic load has been applied in terms of amplitude as a function of total time to a rigid pin fitted into the hole of the specimen, where the rigid pin and the hole surfaces are treated as contact surfaces. The cracks have been grown under constant amplitude loading with K_{max}=6.6 MPa$\sqrt{m}$ and K_{min}=0.66 MPa$\sqrt{m}$ (i.e., R=0.1). The crack propagation is simulated by debonding the crack tip node at the maximum load of every cycle by specifying the crack growth with respect to a reference point (the initial crack tip) as a function of total time. Debonding of the crack tip node at the maximum load has been chosen following McClung and Sehitoglu (1989), who found no significant influence of the debonding load on the crack opening stress. Each time the crack extends over a distance of 2.5 μm in plane stress and 1 μm in plane strain, corresponding to the size of one element. For simulating a fatigued-overloaded-fatigued crack a 100% (13.2 MPa$\sqrt{m}$) overload has been introduced in the amplitude data at a crack length of 25.2 mm. To simulate a fatigued-overloaded crack a 100% (13.2 MPa$\sqrt{m}$) overload has been applied in a separate step at the end of growing the 0.3 mm crack i.e., at the final crack length of 25.3 mm.

The displacements (contact opening) of the nodes on the crack surface were monitored during loading and unloading to determine the opening and closure loads, which is a widely used technique for crack closure evaluation in finite element analysis (Fleck and Newman, 1988, Pommier and Bompard, 2000). In traditional finite element definition, the opening load is the load at which the crack surfaces separate at the first node behind the crack tip during the loading portion of the fatigue cycle; on the other hand the closure load is the load at which the crack

surfaces contact at the first node behind the crack tip during the unloading portion of the fatigue cycle (Newman, 1997, Wei and James, 2000, Zhao et al., 2004).

The material response of aluminium alloy 5091 is modelled to be elastic-plastic by a separate definition of the elastic and the plastic part of the uniaxial true stress-strain curve (Figure 6.2), which allows the incremental plasticity theory implemented in ABAQUS to be employed in the analysis. The uniaxial stress-strain relations for the elastic and the plastic parts can be given as:

$$\sigma = E\varepsilon \quad \text{for } \varepsilon < \frac{\sigma_y}{E} \tag{6.1}$$

$$\sigma = \sigma_y \left(1 + \frac{\varepsilon_p E}{\sigma_y}\right)^n \quad \text{for } \varepsilon \geq \frac{\sigma_y}{E} \tag{6.2}$$

where σ is the true stress, ε is the true strain, E is the modulus of elasticity, σ_y is the uniaxial yield strength, ε_p is the true plastic strain and n is the strain hardening exponent. Equation 6.2 represents the Ramberg-Osgood power hardening law. To generalise the uniaxial material response to multiaxial states of stress the von Mises yield criterion is used with an associated flow rule implemented in ABAQUS. The mechanical properties of the material are: yield strength 448 MPa, ultimate tensile strength 517 MPa, modulus of elasticity 78 GPa, Poisson's ratio 0.345 and bulk fracture toughness 29.7 MPa$\sqrt{m}$ (Schelleng et al., 1985).

The cyclic plasticity was taken into account by using a combined (nonlinear isotropic/ kinematic) hardening model implemented in ABAQUS. Geometric non-

linearity was taken into account to consider possible large deformations in the material near the crack tip.

6.3 Crack closure measurement

Two aluminium alloy 5091 compact tension specimens were used to prepare fatigued (F), fatigued-overloaded (FO) and fatigued-overloaded-fatigued (FOF) cracks. One specimen was used for the fatigued and fatigued-overloaded cracks and the other one was used for the fatigued-overloaded-fatigued crack. The specimens were prepared according to standard ASTM E647, and were fatigue cracked under constant amplitude loading (constant ΔK) in an MTS servo-hydraulic test system with K_{max}=6.6 MPa$\sqrt{m}$, K_{min}=0.66 MPa$\sqrt{m}$ and R=0.1. For both specimens, the specimen width, W and the initial crack length, a_o were 50 mm and 15.2 mm respectively. For the fatigued and fatigued-overloaded cracks, the specimen thickness, B and the final crack length, a were 12.25 mm and 26.7 mm respectively. To create the fatigued-overloaded crack using same specimen (fatigued), an overload of 13.2 MPa$\sqrt{m}$ (100%) was applied at the final crack length (26.7 mm). For the fatigued-overloaded-fatigued crack, the specimen thickness, B and the final crack length, a were 12 mm and 26.7 mm respectively. In this case an overload of 13.2 MPa$\sqrt{m}$ (100%) was applied at a crack length of 26.6 mm, i.e., 0.1 mm behind the final crack tip. A compact tension specimen with all characteristic dimensions is shown in Figure 6.3.

For crack closure measurement, a conventional compliance technique (Elber, 1971) was used as recommended in standard ASTM E647. For both specimens, clip

gauges were attached at the crack mouth and strain gauges were attached at the mid-height location on the back face as shown in Figure 6.3. The methods of using a clip gauge at the crack mouth and a back face strain gauge are widely-used for crack closure measurement, giving a global crack opening/closure value. During the experiment, the specimens were loaded in an MTS servo-hydraulic test system, where load versus displacement and strain data were recorded during loading and unloading of the specimens in a single load cycle using a computerised data acquisition system.

In compliance crack closure analysis, load versus displacement or strain data for the cracked specimen are plotted. A typical load-displacement curve for a load cycle is shown in Figure 6.4. Between points A and B the load-displacement curve is linear, where the slope of the curve (compliance or stiffness) is equal to the slope of the uncracked specimen. At this stage the crack remains fully closed. With increasing load, the curve shows nonlinearity from point B, where the crack starts to open to point C, where the crack becomes fully open. With further increasing load, the slope of the load-displacement curve again attains a constant value as shown between points C and D, which remains constant with further increase of load until it causes large-scale yielding near the crack tip. The unloading curve follows a path similar to the loading curve as shown in Figure 6.4.

6.4 Results

The finite element results are presented in Figures 6.5 to 6.10. Figures 6.5 to 6.8 show the variation of contact opening along the crack surfaces behind the crack tip

for the fatigued, fatigued-overloaded and fatigued-overloaded-fatigued cracks for applied K=6.6 (K_{max}), 3.6 and 0.66 (K_{min}) MPa$\sqrt{m}$ in plane stress and plane strain. Figures 6.5 & 6.6 show the contact opening profiles in plane stress. Figure 6.5a-c shows a comparison of the contact opening profiles under the three different loads for each crack type in plane stress. Figure 6.5a shows that for the fatigued crack, the displacements between the crack surfaces decrease as the load decreases from K_{max} (6.6 MPa$\sqrt{m}$). At K_{min} (0.66 MPa$\sqrt{m}$) a complete closure between the crack surfaces occurs. The application of a 100% (13.2 MPa$\sqrt{m}$) overload causes the crack tip to deform plastically. Consequently, the contact openings under each load (under baseline level) increase and the crack closure disappears at K_{min} as shown in Figure 6.5b. Figure 6.5c shows that with a crack growth of 0.1 mm from the overload point, the contact openings between the overload point and the crack tip at K_{max} appear to be much lower than the opening values obtained in this region at K_{max} before the application of the overload (Figure 6.5a). Figure 6.5c further shows that the overload leads to a partial closure at K=3.6 MPa$\sqrt{m}$ and a complete closure at K_{min} between the overload point and the current crack tip. Figure 6.6a-c shows a comparison of the contact opening profiles for the three different crack types under each applied loading (K=6.6, 3.6 and 0.66 MPa$\sqrt{m}$) in plane stress.

Figures 6.7 & 6.8 show the contact opening profiles in plane strain. Figure 6.7a-c shows a comparison of the contact opening profiles along the crack surfaces under the three different loads for each crack type (fatigued, fatigued-overloaded and fatigued-overloaded-fatigued) in plane strain. Figure 6.7a shows that for the fatigued crack, as in plane stress, the displacements between the crack surfaces decrease as

the load decreases from K_{max} (6.6 MPa$\sqrt{m}$), however no crack closure appears to occur at K_{min} (0.66 MPa$\sqrt{m}$). As in plane stress, the application of a 100% (13.2 MPa$\sqrt{m}$) overload causes the crack tip to deform plastically. Consequently, the contact openings under each load (under baseline level) increase as shown in Figure 6.7b. With 0.1 mm crack growth from the overload point, the crack leaves a plastically deformed region (overload hump) in the vicinity of the overload point at baseline level loading (K=6.6, 3.6 and 0.66 MPa$\sqrt{m}$) as shown in Figure 6.7c. Here the crack is fully open at K_{max} and K=3.6 MPa$\sqrt{m}$, but a local closure occurs in the overload-affected region at K_{min} (0.66 MPa$\sqrt{m}$). Figure 6.8a-c shows a comparison of the contact opening profiles for the three different crack types under each loading (K=6.6, 3.6 and 0.66 MPa$\sqrt{m}$) in plane strain. The contact opening profiles (both in plane stress and plane strain) obtained in the present work are consistent with the results obtained by Sander and Richard (2005) in their finite element analysis in plane stress using aluminium alloy 7075-T651 compact tension shear (CTS) specimen geometry.

Figure 6.9a shows the variation of contact opening with applied stress intensity factor at the first node behind the crack tip during loading (opening) and unloading (closure) for the fatigued crack in plane stress. Here the opening and the closure loads appear to be 3.32 MPa$\sqrt{m}$ and 2.95 MPa$\sqrt{m}$ respectively. Figure 6.9b shows the variation of contact opening with applied stress intensity factor for the fatigued-overloaded-fatigued crack in plane stress. Here the opening and the closure loads appear to be 2.69 MPa$\sqrt{m}$ and 2.66 MPa$\sqrt{m}$ respectively. Both for the fatigued and fatigued-overloaded-fatigued cracks, the closure load appears to be lower than the

opening load. Figure 6.10a&b shows the variation of contact opening with applied stress intensity factor at the nodal position in the overload-affected zone (between the overload point and the crack tip) with the maximum opening and closure levels for the fatigued-overloaded-fatigued crack in plane stress and plane strain. Here the opening and closure loads appear to be identical, where $K_{op}=K_{cl}=5.92$ MPa$\sqrt{m}$ in plane stress and $K_{op}=K_{cl}=2.75$ MPa$\sqrt{m}$ in plane strain.

Results of the experimental compliance crack closure investigation for the fatigued, fatigued-overloaded and fatigued-overloaded cracks are shown in Figures 6.11 to 6.16. For the fatigued crack, the load-displacement curves from the clip gauge during loading (opening) and unloading (closure) are shown in Figure 6.11a&b. The load-strain curves from the back face strain gauge for this crack are shown in Figure 6.12a&b. The position of the crack opening load on each curve is shown by a black circle. It is seen from Figures 6.11 and 6.12 that both from the clip gauge and back face strain gauge the opening load appears to be about 0.5 MPa$\sqrt{m}$, which is less than K_{min} (0.66 MPa$\sqrt{m}$). Results for the fatigued-overload crack in Figures 6.13 and 6.14 and for the fatigued-overloaded-fatigued crack in Figures 6.15 and 6.16 also show similar opening levels, which apparently show no noticeable effect of overload on the crack opening level.

6.5 Discussion

Plasticity-induced crack closure for the fatigued, fatigued-overloaded and fatigued-overloaded-fatigued cracks in aluminium alloy 5091 compact-tension specimens has been investigated using finite element analysis and a compliance-based experimental

technique. Finite element investigation has been performed in plane stress and plane strain. The finite element results show that for constant amplitude fatigue (with K_{max}=6.6 MPa$\sqrt{m}$ and K_{min}=0.66 MPa$\sqrt{m}$), crack closure occurs in plane stress but not in plane strain (Figures 6.5a and 6.7a). From the stress field analysis in Chapter 5 it is obvious that for constant amplitude fatigue (with K_{max}=6.6 MPa$\sqrt{m}$ and K_{min}=0.66 MPa$\sqrt{m}$) compressive residual stresses develop in the crack tip region at K_{min}, in plane stress but not in plane strain. Here a plastic zone develops at the crack tip at K_{max} in plane stress, which is compressed at K_{min} resulting in compressive residual stresses in the crack tip region. Therefore, the crack closure in plane stress for the fatigued crack is due to the compressive residual stresses at the crack tip at K_{min} as the crack grows through the compressive residual stress zone. These results support the argument of McEvily and Ishihara (2001) that the compressive residual stresses at the crack tip and the crack closure behind the crack tip on the crack flanks are intimately related. The current results are consistent with Zhao et al. (2004), who found crack closure in plane stress but not in plane strain in their finite element analysis using a compact tension geometry. Fleck and Newman (1988) also showed using finite element analysis that in plane strain closure does not occur in a bend specimen. It can be mentioned here that both compact tension and bend specimens have a tensile T-stress, which resists material flow parallel to the crack flanks towards the crack tip. Besides, the out-of-plane deformation is constrained in plane strain. Therefore, plasticity-induced crack closure is less likely in compact tension and bend specimen geometries in plane strain due to the lack of plasticity at the crack tip, particularly under low fatigue loading.

Application of a 100% (13.2 MPa$\sqrt{m}$) overload (fatigued-overloaded crack) in the

FE model results in crack closure disappearing immediately in plane stress due to the higher tensile plastic deformation at the crack tip; however the crack closure reappears in plane stress and local closure occurs in plane strain in the overload-affected region as the crack grows further 0.1 mm from the overload point (fatigued-overloaded-fatigued crack) (Figures 6.5c and 6.7c). Here the closure level is higher in plane stress due to the higher overload plastic deformation at the crack tip, which results in higher compressive residual stresses in the crack tip region at K_{min} in plane stress immediately following the overload (Chapter 5). Figure 6.5c shows that even at K=3.6 MPa$\sqrt{m}$ in plane stress the crack is partially closed between the overload point (x=–0.1 mm) and the crack tip. These results seem to support the argument of Bichler and Pippan (1999) that an overload results in crack tip blunting, which causes a decrease in near field closure. Consequently, crack growth acceleration occurs immediately following a single overload up to about 20-50 cycles and then the growth rate decreases below the steady state level as the crack passes through the overload-affected zone. Sadananda et al. (1999) also discussed that an overload can produce very short initial acceleration before significant retardation occurs. They mentioned that this initial acceleration depends on the overload ratio and material flow behaviour.

In the numerical simulations, the fatigued crack shows higher opening and closure levels (based on the separation and contact of the crack surfaces at the first node behind the crack tip) than the fatigued-overloaded-fatigued crack in plane stress (Figures 6.9a&b). This is due to the fact that for the fatigued-overloaded-fatigued crack a high level of closure has occurred in the overload-affected region behind the crack tip in plane stress (Figure 6.10a), which has reduced the near field closure.

However, both for the fatigued and fatigued-overloaded-fatigued cracks the closure level appears to be lower than the opening level in plane stress. Using a middle tension specimen geometry, Lee and Song (2005) also found a lower closure level than the opening level in plane strain finite element analysis (with stress ratio, R=0). In plane strain for the fatigued-overloaded-fatigued crack a significant level of local closure occurs in the overload-affected region (Figure 6.10b) although no near field closure (closure at the first node behind the crack tip) occurs due to the relatively small overload plastic zone (Figure 6.7c).

The finite element results show noticeable differences in the size and shape of the contact opening profiles, between plane stress and plane strain, for all simulated cracks (fatigued, fatigued-overloaded and fatigued-overloaded-fatigued), under the entire range of loading (Figures 6.5 and 6.7). The contact opening profiles presented here show similarities with the results obtained by Sander and Richard (2005) in their finite element analysis in plane stress using aluminium alloy 7075-T651 compact tension shear (CTS) specimen geometry.

The results from the experimental compliance measurements show low opening levels (about 0.5 MPa$\sqrt{m}$), which are even smaller than K_{min} (0.66 MPa$\sqrt{m}$) regard-less of loading history (fatigued, fatigued-overloaded, fatigued-overloaded-fatigued) (Figures 6.11 to 6.16). The experimental opening loads for the fatigued, fatigued-overloaded, fatigued-overloaded-fatigued cracks were expected to be different as predicted by the finite element analysis, however no quantitative agreement was expected between the finite element and experimental results. This is because, in two-dimensional (plane stress and plane strain) finite element analysis local closure

is considered, whereas the experimental compliance method provides an average value of crack closure over the entire crack front. The global compliance methods (using a clip gauge at the crack mouth and a back face strain gauge) employed in this investigation, have relatively low sensitivity (Skorupa et al., 2007, Carboni, 2007), which may not have been able to account for the relatively low closure levels in the specimens. This may be a reason why the experimental results do not identify the effect of the overload on the opening levels. In order to obtain more meaningful results, attempts have been made to measure local compliances using strain gauges on the side face of the specimens just ahead of the crack tips. However, due to the nonlinearities associated with the load-strain curves, the results have not been able to identify the opening loads for the cracks.

6.6 Conclusion

This chapter investigates numerically and experimentally the plasticity-induced crack closure for the fatigued, fatigued-overloaded and fatigued-overloaded-fatigued cracks in aluminium alloy 5091 compact tension specimens. The finite element results show that for a constant amplitude fatigue (with K_{max}=6.6 MPa$\sqrt{m}$ and K_{min}=0.66 MPa$\sqrt{m}$) crack closure occurs in plane stress but not in plane strain. A 100% (13.2 MPa$\sqrt{m}$) overload removes the crack closure immediately in plane stress creating a monotonic plastic zone at the crack tip. However, with 0.1 mm crack growth from the overload point, crack closure reappears in plane stress and local closure occurs in the overload-affected zone in plane strain.

The plane stress finite element results show that the closure levels are lower than the

opening levels both for the fatigued and fatigued-overloaded-fatigued cracks. Further, it can be noted that in plane stress both the opening and closure levels appear to be lower in the fatigued-overloaded-fatigued crack than in the fatigued crack. This is because in plane stress, a high level of closure associated with the overload-affected region in the fatigued-overloaded-fatigued crack diminishes the near field closure (closure at the first node behind the crack tip).

Finally, the results from the experimental compliance measurements show small opening levels, which are even less than K_{min} (0.66 MPa$\sqrt{m}$) regardless of the loading history of the cracks. Thus, the experimental results indicate no crack closure for the fatigued crack. Moreover, the experimental results apparently do not identify any effect of the overload on the opening levels for the fatigued-overloaded and the fatigued-overloaded-fatigued cracks.

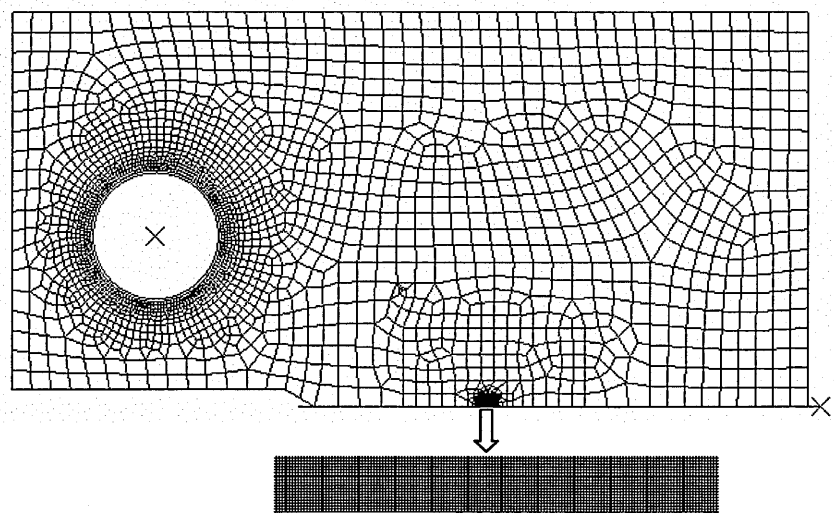

Figure 6.1: Finite element mesh used in crack closure investigations.

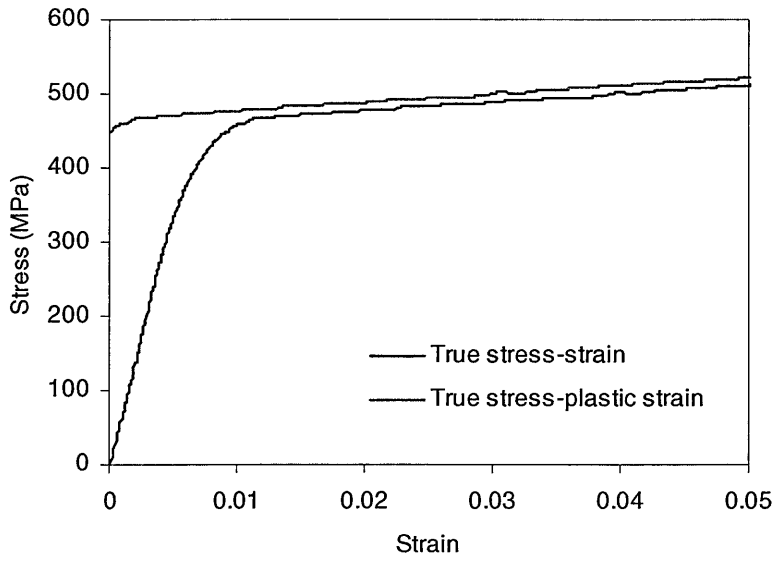

Figure 6.2: Uniaxial true stress-strain curve and the plastic part of the curve for aluminium alloy 5091.

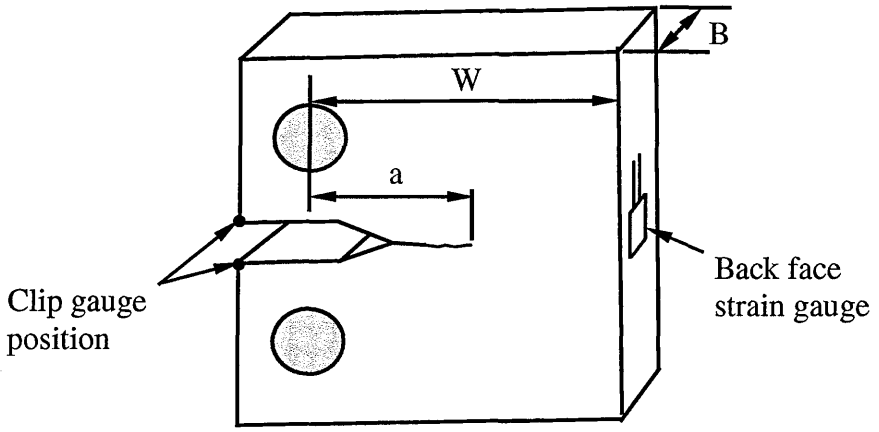

Figure 6.3: Compact tension specimen showing displacement and strain measurement locations.

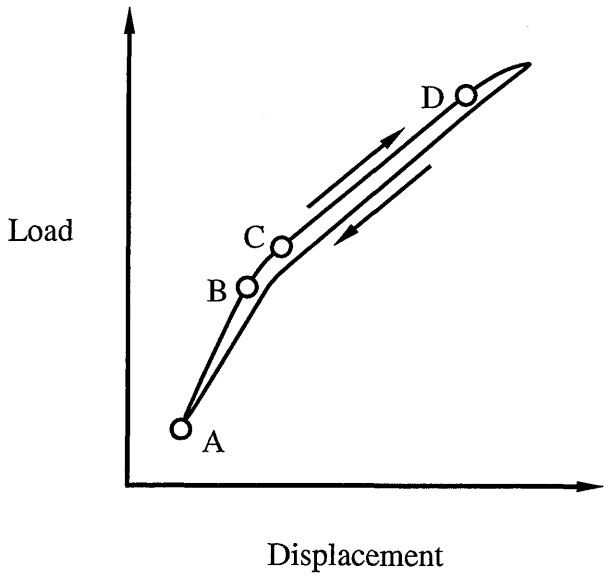

Figure 6.4: A typical load-displacement curve for compliance crack closure measurement.

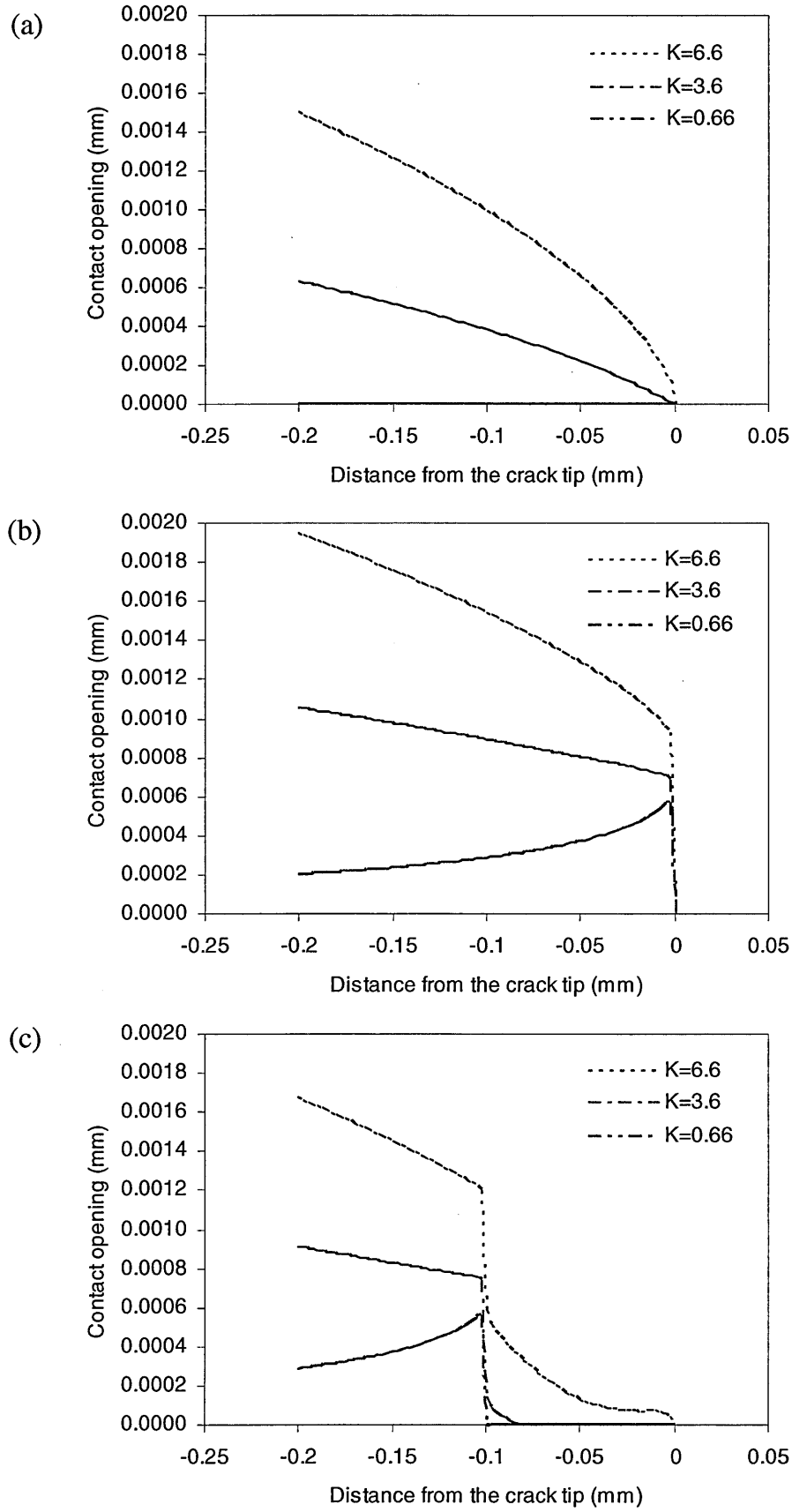

Figure 6.5: Contact opening along the crack surfaces for three different applied K (MPa$\sqrt{m}$) in plane stress: (a) fatigued, (b) fatigued-overloaded and (c) fatigued-overloaded-fatigued cracks.

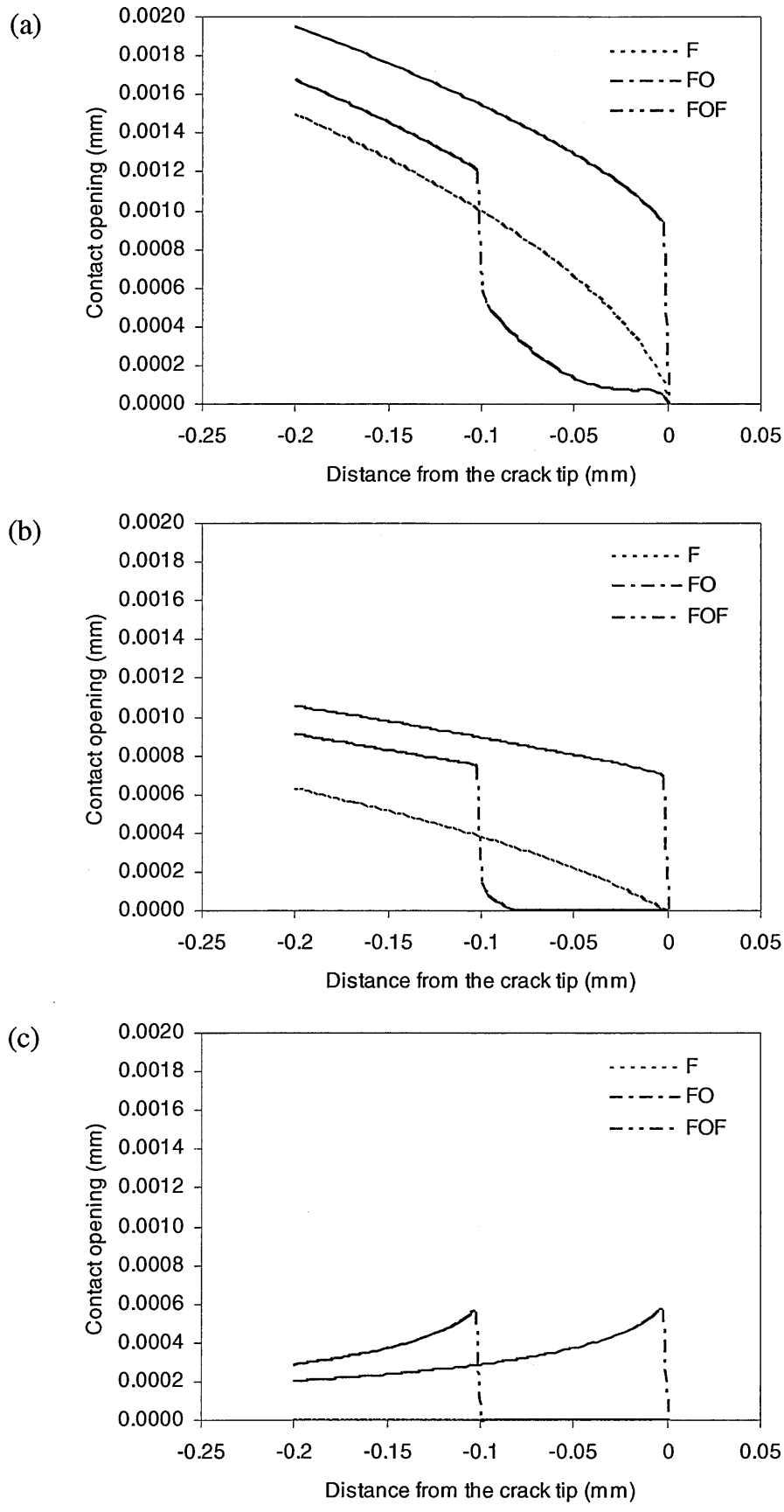

Figure 6.6: Contact opening along the crack surfaces for the fatigued, fatigued-overloaded and fatigued-overloaded-fatigued cracks in plane stress: (a) K=6.6 MPa$\sqrt{m}$, (b) K=3.6 MPa$\sqrt{m}$ and (c) K=0.66 MPa$\sqrt{m}$.

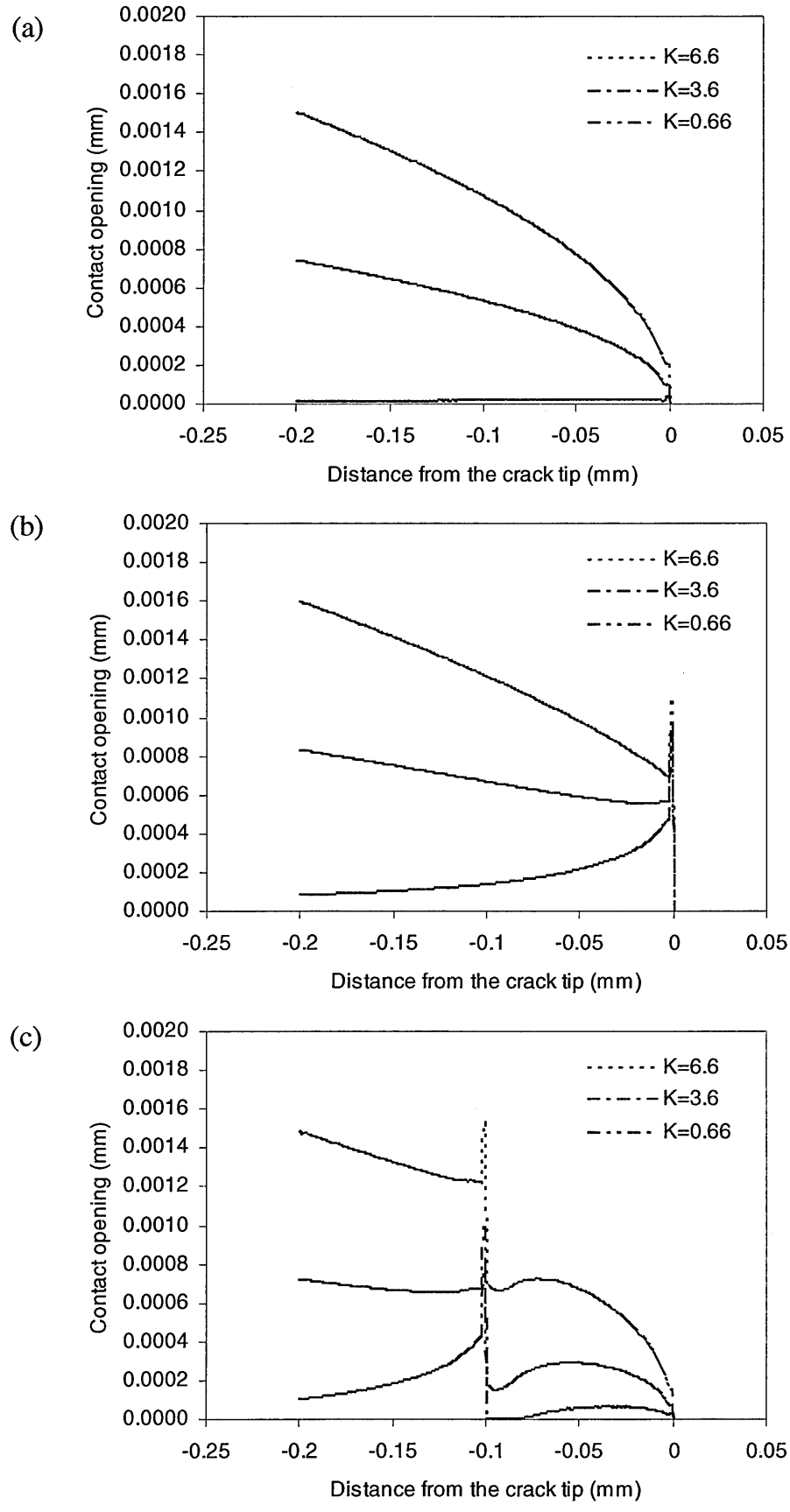

Figure 6.7: Contact opening along the crack surfaces for three different applied K (MPa$\sqrt{m}$) in plane strain: (a) fatigued, (b) fatigued-overloaded and (c) fatigued-overloaded-fatigued cracks.

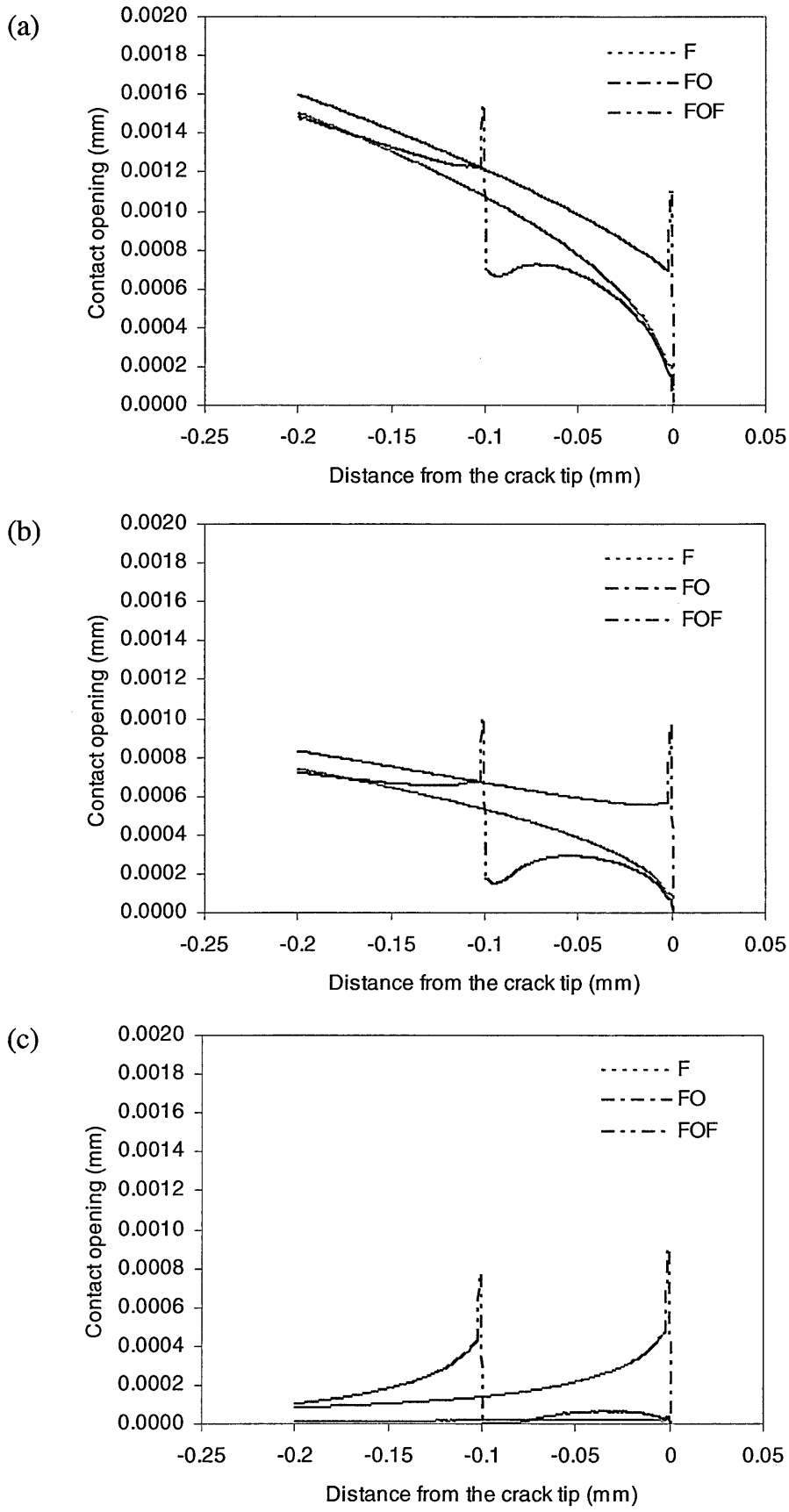

Figure 6.8: Contact opening along the crack surfaces for the fatigued, fatigued-overloaded and fatigued-overloaded-fatigued cracks in plane strain: (a) K=6.6 MPa$\sqrt{m}$, (b) K=3.6 MPa$\sqrt{m}$ and (c) K=0.66 MPa$\sqrt{m}$.

(a)

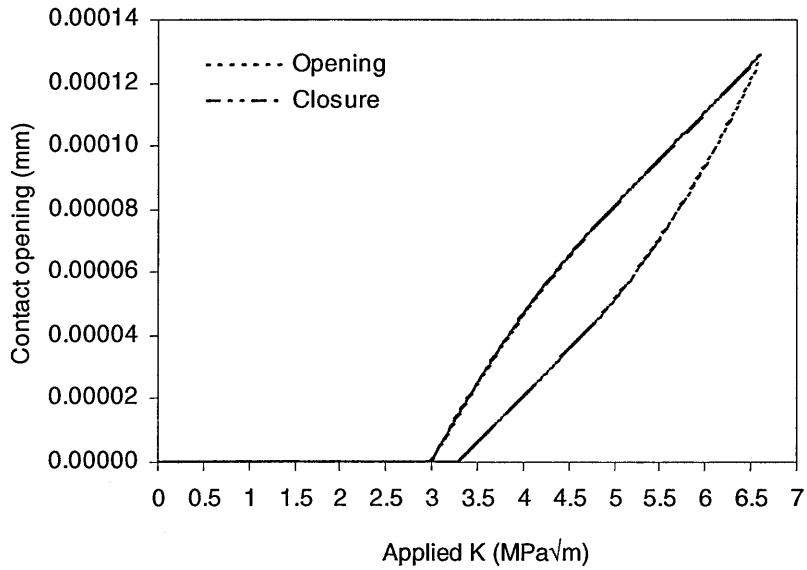

(b)

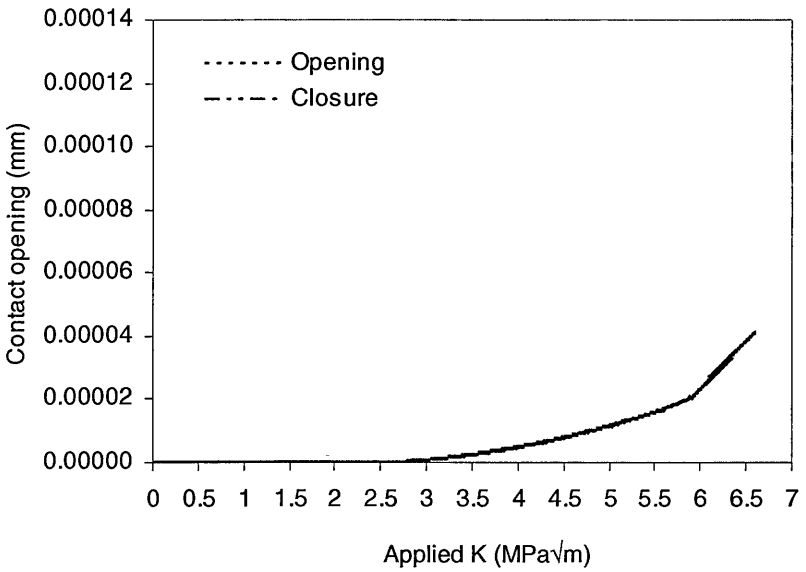

Figure 6.9: Variation of contact opening with applied stress intensity factor at the first node behind the crack tip in plane stress: (a) fatigued crack, (b) fatigued-overloaded-fatigued crack.

(a)

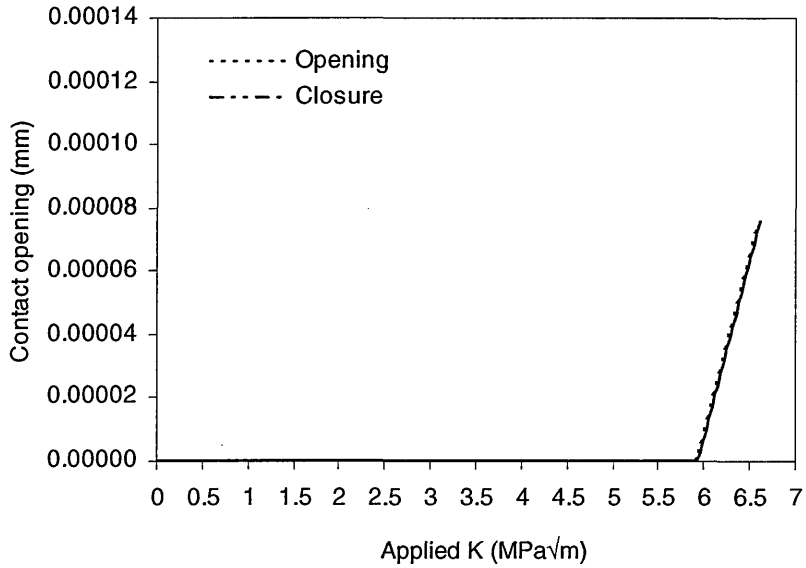

(b)

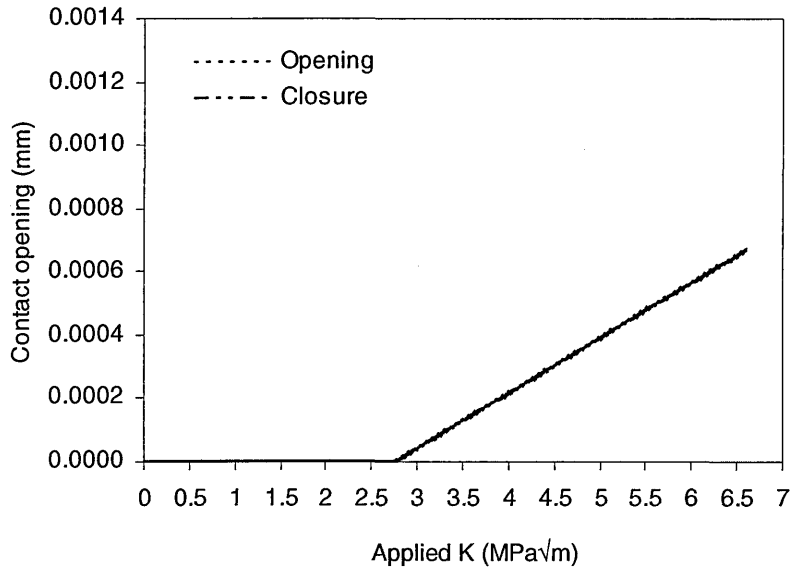

Figure 6.10: Variation of contact opening with applied stress intensity factor at the nodal position between the overload point and the crack tip with the maximum opening and closure levels for the fatigued-overloaded-fatigued crack: (a) plane stress, (a) plane strain.

(a)

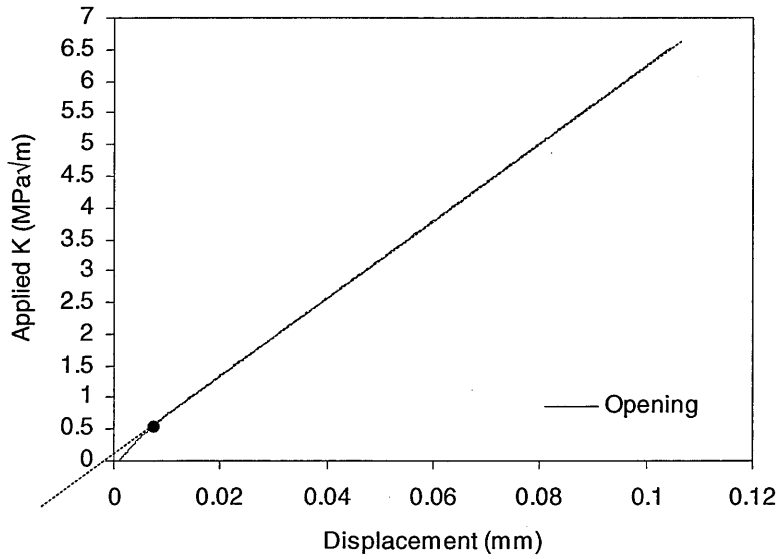

(b)

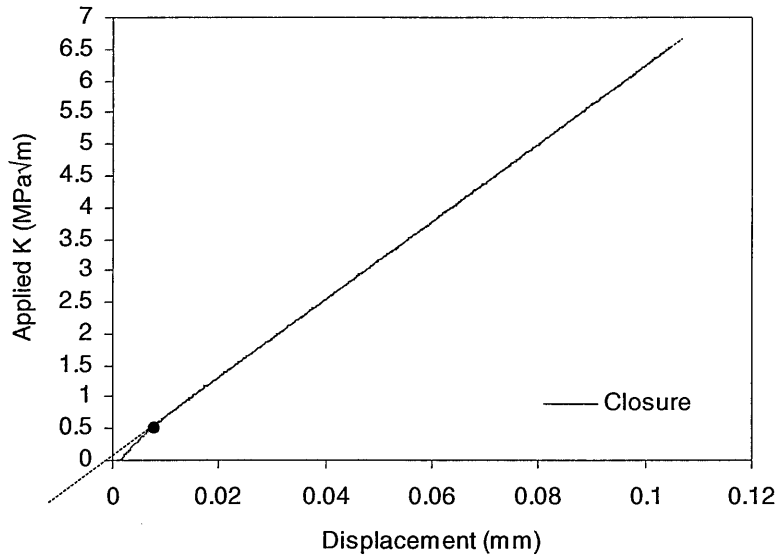

Figure 6.11: Load-displacement curve for the fatigued crack using clip gauge at the crack mouth: (a) loading, (b) unloading.

(a)

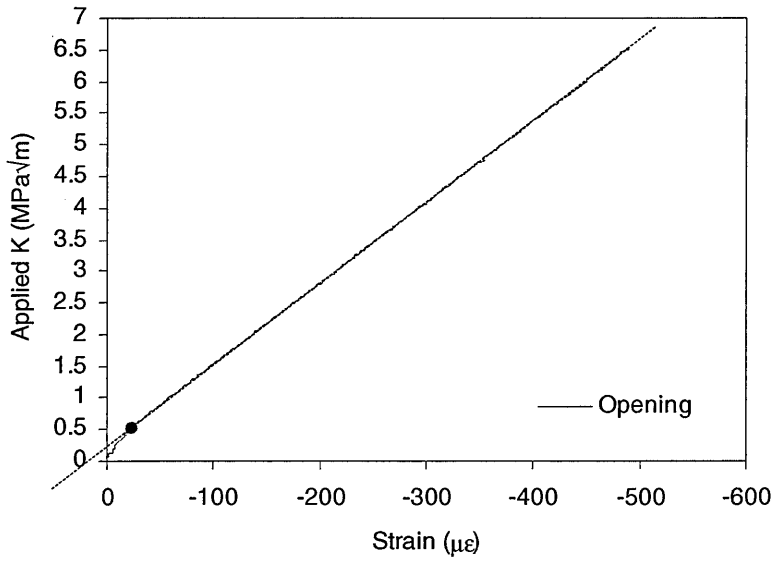

(b)

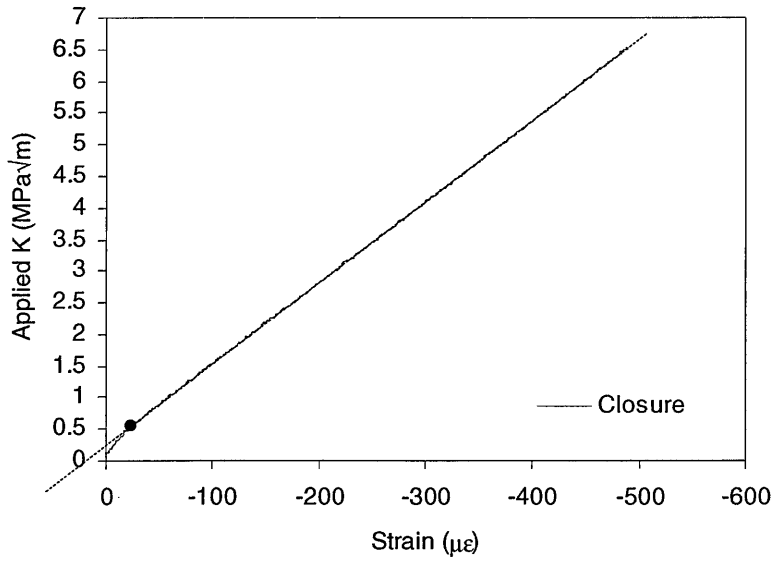

Figure 6.12: Load-strain curve for the fatigued crack using back face strain gauge: (a) loading, (b) unloading.

(a)

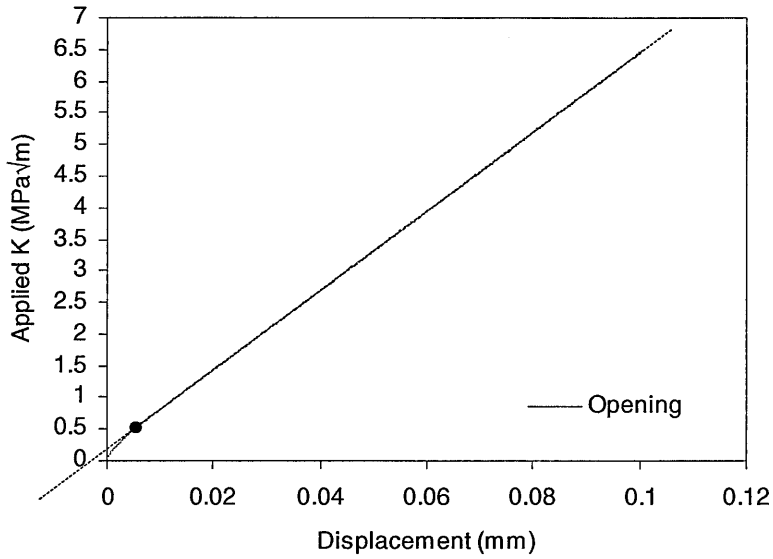

(b)

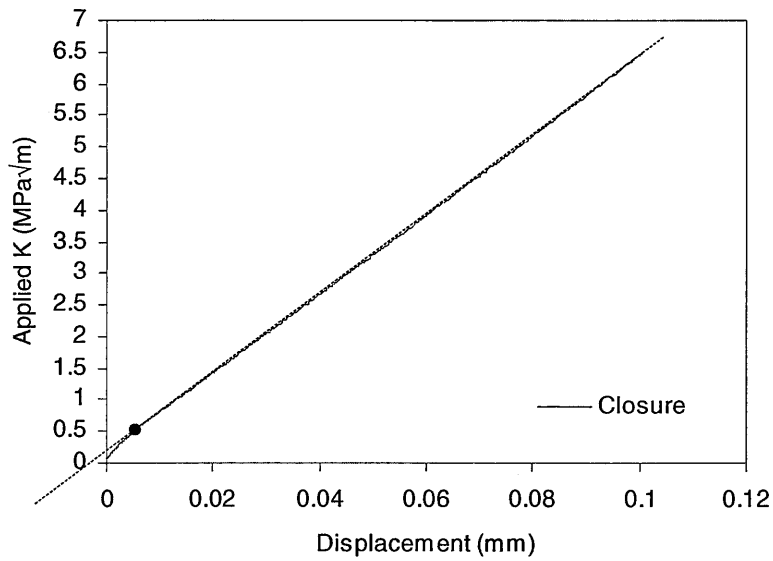

Figure 6.13: Load-displacement curve for the fatigued-overloaded crack using clip gauge at the crack mouth: (a) loading, (b) unloading.

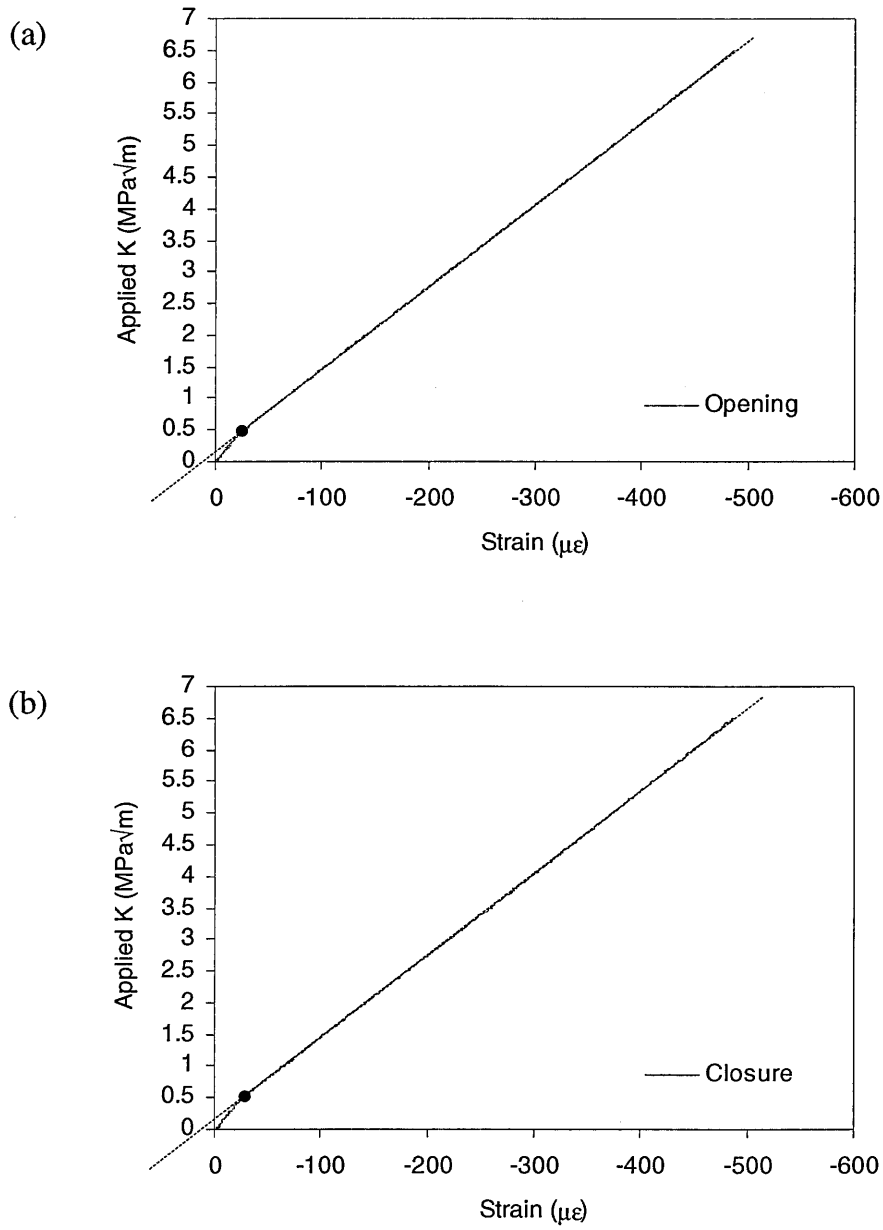

Figure 6.14: Load-strain curve for the fatigued-overloaded crack using back face strain gauge: (a) loading, (b) unloading.

(a)

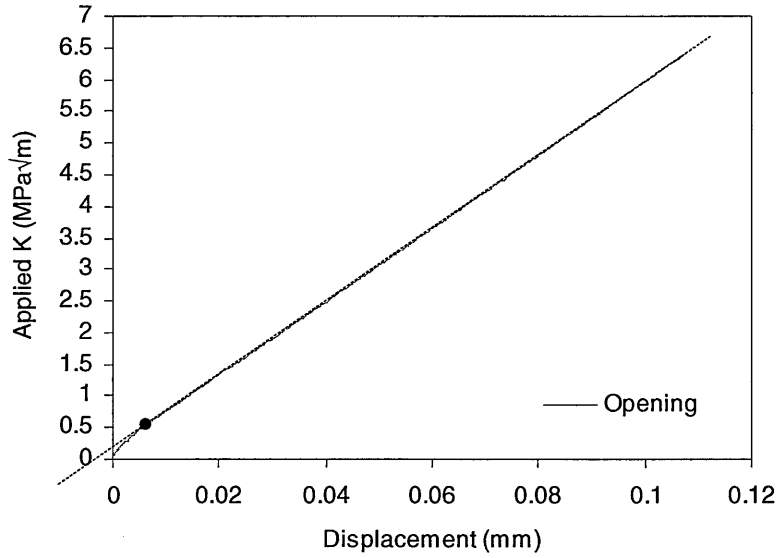

(b)

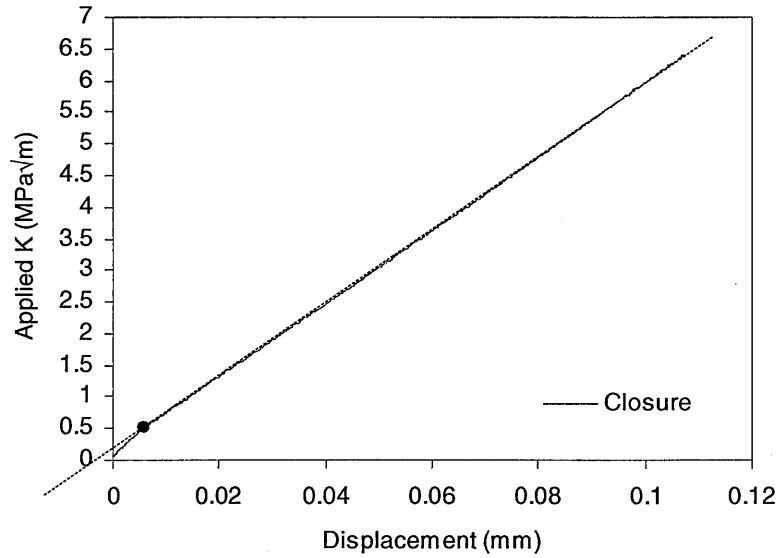

Figure 6.15: Load-displacement curve for the fatigued-overloaded-fatigued crack using clip gauge at the crack mouth: (a) loading, (b) unloading.

(a)

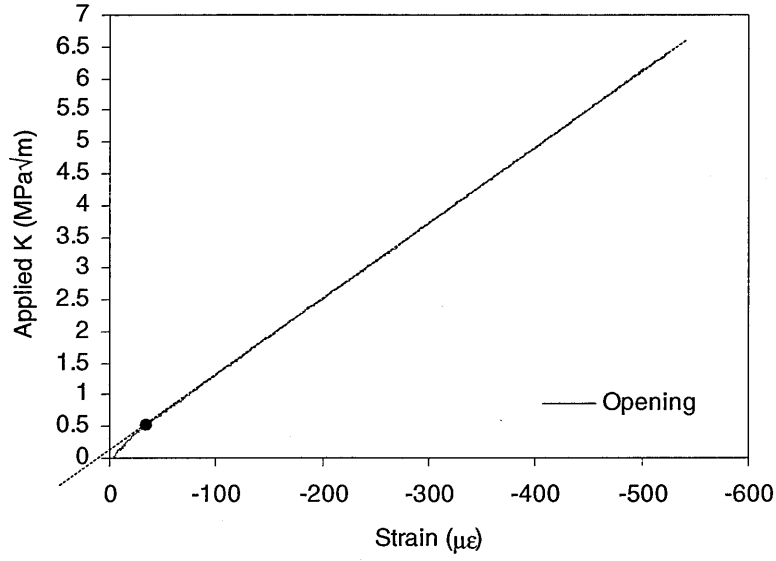

(b)

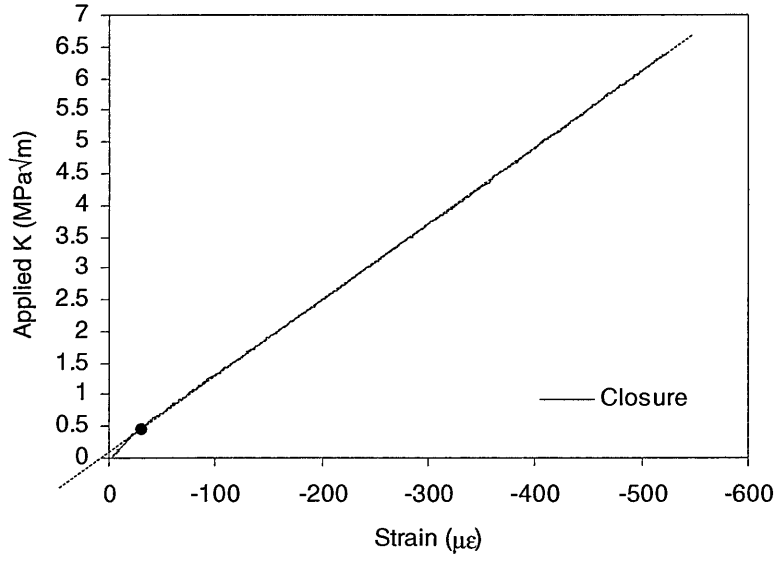

Figure 6.16: Load-strain curve for the fatigued-overloaded-fatigued crack using back face strain gauge: (a) loading, (b) unloading.

Chapter 7 Conclusions and future work

7.1 Conclusions

In the present work, the crack tip strain and stress fields and plasticity-induced crack closure for fatigued, fatigued-overloaded and fatigued-overloaded-fatigued cracks have been investigated in aluminium alloy 5091. The strain and stress fields around the crack tips have been investigated in the interior of compact tension specimens using energy dispersive X-ray diffraction (EDXRD). The fatigued specimen results have been compared with the results obtained by the analytical solution given by Westergaard (1939). A detailed finite element investigation of the stress fields around the fatigued, fatigued-overloaded and fatigued-overloaded-fatigued cracks has been performed in plane stress and plane strain. The finite element results have been compared with the stresses obtained by energy dispersive X-ray diffraction. Plasticity-induced crack closure for the compact tension specimens has been investigated using finite element analysis and the experimental compliance technique.

The energy dispersive X-ray diffraction results in Chapter 4 provide a clear picture of the strain and stress distributions around the fatigued, fatigued-overloaded and fatigued-overloaded cracks in the interior of the specimens (in plane strain region) under various levels of applied loading. In the stress maps and stress profiles for the fatigued-overloaded specimen, the overload effects have been identified by the compressive residual stresses in the crack tip region at K=3.6 and 0.66 (K_{min}) MPa$\sqrt{m}$. The results show that the compressive residual stresses in the vicinity of

the crack tip increase in magnitude and spatial extent with decreasing applied load. The compressive longitudinal residual stresses in the vicinity of the crack tip are mainly responsible for crack retardation. The experimental results also show compressive longitudinal stresses along the crack plane behind the crack tip for all the specimens regardless of loading history and applied loading, although the compressive longitudinal stresses are expected only when the crack is closed, i.e., when the crack surfaces contact. However, in the region ahead of the crack tip in all the specimens, the stresses are consistent with the theoretical predictions.

At K_{max} (6.6 MPa$\sqrt{m}$) the experimental crack tip strains and stresses for the fatigued and fatigued-overloaded-fatigued specimens show good agreement. At K=3.6 MPa$\sqrt{m}$ the comparison between the fatigued-overloaded and fatigued-overloaded-fatigued specimen results show how an overload reduces the strains and stresses in the crack tip region inside the specimen. Moreover, at K_{max} for the fatigued specimen, the experimental stresses ahead of the crack tip show good overall agreement with the analytical results obtained by the Westergaard equations.

The finite element results in Chapter 5 show that an overload reduces the crack tip stresses both at K_{max} and K_{min} both in plane stress and plane strain. Both from the stress profiles in Chapter 5 and contact opening profiles in Chapter 6 it can be concluded that for a constant amplitude fatigue (with K_{max}=6.6 MPa$\sqrt{m}$ and K_{min}=0.66 MPa$\sqrt{m}$), crack closure occurs in plane stress, but not in plane strain as no compressive longitudinal stress develop at the crack tip at K_{min} in plane strain. A 100% (13.2 MPa$\sqrt{m}$) overload causes the crack closure to disappear subsequently in plane stress, but compressive residual stresses ahead of the crack tip region at K_{min}

increase. Subsequent to the overload, compressive residual stresses also develop at the crack tip at K_{min} in plane strain. As a result, with a further 0.1 mm crack growth from the overload point, crack closure occurs all the way from the overload point in plane stress and local closure occurs in the overload-affected region in plane strain. Although the finite element results show that crack closure does not occur in the compact tension geometry in plane strain under constant amplitude fatigue, the resulting closure subsequent to the overload indicates that crack closure may occur in plane strain in compact tension geometry under constant amplitude fatigue if the load (ΔK and K_{max}) is increased.

The finite element investigations of the stress fields in Chapter 5 and crack closure in Chapter 6 show that crack closure occurs for a growing fatigue crack only when compressive residual stresses develop at the crack tip at K_{min} of the loading cycle. The higher the levels of the compressive residual stresses are, the higher the level of crack closure will be. The levels of the compressive residual stresses in the crack tip region are dependent on the size of the tensile plastic zone at the crack tip. These results show that the compressive residual stresses at the crack tip and the crack closure behind the crack tip on the crack flanks are intimately related.

The experimental stresses from the energy dispersive X-ray diffraction measurements show good overall agreement with the plane strain finite element results as the stresses were measured along the mid-thickness of the specimens. It should be mentioned here that most of the previous experimental crack tip stress field investigations were restricted to the near surface (plane stress) region due to the unavailability of an appropriate technique. This work shows the suitability of the

energy dispersive X-ray diffraction for measuring local stresses inside components with high stress gradients.

The results from the experimental crack closure analysis (using a clip gauge at the crack mouth and a back face strain gauge) show low opening levels for all crack types with little or no variation, and thus do not identify the effect of overloading predicted by the finite element analysis. Nevertheless, it is worth mentioning here that the experimental compliance method provides an average value of crack closure over the entire crack front, whilst the two-dimensional finite element model considers localised closure effects. The results from the strain gauge near the crack tip have not been able to identify the opening loads due to the nonlinearities associated with the load-strain curves.

In summary, this work experimentally and numerically investigates the variation of the stress and strain distributions around the crack tips deep inside the aluminium alloy 5091 compact tension specimens (in plane strain region) under in-situ loading for constant amplitude fatigue as well as during and after an overload event. Good agreement between the EDXRD and numerical results enhance the confidence in both EDXRD and numerical methods for stress field investigation inside the thick components. This is thought to be the first investigation of the stress and strain fields around fatigue cracks deep inside the loaded aluminium alloy 5091 specimens. This work also provides a clear understanding of the plasticity-induced crack closure phenomenon in aluminium alloy 5091 compact tension specimens. It is therefore firmly believed that this research has advanced the knowledge and understanding of stress and strain behaviour around fatigue cracks deep inside the specimens, and

plasticity-induced crack closure, and thus has met the aims initially set out in Chapter 1:

- To investigate the 2D crack tip strain and stress fields deep within the loaded aluminium alloy 5091 compact tension specimens using what is believed to be the first direct EDXRD measurements at a high spatial resolution.
- To presentent results under in-situ loading for constant amplitude fatigue as well as during and after an overload event.
- To compare and validate experimental results to those established by the results obtained using finite element analysis.
- To provide a clear understanding of the plasticity-induced crack closure phenomenon in aluminium alloy 5091 compact tension specimens under constant amplitude fatigue and after a single overload event.

7.2 Future work

The present work has investigated in detail the crack tip stress and strain fields and plasticity-induced crack closure for fatigue cracks in aluminium alloy 5091 using compact tension specimens. However, this work can be extended further in future.

Although the energy dispersive X-ray diffraction results provide a clear picture of the strain and stress fields around fatigue cracks inside the specimens under different applied loads, the overload position on the crack flanks 0.1 mm behind the crack tip in the fatigued-overloaded-fatigued specimen has not been identified from the strain and stress distributions. In the present investigation the specimens were fatigue

cracked under relatively small loads (K_{max}=6.6 MPa$\sqrt{m}$ and K_{min}=0.66 MPa$\sqrt{m}$), and an overload of 13.2 MPa$\sqrt{m}$ (100%) was also relatively small to cause sufficient plasticity within the specimen (in plane strain region). In future, compact tension specimens can be prepared with higher cyclic loading and overloads, in order to obtain more plasticity inside the specimens (in plane strain region) for performing energy dispersive X-ray diffraction investigations. Moreover, it would be very interesting to use middle tension (MT) specimens in the investigations as the middle tension specimen has a compressive T-stress, which would have a different effect on the crack tip stress fields and plasticity-induced crack closure. In addition to aluminium alloy 5091 other fine-grained materials such as SC1 (spray-cast alloy 1) and SC2 (spray-cast alloy 2) can also be investigated. SC1 and SC2 are two aluminium alloys with a grain size of 3-5 μm and 5-20 μm respectively (Venning et al., 2006).

In future, fatigue crack growth can be modelled to investigate the influence of load range (ΔK), load ratio (R) and overload on plasticity-induced crack closure in different specimen geometries and for different materials. The present finite element results show that crack closure does not occur in plane strain for a constant amplitude fatigue in compact tension geometry. However, when the crack is grown further after the application of a 100% overload, crack closure occurs in the overload-affected zone in plane strain. These results indicate that crack closure may occur in plane strain in compact tension geometry under constant amplitude fatigue if the load is increased. Therefore, by changing ΔK and R in the FE model this aspect of crack closure can be investigated. A more realistic three-dimensional (3D) finite element model can also be attempted to investigate geometry and loading

effects on crack closure. A 3D model can be useful to locate the incidence of crack closure precisely within a specimen. Furthermore, more efforts may be made to measure crack closure in the specimens using local compliance method (using strain gauge near the crack tip).

References

ABAQUS, Inc., (2004), ABAQUS Version 6.5.

Allison, J.E., (1979), Fracture Mechanics, ASTM STP 677, (C.W. Smith, Ed.), American Society for Testing and Materials, pp. 550-562.

Anderson, T.L., (1995), Fracture Mechanics Fundamentals and Applications, 2nd Edition, CRC Press, Inc., p. 89.

ASTM E 399-90, (1990), Standard Test Method for Plane-Strain Fracture Toughness of Metallic Materials, American Society for Testing and Materials, Philadelphia.

ASTM E 647-00, (2002), Standard test method for measurement of fatigue crack growth rates, In: Annual book of ASTM standards.

Ashbaugh, N.E., Dattaguru, B., Khobaib, M., Nicholas, T., Prakash, R.V. and Ramamurthy, T.S., (1997), Experimental and analytical estimates of fatigue crack closure in an aluminium-copper alloy, Part II: a finite element analysis, Fatigue and Fracture of Engineering Materials and Structures, Vol. 20, pp. 963-974.

Banerjee, S., (1984), AFWAL-TR-84-4031, A review of crack closure, Materials Laboratory, Air Force Wright Aeronautical Laboratories, Air Force Systems Command, Wright-Patterson Air Force Base, Ohio.

Bichler, C. and Pippan, R., (1999), Direct observation of residual plastic deformation caused by a single tensile overload, ASTM STP 1343, pp. 270-291.

Blankenship, C.P., Jr., Bray, G.H., Kaisand, L.R. and Starke, E.A., Jr., (1995), Low cycle fatigue behavior of two Al-Li alloys, Fatigue Fract. Engng Mater. Struct., Vol. 18, pp. 551-564.

Bray, G.H., Reynolds, A.P. and Starke, E.A., Jr., (1992), Mechanisms of fatigue crack retardation following single tensile overloads in powder metallurgy aluminium alloys, Metallurgical Transactions A, Vol. 23A, pp. 3055-3066.

Carboni, M., (2007), Strain-gauge compliance measurements near the crack tip for crack closure evaluation: Applicability and accuracy, Engineering Fracture Mechanics, Vol. 74, pp. 563-577.

Croft, M., Zhong, Z., Jisrawi, N., Zakharchenko, I., Holtz, R.L., Skaritka, J., Fast, T., Sadananda, K., Lakshmipathy, M. and Tsakalakos, T., (2005), Strain profiling of fatigue crack overload effects using energy dispersive X-ray diffraction, International Journal of Fatigue, Vol. 27, pp. 1408-1419.

Damri, D. and Knott, J.F., (1991), Transient retardation in fatigue crack growth following a single peak overload, Fatigue Fract Engng Mater Struct, Vol. 14, pp. 709-719.

Daymond, M.R. and Withers, P.J., (1996), Scr. Mater., Vol. 35, pp. 1229-1234.

Donahue, R.J., Clark, H.M., Atanmo, P., Kumble, R. and McEvily, A.J., (1972), Crack Opening Displacement and the Rate of Fatigue Crack Growth, International Journal of Fracture Mechanics, Vol. 8, pp. 209-219.

Elber, W., (1970), Fatigue Crack Closure Under Cyclic Tension, Engineering Fracture Mechanics, Vol. 2, pp. 37-45.

Elber, W., (1971), The significance of fatigue crack closure, ASTM STP 486, pp. 230-242.

Fitzpatrick, M.E., Fry, A.T., Holdway, P., Kandil, F.A., Shackleton, J. and Suominen, L., (2002), Determination of Residual Stresses by X- Ray Diffraction-A Good Practice Guide, National Physical Laboratory, London.

Fleck, N.A., (1982), Technical Report, CUED/C/MATS/TR-89, Cambridge University Engineering Department.

Fleck, N.A. and Smith, R.A., (1982), Crack closure-is it just a surface phenomenon? International Journal of Fatigue, July 1982, Butterworth & Co (Publishers) Ltd, pp. 157-160.

Fleck, N.A., (1986), Finite element analysis of plasticity-induced crack closure under plane-strain conditions, Engineering Fracture Mechanics, Vol. 25, pp. 441-449.

Research Conference Proceedings, Vol. 4.

James, M.N., Hattingh, D.G., Hughes, D.J., Wei, L.-W., Patterson, E.A. and Quinta Da Fonseca, J., (2004), Synchrotron diffraction investigation of the distribution and influence of residual stresses in fatigue, Fatigue Fract Engng Mater Struct, Vol. 27, pp. 609-622.

Klesnil, M. and Lukas, P., (1972), Influence of Strength and Stress History on Growth and Stabilization of Fatigue Cracks, Engineering Fracture Mechanics, Vol. 4, pp. 77-92.

Knapp, G.S., Beno, M.A. and You, H., (1996), Annual Review of Materials Science, 26, 693

Kunz, C., (1979), Properties of synchrotron radiation, in Synchrotron Radiation-Techniques and Applications, C. Kunz (editor), Springer Verlag: Berlin. pp. 1-24.

Lang, M. and Marci, G., (1999), The influence of single and multiple overloads on fatigue crack propagation, Fatigue Fract Engng Mater Struct, Vol. 22, pp. 257-271.

Larson, A.C. and Von Dreele, R.B., (2000), General Structure Analysis System (GSAS), Los Alamos National Laboratory Report LAUR 86-748.

LeBail, A., Duroy, H. and Fourquet, J.L., (1988), Mater: Res. Bull. 23, 447.

Lebrun, J.L., Gergaud, P., Ji, V. and Belassel, M., (1995), J. Phys. (France) IV, Vol. 4, pp. 265-268.

Lee, H.-J. and Song, J.-H., (2005), Finite-element analysis of fatigue crack closure under plane strain conditions: stabilization behaviour and mesh size effect, Fatigue Fract Engng Mater Struct, Vol. 28, pp. 333-342.

Lienert, U., Poulsen, H.F. and Kvick, Å., (2001), AIAA Journal, 39, pp. 919-923.

Mageed, A.M.A., Pandey, R.K. and Chinadurai, R., (1992), Materials Science and Engineering, A150, pp. 43-50.

Matsuoka, S. and Tanaka, K., (1978), Delayed retardation phenomena of fatigue crack growth in various steels and alloys, J. Mater Sci, Vol. 13, pp. 1335-1353.

McClung, R.C. and Sehitoglu, H., (1989), On the finite element analysis of fatigue crack closure-1. Basic modelling issues, Engineering Fracture Mechanics, Vol. 33(2), pp. 237-252.

McClung, R.C., Thacker, B.H. and Roy, S., (1991), Finite element visualization of fatigue crack closure in plane-stress and plane-strain, International Journal of Fracture, Vol. 50, pp. 27-49.

McEvily, A.J., (1988), On Closure in Fatigue Crack Growth, ASTM STP 982, American Society for Testing and Materials, Philadelphia, pp. 35-43.

McEvily, A.J. and Ishihara, S., (2001), On the retardation in fatigue crack growth rate due to an overloading: a review, In: Proceedings of the Fatigue 2001 SAE Brazil International, Sao Paulo, Brazil.

Mises, R., (1913), Göttinger Nachrichten Math. Phys. Klasse p. 582.

Newman, J.C., (1976), In Mechanics of Crack Growth, ASTM STP 590, American Society for Testing and Materials, pp. 281-301.

Newman, J.C., (1997), The merging of fatigue and facture mechanics concepts: a historical perspective, In: Underwood J.H. et al. editors, Fatigue and fracture mechanics, ASTM STP 1321, pp. 3-5.

Ogura, K. and Ohji, K., (1977), In Engineering Fracture Mechanics, Vol. 9, pp. 471-480.

Paris, P.C., Gomez, M.P. and Anderson, W.P., (1961), A rational analytical theory of fatigue, The Trend in Engineering, Vol. 13, pp. 9-14.

Paris, P.C. and Erdogan, F., (1963), A Critical Analysis of Crack Propagation Laws, Journal of Basic Engineering, Transactions ASME Series D, Vol. 85, pp. 528-534.

Pommier, S. and Bompard, P., (2000), Bauschinger effect of alloys and plasticity-induced crack closure: A finite element analysis, Fatigue and Fract Engng Mater Struct, Vol. 23, pp. 129-139.

Pook, L.P., (1983), The Role of Crack Growth in Metal Fatigue, Metals Society: London.

Pratihar, S., (2006), Residual stress measurement on different length scales using neutron and synchrotron X-ray diffraction, PhD thesis, Department of Materials Engineering, The Open University, Milton Keynes, UK.

Ramos, M.S., Pereira, M.V., Darwish, F.A., Motta, S.H. and Carneiro, M.A., (2003), Effect of single and multiple overloading on the residual fatigue life of a structural steel, Fatigue Fract Engng Mater Struct, Vol. 26, pp. 115-121.

Rice, J.R., (1967), Mechanics of Crack-Tip Deformation and Extension by Fatigue, ASTM STP 415, American Society for Testing and Materials, Philadelphia, pp. 247-309.

Rice, J. R., (1974), Limitations to the small scale yielding approximation for crack tip plasticity, Journal of the Mechanics and Physics of Solids, Vol. 22, pp.17-26.

Riekel, C., (2003), The use of synchrotron radiation for materials research, in Analysis of residual stress by diffraction using neutron and synchrotron radiation, M.E. Fitzpatrick and A. Lodini (editors), Taylor & Francis, London, pp. 28-44.

Roychowdhury, S. and Dodds, R.H., Jr., (2005), Effects of an overload event on crack closure in 3-D small-scale yielding: finite element studies, Fatigue Fract Engng Mater Struct, Vol. 28, pp. 891-907.

Sadananda, K., Vasudevan, A.K., Holtz, R.L. and Lee, E.U., (1999), Analysis of overload effects and related phenomena, International Journal of Fatigue, Vol. 21, pp. 233-246.

Sander, M. and Richard, H.A., (2005), Finite element analysis of fatigue crack growth with interspersed mode I and mixed mode overloads, International Journal of Fatigue, Vol. 27, pp. 905-913.

Sander, M. and Richard, H.A., (2006), Experimental and numerical investigations on the influence of the loading direction on the fatigue crack growth, International Journal of Fatigue, Vol. 28, pp. 583-591.

Schelleng, R.D., Gilman, P.S. and Donachie, S.J., (1985), Aluminiunm-magnesium-lithium forging alloy made by mechanical alloying, 17th National SAMPE Technical Conference, October 22-24, pp. 106-115.

Schijve, J., (1961), Fatigue crack propagation in light alloy sheet material and structures, Adv. Aeronaut. Sci., Vol. 3, pp. 387-408.

Sherry, A.H., France, C.C. and Goldthorpe, M.R., (1995), Compendium of T-stress solutions for two and three-dimensional cracked geometries, Fatigue and Fracture of Engineering Materials and Structures, Vol. 18, pp. 141-155.

Shin, C.S. and Fleck, N.A., (1987), Overload retardation in a structural steel, Fatigue Fract Engng Mater Struct, Vol. 9, pp. 379-393.

Skorupa, M., Machniewicz, T. and Skorupa, A., (2007), Applicability of the ASTM compliance offset method to determine crack closure levels for structural steel, International Journal of Fatigue, Vol. 29, pp. 1434-1451.

Steuwer, A., Santisteban, J.R., Turski, M., Withers, P.J. and Buslaps, T., (2004), High-resolution strain mapping in bulk samples using full-profile analysis of energy-dispersive synchrotron X-ray diffraction data, Journal of Applied Crystallography, Vol. 37, pp. 883-889.

Steuwer, A., Edwards, L., Pratihar, S., Ganguly, S., Peel, M., Fitzpatrick, M.E., Marrow, T.J., Withers, P.J., Sinclair, I., Singh, K.D., Gao, N., Buslaps, T. and Buffière, J.-Y., (2006), In situ analysis of cracks in structural materials using synchrotron X-ray tomography and diffraction, Nuclear Instruments and Methods in Physics Research B, Vol. 246, pp. 217-225.

Sun, W. and Sehitoglu, H., (1992), Residual stress fields during fatigue crack growth, Fatigue Fract. Engng Mater. Struct., Vol. 15, pp. 115-128.

Tamura, N., Macdowell, A.A., Celestes, R.S., Padmore, H.A., Valek, B., Bravman, J.C., Spolenak, R., Brown, W.L., Marieb, T., Fujimoto, H. and Batterman, B.W., (2002), Applied Physics Letters, 20, 3724.

Toribio, J. and Kharin, V., (2006), Crack-tip stress-strain fields during cyclic loading and effect of overload, International Journal of Fracture, Vol, 139, pp. 333-340.

Tresca, H., (1864), Comptes Rendus Acad. Sci, Paris 59, p. 754.

Tsakalakos, T., Croft, M., Jisrawi, N., Holtz, R. and Zhong, Z., (2006), Measurement of residual stress distributions by energy dispersive X-ray diffraction synchrotron radiation, Proceedings of the Sixteenth International Offshore and Polar Engineering Conference, May 28-June 2, San Francisco, California, USA, pp. 57-64.

Venning, L., Hogg, S.C., Sinclair, I. and Reed, P.A.S., (2006), Fatigue crack growth and closure in fine-grained aluminium alloys, Materials Science and Engineering A, Vol. 428, pp. 247-255.

Wang, H., Buchholz, F.-G., Richard, H.A., Jägg, S. and Scholtes, B., (1999), Numerical and experimental analysis of residual stresses for fatigue crack growth, Computational Materials Science, Vol. 16, pp. 104-112.

Ward-Close, C.M., Blom, A.F. and Ritche, R.O., (1989), Mechanisms associated with transient fatigue crack growth under variable-amplitude loading: an example and numerical study, Engng Fract Mech, Vol. 32, pp. 613-638.

Webster, P.J., Mills, G., Wang, X.D., Kang, W.P. and Holden, T.M., (1996), J. Neutr. Res., Vol. 3, pp. 223-240.

Weertman, J., (1966), Rate of Growth of Fatigue Cracks Calculated from the Theory of Infinitesimal Dislocations Distributed on a Plane, International Journal of

Fracture Mechanics, Vol. 2, pp. 460-467.

Wei, L.-W. and James, M.N., (2000), A study of fatigue crack closure in polycarbonate CT specimens, Engineering Fracture Mechanics, Vol. 66, pp. 223-242.

Westergaard, H.M., (1939), Bearing Pressures and Cracks, Journal of Applied Mechanics, Vol. 6, pp. 49-53.

Wheeler, O.E., (1972), Spectrum loading and crack growth, Journal of Basic Engineering, Vol. 94, pp. 181-186.

Williams, M.L., (1957), On the Stress Distribution at the Base of a Stationary Crack, Journal of Applied Mechanics, Vol. 24, pp. 109-114.

Winick, H., (1980), Properties of synchrotron radiation, in Synchrotron Radiation Reseacrh, H. Winick and S. Doniach (editors), Plenum Press: New York. pp. 11-26.

Withers, P.J. and Bhadeshia, H.K.D.H., (2001), Overview, Residual stress, Part 1-Measurement techniques, Materials Science and Technology, Vol. 17, pp. 355-365.
Withers, P.J. and Bhadeshia, H.K.D.H., (2001), Overview, Residual stress, Part 2-Nature and origins, Materials Science and Technology, Vol. 17, pp. 366-375.

Withers, P.J., (2001), in Encyclopaedia of materials science and technology, (ed. K.H.J. Buschow et al.), Oxford, Pergamon.

Withers, P.J. and Webster, P.J., (2001), Strain, Vol. 37, pp. 19-33.

Withers, P.J., (2001), Residual Stresses: Measurement by Diffraction, Encyclopaedia of Materials: Science and Technology, pp. 8158-8170.

Withers, P.J., (2003), Use of synchrotron X-ray radiation for stress measurement, in Analysis of residual stress by diffraction using neutron and synchrotron radiation, M.E. Fitzpatrick and A. Lodini (editors), Taylor & Francis, London, pp. 170-189.

Zhao, L.G., Tong, J. and Byrne, J., (2004), The evaluation of the stress-strain fields near a fatigue crack tip and plasticity-induced crack closure revisited, Fatigue Fract Engng Mater Struct, Vol. 27, pp. 19-29.